

STAVEBNÍ OBZOR

ČÍSLO 3/2017

Obsah čísla:

A FULL-SCALE MEASUREMENT OF WIND ACTIONS AND EFFECTS ON A SEA-CROSSING BRIDGE

Yi Zhou, Limin Sun, Mowen Xie

NANOTECHNOLOGY IN THE CULTURAL HERITAGE – INFLUENCE OF NANOSPENSIONS ADOPTED BY NANOPARTICLES OF TiO₂ FOR CLEANING THE SURFACE OF HISTORICAL PLASTERS

Klára Kroftová, Markéta Šmidtová, Ivo Kuřitka a David Škoda

ANALYSIS ON THE INFLUENCE OF ACCUMULATION EFFECT OF LANDSCAPE COLOR ON TRAFFIC SAFETY IN THE FOGGY SECTIONS OF EXPRESSWAYS

Xilei Li, Boming Tang, Qianghui Song

HYBRID CONTINUUM-DISCONTINUUM MODELLING OF ROCK FRACUTRE PROCESS IN BRAZILIAN TENSILE STRENGTH TEST

Huaming An, Hongyuan Liu, Xuguang Wang, Jianjun Shi, Haoyu Han

DEVELOPMENT AND PROSPECT OF ROOT PILES IN TUNNEL FOUNDATION REINFORCEMENT

Hao Ding, Linjian Su, Jinxing Lai, Yuanhang Zhang

STRENGTHENING OF A REINFORCED CONCRETE BRIDGE WITH PRESTRESSED STEEL WIRE ROPES

Kexin Zhang, Quansheng Sun

APPLICATION OF DEPTH-FIRST SEARCH METHOD IN FINDING RECIRCULATION IN MINE VENTILATION SYSTEM

Huaming An, Jianjun Shi, Xuguang Wang, Lixing Lyu

COMPARISON OF SELECTED PHYSICAL PROPERTIES OF TESTED NANOSUSPENSIONS – THE RESULTS OF THE EXPERIMENTAL RESEARCH OF THE DEGREE OF SEDIMENTATION AND THE DEPTH OF PENETRATION IN REFERENCE MATERIALS IN LABORATORY CONDITIONS

Klára Kroftová, Markéta Šmidtová, Ivo Kuřitka, David Škoda

CALIBRATION OF VISSIM MODEL FOR MULTILANE HIGHWAYS USING SPEED FLOW CURVES

Seelam Srikanth, Arpan Mehar, Asish Parihar

APPLICATION OF AEM IN PROGRESSIVE COLLAPSE DYNAMICS ANALYSIS OF R.C. STRUCTURES

Osama El-Mahdy, El-Sayed El-Kasaby, Hala Abusafa, Amr El-Gamal

RESEARCH ON RISK CLASSIFICATION METHOD OF ASSEMBLY OCCUPANCIES

Hao Yu

A FULL-SCALE MEASUREMENT OF WIND ACTIONS AND EFFECTS ON A SEA-CROSSING BRIDGE

Yi Zhou¹, Limin Sun^{2,*} and Mowen Xie¹

1. *University of Science & Technology Beijing, Department of Civil Engineering, Beijing, China; zhouyi@ustb.edu.cn (Y. Z.); mowenxie@ustb.edu.cn (M. X.)*
 2. *State Key Laboratory of Disaster Reduction in Civil Engineering, Tongji University, Shanghai, China; lmsun@tongji.edu.cn*
- * *Corresponding Author*

ABSTRACT

Wind loading is critical for the large-span and light-weight structures, and field measurement is the most effective way to evaluate the wind resistance performance of a specific structure. This study investigates the wind characteristics and wind-induced vibration on a sea-crossing bridge in China, namely Donghai Bridge, based on up to six years of monitoring data. It is found that: (1) there exists obvious discrepancy between the measured wind field parameters and the values suggested by the design code; and the wind records at the bridge site is easily interfered by the bridge structure itself, which should be considered in interpreting the measurements and designing structural health monitoring systems (SHMS); (2) for strong winds with high non-stationarity, a shorter averaging time than 10-min is preferable to obtain more stable turbulent wind characteristics; (3) the root mean square (RMS) of the wind-induced acceleration of the girder may increase in an approximately quadratic curve relationship with the mean wind speed; and (4) compared to traffic load, the wind dominates the girder's lateral vibration amplitude, while the heavy-load traffic might exert more influence on the girder's vertical and torsional vibrations than the high winds. This study provides field evidence for the wind-resistant design and evaluation of bridges in similar operational conditions.

KEYWORDS

Sea-crossing bridge, Wind field, Wind-induced vibration, Structural health monitoring

1. INTRODUCTION

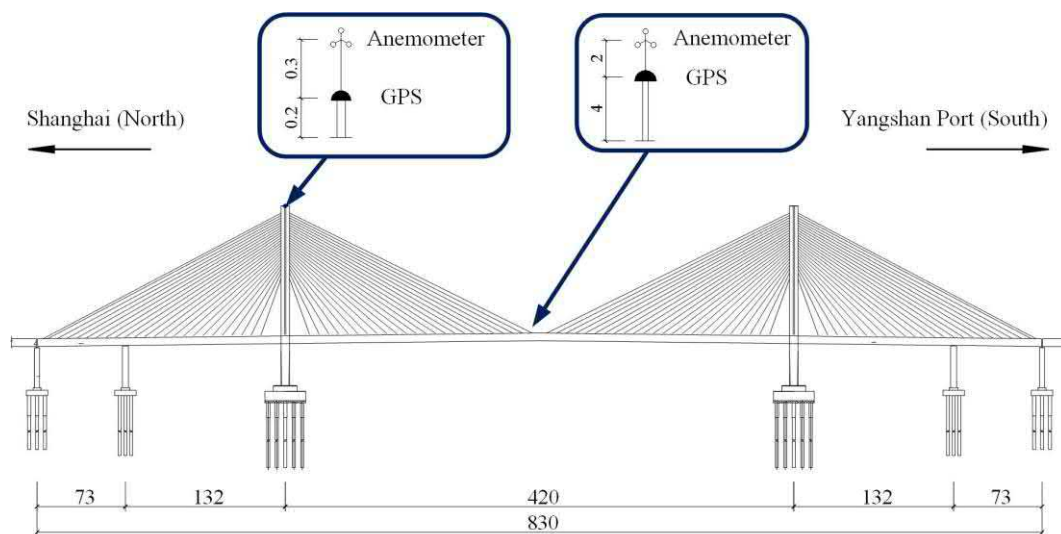
Wind is one of critical loads on large-span and light-weight structures. As the new span record continues to refresh, wind resistance performance of bridges is becoming more and more important. With the development of the structural health monitoring (SHM) technology, many long-span bridges around the world are equipped with structural health monitoring systems (SHMS) to monitor the wind fields on site and the wind-induced responses of structures [1]. Compared with wind tunnel experiments and numerical simulation, field measurement is a more straightforward and effective way to determine the wind-induced responses of the real bridges under the real wind loading. In recent years, the SHM-based researches on wind resistance of bridges have attracted an increasing amount of attention. Case studies include the Tsing Ma Suspension Bridge[2], Runyang Suspension Bridge [3], Sutong Bridge [4], Dongting Lake Bridge [5], Xihoumen Suspension Bridge [6-7], Hangzhou Jiubao Bridge [8], Humber Bridge [9], Akashi Kaikyo Bridge [10], Hakucho Bridge [11], Fred Hartman Bridge [12], and so on.

Each bridge has its own structural configuration and wind field characteristics. As a result, the field observation of wind effects may vary greatly among different bridges, and thus separate

studies are required for individual cases. Based on six years of monitoring data from Donghai Bridge in China, the authors investigated the wind actions and effects on this famous sea-crossing bridge. With a total length of 32.5 km, Donghai Bridge is a super infrastructure which links Shanghai City and the Yangshan Deepwater Container Port. It is located in the typhoon-prone area of the northwestern Pacific Ocean, so the severe wind field is remarkably distinct from the inland bridges. Meanwhile, 80% of the vehicles traversing the bridge are heavy-load container trucks, resulting in a higher level of traffic load than ordinary highway bridges. Hence, both the dynamic effects of high winds and heavy-load traffic are significant on this bridge. The unique environmental and operational conditions make the full-scale measurement research on Donghai Bridge extremely valuable.

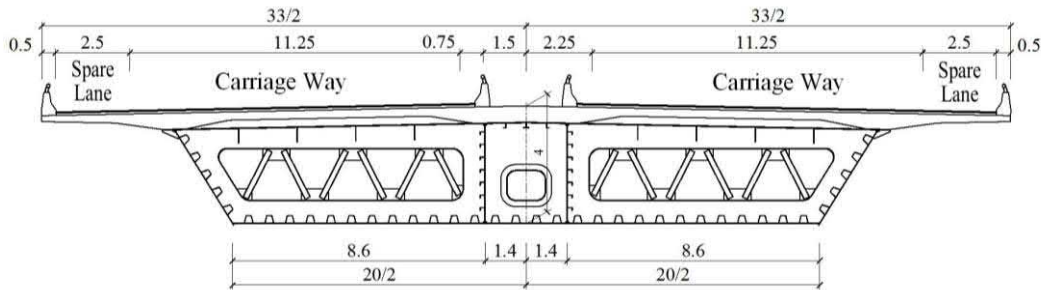
In order to support the bridge management and maintenance, an advanced SHMS was installed on Donghai Bridge in 2006. The majority of sensors are deployed on the main navigational opening (hereinafter referred to as Donghai Bridge for brevity), which is a twin-pylon cable-stayed bridge with a three-cell, steel-concrete composite box girder (Figure 1). There are two anemometers in the monitoring system, one in the mid-span of the girder and the other on the top of the north tower (Figure 1). They can measure wind speed and direction in the horizontal plane with a wind speed range of 0.4 m/s–75 m/s, and have a sampling frequency of 1 Hz. The elevations of the two anemometers are respectively 159.50 m and 58.15 m above the sea level incorporating the sensor’s masts. The vast amount of monitoring data recorded by them provides a solid basis for this study.

The rest of this paper consists of three parts. Section 2 discusses the statistical characteristics of the on-site wind field from 2007–2012. The measured parameters are compared with the suggested values in China’s “Wind-Resistant Design Specification for Highway Bridges” [13] (hereinafter referred to as the Code) or the assumed values in the design stage [14], with an attempt to feedback the design assumptions of Donghai Bridge. Section 3 deliberates on the wind-induced acceleration of the girder, and compares the dynamic effects of strong wind and heavy-load traffic on the bridge vibration. The findings would provide reference information for the traffic control of Donghai Bridge under strong winds, and also benefit the wind-resistant evaluation of bridges in similar operational conditions. Finally, the summary of this paper is presented in the last part.



(a) Elevation view

Fig. 1 - Donghai Bridge and the anemometers on it (units: m)



(b) Standard cross-section of girder

Fig. 1 - Donghai Bridge and the anemometers on it (units: m)

2. WIND CHARACTERISTICS

The records of wind direction and wind speed over six years are retrieved and processed through the conventional vector decomposition method [15] with 10-min averaging time intervals to obtain 10-min mean wind speed \bar{U} as well as along-wind (longitudinal) and across-wind (transverse) turbulent wind speeds (i.e., u and v , respectively). After excluding outliers in the measurements, the characteristics of mean winds and turbulent winds at the bridge site are computed based on approximately 270,000 10-min data sets from the bridge deck and 230,000 from the top of the tower.

2.1. Wind direction frequency

Figures 2 and 3 show the wind roses of the 10-min mean wind at the bridge deck and at the top of tower for six years respectively. The wind speed groups in the figures are based on the Beaufort wind scale [16] without height modification; and the radial length in the wind rose is proportional to the percentage of the data sets for a given wind speed and direction in the total number of data sets, while the tangential length of the plots is meaningless but just for enhancing visualization. There is a clear difference in the prevailing wind direction between the two measuring points. This might be attributed to the deflection of near-ground wind or, more likely, to the disturbance of wind fields caused by the bridge structure.

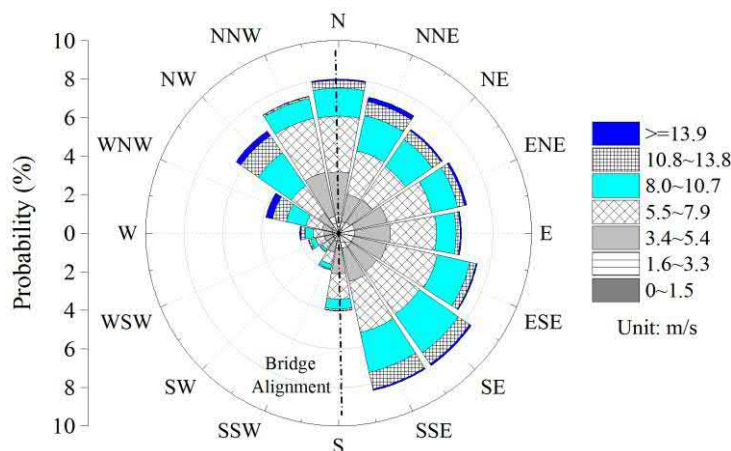


Fig. 2 - Measured wind frequency at the deck

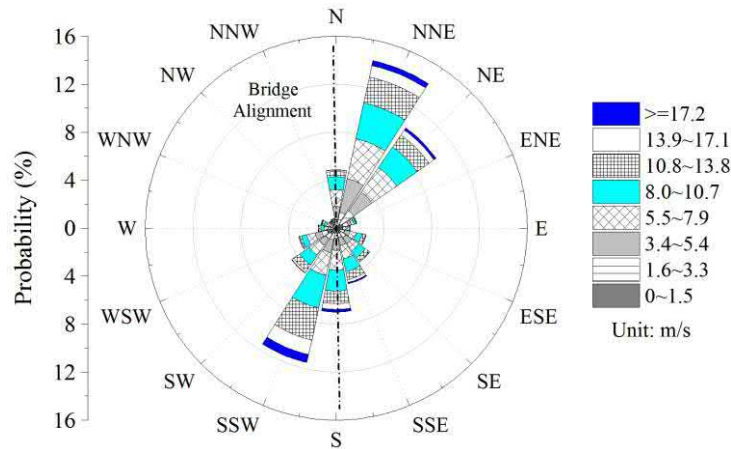


Fig. 3 - Measured wind frequency at the tower top

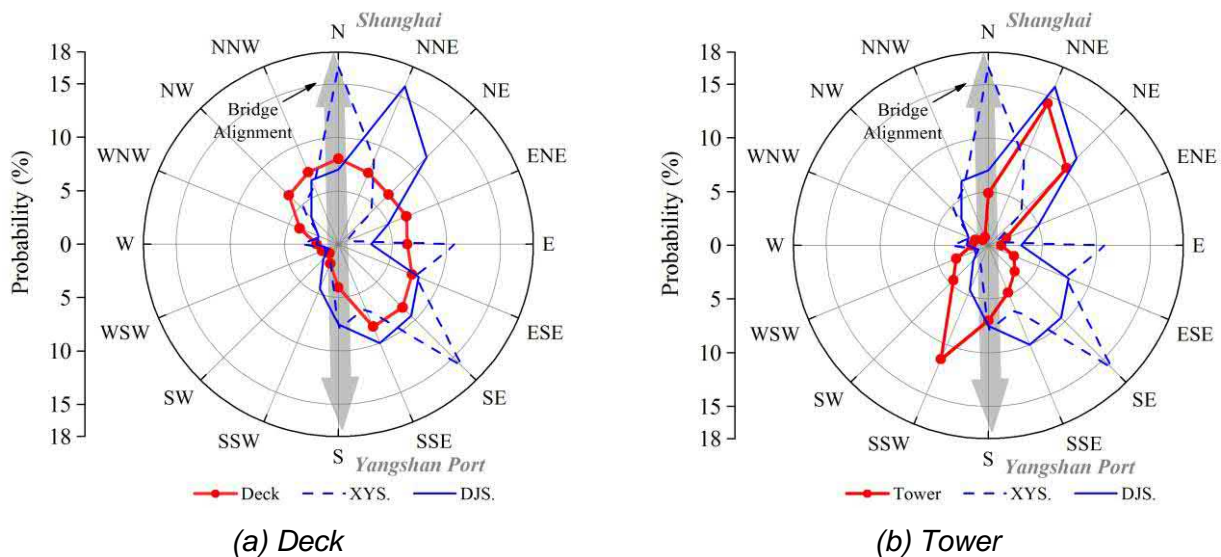


Fig. 4 - Measured wind frequencies versus design values

In the design stage of Donghai Bridge, the wind characteristics at the bridge location was inferred using the wind data from two nearby weather stations in Dajishan (denoted as “DJS”) and Xiaoyangshan (denoted as “XYS”), which are approximately 21 km and 12 km away from the bridge, respectively. As Figure 4 shows, the measured wind direction frequencies are also significantly different with those at the DJS and YYS, indicating a weak correlation between the two points 20 km apart in this sea area.

2.2. Mean wind profile

Using the data sets from the tower top and the bridge deck during the periods when both anemometers are normal, the mean wind profile is estimated based on the power-law profile suggested in the Code [13]:

$$\frac{\bar{U}_T}{\bar{U}_D} = \left(\frac{Z_T}{Z_D} \right)^\alpha \tag{1}$$

where, U and Z respectively represent the 10-min mean wind speed and the altitudes of the measuring points, while the subscripts T and D denote the tower top and bridge deck. The estimated average roughness index α is 0.15, which is higher than the design value ($\alpha = 0.10$). Actually, the dispersion of the fitted index α around the averaged value is considerable, which might result from the influence of the bridge structure on the measurements (Figure 5). The most frequent value in Figure 5 is 0.275.

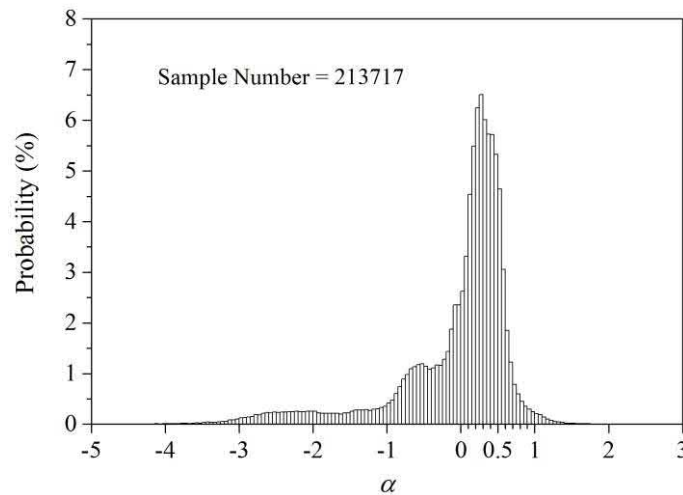


Fig. 5 - Distribution of the fitted roughness index α

2.3. Characteristics of fluctuating winds

Turbulence intensity and integral length scale are calculated to characterize the wind pulsation. Considering the girder is of more interest for structural evaluation, only the measurement at the bridge deck is taken into account here. The average values of the turbulence intensities for longitudinal (along-wind) and transverse (across-wind) components are $I_u = 13.8\%$ and $I_v = 14.6\%$, respectively, which are higher than the values suggested in the Code (i.e., $I_u = 11\%$ and $I_v = 0.88I_u = 9.7\%$) at the height of 50–70 m for the open water. Because the distribution patterns of I_u and I_v at the deck height are similar, Figure 6 only shows the distribution of I_u . Moreover, there is a strong correlation between the measured turbulence intensity in the two directions. The ratio of I_v to I_u is approximately 0.868, which is very close to the suggested value of 0.88 in the Code (Figure 7).

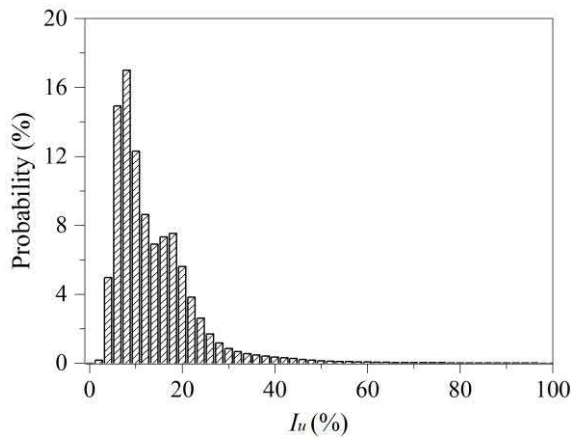


Fig. 6 - Distribution of I_u at the deck level

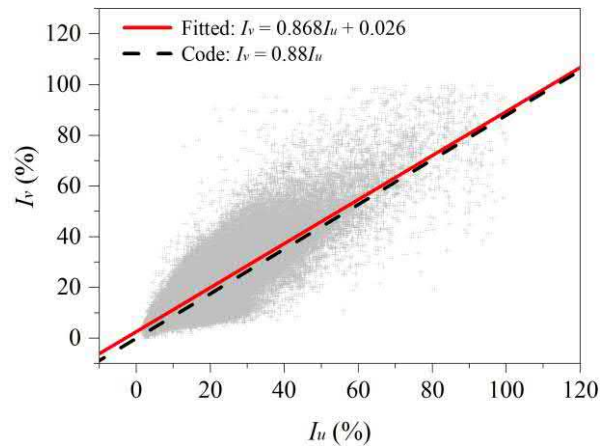


Fig. 7 - Scatter plot of I_u and I_v at the deck level

The turbulent integral length scale reflects the average size of vortices in a fluctuating wind, and we discuss only the integral length scales of longitudinal and transverse turbulent wind in the along-wind direction, i.e. L_u^x and L_v^x . Their distributions at the height of the girder are also close to each other, and Figure 8 displays the case of L_u^x . The measured averages of L_u^x and L_v^x are 89.08 m and 53.09 m, respectively, both of which are smaller than the values of $L_u^x=120$ m and $L_v^x=60$ m suggested in the Code. Together with the aforementioned turbulence intensity observations, the winds at the deck level of the Donghai Bridge have a lower stationarity and stronger turbulence than the suggestions in the Code.

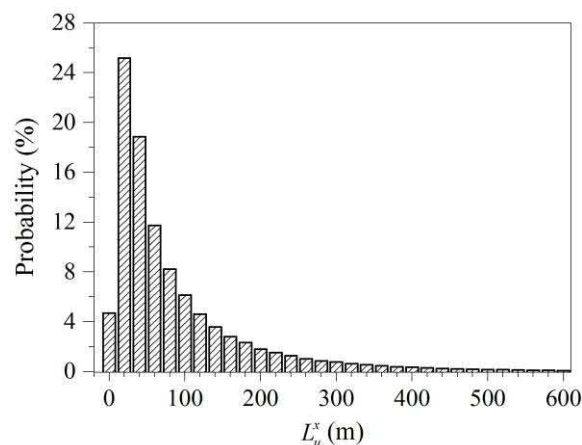


Fig. 8 - Distribution of L_u^x at the deck level

In addition, the variation of wind characteristics with the wind direction is further investigated. The average values of the deck-level I_u , I_v , L_u^x , and L_v^x in different directions are illustrated in Figures 9 and 10. It is noted that a higher turbulence intensity and a smaller integral length scale are observed in the NS direction, indicating the winds along the bridge axis fluctuate more than those in other directions. This probably results from the disturbance of the airflow by the bridge structure.

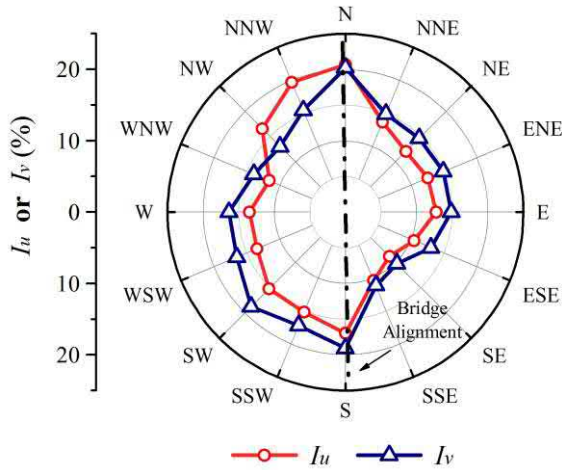


Fig. 9 - Changes in I_u and I_v with wind direction

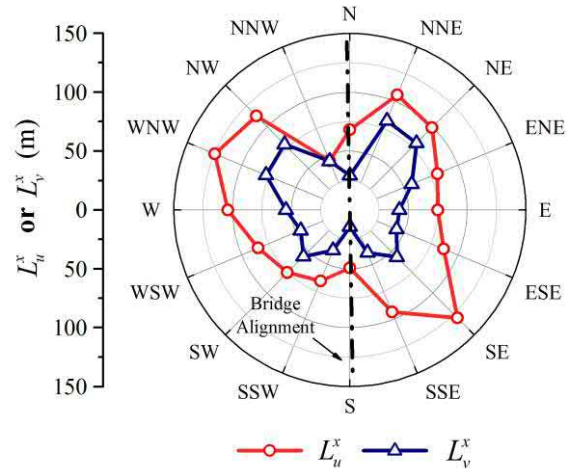


Fig. 10 - Changes in L_u^x and L_v^x with wind direction

2.4. Characteristics of strong winds

The strong wind characteristics at the Donghai Bridge are explored based on five typhoon events (i.e. Whipa, Krosa, Muifa, Haikui, and Bolaven) and a severe convective weather event on August 22, 2008 (denoted as the 8-22 storm). All the six events have an instantaneous wind speed exceeding 25 m/s. Although the 10-min mean wind speed of strong winds are considerably higher than the general winds, however, the turbulence intensity and integral length scale do not show any quantitative pattern.

Actually, due to the increase of non-stationarity, a 10-min averaging duration for wind field analysis may overestimate the turbulent characteristics of strong wind events, and thus a shorter averaging duration is preferable. The 8-22 storm is taken as an example to explicate this issue in Figure 11. When the averaging time interval decreases from 10-min to 1-min, the mean wind speed and direction become closer to the original measurements, and the slowly time-varying trend components in turbulent winds reduce accordingly. The reduction of the low-frequency components will decrease the standard deviation σ_u and the autocorrelation function $R_u(\tau)$ of the turbulent wind, and thereby further reduce the turbulent parameters I_u and L_u^x , which depend on σ_u and $R_u(\tau)$ respectively, as shown in Figure 11. Additionally, the “bump” on the I_u curves at 17:49 in Figure 11 arises because the 1-min mean wind speed \bar{U} , which is the denominator of the calculation formulas $I_u = \sigma_u / \bar{U}$, is close to zero.

Utilizing the data sets during periods with a 10-min mean wind speed higher than 20 m/s, Table 1 compares the 10-min and 1-min averaged turbulent characteristics of the six strong wind events. The parameters calculated based on 1-min time intervals are not only smaller than those with 10-min averaging intervals, but also vary less among different strong winds. Except for the 8-22 storm, the relative reduction of I_u and L_u^x are approximately 20% and 65% respectively, as the averaging time interval decreases from 10-min to 1-min.

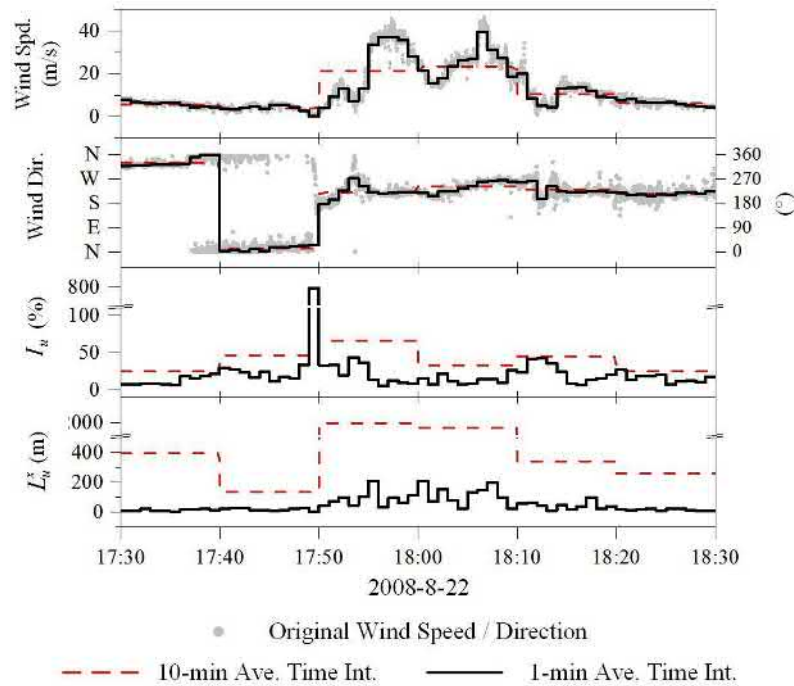


Fig. 11 - Comparison of the wind characteristics during the 8-22 storm using different averaging time intervals

Tab. 1 - Strong wind characteristics calculated using different averaging time intervals

	I_u (%)			L_u^x (m)		
	10-min (1)	1-min (2)	(3) = (2)/(1)	10-min (4)	1-min (5)	(6) = (5)/(4)
Wipha	8.00	6.37	0.796	184.46	68.13	0.369
Krosa	8.53	6.68	0.783	365.92	71.30	0.195
8-22 Storm	49.52	11.98	0.242	1638.98	111.16	0.068
Muifa	10.41	8.51	0.817	334.23	73.14	0.219
Haikui	16.58	15.06	0.908	135.82	69.83	0.514
Bolaven	10.29	7.85	0.763	255.16	91.39	0.358

3. WIND EFFECTS

This section focuses on the wind-induced vertical acceleration \ddot{V} , lateral acceleration \ddot{H} , and torsional (angular) acceleration $\ddot{\alpha}$ at the mid-span section of the girder of Donghai Bridge. Usually, the dynamic effects of the wind and traffic loading are mixed up under operation of a bridge. Fortunately, over the period 2007–2012, Donghai Bridge was once closed to traffic during typhoons Krosa, Muifa, Haikui, and Bolaven, which provided an opportunity for us to investigate the wind effects separately. Thus, these typhoon events were selected for detailed study.

3.1. Structural vibration during high winds

According to the monitoring data recorded during bridge closure for the three typhoon events, i.e. Krosa, Muifa, and Bolaven, Figure 12 shows the correlation of the root mean square (RMS) of the vertical acceleration \ddot{v} and the absolute values of the 10-min mean speed of the orthogonal crosswind (projection of the wind speed perpendicular to the bridge axis, with the positive direction of the wind from west to east). Although the girder's vertical acceleration does not approach zero in a low wind speed, however, there exists a roughly quadratic curve relation between them when the crosswind speed exceeds 13 m/s. This may be attributed to the fact that the wind pressure is proportional to the square of the wind speed. Similar observations of the quadratic curve relation may also be found in the torsional vibration of the girder. But for the most violent typhoon during the period 2007–2012, i.e. Haikui, the acceleration RMS does not indicate any qualitative trend with the increasing wind speed, as the data points in Figure 13 is highly scattered. This finding demonstrates the complexity of the aerodynamic effects, and it is also probably because the wind measuring point at the deck is so limited that it did not depict the severe wind field correctly during Haikui.

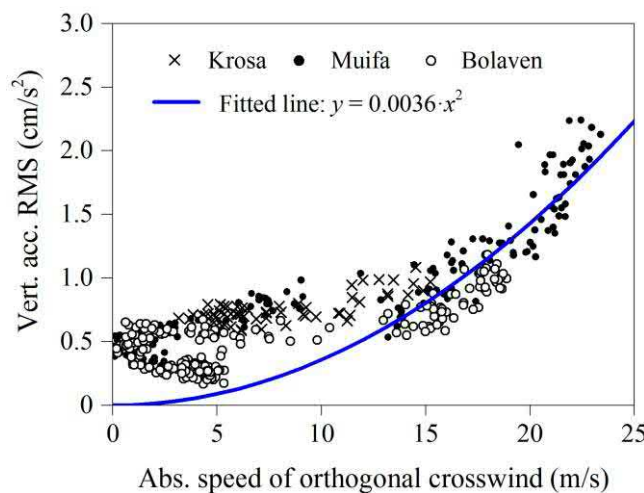


Fig. 12 - Vertical acceleration RMS at mid-span versus wind speed during bridge closure

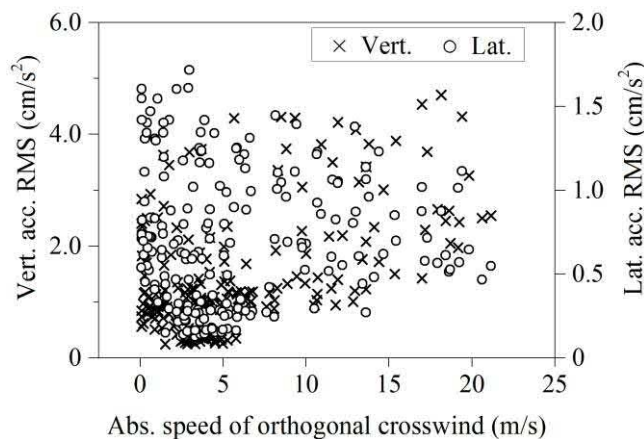


Fig. 13 - Acceleration RMS at mid-span versus wind speed during the Haikui typhoon event

3.2. Comparison between high wind and traffic effects

As China's first offshore sea-crossing bridge with the majority traffic being container trucks, Donghai Bridge has a unique operational condition and is suitable to compare the dynamic effects of high winds and heavy-load traffic on vibration of the girder. Figure 14 shows the evolution of the mid-span acceleration responses during the typhoon Haikui. The acceleration responses in the bridge closure period are dramatically different from the normal traffic period. Clearly, both high winds and heavy-load traffic have a non-negligible impact on the girder vibration.

Table 2 further compares the instantaneous maximum acceleration at mid-span of Donghai Bridge in two different periods: (1) during the bridge closure periods of four typhoon events, when there is the presence of high winds but without traffic load and (2) during normal traffic periods, when there is the absence of high winds but with traffic load. It can be seen from Figure 14 and Table 2, the traffic load is the dominant factor for the vertical and torsional vibration of the girder of Donghai Bridge, because only such an extremely strong typhoon as Haikui can excite the vertical/torsional acceleration to the same level as the traffic load. However, the dominant factor for the lateral vibration of girder is the wind load. The lateral acceleration amplitude in typhoon events is equal to several times that induced by the traffic load, which is understandable for the lateral vibration not being coincidental with the principal acting direction of the traffic on bridges.

Actually, the sensitivity of the structural vertical/torsional vibration to the wind and traffic load depends on the structural configuration and the level of traffic loading. For the Donghai Bridge, the heavy-load traffic dominates the vertical vibration, so the vertical acceleration RMS at the mid-span has a quite weak correlation with the mean wind speed, as shown in Figure 15(a). But for the Shanghai Yangtze River Bridge, a 730 m central span cable-stayed bridge, the vertical/torsional vibration is still dominated by the wind load. This is indicated by Figure 15(b), where a high acceleration RMS almost corresponds to the high wind periods, and the data points can also be fitted by a quadratic curve like Figure 12. It should be noted that the Shanghai Yangtze River Bridge has lower natural frequencies and thus more sensible to the wind action than the Donghai Bridge; also, it undertakes a conventional highway load, not the heavy-load container trucks. These might be the reasons why the vibration of the two bridges have different sensitivity to the wind and traffic load.

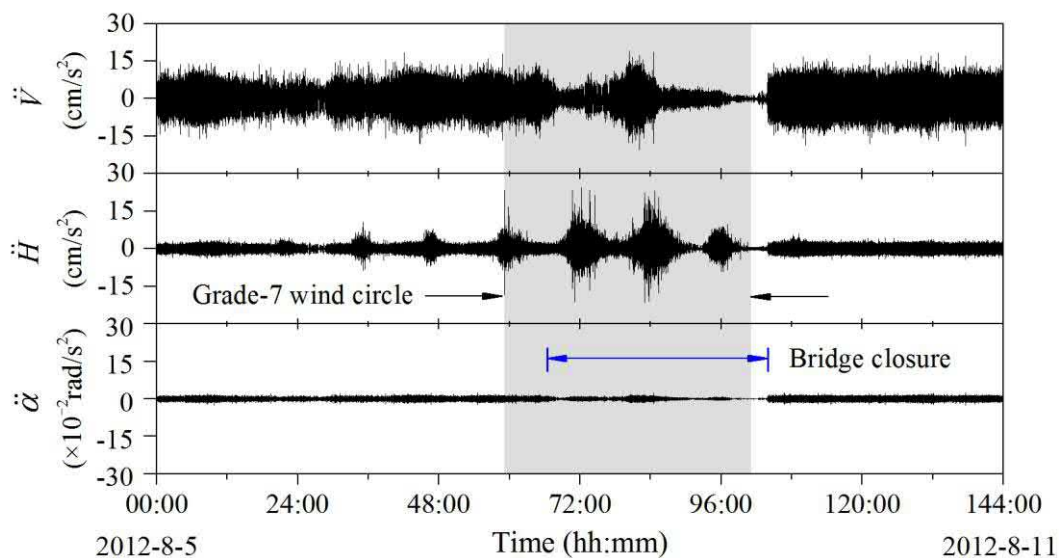


Fig. 14 - Acceleration responses at mid-span during the Haikui typhoon event

Tab. 2 - Maximum acceleration at mid-span between the bridge closure and post-typhoon periods

	Vertical maximum acceleration (cm/s ²)		Lateral maximum acceleration (cm/s ²)	
	During bridge closed (wind dominates)	After typhoons (traffic dominates)	During bridge closed (wind dominates)	After typhoons (traffic dominates)
Krosa	5.23	17.55	28.17	3.85
Muifa	9.18	16.73	12.03	4.95
Haikui	19.02	18.31	24.55	5.98
Bolaven	5.05	20.06	10.26	4.93

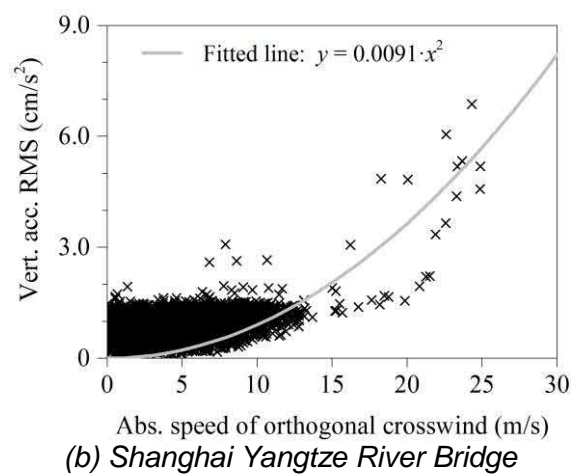
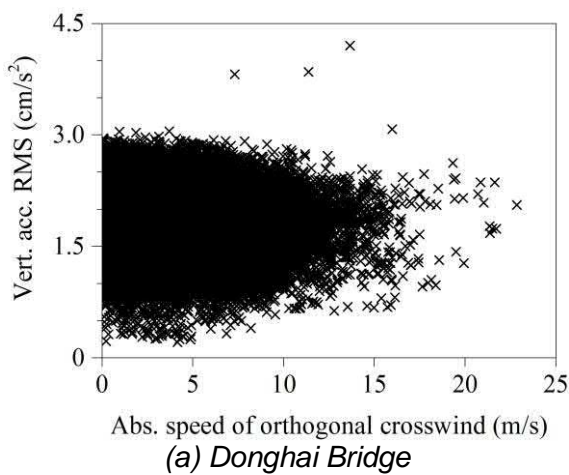


Fig. 15 - Scatter plots of vertical acceleration RMS at mid-span versus wind speed

4. CONCLUSION

The present study discusses the wind field characteristics and the wind-induced vibration responses for a sea-crossing bridge based on the six years of SHM data. In order to validate the design assumptions and understand the structural behaviours, we made a valuable comparison in terms of the measured and assumed wind parameters and also compared the respective contributions of high wind and traffic to the bridge vibration. The following conclusions are drawn:

(1) There exists obvious discrepancy between the measured wind parameters and the values suggested by the design Code, so it is necessary to feedback the design assumptions through the field monitoring. The wind records at the bridge site is easily interfered by the bridge structure itself, which should be considered in interpreting the measurements and designing SHMS.

(2) For strong winds with high non-stationarity, it is preferable to adopt a shorter averaging time than 10-min to calculate turbulent wind parameters. The turbulent characteristics of strong winds over 1-min time intervals are remarkably smaller and vary less among different strong winds than those over 10-min time intervals.

(3) The field measurement demonstrates the complexity of the structural vibrations induced by wind, and the RMS of wind-induced acceleration of the girder may have approximately a quadratic curve relationship with the mean wind speed.

(4) Compared to traffic load, the wind dominates the girder's lateral vibration amplitude, whereas the heavy-load traffic may exert more influence on the girder's vertical and torsional vibrations than the high winds, such as the case in Donghai Bridge.

This study provides field evidence for the wind-resistant design and evaluation of bridges in similar operational conditions.

ACKNOWLEDGEMENTS

The authors express their profound appreciation for the financial support provided by the projects of the National Natural Science Foundation of China (Grant No.: 51608034), the China Postdoctoral Science Foundation (Grant No.: 2016M600925), the Fundamental Research Funds for the Central Universities (Grant No.: FRF-TP-16-012A1), and the National Basic Research Program of China (973 Program, Grant No.: 2013CB036305). We also would like to thank the Shanghai Donghai Bridge Management Co.,Ltd. and the Shanghai Just One Technology Development Co.,Ltd. for the great assistance.

REFERENCES

- [1] Xu, Y., 2013. Wind Effects on Cable-supported Bridges (John Wiley & Sons, Singapore)
- [2] Xu Y., Guo W., Chen J., et al., 2007. Dynamic Response of Suspension Bridge to Typhoon and Trains. I: Field Measurement Results. *Journal of Structural Engineering*, vol. 133(1): 3-11
- [3] Wang H., Guo T., Tao T., et al., 2016. Study on Wind Characteristics of Runyang Suspension Bridge Based on Long-term Monitored Data. *International Journal of Structural Stability and Dynamics*, vol. 16: 1640019
- [4] Wang H., Li A., Niu J., et al., 2013. Long-term Monitoring of Wind Characteristics at Sutong Bridge Site. *Journal of Wind Engineering and Industrial Aerodynamics*, vol. 115(0): 39-47
- [5] Ni Y., Wang X., Chen Z., et al., 2007. Field Observations of Rain-Wind-Induced Cable Vibration in Cable-Stayed Dongting Lake Bridge. *Journal of Wind Engineering and Industrial Aerodynamics*, vol. 95(5): 303-328
- [6] Liu M., Liao H., Li M., et al., 2012. Long-term Field Measurement and Analysis of the Natural Wind Characteristics at the Site of Xi-Hou-Men Bridge. *Journal of Zhejiang University Science A*, vol. 13(3): 197-207
- [7] Li H., Laima S., Zhang Q., et al., 2014. Field Monitoring and Validation of Vortex-induced Vibrations of a Long-Span Suspension Bridge. *Journal of Wind Engineering and Industrial Aerodynamics*, vol. 124(0): 54-67
- [8] Chen B., Wang X., Sun D., et al., 2014. Field Measurement of Near-ground Wind Characteristics of Typhoon Haikui at Site of Jiubao Bridge. *Bridge Construction*, vol. 44(4): 34-39 (in Chinese)
- [9] Brownjohn J., Zasso A., Stephen G., et al., 1995. Analysis of Experimental Data from Wind-induced Response of a Long Span Bridge. *Journal of Wind Engineering and Industrial Aerodynamics*, vol. 54–55(0): 13-24
- [10] Miyata T., Yamada H., Katsuchi H., et al., 2002. Full-scale Measurement of Akashi–Kaikyo Bridge During Typhoon. *Journal of Wind Engineering and Industrial Aerodynamics*, vol. 90(12–15): 1517-1527
- [11] Abe M., Fujino Y., Yanagihara M., et al., 2000. Monitoring of Hakucho Suspension Bridge by Ambient Vibration Measurement. In: *Proceedings of SPIE*, Volume 3995 (SPIE, Bellingham)
- [12] Joseph A., Nicholas P., 2000. A Comparison of Full-scale Measurements of Stay Cable Vibration. In: *Proceedings of Structures Congress 2000* (ASCE, Reston)
- [13] Ministry of Transport of the People's Republic of China, 2004. Wind-resistant Design Specification for Highway Bridges (JTG/T D60-01—2004). Beijing: China Communications Press (in Chinese)
- [14] Zhu Z., 2007. Wind-induced Response Analysis for Main Navigation Channel Bridge of the East Sea Bridge. Master Thesis of Tongji University, Shanghai (in Chinese)
- [15] Xu Y., Chen J., 2004. Characterizing Nonstationary Wind Speed Using Empirical Mode Decomposition. *Journal of Structural Engineering*, vol. 130(6): 912-920
- [16] Simiu E, Scanlan R H. *Wind Effects On Structures : Fundamentals and Applications to Design*. 3rd ed. New York: John Wiley & Sons, 1996.

NANOTECHNOLOGY IN THE CULTURAL HERITAGE - INFLUENCE OF NANOSPENSIONS ADOPTED BY NANOPARTICLES OF TiO₂ FOR CLEANING THE SURFACE OF HISTORICAL PLASTERS

Klára Kroftová¹, Markéta Šmidtová², Ivo Kuřitka³ a David Škoda³

1. CTU in Prague, Faculty of Civil Engineering, Department of Architecture, Prague, Thákurova 7, Czech Republic; klara.kroftova@seznam.cz
2. CTU in Prague, Faculty of Civil Engineering, Department of Building Structures, Prague, Thákurova 7, Czech Republic; smidtmar@fsv.cvut.cz
3. Polymer Centre Zlín, Faculty of Technology, Zlín, třída Tomáše Bati 5678, Czech Republic; kuritka@utb.cz, diskoda@utb.cz

ABSTRACT

The continuous development of nanostructure and the study of physico - chemical processes in the nanometer range lead to new methods that can slow down the degradation processes of a work of art, or even restore damage caused, for example, by an inappropriate restoration process. The use of nanosuspensions based on calcium hydroxide is probably the most widespread application of nanomaterials in heritage care, especially in the field of hardening of lime building materials (plaster, limestone, etc.). In combination with titanium dioxide, it should be a successful suspension in the fight against biological agents, surface contamination or in the protection of UV-resistant building materials.

KEYWORDS

Calcium hydroxide, TiO₂, photocatalysis, nanosuspension, cleaning, antimicrobial

INTRODUCTION

Between the most common tasks encountered in the restoration of historic buildings, belongs the purification, desalting and consolidation of various types of construction materials. The biocorrosion of construction materials can be caused by bacteria, algae, lichens, plants and animals. These living organisms are able to adapt to a wide range of documents and their growth is not only affected by climatic conditions, but also by the surface moisture, chemical composition, structure and texture porosity materials.

In recent decades, nanotechnologies have become increasingly important in the area of cultural heritage care, which can facilitate the cleaning of contaminated surfaces, run self-cleaning processes and act antimicrobially, or protect the material from the negative effects of UV radiation and others. The application of nanomaterials in the care of monuments has been verified in the last approximately 15 years mainly in the form of nanosuspensions, resp. nanoemulsions based on hydroxides (especially calcium, barium, magnesium, etc.), carbonates and, in some cases, sulphates [1-3]. The advantage of the application of nanomaterials is the possibility of achieving a high penetration depth into the structure of the materials (mainly depending on the pore system and the moisture content of the material) and high efficiency while preserving the original material matter.

The use of nanomaterials is proven in practice in the deacidification of movable artworks (paper, textiles, leather [4-7]), cleaning of surfaces of historical monuments (eg. titanium hydroxide nanosuspension, nanoemulsion of organic solvents in water etc. [8-10]) and for the consolidation of porous materials (eg. plasters, limestone or eg wall paint etc., nanodispersion of calcium hydroxide [1-3]). Successful applications of nanomaterials in crack injection or in the remediation of building materials found in humid or chemically contaminated environments and other are also documented in foreign practice [11-12].

Within the development of nanomaterials, metal oxides, especially ZnO and TiO₂, have been shown to be useful for protection against microorganisms and UV degradation due to their antifungal and antibacterial effects [13-15]. From foreign publications is known the efficiency of titanium coatings deposited on historic architectural stone surfaces as self-cleaning [16-18]. Experience in the application of oxides with different physical properties and the principles of their effects on restored materials have only recently appeared in the literature and the development of these materials is at the beginning.

The photocatalytic properties of TiO₂ were discovered by Fujisima and Honda, who first used titanium dioxide to decompose chemicals [19-20]. Titanium dioxide (TiO₂) is one of the most important and commercially available photocatalysts due to its excellent efficiency (even under low solar irradiation), low cost, compatibility with a large number of materials and good stability, where the use of photocatalytic reactions decompose the most inorganic and organic pollutants due to UV radiation. Titanium dioxide is a semiconductor material and is mainly used in anatase form. Due to its antibacterial effects, it is applied in various fields, such as water and air purification, paintings, glasses, or the cosmetics industry.

The TiO₂ nanocrystals, in the form of anatase, have a particle size in the range of several nm to 30 nm. Due to light with a shorter wavelength than 388 nm, they activate and remove oxygen atoms from some TiO₂ molecules. Next to each other coexist the hydrophilic regions depleted by oxygen and hydrophobic, unchanged (uncharged) regions. Due to the close proximity of these areas (these are areas in the order of several hundred nm²), the water droplets lose their spherical shape and form a continuous film that prevents adhesion of the pollutant to the surface [21]. This synergy of effects allows to maintain aesthetic properties, improve surface properties and slow degradation processes caused by dirt.

The photocatalytic effect of titanium dioxide produced by ultraviolet light is influenced by the size and shape of the particles and their specific surface. It is necessary to emphasize that UV radiation is absolutely necessary for the course of the reaction and that TiO₂ has a catalyst function and therefore does not decrease. However, to maintain long-lasting high efficiency, it is necessary to maintain surfaces (treated with TiO₂) and remove reaction products (eg. by water or rain).

The TiO₂ nanoparticles themselves are chemically inert, very stable over time and, according to their current knowledge, non-toxic to humans. The presence of metal oxides such as WO₃, ZrO₂, MoO₂, or also CdS and the doping of TiO₂ by nitrogen can significantly affect the course of photocatalysis [22]. However, the problem of dispersed TiO₂ nanoparticles in the nanocoating is the tendency to form clumps after a certain period of time in the liquid environment. This leads to enlargement of the average particle size of TiO₂ and the photocatalytic potential decreases.

MATERIALS AND METHODS

The goal of laboratory research was to create a multifunctional nanoparticle and titanium dioxide based compound that would give very good results to historic surfaces (especially plaster and stone) in the mean of self-cleaning surface and simultaneously to add the missing binder. Applying nanomaterial would not change the original appearance, as a result of the photocatalytic phenomenon would reduce the rate of deposition of pollutants and thus slow the development of degradation processes. TiO₂ nanoparticle suspension allows thin transparent coatings on the

surface of the treated material to act as a preventive protective system activated by solar UV radiation while reducing existing pollution and retarding degradation processes.

The incorporation of TiO_2 into nanosuspension of calcium hydroxide was carried out within the framework of the NAKI research project in cooperation with the TBU Polymer Systems Center in Zlín.

For the preparation of nanosuspensions were used the following chemicals: Calcium methoxide ($\text{Ca}(\text{OCH}_3)_2$, 97 %, $M_w = 102,15 \text{ g mol}^{-1}$), Titanium(IV) isopropoxide ($\text{Ti}(\text{OC}_3\text{H}_7)_4$, 97 %, $M_w = 284,22 \text{ g mol}^{-1}$) and isopropyl alcohol (p.a.) were purchased by Sigma-Aldrich.

The nanosuspension of $\text{Ca}(\text{OH})_2$ (Ca1) was produced by hydrolysis of calcium methoxide $\text{Ca}(\text{OCH}_3)_2$ (average particle size according to DLS 298 nm, Figure 1, Table 1, [23]). The nanosuspension sample CaTi1 was prepared by hydrolysis of $\text{Ca}(\text{OCH}_3)_2$ and $\text{Ti}(\text{OC}_3\text{H}_7)_4$ mixture in isopropyl alcohol/water solvent. The reaction mixture was stirred at room temperature, the obtained suspension was separated by centrifugation and washed with water and isopropyl alcohol. The final product was dried in the oven at $80 \text{ }^\circ\text{C}$ for 1 hour. Yield = 4,21 g (81 %), (theoretical yield 5,20 g). See the Table 1 for more details.

The nanolime suspension was prepared by dissolving 0.75 g of the product in 250 ml of isopropyl alcohol. To increase the homogeneity of the resulting dispersion, the suspension was placed in an ultrasonic bath for 1 hour.

Table 1 - Precursor amounts and product yields

sample	precursor	m precursor (g)	n precursor (mmol)	yields (g)
Ca1	$\text{Ca}(\text{OCH}_3)_2$	7,18	70,2	4,21
CaTi1	$\text{Ca}(\text{OCH}_3)_2$	5,79	56,6	4,95
	$\text{Ti}(\text{OC}_3\text{H}_7)_4$	5,61	19,7	

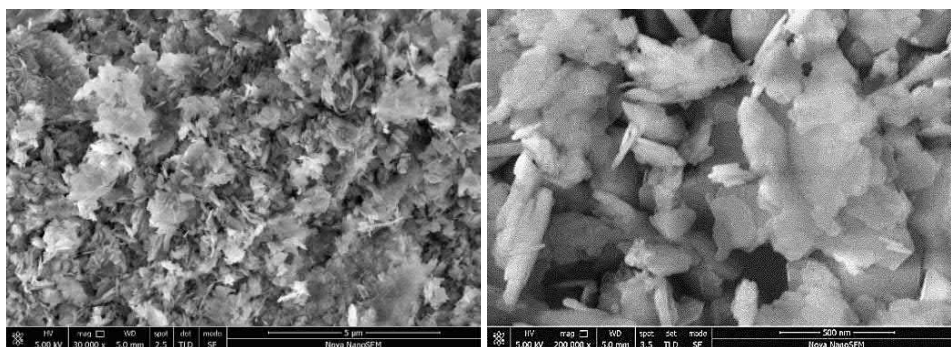


Fig. 1 - SEM images of the test product of nanosuspension Ca1 without dopant TiO_2 . There are well visible hexagonal, very thin (approx. 50 nm) platelet crystals on the images (Nova NanoSEM (FEI) with Schotky field emission electron source (0.02–30 keV) and TLD detector, Photo CPS UTB Zlín)

For the identification of crystalline phases and confirmation of presence of $\text{Ca}(\text{OH})_2$ in prepared products powder XRD diffraction analysis was employed. Powder XRD patterns were recorded on Rigaku MiniFlex 600 equipped with a CoK_α ($\lambda = 1.7903 \text{ \AA}$) X-ray tube (40 kV, 15 mA). Diffraction patterns are displayed in Figure 2. All diffractions are assigned to $\text{Ca}(\text{OH})_2$ phase and

they correspond to the JCPDS database card number 076-0571. In the case of sample CaTi1 with the titanium, no diffractions related to TiO_2 were detected. The absence of TiO_2 diffractions means that titanium species are presented in the amorphous form. This amorphous form is characterized most probably by oligomeric titanium oxo clusters with tetracoordinated and hexacoordinated titanium atoms.

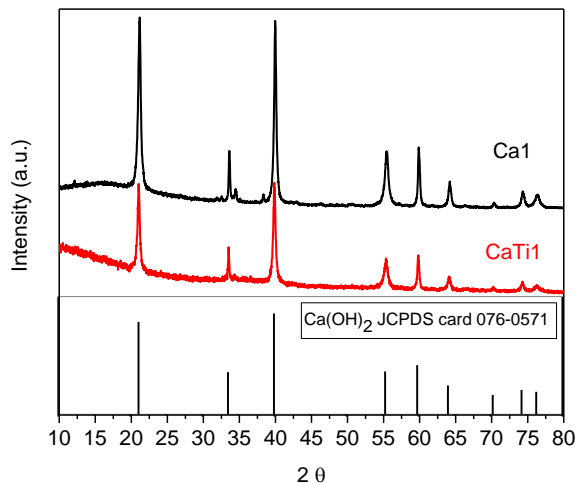


Fig. 2 - The XRD diffractogram of the tested nanosuspension of Ca1 and CaTi1 and their comparison with the $\text{Ca}(\text{OH})_2$ library diffractogram

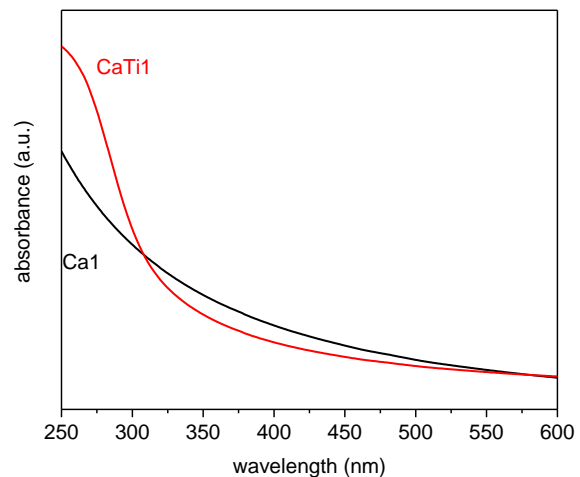


Fig. 3 - UV-Vis spectra of nanosuspensions Ca1 and CaTi1.

The important factor of $\text{Ca}(\text{OH})_2$ nanosuspensions is the size of nanoparticles. The nanoparticle sizes were measured by dynamic light scattering method. DLS size distribution measurements were performed on the Zetasizer Nano ZS from Malvern. Obtained results are illustrated in Table 2. For the comparison of nanoparticle size, commercially available nanosuspension CaLoSiL® was used within this measurement as well. Based on the obtained values we can conclude, that both $\text{Ca}(\text{OH})_2$ and $\text{Ca}(\text{OH})_2/\text{TiO}_2$ nanodispersions prepared via hydrolysis of the alkoxides provides the systems with the nanoparticle size close to commercial CaLoSiL®.

Table 2 - Particle size measurements by DLS method.

sample	average		
	Z-Ave (nm)	Peak1 (nm)	PDI
Ca1	298	275	0,269
CaTi1	249	241	0,231
CaLoSiL®	146	176	0,172

UV-Vis spectroscopy is important characterization technique for titanium species. Titanium dioxide exhibits absorption in UV region. This property is also crucial for the photocatalytic efficiency. With the application of UV-vis spectroscopy we can determine presence of Ti species represented by oligomeric titanium oxo clusters with tetracoordinated and hexacoordinated titanium atoms in mixed $\text{Ca}(\text{OH})_2/\text{TiO}_2$ nanosuspensions. UV-Vis spectra measurements were performed on Perkin-Elmer Lambda 1050 with the Xe lamp and are displayed in Figure 3. Significant difference between $\text{Ca}(\text{OH})_2$ (Ca1) and mixed $\text{Ca}(\text{OH})_2/\text{TiO}_2$ (CaTi1) nanosuspension is

observed in UV region where absorption of Ti species takes place. This absorption is represented by the steep increase of absorbance at ca. 330 nm.

CONCLUSION

From the results obtained, it is obvious that the use of prepared lime nanosuspension with TiO₂ dopant as a protective and self-cleaning layer of building materials exposed to weathering and UV radiation is promising. The present preparation of Ca(OH)₂ and Ca(OH)₂/TiO₂ nanosuspension by the hydrolysis of alkoxides yields results that are close to the commercial CaLoSiL® material. The advantage of the hydrolytic method is the purity of the resulting product and the relatively small particle size. The addition of titanium isopropoxide to the reaction mixture makes it possible to obtain Ca(OH)₂ nanoparticles with Ti species that will function as photocatalytically active centers. In our case, Ti species are amorphous in form of oligomeric titanium oxo clusters.

The issue of the preparation and application of a multifunctional suspension is still subject of laboratory testing. Identifying suitable manufacturing processes could lead to the practical use of nanosuspension in building and conservation practice.

ACKNOWLEDGEMENTS

The results of the research carried out under this contribution have been achieved with the financial support of the NAKI II project DG16P02M005 "*Development and research of materials, processes and technologies for the restoration, preservation and consolidation of historical brick structures and surfaces and systems for the preventive protection of historical and listed buildings endangered by anthropogenic and natural hazards* (2016 - 2011, MK0 / DG)".

REFERENCES

- [1] Machačko, L. et al, 2012. Testování „nanosuspenzí“ na bázi hydroxidu vápenatého v rámci projektu Stonecore, In. Sborník semináře Nanomateriály v památkové péči, STOP, str. 32 – 36
- [2] Rathouský, J., 2012. Nanovápno pro konsolidaci porézních materiálů – principy, mechanismy, In. Sborník semináře Nanomateriály v památkové péči, STOP, str. 28 – 31
- [3] Škrdlantová, M. et al. 2012. Laboratorní použití micelárních roztoků a mikroemulzí při čištění historických materiálů. In. Sborník semináře Nanomateriály v památkové péči, STOP, str. 18 – 22
- [4] Baglioni, P. et al. 2012. Nano-Materials for the Conservation and Preservation of Movable and Immoveable Artworks, Progress in Cultural Heritage Preservation – EUROMED 2012, dostupné online: https://www.researchgate.net/publication/270365605_Nano-Materials_for_the_Conservation_and_Preservation_of_Movable_and_Immoveable_Artworks
- [5] Poggi, G. et al. 2010. Hydroxide Nanoparticles for Deacidification and Concomitant Inhibition of Iron-Gall Ink Corrosion of Paper, Langmuir, 26 (24), pp 19084–19090
- [6] Kwitkowska, A. et al. 2014. A.Paper deacidification with the use of magnesium oxide nanoparticles, Forestry and Wood Technology № 85, p.144-148, dostupné online: http://agro.icm.edu.pl/agro/element/bwmmeta1.element.agro-4b9d7961-05a7-43ed-9339-708f4ba9365a/c/144_Annals85.pdf
- [7] Giorgi, R. et al. 2002. Nanotechnologies for Conservation of Cultural Heritage: Paper and Canvas Deacidification, Langmuir, 18 (21), pp 8198–8203
- [8] Graziani, L. et al, 2014. Durability of self-cleaning TiO₂ coatings on fired clay brick facades: Effect of UV exposure and wet & dry cycles, Building and Environment, 2014, Vol.71, p.193-203 Dostupný online: <http://www.sciencedirect.com/science/article/pii/S0360132313002904>.
- [9] Quagliarini, E. et al. 2012. Smart surfaces for architectural heritage: Preliminary results about the application of TiO₂ based coating on travertine, Journal of Cultural Heritage, Vol.13, p.204-209

- [10] Quagliarini, E. et al. 2013. Self-cleaning materials on Architectural Heritage: Kompatibility of photo-induced hydrophilicity of TiO₂ coatingy on stone surfaces, *Journal of Cultural Heritage*, Vol.14, p.1-7
- [11] Gavenda, M. et al. 2005. Consolidación y restauración de revocos esgrafiados en la iglesia parroquial de Nuestra Señora de la Asunción de Traiguera, *Loggia Restoration*, Año VIII, No.18, p.64-69
- [12] Liu, T. et al. 2010. Structure stability and corrosion resistance of nano-TiO₂ coatings on aluminum in seawater by a vacuum dip-coating method, *Surface and Coatings Technology*, Volume 205, Issue 7, p. 2335–2339
- [13] De Filpo, G. et al. 2013. Preventing fungal growth in wood by titanium dioxide nanoparticles, *INTERNATIONAL BIODETERIORATION & BIODEGRADATION*, vol. 85 pp. 217–222
- [14] Pinho, L. et al. 2013. A novel TiO₂–SiO₂ nanocomposite converts a very friable stone into a self-cleaning building material. *Applied Surface Science* [online]. Vol. 275, s. 389-396 [cit. 2013-11-14]. DOI: 10.1016/j.apsusc.2012.10.142. ISSN 0169-4332. Dostupný online: <http://www.sciencedirect.com/science/article/pii/S0169433212018831>.
- [15] Gomez-Ortiz, N. et al. 2013. Antifungal Coatings Based on Ca(OH)₂ Mixed with ZnO/TiO₂ Nanomaterials for Protection of Limestone Monuments, *ACS APPLIED MATERIALS & INTERFACES* Vol. 5 Iss. 5 Pp. 1556-1565
- [16] Revuru, A. N. et al.: Photo Catalytic Activity of Anatase TiO₂/PVA Film Coated Plate. In: *Advanced Materials Research*, 584, 396 (2012).
- [17] Allen, G. C. et al. 2002. Photocatalytic oxidation of NO_x gases using TiO₂: a surface spectroscopic approach. In: *Environmental Pollution* 120, pp. 415–422.
- [18] Wang, H. et al. 2013. Multifunctional nanocomposites for paper conservation, *STUDIES IN CONSERVATION* Volume: 58 Issue: 1 Pages: 23-29
- [19] Fujishima, A. 2005. Discovery and applications of photocatalysis – Creating a comfortable future by making use of light energy. In: *Japan Nanonet Bulletin*, 44th Issue
- [20] Hashimoto, K. et al. A. TiO₂ Photocatalysis: A Historical Overview and Future Prospects, *Japanese journal of applied physics*, vol. 44, No. 12, p. 8269 – 8285, dostupné online: https://www.jsap.or.jp/jsapi/Pdf/Number14/04_JJAP-IRP.pdf
- [21] Bílý, P. et al. Experimentální studie vlivu nanomateriálů na fotokatalytické vlastnosti betonu, dostupné online: <http://stavba.tzb-info.cz/beton-malty-omitky/14178-experimentalni-studie-vlivu-nanomaterialu-na-fotokatalyticke-vlastnosti-betonu>
- [22] Hochmannová, L. et al. 2010. Vliv nanočástic TiO₂ a ZnO na fotokatalytické a mikrobiální činky silikátových nátěrů, *Chem. Listy* 104, 940-944
- [23] Kroftová K., et al. 2017. Synthesis nanolime suspensions and their potential use in cultural heritage preservation, conference EASEC-15, October 11-13, Xi'an, China

ANALYSIS ON THE INFLUENCE OF ACCUMULATION EFFECT OF LANDSCAPE COLOR ON TRAFFIC SAFETY IN THE FOGGY SECTIONS OF EXPRESSWAYS

Xilei Li¹, Boming Tang¹, and Qianghui Song^{2,3}*

1. *College of Civil Engineering, Chongqing Jiaotong University, Chongqing, 400074, P.R.China;*
2. *Logistical Engineering University, Chongqing Key Laboratory of Geomechanics & Geoenvironment Protection, Chongqing, 401311, P.R.China (corresponding author), email: songbook@163.com;*
3. *Chongqing Institute of Geology and Mineral Resources, Chongqing, 400042, P.R.China*

ABSTRACT

The landscape color of expressways has a significant impact on a driver's visual response, thus affecting the incidence of expressways traffic accidents. Although this problem has been analyzed and discussed from different angles, there is rare quantitative analysis on the influence of accumulation effect of landscape color on the traffic safety in foggy sections of expressways. In this paper, the color combination and stroboflash of fog lamps on both sides of the road were designed from the perspective of the color research of road landscapes, and the cumulative effect of colors and stroboflash of fog lamps on the drivers' mind was also studied. Then the interactive cumulative model based on landscape color and driving time in heavy-fog environment was established. Finally, multi-group of fog-lamp colors and spacing experiment program allowing a visibility of 200–500m in fog environments was designed by using Tobii eye-movement instrument and the UC-win/Road simulation software. According to the program, simulations were performed on several drivers to test the influence of road-landscape colors in foggy environments on the drivers' visual psychology. The results of the simulation experiment showed that the colors and stroboflash of fog lamps on both sides of the road have a positive effect on the drivers' safety when the visibility range is 200–500m, and the driving speed is less than 70 km/h, in addition, the red and yellow were found to have the largest influence among all the studied colors. These results show that it is necessary to design landscape colors in the foggy sections of expressways.

KEYWORDS

Foggy sections of expressways, Road landscape, Landscape color, Cumulative effect

INTRODUCTION

When people observe objects, the primary visual reaction is caused by color. Road color is considered as one of the main influencing factors of road landscapes. Therefore, the design of road landscapes is based on several factors such as road-surface color and line trend. However, during the process of expressways-landscape design, the total design of road landscape is often emphasized, resulting in neglecting the local layout of special foggy expressways areas. The foggy sections of expressways is a serious area affected by heavy-fog weather. Moreover, secondary accidents may easily occur owing to the low visibility. So far, related studies have shown that low

road visibility and high tension observed on a driver's optic nerve in the foggy sections of expressways may produce visual fatigue, thereby resulting in traffic accidents. Thus, whether the road traffic color design can be used for reference, and how to learn from the road traffic color design and through the road landscape color matching in fog environment, to reduce the driver's visual fatigue to some extent, is a meaningful problem worthy to be discussed.

Many scholars pay significant attention to research on the traffic safety in heavy-fog environment. The analysis on influencing factors of traffic safety in heavy fog environment includes the following aspects: the formation mechanism of fog, visibility detection in the foggy sections of expressways, traffic inducement in foggy areas, information warning in foggy area, crisis principle analysis in foggy sections of expressways and etc. The traffic guidance through combing different colors of induction lamp with different driving environments was conducted in Japan. Also, a fog-area traffic-monitoring system set in the national expressway from Beijing to Zhuhai, was considered as an earlier application of a "red and yellow fog-lamp guidance system" that can be used to solve the fog-area traffic-safety problems in China [1]. Fu [2] and Jiang et al. [3] emphasized the necessity and importance of installing safety facilities in foggy areas. Qian's [4] studies suggest that the drivers' sight may be influenced by flicker asynchronization if fog lights were installed on both sides of the road, from the perspective of the visual psychology of the drivers. The fog lamps type selection and calculation method were established by Yang [5] from the fog lamps longitudinal and transverse location and installation height, the fog lamps engineering design theory, in view of the fog lamp brightness and diameter. Much research has been done both at home and abroad from the fog area road traffic safety guidance [6-8], however, these researches focused more from the viewpoint of security equipment and modern network technologies for building guidance systems, rather than from the perspective of landscape color or design to improve road traffic safety in foggy areas.

In the research of the color effect on visual psychology of drivers, Wang et al. [9] used MRI (Magnetic Resonance Imaging) to detect features of color and motion perception in the brain, thus improving the understanding of brain structure and functions of human color perception and motion perception. Yuan and Hu [10] introduced some information on the application of color to landscapes. Zhang et al. [11] discussed some aspects of color psychology and analyzed the application to traffic security considering factors such as the colors of road and accessory facilities, traffic-sign color, vehicle color, the colors of pedestrian clothes, and the road landscape. By using methods from safety psychology, color psychology, and qualitative analysis, Yuan et al. [12] and Lee et al. [13] analyzed the influence of vehicle colors on traffic safety and drivers' reaction and proposed ideas for safe color design as well as principles, system, and steps for safe vehicle-color design. Li [14] and Siogkas et al. [15] introduced the functions of color, environment and people for protecting traffic safety in view of urban traffic and provided basic research for the design of urban-traffic safety colors. Based on the different psychological effects brought by color vision and visibility research under different weather conditions, Xu et al. [16] proposed the design framework for a road-traffic color system. Zhang et al. [17] studied urban road-traffic colors, proposed an assessment indicator system for such colors and created an evaluation and optimization model. Dai and Deng [18] believed colored pavement promotes the safety of road traffic suggested the use of colored pavement to promote traffic safety in highways. Shen et al. [19] analyzed the influence of colors on road-traffic safety and preliminarily discussed colors and color combinations in traffic systems. Wang et al. [20] studied the influence of roadside landscape colors in highways on the heart rate of drivers. By improving the light and dark adaptability of portal, Zhang et al. [21] improved the safety of road sections through planting plants separately with three colors in different sections and speed cutting signal, put forward some color treatment measure in walls of tunnels, and integrated portal safety and functions of landscape effectively. Tao et al. [22] simulated different colors in tunnel portals using an eye tracker and the 3D-MAX software and analyzed the influence of landscape colors in tunnel portals on the drivers' heart rate.

Above papers focus on the influence of colors on road traffic safety, however, not involving the influence of colors on the visual psychology of drivers resulting from the cumulative effect of low visibility and dull road landscapes in heavy-fog environments where the drivers' visual range is limited. With large national territorial area, complex network environment and wide range of the foggy sections of expressways in China, it is necessary to study the influence of the cumulative effect of road landscape colors in the foggy sections on visual psychology of drivers.

In this study, the color combination and stroboflash of roadside fog lamps from the point of view of landscape colors in road were designed, the research drivers' mental cumulative effect caused by colors and stroboflash of fog lamps was analyzed, traffic safety guidance in fog environment was proposed and the simulation experiment using eye tracker and UC-win/Road simulation software was done. The main goal is to assess the influence of colors and stroboflash of roadside fog lamps on the driving safety.

2. THE APPLICATION OF COLORS IN THE FIELD OF ROAD TRAFFIC

2.1. The influence of colors on road traffic safety

As we all know, in the field of traffic safety, color is the preliminary information perceived by vision and directly affects traffic safety. The comparison of the attention of human eye to color and to shape is shown in Figure 1. The figure tells us: at first view, people pay 80% attention to color; 2 minutes later, the attention paid to shape increases to 20% while that of to color decreases to 60%; 4 minutes later, people pay 50% attention to shape; 5 minutes later, the influence of color decreases to 50% [23]. Therefore, color is the most easily perceived information, which directly influences operations of drivers and driving safety.

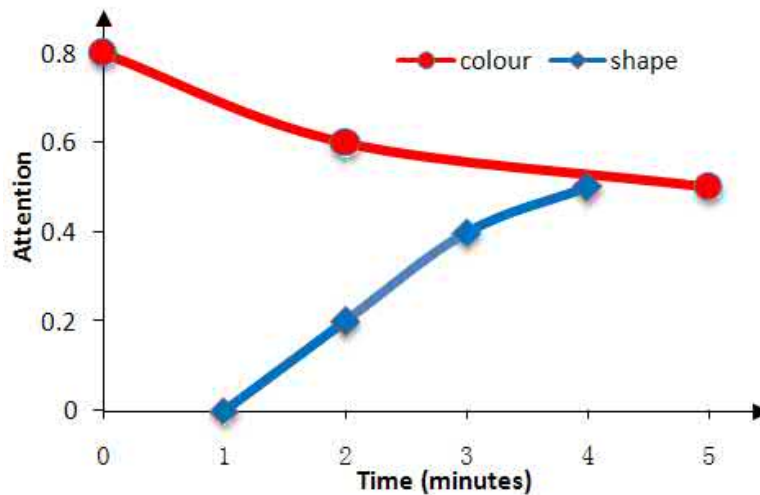


Fig. 1 - The Comparison of the attention of human eye to color and to shape

2.2. Color selection in road traffic

According to the theory of color vision [24], red, yellow, and green, which are highly related to human vision and mental reaction, are always used as signals in the traffic field. The human retina contains one type of rod photoreceptor cells and three types of cone photoreceptor cells. The rod photoreceptor cells are most sensitive to yellow light, whereas the three types of cone

photoreceptor cells are separately most sensitive to red, green, and blue. Red and green are most easily distinguished by human beings because of this vision structure. Although yellow and blue are also easily distinguished, our eyes distinguish red and green better because there are relative fewer photoreceptor cells which are sensitive to blue and yellow lights. The psychological impact of common colors on people is shown in Table 1 [12]. It can be seen that colors may show active and drastic meanings; to express a hot or drastic meaning, red is the best choice, and yellow ranks the second; Green implies coldness and calmness. Therefore, red light is used as the forbidding signal in traffic engineering, yellow is used as the warning signal and green is used as the passing signal.

Tab. 1 - The psychological impact of common colors on people (modified from Ouyang et al. [25])

Color	Anger	Vigilance	Power	Enthusiasm	Exciting	Warmth	Quiet	Hope	Distance	Cold	Relaxed	Heavy
Red	Δ	Δ		Δ	Δ	Δ						Δ
Orange		Δ	Δ		Δ	Δ						
Yellow				Δ	Δ	Δ					Δ	
Green							Δ	Δ	Δ	Δ		
Blue									Δ	Δ		Δ
Purple									Δ	Δ		Δ
White											Δ	
Black												Δ

Note: "Δ" in the table refers to the existence of certain psychological effect or association.

At present, as to the urban road landscape design in China, people tend to focus on road structure and solving of traffic capacity, while regard road landscape design as an independent issue, which separates road landscape design, road geographical environment, road linear programming and road natures. There are few researches on special landscape design aiming at local regions with special linear structure, special climate characteristics or other special geographical features. With the improvement of national expressways system, in 2014, the Ministry of Public Security (MPS) of China showed that there are 1468 road sections in expressways with more than 3 foggy periods every year, and multiple vehicle rear-end and secondary accidents are typical features of accidents in fog sections. It is in urgent need to improve driving safety in the foggy sections of expressways. Installing induction fog lamps is one of solutions to improve driving safety in fog sections at present. However, when setting fog lamps, engineers only analyze installation interval from engineering perspective. This paper aims at setting fog lamps and designing landscape colors in a fog section from perspectives of road landscape design and visual psychology of drivers. It can be seen from Figure 2, that there is a certain linear relation between pupil area and driving speed. Figure 3 shows drivers' distances of visual cognition on different colors at night. It can be seen from Figure 3, that drivers have different distances of visual cognition on different colors. Fog environment brings low visibility. The moving distances of visual cognition on green and black are the most short among several colors. Unfortunately, black, grey and green are three dominant tones in fog sections. Therefore, it is necessary to design landscape colors in the foggy sections of expressways.

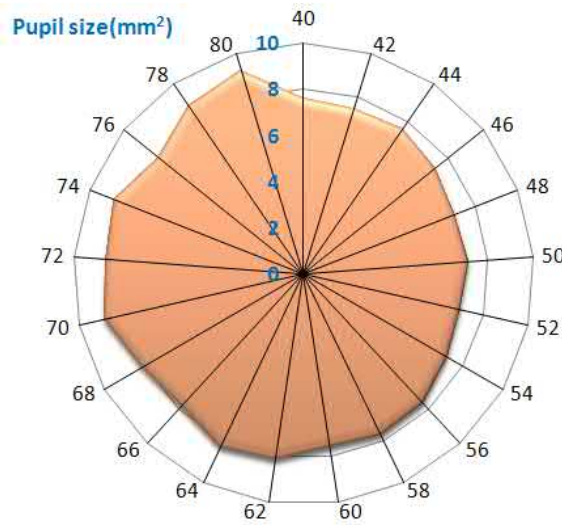


Fig. 2 - The relationship between the pupil area of the human eye and the driving speed

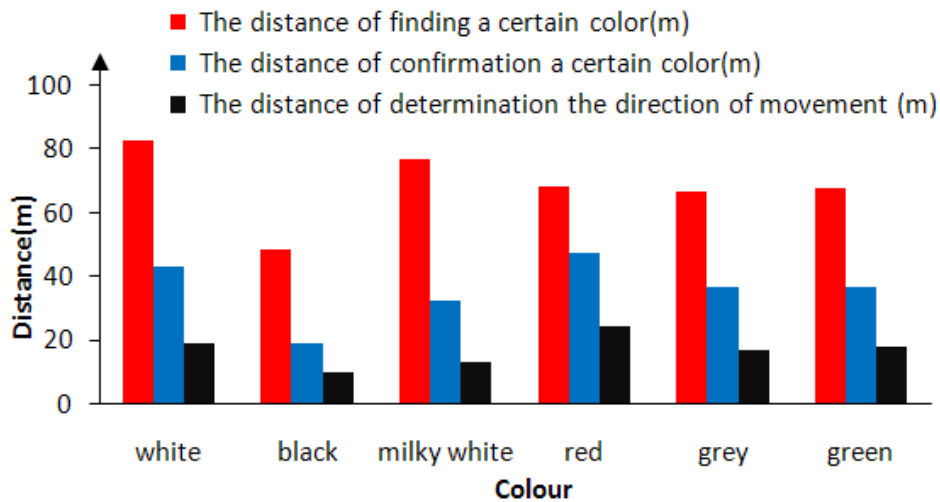


Fig. 3 - The comparison of the visual cognition distance of different colors at night

3. ANALYSIS OF THE CUMULATIVE EFFECT OF HEAVY FOG ENVIRONMENT AND LANDSCAPE COLORS

The cumulative effects can be regarded as the superposition or reduction effect of factors with same or different natures based on spatial and temporal scale (Li et al. [26]). The cumulative effect model includes three parts: the cumulative source, the cumulative approach and the cumulative effect. The cumulative source is divided into the single project cumulative source and the multi-project cumulative source. The cumulative approach contains addition function and interaction function. The cumulative effects are shown in following Table 2.

Tab. 2 - The function of the cumulative effect

Accumulative source	Accumulative way	Accumulative effect
Single source	Plus	Single source superposition
	Interactive	Single source interactive superposition
Multi source	Plus	Multi - source superposition
	Interactive	Multi- source interactive superposition

As shown in Figure 4, without being effectively planned, the accumulation of all factors of landscapes in expressways, including dull colors, unscientific lines, scrambled landscape, and low visibility, will make drivers more tired and increase the risk of road traffic. In the heavy fog environment, low road visibility, increased slippery index in the foggy sections and accumulation of multiple factors will result in a threshold value accumulation effect. To be specific, when the accumulated results of multiple factors exceed certain threshold, the quantitative accumulation leads to qualitative transformation, as shown in Figure 5. The various elements of the driving environment of expressways contain: people, vehicle and road. The elements of road include: visibility, road landscape, the shape of the line, and road slippery index and so on. These factors may bring interactive and cumulative effect to the driver, and then delivered to the vehicle and traffic safety. When the cumulative effect reaches a certain threshold value, it has an impact on traffic safety.



Fig. 4 - Expressways heavy fog environment

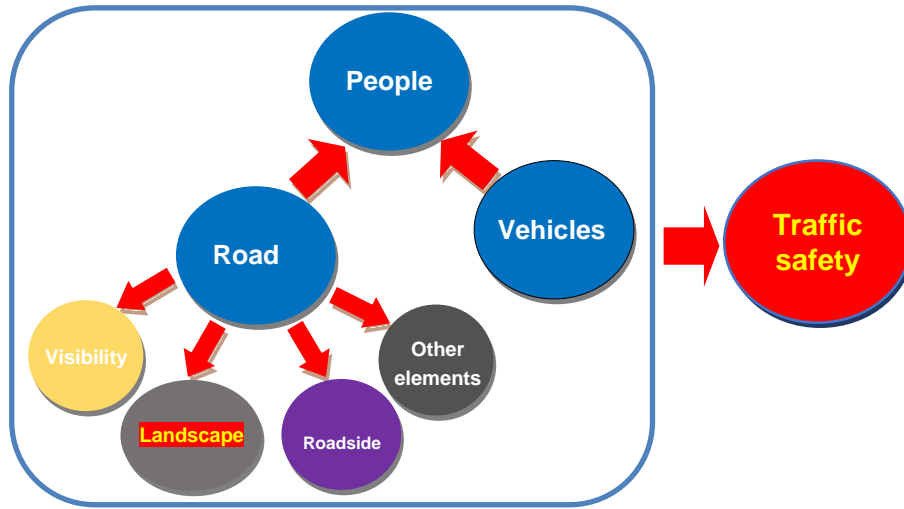


Fig. 5 - The synergistic accumulation of the influencing factors of traffic safety in the foggy sections of expressways

Based on the cumulative effect and according to Figure 5, the following cumulative model can be got,

$$AF = \beta_{xt}RAF + \beta_{yt}PAF + \beta_{zt}VAF \tag{1}$$

AF means the cumulative effect value; RAF means the cumulative source; PAF means the cumulative source of driver; VAF means the cumulative source of vehicle; β_{xt} , β_{yt} and β_{zt} means the cumulative effect index, and in general, $\beta_{xt} + \beta_{yt} + \beta_{zt} = 1$.

$$\begin{cases} \beta_{xt}, \beta_{yt}, \beta_{zt} > 0 \\ \beta_{xt}, \beta_{yt}, \beta_{zt} = 0 \\ \beta_{xt}, \beta_{yt}, \beta_{zt} < 0 \end{cases} \tag{2}$$

In formula (2), $\beta_{xt}, \beta_{yt}, \beta_{zt} > 0$ means positive cumulating. $\beta_{xt}, \beta_{yt}, \beta_{zt} = 0$ means no cumulating. $\beta_{xt}, \beta_{yt}, \beta_{zt} < 0$ means reversed cumulating.

In this paper, RAF means the cumulative source of road, and β_{xt} means the cumulative coefficient of road. β_{xt} is determined by the visibility cumulative coefficient β_{vaf} , the cumulative coefficient of landscape color β_{lcaf} , and the cumulative coefficients of other factors β_{oaf} . The value model of the cumulative coefficient of road β_{xt} is as follows:

$$\beta_{xt} = \delta_v t_v \beta_{vaf} + \delta_l t_l \beta_{lcaf} + \delta_o t_o \beta_{oaf} \quad (3)$$

δ_v , δ_l and δ_o means the value coefficients and t_v , t_l and t_o means the action time of the cumulative coefficients.

In this paper, β_{yt} the cumulative coefficient of *PAF* can be measured by mental tension index of a driver. In experiment, the mental tension index of a driver refers to pupil area of the driver tested by eye tracker. At the same time, in the heavy fog environment, the driving time of drivers influences their mental tension indexes to some extent. Therefore, the value model of β_{yt} is as follows:

$$\beta_{yt} = \delta_i \Delta T \beta_{iaf} + \delta_p t_p \beta_{paf} \quad (4)$$

As to the cumulative impact value of *VAF*, we mainly consider the speed of vehicles, and cumulative indexes in different speeds. The interactive cumulative model based on landscape color and driving time can be derived by formula 1, 3 and 4.

$$AF = (\delta_v t_v \beta_{vaf} + \delta_l t_l \beta_{lcaf} + \delta_o t_o \beta_{oaf})RAF + (\delta_i \Delta T \beta_{iaf} + \delta_p t_p \beta_{paf})PAF + \beta_{zt} VAF \quad (5)$$

In formula 5, ΔT means the absolute driving time of driver in heavy fog environment. β_{iaf} means the cumulative coefficient of absolute driving time ΔT in heavy fog environment. β_{paf} means the cumulative coefficient of mental tension index within absolute driving time in heavy fog environment. δ_i and δ_p means the value coefficients.

After simplifying formula 5, we can get formula 6:

$$AF = RAF \cdot \sum \delta_{RAF} t_{RAF} \beta_{RAF} + PAF \cdot \sum \delta_{PAF} t_{PAF} \beta_{PAF} + \beta_{zt} VAF \quad (6)$$

δ_{RAF} is the cumulative value coefficient of *RAF*; t_{RAF} is the cumulative action time of *RAF*; β_{RAF} is the cumulative coefficient of *RAF*; β_{PAF} is the cumulative value coefficient of *PAF*; t_{PAF} is the cumulative action time of *PAF*; β_{PAF} is the cumulative coefficient of *PAF*.

4. THE SIMULATION EXPERIMENT ON LANDSCAPE COLOR SELECTION IN FOG AREA OF EXPRESSWAYS

4.1. The scheme of simulation experiment

According to the viewpoint of Gao et al. [27], the driving speed should be limited to 80 km/h when the visibility level in the foggy sections of expressways is between 200 m~500 m. This speed is the crest speed of most road sections. In this environment, the outline and linear shape of road, whose influence on driver decreases gradually along with the decreasing of visibility, influence traffic safety in the heavy fog environment. In this research, the software called UC-win/Road (version 4.0) was used to simulate the heavy fog environment with visibility of 200m~500m. According to the actual device using standards, induced lights are set in fog section with the

interval of 30m. Scenes were simulated according to different road landscape formed under the opening and closing conditions of fog lamps. We made simulation experiment to multiple drivers with Tobii Eye Tracker by comparing different vehicle models, driving speeds and time.

Six drivers with good health and proficient driving skill were selected in this experiment. See Table 3 for information of drivers. To optimize the experiment and decrease influences of other physiological factors on driving status, participants are required to sleep well before and keep good mental state in the experiment without drinking wine, coffee or taking medicine.

Tab. 3 - Some information about drivers in the experiment

Sex	Age	Driving Experience	Health Condition	Familiarity	Career
Man	26	2	Good	Unfamiliar	Student
	31	6			Teacher
	37	8			Doctor
	43	18			Driver
Woman	28	4	Good	Unfamiliar	Student
	33	5			Teacher

4.2. The experimental process

Before the experiment, firstly install and debug Tobii eye tracker, prepare driving simulation video, and request drivers to respectively see driving simulation videos with different colors and intervals. During the experiment, the eye tracker will record the variable parameters of drivers' fixation points in three-dimensional space in real time, record simulation video and drivers' facial expressions, and provide basis for data analysis and dealing in the future. To ensure the effectiveness of data, other influencing factors must be eliminated. Drivers will be required to be tested again one week later. After removing abnormal data, the mean values of two experiment data are regarded as the results of the change of the driver's visual indicator.

4.3. Analysis of experimental results

Figure 6 shows the sensitivity of different participants with different driving speeds in a fog environment with visibility of 200m~500m. It can be known from Figure 6 that, drivers have the highest sensitivity on color when the driving speed is 40km/h. Later, their sensitivity on color decreases along with the increasing of driving speed.

To better show the influences of colors on drivers' pupil area under different driving speeds, the changing conditions of the influences of colors on drivers' pupil area in the speed of 40 km/h-80 km/h in fog environment with visibility of 200 m~500 m are shown in Figure 7 and Figure 8.

It can be seen from the pupil area change rates in different speeds from Figure 6 to Figure 8, the change rates of drivers' pupil area under different colors increase along with the increasing of driving speed, while it keeps stable when driving speed is from 62 km/h-80 km/h. It can be known from the relation of drivers' psychological states and change rates of pupil area that, when the driving speed is 40km/h, drivers are comfortable when seeing colors, except red and yellow, or combination of colors. Drivers are out of the demarcation points of tension and comfort when seeing colors of red and yellow. Along with the increasing of driving speed, both red and yellow make drivers nervous, and have obvious influence on increasing rate of pupil area. Other colors or combination of colors make drivers comfortable. The reasons for the above phenomenon is that,

color is the main influencing factor of change rate of pupil area when the driving speed is low, while color and driving speed, which increase change rate of pupil area, jointly influence pupil area and change rates when driving speed increases. When driving speed increases to certain value, the influence of color and speed on change rates of pupil area keeps stable, and the change rates keep stable too. Therefore, the drivers' psychological states are jointly influenced by road colors and driving speeds.

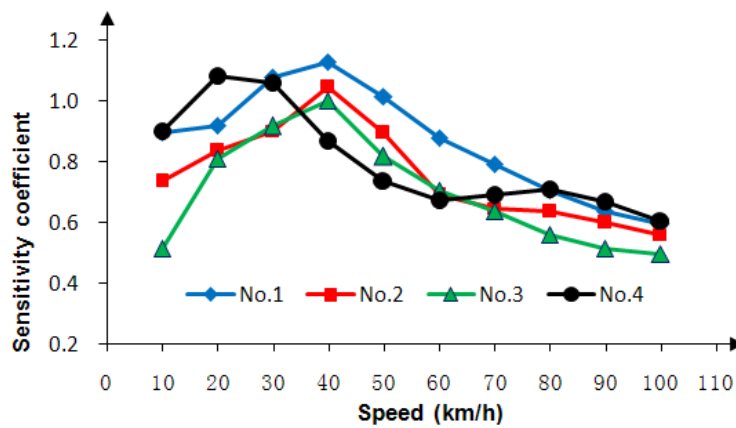


Fig. 6 - The sensitivity of the driver to color in different speeds

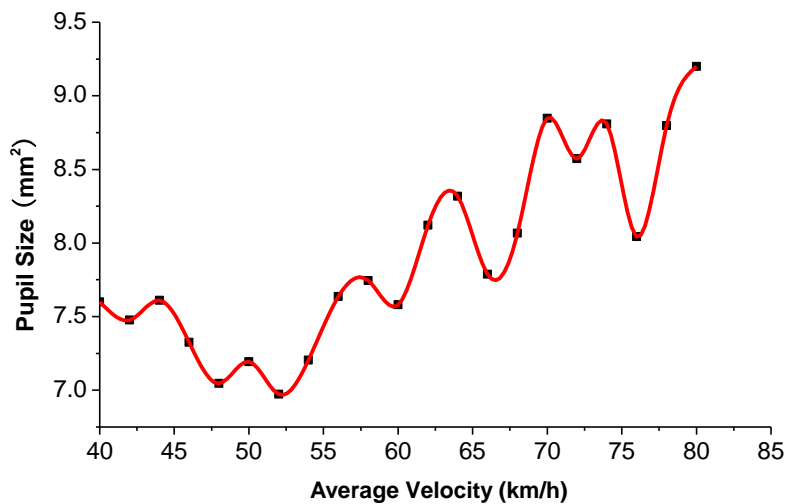


Fig. 7 - The relationship between the human eye's pupil area and the driving speed

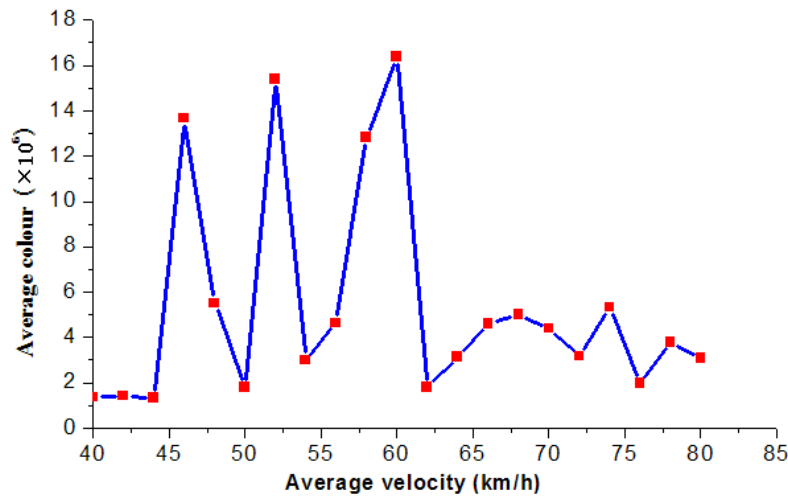


Fig. 8 - The relationship between driving speed and average color

It can be seen from Figure 9 that drivers drive slower when fog lamps are open. It costs them more time to pass fog section when fog lamps are open. On the surface, drivers drive more efficiently when fog lamps are closed. However, from Figure 9, the driving speed range is 80 km/h~200 km/h when fog lamps are closed, which is faster than threshold value of driving speed in fog environment and is an improper driving speed. When fog lamps are open, the driving speed range is 60 km/h~100 km/h, which is a range of normal speed.

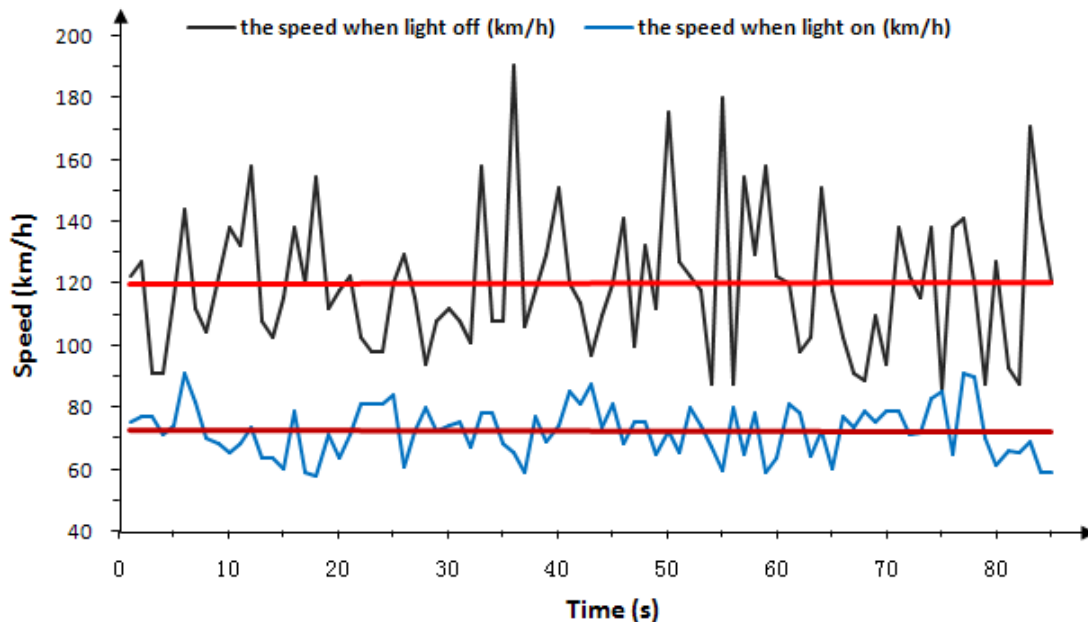


Fig. 9 - Contrast the two speed of induction lamp open and closed

The drivers' field of view decreases when speed increases. Their long apparent distance point extends forward with the rising of speed, while valid field of view narrows. The dynamic long apparent distance point refers to the distance from the longest point saw by driver to eyes of driver

during high speed driving. Not everything within dynamic field of view draws attention of drivers. Traffic environment in dynamic long apparent distance point does not influence driving behavior because there is an alertness distance, which is shorter than long apparent distance, of drivers within the dynamic apparent distance. The alertness distance refers to the distance in which drivers will be drew attention by obstacles or other influencing factors, and take relevant operations. It is showed by this experiment that drivers' controlling on speed is mainly influenced by long apparent distance point and alertness distance, which is specifically showed in Figure 10. From Figure 10, we can find that traffic accidents in the foggy sections of expressways happen more frequently when there is no color induction in fog environment.

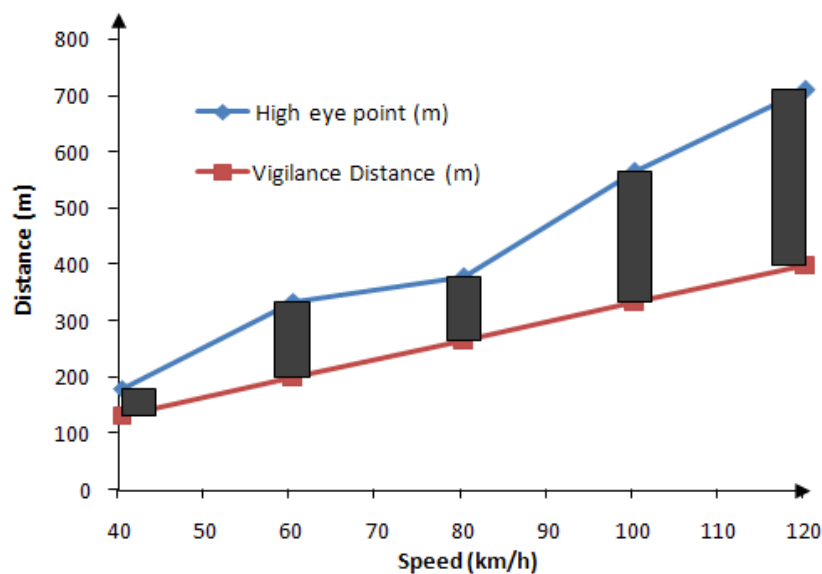


Fig. 10 - The influence relation about speed, high eye point and the warning distance

4.4. Curve fitting of cumulative effect model

To better analyze date, the following fitted curve is got by verifying with cumulative effect model created in previous section and giving curve fitting to cumulative effect function:

$$\begin{cases} y_1 = 0.0336x_1^4 - 0.6588x_1^3 + 3.1799x_1^2 + 6.6584x_1 - 1.0667 \\ y_2 = 0.0196x_2^4 - 0.2997x_2^3 + 0.1919x_2^2 + 14.369x_2 - 9.8219 \\ y_3 = 0.0196x_3^4 - 0.2997x_3^3 + 0.1919x_3^2 + 14.369x_3 - 9.8219 \\ y_4 = 0.0113x_4^4 - 0.1282x_4^3 - 0.7854x_4^2 + 15.994x_4 - 9.0046 \end{cases} \quad (7)$$

R²-the test of goodness of fit of the model, are separately 0.9948, 0.99, 0.99 and 0.9706, which shows that the landscape colors formed by open and closed fog lamps influence drivers' driving speed and pupil area to some extent.

5. CONCLUSIONS

When the visibility in the foggy sections of highway is less than 500m, the sight of the driver will be seriously affected, although the meteorological department would issue yellow warning of disaster, but often still cannot prevent a lot of serious traffic accidents. In view of this problem, although many scholars have analyzed and discussed from different angles, there is rare quantitative analysis on the influence of accumulation effect of landscape color on the traffic safety in the foggy sections of expressways. Therefore, according to the model derivation and simulation experiment analysis, the following conclusions are obtained.

(1) Drivers are very sensitive to the color of road landscapes, which has an impact on road-traffic safety. In the fog environment with visibility of 200m-500m, when the road landscape color is yellow, the pupil area of the driver through the fog area is the largest, followed by red. At the same driving speed, the influence sequence of colors on the driver's pupil area is yellow > Red > yellow-white > red-white > orange > white.

(2) Based on the cumulative effects of the fog environment and the landscape color of expressways, the interactive cumulative model based on landscape color and driving time in heavy fog environment was deduced. Because multiple influencing parameters including the speed of the vehicle, the cumulative index under different speeds, the cumulative value coefficient, the accumulated time, the cumulative coefficient and the cumulative action time were considered in the proposed model, so the model is more close to the real scene of the highway traffic in fog environment.

(3) By using the Tobii eye tracker and UC-win / Road simulation software, multi-group of the fog lamp color and spacing experiment program with 200m-500m visibility in fog environment was designed, and according to the program, the simulation experiments on several drivers were carried out to test the influence of road landscape color in fog environment on drivers' visual psychology. The simulation experiment results show that the smaller the driving speed, the greater the visual impact of the road landscape color on the driver; with the increment of the driving speed, the pupil area also shows a growing trend, this indicates that the driver's psychological stress levels is proportionate to the driving speed; while when the driving speed exceeds 70km/h, the influence of color on change rate of pupil area tends to be stable, and the landscape color has relative lesser influence on the visual psychology of the driver at this time.

(4) Based on the interactive cumulative model and simulation experimental data analysis, we can see that in the fog environment with visibility between 200m and 500m, the red and yellow have a great influence on the visual psychology of the driver, and along with the increasing of the driving speed, the visual psychological effects of these two kinds of color on the driver is more significant than the other colors. Thus, the installation of red and yellow fog lights on both sides of the road can effectively alleviate the psychological tension of the driver in the heavy fog environment.

ACKNOWLEDGMENT

This research was substantially supported by the National Science Foundation of China (Grant No. No. 51678098), the Science and Technology Innovation Project of Chongqing Social Work and People's Livelihood Guarantee (cstc2017shmsA00002), the Science and Technology Plan Project of Chongqing Land Resources and Housing Administration (KJ-2017019) and the Scientific Research Innovation Fund to Graduate Student of Chongqing (CYB16112).

REFERENCES

- [1] Li Weimin, Li Aimin, Wu Dui, 2005. Forecasting, predicting and monitoring system in fog area of highways. China Communications Press.
- [2] Fu Zhiming, 2008. A study of traffic safety ensure system ensure system for highway in fog area. Zhejiang University of Technology.
- [3] Jiang Xiancai ,Huang Ke, 2012. Safeguards and effects of road transportation safety in fog. Journal of Harbin Institute of Technology. Vol. 44(6): 86-91.
- [4] Qian Huaifeng, 2013. Intelligent guidance system of expressway fog zone based on beidou satellite-timing. Traffic Engineering. Vol. 22: 98-100.
- [5] Yang Yanqun, Zhuo Xi, Lai Yuanwen, et al., 2009. Control and setting technology of roadside fog lamps on the expressway". Highway Engineering. Vol. 34(2): 86-91.
- [6] Munehiro K, Tokunaga R A, Asano M, et al.,2007. Effect of retro-reflecting performance for traffic signs by driving visibility evaluation under foggy conditions. Proceedings of the Eastern Asia Society for Transportation Studies, pp.337
- [7] Creusen I M, Wijnhoven R G J, Herbschleb E, et al., 2010. Color exploitation in hog-based traffic sign detection// IEEE International Conference on Image Processing, pp.2669-2672.
- [8] Zaklouta F, Stanculescu B, 2011. Segmentation masks for real-time traffic sign recognition using weighted HOG-based trees". Physical Review Letters. Vol. 32(14): 1954-1959.
- [9] Wang Yan, Ma Lin, Jia Fucang, et al., 2003. Functional neuroanatomy of color and motion perception in the humans: an event-related functional magnetic resonance imaging. Chinese Journal of Medical Imaging. Vol. 11(01): 47-50.
- [10] Yuan Jia and Hu Xiaohong, 2004. Application of colors in landscape design in tunnels. Technology of Highway and Transport. Vol. (3): 78-80.
- [11] Zhang Qiang, Chen Yuren and Pan Xiaodong, 2005. Application of color psychology in road traffic safety. East China Highway. Vol. (6): 67-69.
- [12] Yuan Hongwei, Xiao Guiping, Nie Lei, et al., 2006. Exploration of relation between colors and traffic safety. Journal of Safety and Environment. Vol.32 (05): 41-45.
- [13] Lee T, Mimura Y, Inagaki T, et al., 2009. Study on the effect of color pavement intersection based on resident's attitudes to traffic safety in residential area: a case study in toyota city, Aichi. Journal of the City Planning Institute of Japan. Vol. (44): 475-480.
- [14] Li Zhenfu, 2006. Color psychology and city communication safety culture. Safety and Environmental Engineering. Vol. 13(4): 70-73.
- [15] Siogkas G, Skodras E and Dermatas E, 2012. Traffic lights detection in adverse conditions using color, symmetry and spatio temporal information// International Conference on Computer Vision Theory and Applications, pp. 620-627.
- [16] Xu Hongliang, Zhang Taixiong, and Tang Boming et al., 2009. Design of road traffic safety color system based on color perception. Journal of Chongqing Jiaotong University (natural science). Vol. 28(01): 105-107
- [17] Zhang Wenbo, Duan Hui, Wang Haomiao, 2010. Risk assessment and harmony of urban road traffic colors. Science Paper Online. Vol. 05(10): 773-778.
- [18] Dai Fang and Deng Weidong, 2010. Analysis of Traffic Security Improvement of Highway by means of Application of Color Pavement". Technology of Highway and Transport. Vol. (3): 128-130.
- [19] Shen Xiang, Li Qingfu, Wang Di, et al., 2012. Color analysis and design of road traffic safety system based on psychological function of colors. Henan Science. Vol. 30(01): 107-110.
- [20] Wang Linhong, Li Shiwu, Zhou Rubo, et al.,2013. Impact of roadside landscape color on driver mean heart rate. Journal of Jilin University (Engineering and Technology Edition) 43, no.01: 74-80.
- [21] Zhang Mengdong, 2014. Research on portal landscape design onaccount of safety. Heilongjiang Jiao Tong Ke Ji. Vol.(2): 67.
- [22] Tao Panpan, Shang Ting, 2015. Landscape color of tunnel portal based on driver heart rate. Journal of PLA University of Science and Technology (natural science edition). Vol. 16(5): 471-475.
- [23] Da Zhihao, 1986. Colour design knowledge. Translated by Yin Wusong. Popular Science Press.
- [24] Ladd-Franklin Christine,1999. Colour and colour theories. Taylor & Francis.
- [25] Ouyang Wenzhao, Liao Kebing, 2002. Safety man-machine engineering. China Coal Industry Publishing House.
- [26] Li jiacheng, Shen weishou, Lin naifeng, et al., 2013. Study on ecological cumulative effects of qinghai-tibet railway based on remote sensing and geographic information system. Journal of Ecology and Rural Environment. Vol. 29(5): 566-571



[27] Gao Jianping and Zhang Xuguang, 2014. Analyses on driver's visual effect of fog on expressway. Journal of Wuhan University of Technology. Vol.36 (9): 68-72

HYBRID CONTINUUM-DISCONTINUUM MODELLING OF ROCK FRACUTRE PROCESS IN BRAZILIAN TENSILE STRENGTH TEST

Huaming An^{1, 2}, Hongyuan Liu², Xuguang Wang³, Jianjun Shi¹, Haoyu Han²*

1. *School of Civil & Resource Engineering, University of Science & Technology Beijing, China. Email Huaming.an@yahoo.com*
2. *School of Engineering and ICT, University of Tasmania, Australia.*
3. *Beijing General Research Institute of Mining & Metallurgy, China.*

ABSTRACT

A hybrid continuum-discontinuum method is introduced to model the rock failure process in Brazilian tensile strength (BTS) test. The key component of the hybrid continuum-discontinuum method, i.e. transition from continuum to discontinuum through fracture and fragmentation, is introduced in detail. A laboratory test is conducted first to capture the rock fracture pattern in the BTS test while the tensile strength is calculated according to the peak value of the loading forces. Then the proposed method is used to model the rock behaviour during BTS test. The stress propagation is modelled and compared with those modelled by finite element method in literatures. In addition, the crack initiation and propagation are captured and compared with the fracture pattern in laboratory test. Moreover, the force-loading displacement curve is obtained which represents a typical brittle material failure process. Furthermore, the stress distributions along the vertical direction are compared with the theoretical solution. It is concluded that the hybrid continuum-discontinuum method can model the stress propagation process and the entire rock failure process in BTS test. The proposed method is a valuable numerical tool for studying the rock behaviour involving the fracture and fragmentation processes.

KEYWORDS

Hybrid Continuum-Discontinuum, Brazilian Tensile Strength Test, Rock Failure Process, Crack Initiation and Propagation

INTRODUCTION

Understanding the rock failure behaviour can benefit many industrial operations, e.g. mining, tunnelling and demolition of urban structures. Nowadays, the rock behaviour is studied through laboratory test and numerical methods. With the development of the computer technologies, it is possible to carry out large-scale calculation in short time. Thus, numerical methods are widely employed to study the rock failure behaviours in various conditions [1-4].

Numerical methods can be classified according to the hypothesis that the rock is modelled as a continuous or discontinuous materials. Therefore, there are three kinds of numerical methods, i.e. continuum method, discontinuum method, and combined continuum-discontinuum method. As the rock can be considered as continuous material before fractures and cracks occur while it can be treated as discontinuous material after fracture and fragmentation, the combined continuum-discontinuum method might be a better choice to model the entire rock failure processes.

In the paper, a combined continuum-discontinuum method, i.e. hybrid finite-discrete element method is employed to model the rock failure process in Brazilian tensile strength (BTS) test. On the one hand, the modelling of the rock failure process in BTS test is used to calibrate the proposed method since the BTS test is widely studied and a laboratory test is conducted in this research. On the other hand, the modelled failure process of BTS test can be used to demonstrate the capabilities of the proposed method in capturing the rock behaviours under static loading.

Hybrid FEM/DEM Method

Since a hybrid finite-discrete element method merges finite element tools and techniques with discrete element algorithms [5], it is considered to combine the advantages of finite element method in modelling the continuum materials and the discrete element method in simulating the discontinuum materials. In the hybrid FEM/DEM, a typical numerical model is considered to consist of a single discrete body or a number of interactive discrete bodies within general shapes and sizes, each of which is represented by a single discrete element and the interaction of them is governed by contact law [6]. In addition to interacting with each other, each discrete element is discretized into finite elements to capture the transition from continuum to discontinuum i.e. deformability fracture and fragmentation [6]. As the fracture requires activation and growth of many flaws and cracks to complete the failure process, it is reasonable to describe the process in a continuous way considering the continuum and discontinuum of material and transition between them.

The key components of the hybrid FEM/DEM include contact detection and interaction among those individual discrete bodies, deformability and transition from continuum to discontinuum through fracture and fragmentation of individual discrete bodies, temporal integration scheme and computational fluid dynamics [6].

A hybrid FEM/DEM method consists of these essential components has been implemented by Liu et al. [6] on the basis of their previous enriched finite element codes RFPA-RT2D [7] and TunGeo3D [8], and the open-source combined finite-discrete element libraries Y2D and Y3D originally developed by Munjiza [5] and Xiang et al. [9], respectively, which is to be used in this study.

The modelling of rock fracture in Brazilian test involves the fracture and fragmentation of rocks. Correspondingly, the transition from continuum to discontinuum is the key components for the rock fracture modelling in Brazilian test. Therefore, it is introduced briefly here while the detailed introduction can be found in a recent paper published by the authors [10].

Transition from continuum to discontinuum

In the hybrid FEM/DEM, a discrete element is discretized into finite elements while those finite elements are bounded together through a four-node joint element. The transition from continuum to discontinuum, i.e. fracture and fragmentation of rock mass, is implemented through the separation of the joint elements while bonding stresses are involved in the separating processes of joint elements. In the hybrid FEM/DEM, a bonding stress is taken to be a function of the separation between the surfaces of joints elements and cracks are assumed to coincide at the surfaces of the joint elements during fracturing.

The separation δ at any point can be divided into two components in Equation 1

$$\delta = \delta_n n + \delta_s t \quad (1)$$

where n and t are the unit vectors in the normal and tangential directions, respectively, of the surface at such a point, δ_n and δ_s are the magnitudes of the components of δ on the normal and tangential directions, respectively.

Figure 1 illustrates the relationship between the bonding stress and opening/sliding displacement under tension and shear conditions. If the separations in the normal direction δ_n or in the tangential direction δ_s , reach critical displacements i.e. δ_{np} in normal direction or δ_{sp} in tangential direction, determined by the tensile strength σ_t or the shear strength σ_c of the element, damages are assumed to occur. During this period, the bonding stresses are increasing. Then the separations of the joint element continue to increase, i.e. $\delta_n > \delta_{np}$ in normal direction or $\delta_s > \delta_{sp}$ in tangential direction, while the bonding stresses gradually decrease. When the opening of the joint element in normal direction is beyond the ultimate opening displacement δ_{nu} , the joint element is broken and the tensile failure is assumed to occur. The opening of the joint element in tangential direction exceeds a residual opening displacement δ_{sr} , the shear failure is assumed to occur and the bonding stress becomes a purely frictional resistance. Equation 2 illustrates the relationship between the bonding stress and the opening of the joint element in normal direction for tensile failure while the Equation 3 indicates the relationship between the bonding stress and the opening of joint element in tangential direction for shear failure.

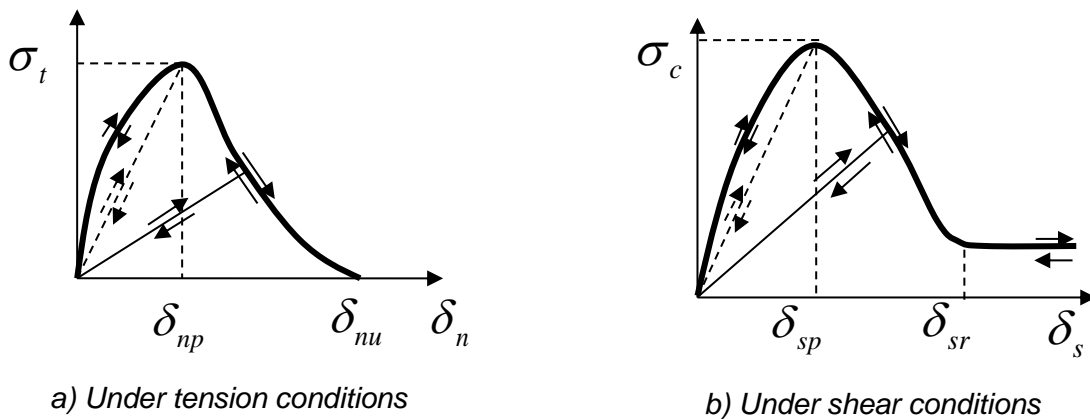


Fig. 1 - Relationship between the bonding stress and opening/sliding displacement under tension and shear conditions

$$\sigma_n = \begin{cases} \left[2 \frac{\delta_n}{\delta_{np}} - \left(\frac{\delta_n}{\delta_{np}} \right)^2 \right] \sigma_t, & \text{if } 0 \leq \delta_n \leq \delta_{np} \\ f(D) \sigma_t, & \text{if } 0 \leq \delta \leq \delta_{nu} \\ 0, & \text{if } \delta \geq \delta_{nu} \end{cases} \quad (2)$$

$$\tau = \begin{cases} \left[2 \frac{\delta_s}{\delta_{sp}} - \left(\frac{\delta_s}{\delta_{sp}} \right)^2 \right] \sigma_c, & \text{if } 0 \leq \delta_s \leq \delta_{sp} \\ g(D) \sigma_c, & \text{if } \delta_{sp} \leq \delta_s \leq \delta_{sr} \\ \sigma_n \tan(\theta_f), & \text{if } \delta_s \geq \delta_{sr} \end{cases} \quad (3)$$

where D is a damage variable between 0 and 1, $f(D)$ and $g(D)$ are damage functions described in the mechanical damage model [7], and θ_f is the joint residual friction angle.

Experimental study of the rock fracture in Brazilian disc test

In the last few decades, the BTS test has been developed mainly for determining the tensile strength of the rock and rock like materials [11, 12]. The BTS test is first proposed by AKazawa (1943) and Carneiro (1943) independently to calculate tensile strength of rock materials [11, 12]. Due to the relatively uniform distribution of the tensile stress along the loaded diameter [13] and its simplicity to prepare, this method is widely accepted as an indirect method to determine tensile strength of rocks.

The conventional equation for determining tensile strength using BTS test is given as follows [14, 15].

$$\sigma_t = \frac{2P}{\pi Dt} \quad (4)$$

where σ_t is the tensile, P is the load at failure, D is the diameter of the test specimen, t is the thickness of the test specimen measured at the centre.

In addition to the tensile strength, the stress distribution of BTS test is also widely studied. Hondros (1959) [16] gave a complete stress solution for Brazilian disc under diametrical compression valid for both plane stress and plan strain condition.

$$\sigma_{xx} = \frac{P}{\pi Rt\alpha} \left\{ \frac{[1 - (\frac{r}{R})^2] \sin 2\alpha}{1 - 2(\frac{r}{R})^2 \cos 2\alpha + (\frac{r}{R})^4} - \tan^{-1} \left[\frac{1 + (\frac{r}{R})^2}{1 - (\frac{r}{R})^2} \tan(\alpha) \right] \right\} \quad (5)$$

$$\sigma_{yy} = -\frac{P}{\pi Rt\alpha} \left\{ \frac{[1 - (\frac{r}{R})^2] \sin 2\alpha}{1 - 2(\frac{r}{R})^2 \cos 2\alpha + (\frac{r}{R})^4} + \tan^{-1} \left[\frac{1 + (\frac{r}{R})^2}{1 - (\frac{r}{R})^2} \tan \alpha \right] \right\} \quad (6)$$

where P is the applied load, R is the disc radius, r is the distance from centre of the disc, t is the disc thickness, 2α is the angular distance of load arc, σ_{xx} and σ_{yy} are stresses along the horizontal and vertical directions respectively

The fracture initiation and propagation of Brazillian disc test were also investigated. For a valid Brazilain disc test for measuring the tensile strength, the failure is supposed to originate at the centre of the disc and the guarantee of crack initiation at the centre of the specimen is that the loading angle corresponding to the flat end width must be greater than a critical value. However, the fracture still may initiates away from the centre of the test disc [17] or occurs at the loading points [18].

In this section, the BTS test is conducted in the laboratory to capture the fracture pattern of Brazilian disc under diameter forces. Figure 1 shows the simple of granite rock. The diameter of the disc is 50mm while the thickness of the disc is 25mm.



Fig.1 - Rock simple for Brazilian test

Figure 2 illustrates hydraulic testing machine which is used to conduct the BTS test. The disc is placed between two curved loading jaws. The curved loading jaw moves at the speed of 0.02mm/min.

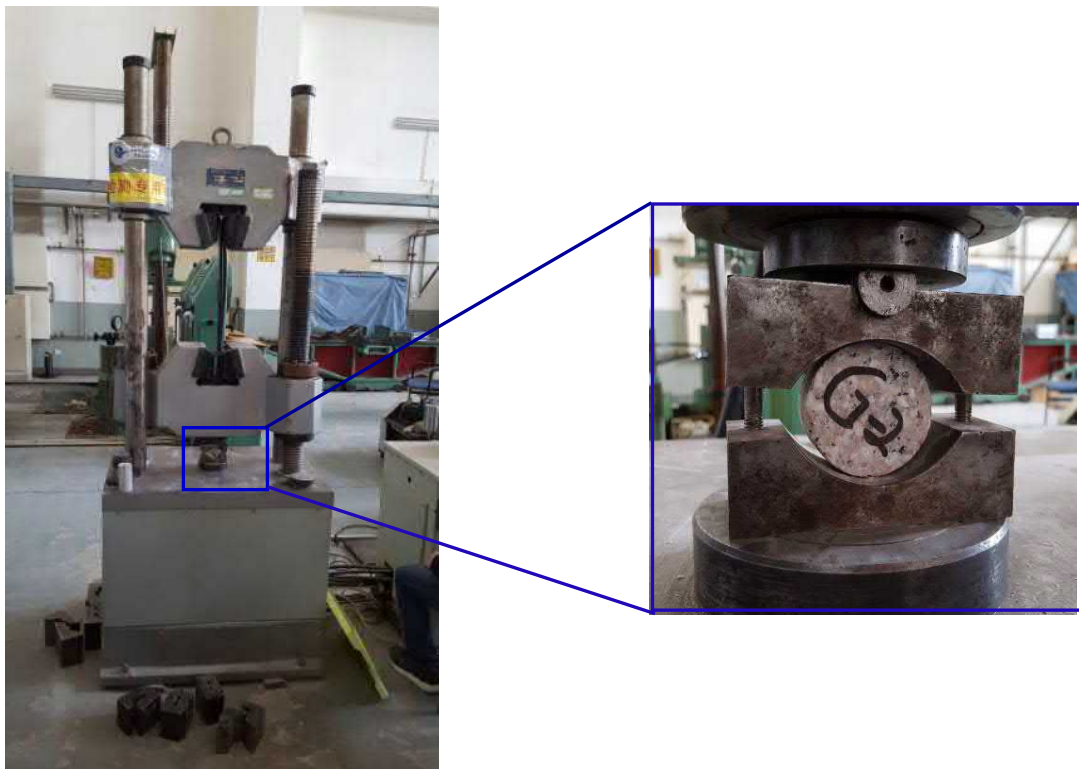


Fig.2 - Hydraulic testing machine for Brazilian test



Fig.3 - Fracture pattern of BTS test

Figure 3 demonstrates rock failure pattern of the BTS test. It can be seen that the rock crack is the loading diameter. According to the fracture initiation and propagation of BTS test investigated by Colback (1966), the experimental result indicates that the experiment in this research is valid for calculating the tensile strength of the sample as the crack is along the loading diameter.

The recorded loading force is 24.79kN, which can be used to calculate the tensile strength of the sample. According to Equation 4, the tensile strength of the sample is calculated as follows.

$$\sigma_t = \frac{2P}{\pi Dt} = \frac{2 \times 24.79 \text{ kN}}{3.14 \times 0.05 \times 0.025} = 12.63 \text{ Mpa} \quad (7)$$

Hybrid finite-discrete element modelling of the rock failure process in BTS test

In this section, a hybrid finite-discrete element method is employed to model the rock fracture initiation and propagation of the BTS test.

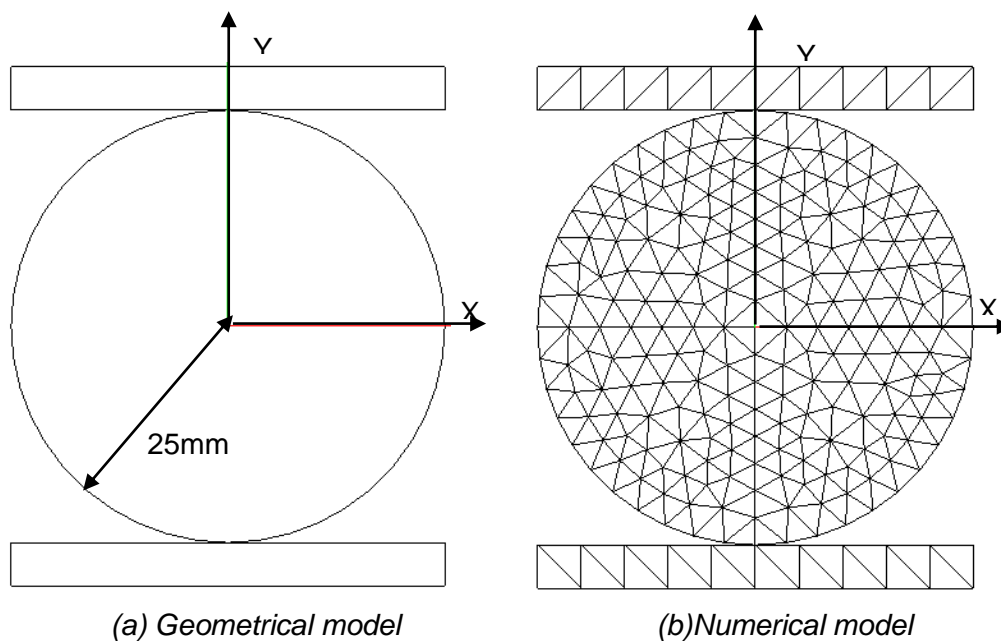


Fig.4 - Geometrical and Numerical model for BTS test

The simulation of the BTS test is simplified as a plan strain problem and only the vertical direction is considered. Figure 4a indicates the geometrical model while Figure 4b illustrates the numerical model. It can be seen in Figure 4a that the diameter of the disc is 25mm and the sample is placed between two loading plates. The numerical model shown in Figure 4b is discretised into finite elements and the fracture and fragmentation modelling is implemented through separation of finite elements.

The material properties of the rock mass in the experimental test (Figure 1) are adopted for the numerical model and the detailed parameters are obtained through BTS test and uniaxial compression strength test. The materials properties of the rock specimen are Young's modulus $E = 60 \text{ GPa}$, Poisson's ratio $\nu = 0.26$, density $\rho = 2600 \text{ Kg m}^{-3}$, tensile strength $\sigma_t = 12 \text{ MPa}$, compressive strength $\sigma_c = 120 \text{ MPa}$, internal friction angle $\Phi = 30^\circ$, surface friction coefficient $u = 0.1$. The material properties of the loading plates follow those of standard steels. During the modelling, two palates move towards each other at 0.1m/s. It should be noted that loading rate is bigger than that in laboratory test. However, the applied loading rate will not significantly influenced the rock properties according to the dynamic rock fracture test by Zhang (2001) [19].

Numerical modelling of the stress wave propagation process

The modelled temporal and spatial distribution of the stress wave under constant displacement increment loading of 0.1m/s are depicted in Figure 5. The stress distributions in the Figure 5 correspond to the minor principal stress while the size can be refereed to colour legend shown at the top of the Figure 5.

As the loading plates contact the sample, the stress waves are induced immediately at the two contact areas as shown in Figure 5 at $0.5\mu\text{s}$. Then the stresses at the two loading ends propagate toward each other at meet at $32.5\mu\text{s}$. As can be seen that the stress is mainly distributed along the loading line and the stress becomes more and more intensive as shown in Figure 5 at $220.5\mu\text{s}$. When the stress along the loading is strong enough, i.e. the tensile stress along the horizontal direction meets the tensile strength of the sample, tensile failure occurs as shown in Figure 5 at $260\mu\text{s}$. After that, the stress still is mainly distributed along the loading line while it is scattered in the disc after the failure completes (Figure 5 from $320\sim 450\mu\text{s}$).

Numerical modelling of the crack initiation and propagation

Figure 6 demonstrates the crack initiation and propagation process in the BTS test. In Figure 6, the red colour represents the tensile failure while the blue colour represents the shear cracks and the boundary of the sample.

As indicated in Figure 5 that the tensile stresses exceed the tensile strength of the material at $261.5\mu\text{s}$, the tensile failure occurs at almost the centre of the disc (Figure 6 at $261.5\mu\text{s}$). Then the cracks propagate along the loading diameter toward to the loading plates. At $290\mu\text{s}$, the cracks initiated from the centre of the disc arrived at the loading areas. As the stresses continue to accumulate at the loading areas in the top and bottom of the disc, the compressive stress exceeds the compressive strength of the sample. Thus, shear failure occurs at the loading vicinity, i.e. the contact areas of the loading palates with the disc, as shown in Figure 6 at $305\mu\text{s}$. As the loading plates continue to move toward each other, the tensile cracks along the loading diameter expand due to the tensile stresses along the horizontal direction induced by compression of the disc on the vertical direction. In addition, the shear cracks at the loading vicinities propagate approximately parallel to the loading diameter (Figure 6 from 320 to $450\mu\text{s}$).

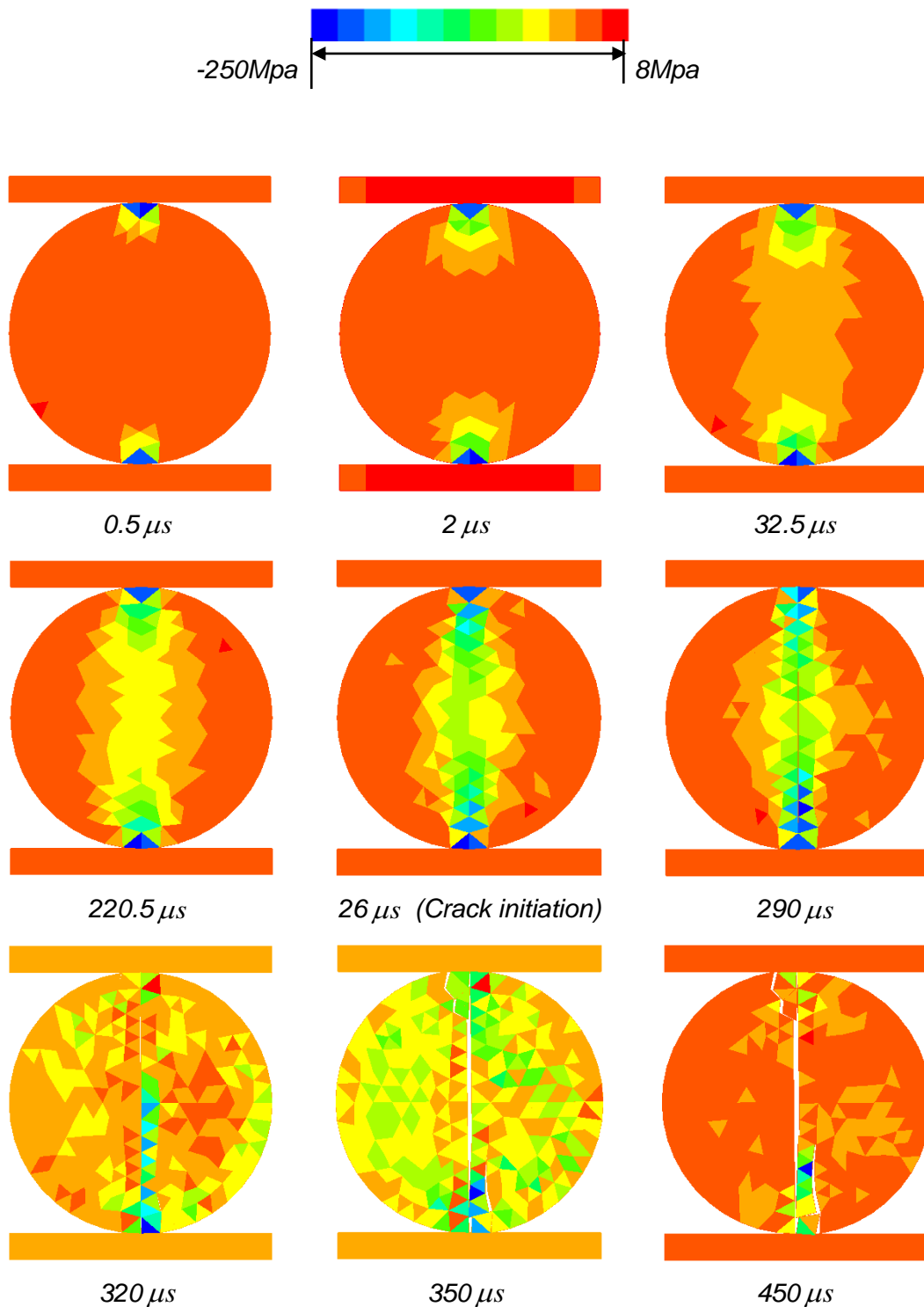


Fig.5 - Stress propagation process of BTS test

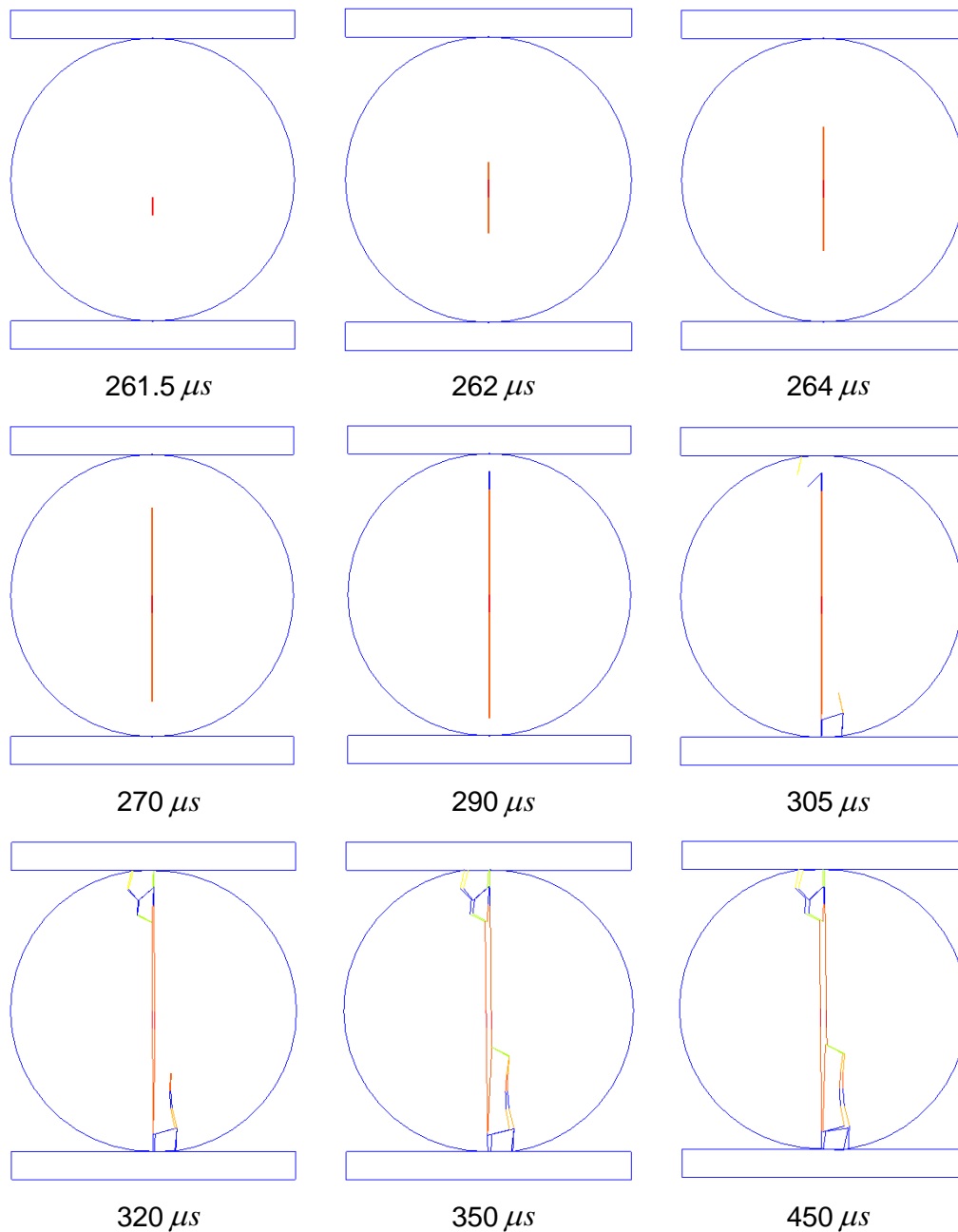


Fig.6 - Crack initiation and propagation of BTS test

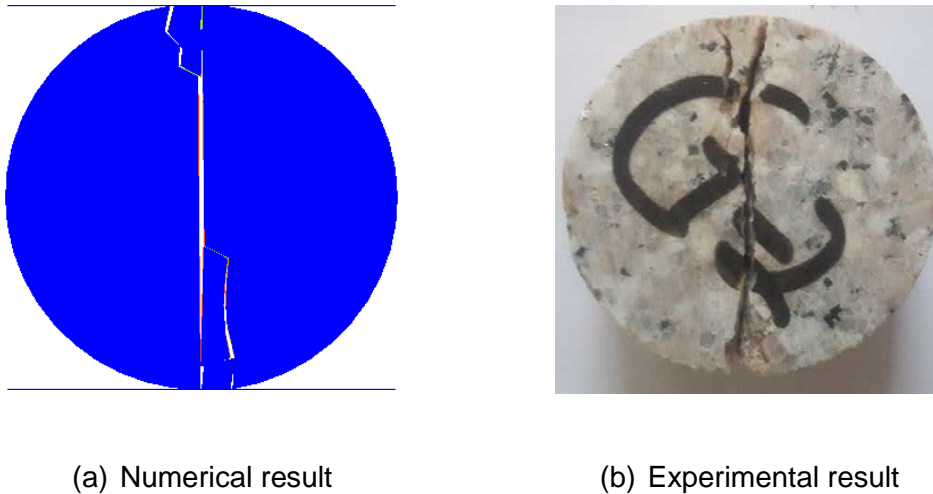


Fig.7 - Comparison of the numerical and experiential results

According to experiments conducted by Malan et al. (1994) [20], a typical fracture propagation in BTS test includes primary tensile cracks along the loading diameter and secondary shear cracks from the loading sides parallel to the primary cracks. Thus hybrid finite-discrete element method obtains a valid failure pattern in BTS test. Figure 7 compares the numerical result with the experimental result. In Figure 7a, the blue colour represents rock mass while the white colour represents cracks. As shown in Figure 7, the modelled result agrees well with the experiential result as follows:

- Both the main cracks are along the loading diameters.
- Both the secondary cracks occur at the loading vicinities
- Both the discs are separated into two halves along the vertical diameters.

Force-loading and Stress along the loading diameter analysis

In this section, the relationship between the force-loading from the top plates and the corresponding displacement is analysed while the stresses distribution along the loading line are compared with the theoretical solutions.

Force-loading displacement analysis

Figure 8 shows the relationship between displacements and loading from the top plate. As shown in the Figure 8, the force increases rapidly as the loading plate moves. Initially, the force-loading displacement is almost linearly (Figure 8 A-B-C). Then the force reaches its peak (Figure 8 D). After that the force decreases gradually for a while (Figure 8 D-E) and decreases sharply to the bottom (Figure 8 E-F). Finally, the force drops to approximately zero as the sample completely loses its bearing capability (Figure 8 G).

The force-loading displacement curve of the BTS test represents a typical behaviour of brittle rock under compression: a compressive deformation region (AB), a linear-elastic deformation region

(BC), a non-linear deformation region (CD), a strain-softening deformation region (DEF) and a residual deformation region (FG).

According to the recorded peak load, i.e. 1.01MN, the tensile strength can be obtained on the basis of Equation 4.

$$\sigma_t = \frac{2P}{\pi Dt} = \frac{2 \times 1.01 \times 10^6}{3.14 \times 0.050 \times 1} = 12.87 \text{Mpa} \quad (8)$$

The modelled tensile strength, i.e. 12.87Mpa is bigger than the input parameter (12Mpa), which is caused by a relatively bigger loading rate (0.1m/s) adopted.

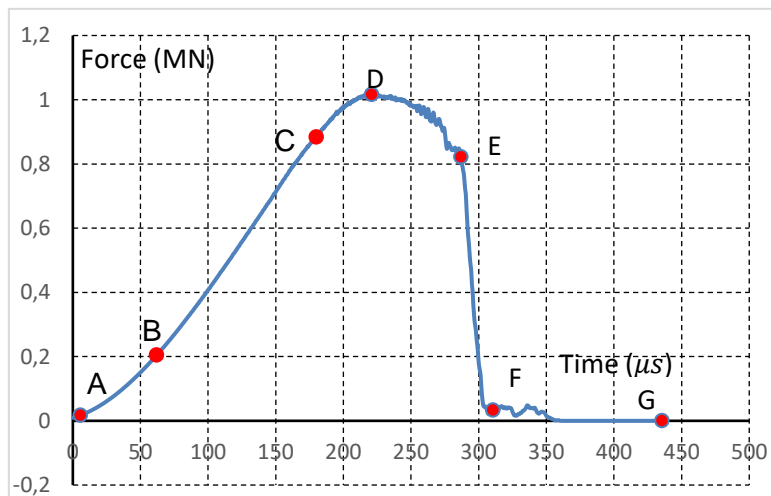


Fig.8 - Force-loading displacement curve

Comparison of the numerical and analytical stresses distribution along the loading diameter

Since the complete stress distribution of BTS test along the loading diameter are given by Hondros (1959), the numerical solution along the loading line is compared with the analytical solution to calibrate the hybrid FEM/DEM method.

The Equation 5 and Equation 6 are used to generate the stress distributions along the loading diameter. In the two equations, P is the peak load, i.e. 1.01MN while 2α is 0.1047, i.e. 6° . Figure 9 illustrates the comparison of Hondros` solution according to Equation 5 and Equation 6 and the numerical solution. In terms of stress in the horizontal direction (σ_{xx}), the analytical or theoretical stress along the loading diameter keeps constant and that is the reason BTS test is used to obtain tensile strength indirectly. The numerical stress in the horizontal direction, i.e. the tensile stress, agrees with the analytical solution as the numerical tensile stress keeps almost constant although there is a slightly fluctuation. Additionally, the horizontal stresses for both numerical and analytical solutions become compressive stresses instead of tensile stresses at the loading points probably due the stress concertation. For the stresses in the horizontal direction (σ_{yy}), the numerical solution also shows a good agreement with the analytical or theoretical solution as they both compressive stress and gradually become strong from the centre of the disc to the loading points.

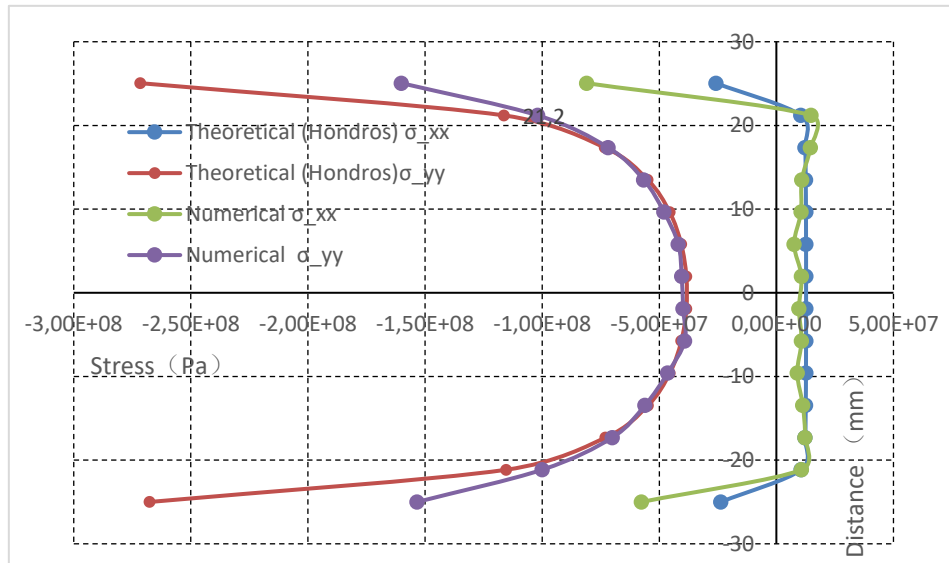


Fig.9 - Theoretical and numerical results of stresses distribution across loaded diameter for disc specimen

CONCLUSION

A combined continuum-discontinuum method, i.e. hybrid finite-discrete element method, is proposed to model the crack initiation and propagation of rock in BTS test. Since the key component, i.e. transition from continuum to discontinuum from fracture and fragmentation, makes the hybrid method superior to the continuum based method, e.g. finite element method, and the discontinuum based method, e.g. discrete element method, the transition from continuum to discontinuum is introduced in detail. Then the proposed method is employed to model the rock failure process in BTS test. In order to calibrate the proposed method, an experimental study is done first to capture the rock failure pattern and to calculate the tensile strength of the rock in BTS test.

The stress propagation is modelled and compared with those well documented in literatures. The crack initiation and propagation are simulated and the modelled result, i.e. rock failure pattern, shows a good agreement with the experimental study. Additionally, the force-loading displacement curve for the simulation is drawn and it represents a typical brittle material failure process. Furthermore, theoretical and numerical solutions for the stresses on the loading line are compared. The numerical solution agrees well with the theoretical solution although there is a slight fluctuation for the tensile stress along the loading line. It is concluded that

- The hybrid method is able to model stress propagation process in BTS test. The stress mainly concentrates on the loading line and the tensile strength is almost constant although the rock is not an elastic material.
- The hybrid method can capture the entire rock failure process in BTS test and the modelled results show good agreements with the experimental result. Additionally, the crack initially generates at the centre of the loading line and propagates toward the two loading points.
- The hybrid method is a valuable numerical tool in modelling the rock initiation and propagation process.

ACKNOWLEDGEMENTS

The research presented in this study forms part of the first author's PhD study at the University of Tasmania under the supervision of the corresponding author, which is partly supported by a two-year visiting PhD scholarship provided by China Scholarship Council (CSC). The CSC's support is greatly appreciated.

REFERENCES

- [1] Liu, H., S. Kou, P.-A. Lindqvist, and C. Tang., 2007. Numerical modelling of the heterogeneous rock fracture process using various test techniques. *Rock mechanics and rock engineering*, Vol.40(2): 107-144.
- [2] Mahabadi, O., B. Cottrell, and G. Grasselli., 2010. An example of realistic modelling of rock dynamics problems: FEM/DEM simulation of dynamic Brazilian test on Barre granite. *Rock mechanics and rock engineering*. Vol.43(6): 707-716.
- [3] Stefanizzi, S., G. Barla, P., 2009. Numerical modeling of standard rock mechanics laboratory tests using a finite/discrete element approach. *Proceedings of the 3rd CANUS Rock Mechanics Symposium*, Toronto.
- [4] Zhu, W. and C. Tang., 2006. Numerical simulation of Brazilian disk rock failure under static and dynamic loading. *International Journal of Rock Mechanics and Mining Sciences*, Vol.43(2): 236-252.
- [5] Munjiza, A., 2004. *The Combined Finite-Discrete Element Method*, Wiley Online Library.
- [6] Liu, H., Y. Kang, and P. Lin, 2013. Hybrid finite-discrete element modelling of geomaterials fracture and fragment muck-piling. *International Journal of Geotechnical Engineering*, Vol. 9(2), 115-131.
- [7] Liu, H., S. Kou, P.-A. Lindqvist, and C., 2004. Tang, Numerical studies on the failure process and associated microseismicity in rock under triaxial compression. *Tectonophysics*, Vol.384(1): 149-174.
- [8] Liu, H., 2010. A numerical model for failure and collapse analysis of geostructures. *Australian Geomechanics*, Vol. 45(3): 11-19.
- [9] Xiang, J., A. Munjiza, and J.P. Latham., 2009. Finite strain, finite rotation quadratic tetrahedral element for the combined finite–discrete element method. *International journal for numerical methods in engineering*, Vol. 79(8): 946-978.
- [10] An, H., et al., 2017. Hybrid finite-discrete element modelling of dynamic fracture and resultant fragment casting and muck-piling by rock blast. *Computers and Geotechnics*, 81:322-345.
- [11] Akazawa, T., 1943. New test method for evaluating internal stress due to compression of concrete (the splitting tension test)(part 1). *J Jpn Soc Civ Eng*, Vol.29: 777-787.
- [12] Carneiro, F., 1943. A new method to determine the tensile strength of concrete. in *Proceedings of the 5th meeting of the Brazilian Association for Technical Rules*, 3d. Section.
- [13] Zhao, X., R. Fowell, J.-C. Roegiers, and C. Xu., 1994. Rock fracture-toughness determination by the Brazilian test, by H. Guo, NI Aziz, LC Schmidt. *Engineering geology*, Vol.38(1): 181-184.
- [14] Andreev, G., A review of the Brazilian test for rock tensile strength determination. Part I: calculation formula. *Mining Science and Technology*, 1991. 13(3): p. 445-456.
- [15] Andreev, G., A review of the Brazilian test for rock tensile strength determination., 1991. Part II: contact conditions. *Mining Science and Technology*, Vol. 13(3): 457-465.
- [16] Hondros, G., 1959. The evaluation of Poisson's ratio and the modulus of materials of a low tensile resistance by the Brazilian (indirect tensile) test with particular reference to concrete. *Australian Journal of Applied Science*, Vol.10(3): 243-268.
- [17] Fairhurst, C., 1964. On the validity of the 'Brazilian' test for brittle materials. in *International Journal of Rock Mechanics and Mining Sciences & Geomechanics Abstracts*. Elsevier.
- [18] Colback, P., 1966. An analysis of brittle fracture initiation and propagation in the Brazilian test. in *1st ISRM Congress*. International Society for Rock Mechanics.
- [19] Zhang, Z., 2001. Laboratory studies of dynamic rock fracture and in-situ measurements of cutter forces for a boring machine, Doctoral Thesis, Lulea university of technology, Lulea, Sweden
- [20] Malan, D., J. Napier, and B. Watson., 1994. Propagation of fractures from an interface in a Brazilian test specimen. *International Journal of Rock Mechanics and Mining Sciences & Geomechanics Abstracts*. Elsevier.

DEVELOPMENT AND PROSPECT OF ROOT PILES IN TUNNEL FOUNDATION REINFORCEMENT

Hao Ding, Linjian Su, Jinxing Lai, Yuanhang Zhang*

School of Highway, Chang'an University, Xi'an 710064, China, laijinxing@chd.edu.cn

ABSTRACT

Over the past couple of decades, root piles as the new tool for addressing a number of tough problems have been gaining a continually increasing interest in tunnel, especially for complex geological conditions. Therefore, in order to promote the development and application of root piles in tunnel engineering, this paper systematically sorts out the research status and development prospect of root piles from the application in foundation underpinning to reinforcement of tunnel foundation. Firstly, the type and development process of root piles are discussed. Secondly, the reinforcement mechanism of the root piles in the tunnel base is refined and combed: the reinforcement mechanism analysis focuses on frictional resistance of soil around pile, soil among piles, and piles. Thirdly, the calculation method of reinforced tunnel foundation is studied from the bearing of vertical load, horizontal load and pile reinforcement design. And through the engineering case, the paper illustrates the reinforcement effect of the root pile in ensuring the stability of the tunnel and the concrete process of the root piles in the tunnel construction. Finally, the problem and development prospect of root piles are discussed, so as to provide new perspectives and fundamental data for the research on tunnel engineering.

KEYWORDS

Tunnel engineering, Root piles, Foundation bottom consolidation, Construction

INTRODUCTION

Owing to socio-economic development and increasing demand in quality of life, the scale and quantity of transportation and engineering construction have exhibited a growing trend. Tunnels, which are underground constructions, provide incomparable advantages; as such, it has also shown a markedly increasing trend. In mountainous areas, tunnels can be used to address problems related to terrain or elevation, improve alignment, shorten mileage, save time, and reduce the destruction of vegetation. In urban areas, they can reduce the land on ground and actively take part in traffic dispersion; in rivers, straits, harbours, and other areas, tunnels exert no influence on waterway navigation, improve comfort, increase concealment, and are not affected by climate [1-2]. With the development of tunnel and subway shield engineering, the foundation treatment becomes an essential aspect of any project. Given the variation in geological conditions, complexity of the construction environment, and structure of stress characteristics, both economical and practical foundation treatment must be considered to effectively shorten the construction period, reduce costs, and increase project benefits [3-6]. Under complex geological conditions, adopting a traditional foundation treatment can lead to poor engineering performance. Thus, root piles are gradually applied to reinforce a tunnel foundation while being used for foundation underpinning of historical buildings. Root piles have become a significant and indispensable technology in underground engineering because they can ensure tunnel stability and

increase the bearing capacity of the tunnel foundation [7]. They are characterized by a small diameter, simple construction technology, light construction equipment, and flexible arrangement. Vertical root piles provide vertical resistance, whereas slanted root piles provide lateral resistance. They can be used flexibly, and with a small investment, that can play a greater role [8]. By sorting out information, the types of root piles reinforcement are shown in Figures 1 and 2.

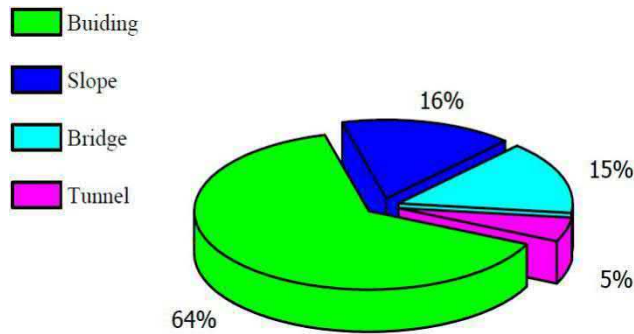


Fig.1 - Reinforcement type of root piles before 2000

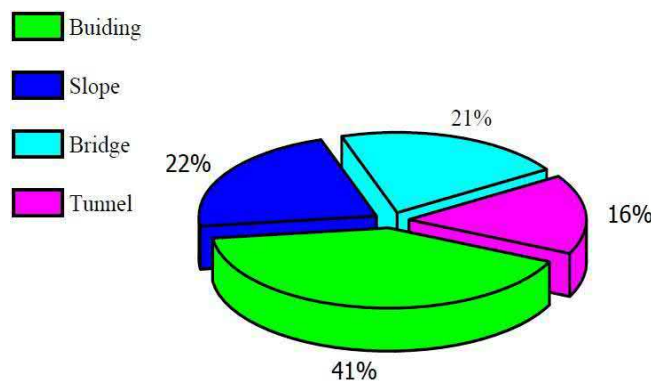


Fig.2 - Reinforcement type of root piles after 2000

Root piles reinforcement has gradually been applied in tunnel engineering and has obtained desirable engineering results [9-10]. When the tunnel foundation is reinforced by root piles, the settlement of the foundation is efficiently reduced, the bearing capacity is improved, and the normal and safe operation of the tunnel is ensured. In addition, the construction of root piles does not require a large site and is applicable in small tunnels. This research systematically elaborates on the development of root piles. Root piles are expounded from the perspectives of reinforcement mechanism, calculation method, tunnel construction, and so on presenting a summary, and discussing the development directions of root piles in the future.

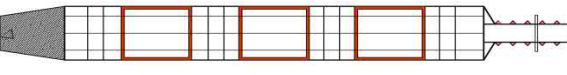
DEVELOPMENT OF ROOT PILES

Category of root piles

Root piles, also known as micropiles, are bored piles with diameters typically ranging from 70 mm to 300 mm and a slenderness ratio of over 30, achieved by drilling, strong reinforcement, and pressure grouting [11–12]. Considered as a new reinforcement structure, its design is inspired by trees in a mountain ridge or jungle [13]. Root piles have different categories in various places. The small diameter of root piles provides more reinforcement, and its construction is similar to that of

the anchor; it is also referred to as a large anchor rod in engineering. Steel bars, steel pipes, or steel-reinforced materials can be added according to the force needed [14–16]. Table 1 presents the classification and types of root piles. Pressure grouting in root pile construction efficiently ensures the close integration of grout and foundation soil [17–18]. Meanwhile, pressure cement grouting can also be extended in the soil around root piles, thereby improving the bearing capacity of a single pile and enhancing the mechanical property of the soil around the pile. After hardening and moulding, grout can bear tensile stress (pressure) [19–21].

Tab. 1 - The classification and types of root piles

The type of root piles	Characteristic	Picture
Pressed of root piles	A press-in sleeve is used, a reinforcement material is placed in the casing, and then a grout is formed to form a pile	
Suspension root piles	The whole length of high-pressure jet grouting to form a spiral-sprayed column reinforcement, interpolating suspended root pile	
End-bearing root piles	The bearing capacity of single pile is much higher than that of other types of root piles	

Development of root piles

Root piles were first developed by Fondedile, and their application was initially restricted by construction technology. They often have a diameter of 100 mm and a bearing capacity of 400 kN and used to be applied as foundation reinforcement of ancient buildings and underpinning engineering [22]. The first engineering case is the reinforcement of a school building in Naples; the root pile adopted was 13 m long and 100 mm wide, made by drilling and grouting. Grouting is made of coarse sand, cement, and water. From Italy, root pile reinforcement subsequently spread to Europe, America, and Japan. Its role is not limited to rehabilitation; it has gradually expanded to subway engineering and rock slope stability reinforcement. In 1993, France cooperated with the Federal Highway Administration (FHWA) to examine root piles. The results indicated that root piles exhibit potential and superior development prospect in addressing difficult problems related to foundation and slope stability. Several related organizations were formed to conduct studies and compile technical specifications and manuals. FHWA compiled a guide for the design and construction of root piles. After the Hyogoken–Nanbu earthquake in 1995, root piles technology was introduced to Japan with the support of International Workshop on Micropiles; subsequently, Japanese Association of High Capacity Micropiles was established for the research and development of root piles. *Design Manual for Root Piles with High Bearing Capacity for Seismic Reinforcement of Existing Pile Foundation* was compiled in 2002.

Since then, root piles have been widely used for underpinning, adding a building layer, loading of factory building foundation and equipment foundation, remediation of dilapidated buildings, tunnel crossing, and foundation pit excavation, among others. With the improvement of root pile technology, the scope of application has extended to tunnel engineering, particularly loess tunnel. For instance, root piles have been adopted for the foundation reinforcement of The Luotuochang Tunnel in the section of the eolian sand stratum because of the desirable reinforcement effects of root piles and the construction quality of engineering ensured by the technique.

REINFORCEMENT MECHANISMS FOR TUNNEL

A hole is created in the foundation by using several techniques. The reinforcement cage and grouting pipe, as required by the design, are inserted into the hole. After the hole is cleaned, stones or fine stone silicon of certain specifications are placed into the hole, and the water in the hole is replaced by cement grout to form pressure grouting (this process is not suitable for putting fine stone silicon), thereby forming a grouting pile with diameters of similar or varying sizes. Owing to the permeation of grout, soil among the piles will be improved in root pile reinforcement; the foundation is referred to as the “composite foundation” of improved soil and root piles [23–24].

Improvement of frictional resistance and tip resistance for soil around piles

According to the construction technology for grouting and pile foundation, static pressure grouting needs to be conducted before the pile is formed, with pressure ranging from 0.3 Mpa to 0.8 Mpa. To permeate the soil around the pile and at the bottom of the pile, construction activities are conducted, such as surface layer sealing, node length control, time control, secondary grouting, and pressure stabilization. The physicochemical properties of soil are improved by compaction, filling, consolidation, replacement, and so on; thus, the space between the pile lining and the surrounding soil is filled with press-in cement grout, and the soil around the piles is in close contact, thereby increasing the contact area for the pile and soil [25–26]. Meanwhile, with hydrolysis and hydration of cement grout, as well as hydration and carbonization of clay particles and cement, the cementation between the root piles and the surrounding soil is enhanced. The frictional resistance between the root piles and the surrounding soil around is considerably improved, and the tip resistance is increased because the soil at the bottom of the pile is improved. The sketch map for grouting is shown in Figure 3.

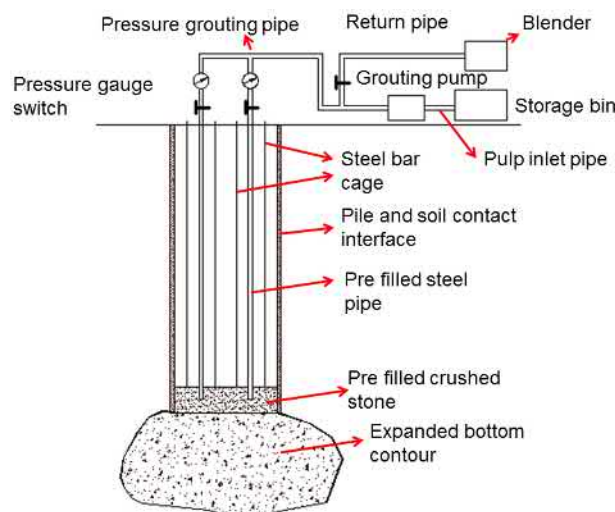
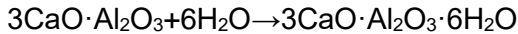


Fig.3 - The sketch map for grouting

(1) *Hydrolysis and hydration of cement grout*

Ordinary Portland cement is composed of CaO, SiO₂, and Al₂O₃; thus, the combination of cement minerals are identified as Ca₃SiO₃, Ca₂SiO₃, Ca₃AlO₃, 4CaO·Al₂O₃·Fe₂O₃, and CaSO₄. A chemical reaction occurs when cement is mixed in water. When the cement mortar is forcibly pressed into the soil, Ca(OH)₂, CaO·SiO₂·H₂O, and CaO·Al₂O₃·H₂O are quickly produced. Over time, cement becomes solid stone, with its strength increased after setting and hardening [27].



Owing to the coagulability of cement, Ca(OH)₂ is separated from a saturated solution of Ca(OH)₂ as an amorphous body and becomes viscid, containing cement particles. The binding force of particles is enhanced; thus, Ca(OH)₂ becomes acicular crystals, penetrates the amorphous bodies of CaSiO₃, and integrates with them, thereby increasing the mechanical strength of cement [28–29].

(2) *Function of clay particles and cement hydrates*

After formation, some cement hydrates continue to harden, resulting in a cement skeleton; some react with surrounding active particles.

① *Function of ion exchange and granulation*

SiO₂ (free) abundant in soil becomes silicate colloidal particles in water. Its chemical equation is written as follows:



The Na⁺ or K⁺ on the surface of silicate colloidal particles can exchange with Ca⁺ in cement hydrate for the small soil particles to grow. In addition, cement combines with the soil mass and becomes cemented soil, sealing the space between soil masses, thus maintaining a satisfactory bearing capacity for an extended time. The specific surface area of colloidal particles generated from cement hydrate is 1,000 times that of original cement particles, thus generating great surface energy. Grouting is used not only to seal the voids in the soil mass but to close weathered cracks as well, improving the strength of cement soil at the macro level [30–32].

② *Hard condensation reaction*

With the continuous development of cement hydration, a large quantity of Ca⁺ is separated from the solution. When the quantity of Ca⁺ exceeds the quantity for ion exchange, some or most of the SiO₂ and Al₂O₃ of clay minerals react with Ca⁺ and gradually generate stable crystal compounds insoluble in water, considerably enhancing the strength of cemented soil.

(3) *Function of carbonation*

The free Ca(OH)₂ in cement hydrate can absorb CO₂ in water and air; carbonization then occurs, generating CaCO₃ insoluble in water. This reaction can increase the strength of cemented soil; however, the process occurs slowly, and the strength increases only slightly. As static pressure grouting is adopted, grout can only be pressed into the void in the soil around the pile. Soil mass covered by cement grout occurs frequently, and particles in soil mass can gradually change its performance caused by the permeation of cement hydrolysate [33–34].

Improvement of soil among the pile

After static grouting, most of the slurry will be squeezed into the holes and seams in the soil among the pile. Under specific pressure, the slurry permeates into the surrounding soil layer in the direction of least resistance, turning the pile body and the surrounding soil layer into an irregular round mixing layer wrapped in cement paste under high pressure, greatly increasing the frictional resistance and horizontal loading competence of piles. Meanwhile, the structure of the adjacent soil is improved, and the density and bearing capacity of the foundation soil are increased. This effect is particularly evident for sand and artificial filled soil. Analysis of the existing practical materials for the project indicates that the strength of the foundation soil among the pile may increase by 10% to 30% after the tree-root pile treatment [35]. After grouting, a slurry diffusing zone, which has undergone variations in materials and physical mechanical properties at the pile-soil interface, can form. The slurry diffusing zone then exhibits an annular distribution around the pile body, as shown in Figures 4 and 5.

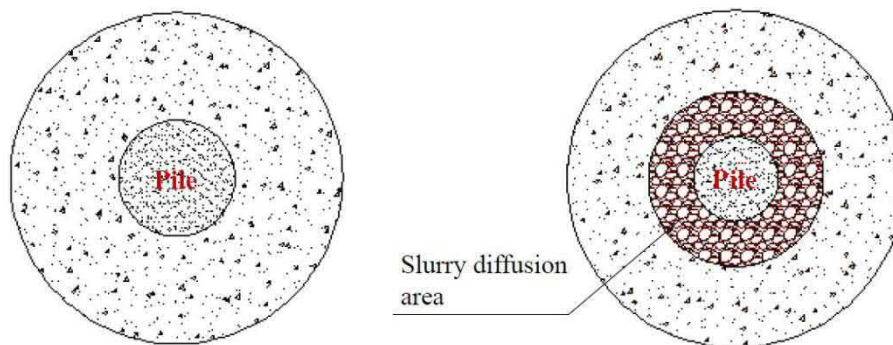


Fig.4 - General rigid pile of composite foundation Fig.5 - Root pile of composite foundation

As illustrated, the generally rigid pile of composite foundation consists of pile and natural soil, which combine and carry the load. The grouting pile composite foundation consists of 3 components: pile, grout diffusion area, and natural soil. These components act together to provide the bearing capacity of the composite foundation. After the cementation of grout at the interface between the pile and the soil, the grouting pile can exert friction on the pile side in full length; the load is transferred to a deeper soil layer, and the load between the piles is reduced accordingly. Meanwhile, the properties of the natural soil within a certain range of the pile are enhanced, and the average modulus of the soil between the piles is increased, thereby improving the composite modulus and reducing the settlement of the composite foundation.

Role of piles in tunnels

As grouting root piles are semi-rigid or rigid, the deformation moduli of the piles are far greater than that of the soil among the piles. When the upper load is carried by the grouting root pile and the surrounding soil, the load of the basement concentrates on the root pile. Static load testing shows that the root piles (occupying about 10% of bearing plate) bear 50% to 60% of total loading, whereas the soil among the piles (occupying about 90% of the bearing plate) only carry 40% to 50 % of the total loading. Therefore, the root piles reduce the stress in the soil layer within a certain depth of the tunnel basement, and decrease the large compression deformation in the bearing layer. After piling, the root piles exert a lateral restraining effect on the soil between piles [36–37], and lateral displacement of the soil between piles is limited. Given the surrounding constraints, the deformation of the soil between the piles is limited, and the settlement of the soil is reduced under the same loading [38–41]. As shown in Figure 6, the tunnel foundation is reinforced by root piles.

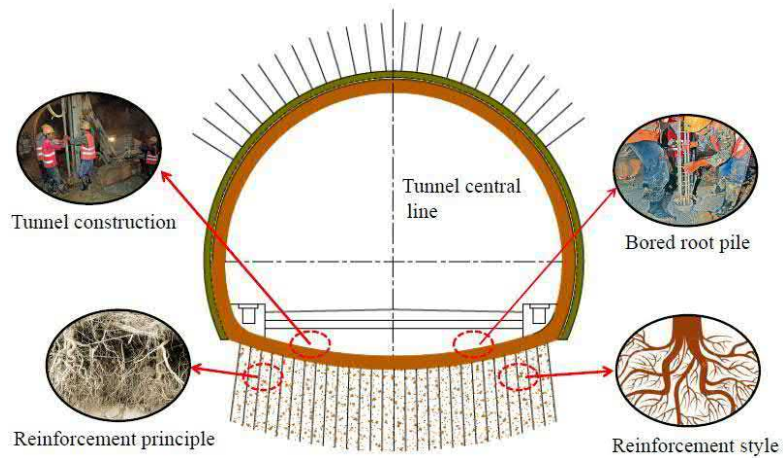


Fig.6 - The tunnel foundation is reinforced by root piles

CALCULATION METHOD STUDY

Vertical load bearing

The tip resistance of the root pile is generally ignored, whereas the frictional resistance is considered in calculating the vertical bearing capacity of a single root pile because of its small diameter. However, when the pile tip is supported on the rock, the pile tip resistance should be considered, and the bearing capacity of the pile is mainly controlled by the material strength of the pile mass [42–46]. Australian engineers have proposed a semi-empirical and semi-theoretical root pile design theory. The vertical bearing capacity of a single pile is mainly provided by friction resistance, without considering the pile tip resistance. Vertical compression of root piles was proposed by Bruce [22] as follows (1): mined by load testing and ultimate bearing

$$P_{C-allow} = \left[\frac{f'_{c-grout}}{FS_{grout}} A_{grout} + \frac{F_{y-steel}}{FS_{y-steel}} (A_{bar} + A_{casing}) \right] \frac{F_a}{FS_{y-steel}} \quad (1)$$

where $f'_{c-grout}$ is the uniaxial tensile strength of grouting (MPa); FS_{grout} is the grouting strength safety factor; A_{grout} is the net area of the grouting section (m^2); $F_{y-steel}$ is the minimum yield stress of the reinforced steel (MPa); $FS_{y-steel}$ is the safety factor of the reinforced steel; A_{bar} is the section area of the reinforced steel (m^2); A_{casing} is the casing section area (m^2); and F_a is the allowed axial stress (MPa) [47–53].

When the bearing capacity of a single pile is determined by the soil, the pile load is transferred to the soil through lateral resistance. The resistance of root piles is mainly determined by the grouting–soil interface. As shown in (2):

$$Q_{su} = \sum_{i=1}^n u_i q_{sui} \quad (2)$$

where u_i is the thickness of the i^{th} layer of the soil around the pile (m); q_{sui} is the ultimate lateral friction of the i^{th} layer of the soil around the pile.

The pile group effect should be considered when calculating the load-bearing capacity of the root pile group. The pile group effect is influenced by the following factors: ratio of the central

distance between two adjacent piles and pile diameter; embedded depth of the pile; connection between the pile tip and the hat beam; pile-group size, and soil properties. The two hypotheses below can be used to confirm the allowable load for the pile–soil complex of which the root pile bears a considerable concentrated loading:

- (1) The stability of a single pile should be considered after the pile group effect.
- (2) The safety of the whole pile cylinder should be considered.

Horizontal load bearing

To calculate the horizontal load-bearing capacity of a single root pile [54–56], if the reinforcement ratio is less than 0.65%, the horizontal load-bearing capacity eigenvalue of a single root pile can be calculated according to the following formula (3):

$$R_{ha} = \left(\frac{0.75\alpha\gamma_m f_t W_o}{\gamma_M} \right) \times (1.25 + 22\rho_g) \quad (3)$$

where α is the horizontal deformation coefficient; γ_m is the plasticity coefficient of the pile section modulus; f_t is the designed tensile strength value of the pile concrete; γ_M is the maximum of the bending moment coefficient; ρ_g is the reinforcement ratio of the pile; W_o is the section modulus of the tension edge of pile conversion sections [57–62].

Pile reinforcement design

(1) The horizontal force of the top of the pile should meet the requirements of the following formula (4), configured with the pile connected to the top of the structural bar; the depth of the pile into the pile diameter is 3 to 5 times.

$$F_1 \leq U d^2 \sqrt[5]{1.5d^2 + 0.5d} \left(1 + \frac{0.9N_1}{rR_1 A} \right) \quad (4)$$

where F_1 is the horizontal force of the single pile top; U is the comprehensive coefficient; d is the diameter of the pile; N_1 is the axial pressure of the pile top; R_1 is the designed strength of the pile; r is the plasticity coefficient of the pile section of the modulus; and A is the pile section area.

(2) For the pile with small horizontal force, the reinforcement ratio can be adjusted from 0.40% to 0.65%.

APPLICATION AND CONSTRUCTION IN TUNNELS

Application in tunnel construction

The Application and Construction are shown in Table 2.

Table 2 - Engineering Example of Reinforcing Tunnel by Tree Root Piles

Number	Name	Reasons of usage	Reinforcement effect
1	Lan Yu railway tunnel [39]	Basement cracking, damage, subsidence, squeezing to both sides and the mud pumping phenomenon is more serious	Monitoring data show that all aspects of the indicators have reached the design and specification requirements
2	Luo Tuochang Tunnel [63]	The geologic condition is very poor, and the aeolian sand has poor self-stability ability	The bearing capacity of composite foundation reaches the design requirements
3	Fan Jingshang Tunnel [64]	The vaults have irregular subsidence and peripheral convergence	The bearing capacity of the root pile fully reaches the design requirements
4	Chang Liangshang Tunnel [65]	Poor condition of the surrounding rock, erosion of groundwater, and defects at the bottom of the tunnel	Invert function is restored, the whole structure stress of the tunnel and the surrounding rock condition is improved
5	Nan Jing Tunnel [66]	Engineering geological and hydrogeological conditions are poor, construction is difficult	The surface settlement is small and the root pile tip displacement is small
6	Liu Yong tunnel [67]	The opencut tunnel is serious settlement, cracking, instability	The settlement, instability and cracking of opencut tunnel have been obviously controlled

Application in soil with a loose structure and high water content

Lanyu Railway is a single-hole double-track tunnel with a total length of 715 m for the Lanyu Railway crossing the debris flow area. The total length of the tunnel is 263 m, and the shallowest depth is only 14 m. The debris flow deposits are composed of round gravel, breccia, and phyllite with different diameters and partially saturated sandy loess. The structure is loose, highly porous, water-saturated, and fluid.

The results indicate that the maximum compressive stress of the support is decreased after root piles are used to reinforce the bottom of the tunnel. The maximum settlement is 4.52 mm, and the maximum vibration velocity of the filling surface of the inverted arch is 62.9 mm/s without using root piles as reinforcement. With root piles, the maximum settlement is 3.16 mm, and the maximum vibration velocity is 24.8 mm/s; without root piles, the maximum settlement is reduced by 30.1%,

and the maximum vibration velocity is reduced by 60.6%. The settlement of the filling arch was controlled by the root piles reinforcement; thus, the vibration velocity is markedly reduced and the stability of the tunnel is improved [39].

Application in eolian sand

Luotuochang Tunnel is located in the contact area between the Liangmao area of Loess Plateau in Northern Shaanxi and the Mu Us Desert. Quaternary loess and the sand cover layer are thinner, and the sand is semi-fixed. Eolian sand is formed by blowing, moving, and accumulating under wind action in the arid area, characterized by loose sand, layered distribution, and poor stability. The tunnel crossing the eolian sand stratum belongs to grade-VI rock. The eolian sand surface at the exit of the tunnel is shown in Figures 7.



Fig.7 - Surface sandy land in tunnel exit section

According to load testing mentioned in Reference [35], the impacts of a single root pile on the reinforcement of a tunnel settlement can be obtained by varying the aggregates, lengths, and diameters of the pile, as shown in Figures. 8, 9, and 10. The effects of the root pile group on tunnel settlement are shown in Figures 11.

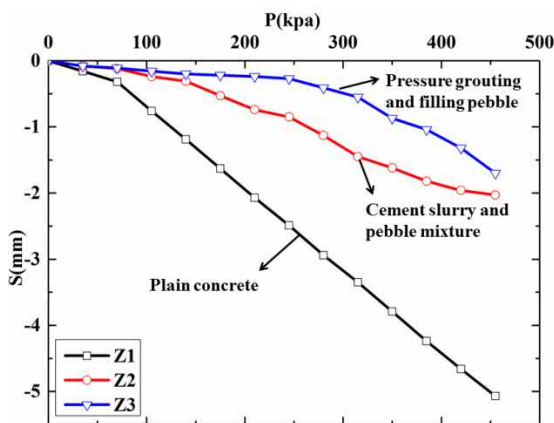


Fig.8 - Different pile aggregates[30]

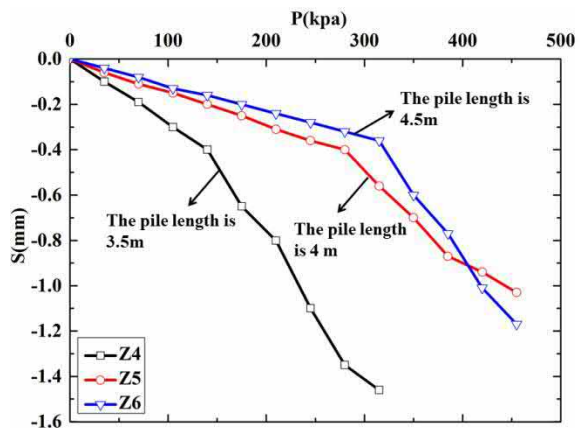


Fig.9 - Different pile lengths[30]

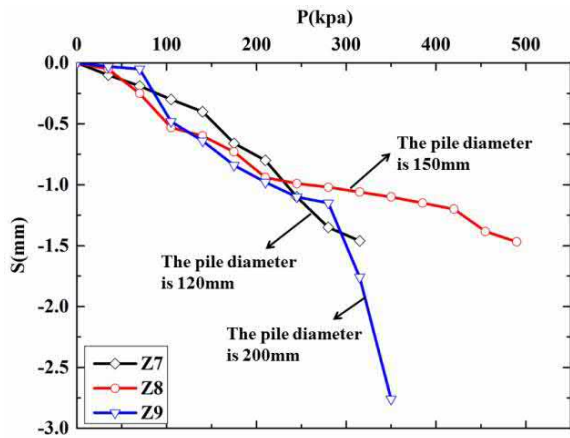


Fig.10 - Different pile diameters[30]

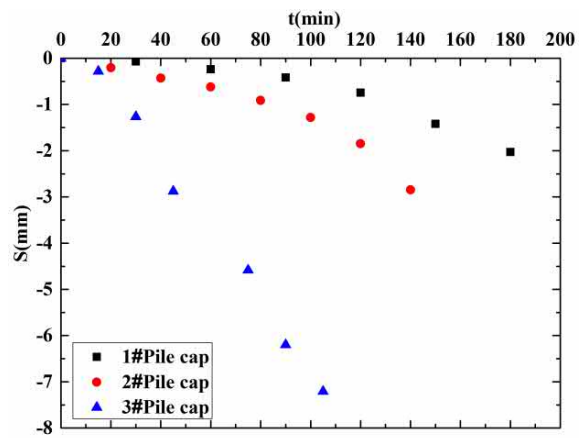


Fig.11 - Tunnel subsidence [30]

- (1) Compared with the Z1 pile, the Z2/Z3 bearing capacities were improved by 86.7% and 226.7%, respectively. Among the 3 pile aggregates, the pile formation process, which first fills the pebble, followed by pressure grouting, can obtain the maximum single pile bearing capacity. In addition, the reinforcement of the tunnel bottom is remarkable.
- (2) The bearing capacity of a single pile markedly increases with an increase in pile length; beyond a certain extent, the single pile bearing capacity increases slowly.
- (3) In the case of a pile forming material, an increase in pile diameter leads to an increase in the bearing capacity of a single pile. If the pile diameter is increased by 25% from 120 mm to 150 mm, the single pile bearing capacity is increased by 67% from 70 kPa to 105 kPa. If the pile diameter increases by 66.7%, the single pile bearing capacity is increased to 135 kPa, reflecting a 92.8% increase. This result indicates a significant improvement for the single pile, and it enhances the stability of the tunnel [30].
- (4) The bearing capacity of the composite foundation of the pile group is markedly improved compared with that of the single pile. For the composite foundation with 3 piles, the bearing capacity of the composite foundation is 3 times higher than that of the single root pile. However, composite foundation formed using 8 piles has a bearing capacity lower than that of a single pile [35].

Constructing root piles in the tunnel

The construction flow chart for root piles is shown in Figure 12.

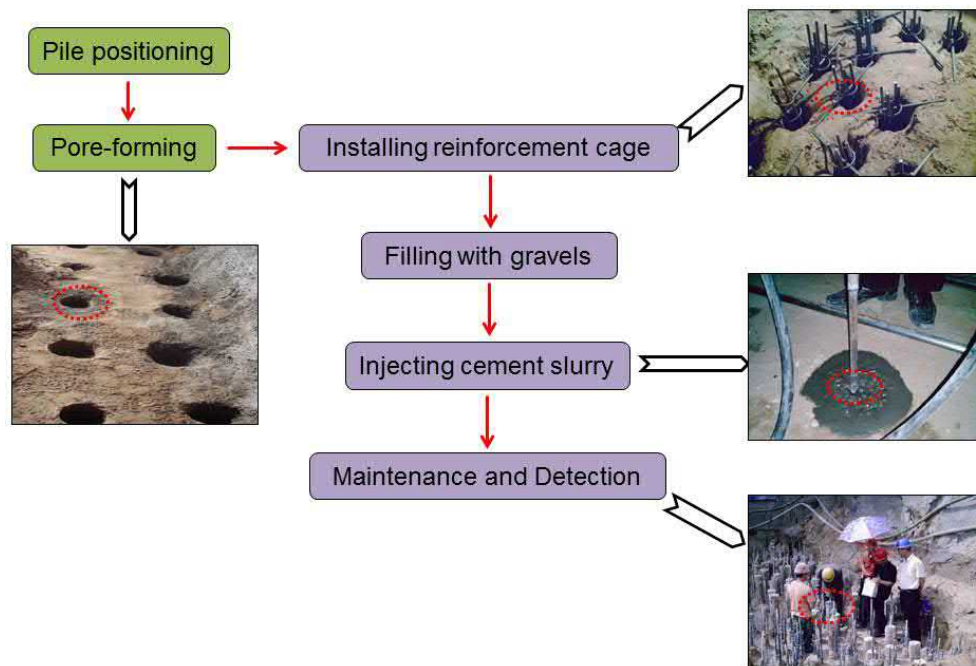


Fig. 12 - Layout chart

- (1) Pile positioning: Pile deviation should be controlled within 20 mm, the vertical deviation of a straight pile should not exceed 1%, and the inclination of the inclined pile should be adjusted according to the design requirements [68–71].
- (2) Pore-forming: An engineering geological drilling machine or the Luoyang shovel can be used to make holes. The Luoyang shovel as the archaeological tool is widely used in Chinese geotechnical engineering, as shown in Figure 13. Water or natural cement slurry are used in drilling, and generally, the casing is not used. A one-section casing is placed near the hole; after the designed elevation is reached, the hole is cleaned until water purification occurs.
- (3) Installing reinforcement cage: When the reinforcement cage is placed, it cannot be forced down under the pressure; thus, it should be placed at the same time to ensure the stability of the hole wall. Two reinforcement cages must be vertical, and the elevation must meet the design requirements.
- (4) Filling with gravel: The gravel should be rinsed with water, and the filled volume shall be controlled 1.15 times as much as the calculated volume. To ensure a uniform backfill of gravel, about 0.2 m² pebble is filled. The shaking reinforcement cage and grouting pipe are shaken for gravel to reach the bottom of the hole [72–74].
- (5) Injecting cement slurry: Grouting pump is used for both cement mortar and mortar. In grouting, the grouting pressure has to be controlled so that slurry can emerge evenly until the holes overflow. Grouting should be continuous; if interrupted, it should be disposed immediately.



Fig.13 - Luoyang shovel

SUMMARY AND PERSPECTIVES

New technologies and methods have been identified since the application of root piles in engineering, and these techniques can be investigated further and used continuously. In addition, the application of root piles in tunnel construction is becoming increasingly prominent, providing reliable measures for the stability of the tunnel foundation. Although root piles have only been recently used in tunnels, such application has developed rapidly. Root piles have their own distinct advantages. In some specific cases, root piles are likely to be the only effective solution; however, some problems still need to be discussed related to their research and application, as follows:

- (1) Root piles generally use filling pile calculation methods; however, the principal method of bearing the root pile is by the lateral friction of pile, and the designed calculation method remains defective. More calculation methods exist for root piles; however, the geological conditions under different methods and the determination of suitable design techniques for specific conditions need further investigation.
- (2) Given that root piles exhibit distinct characteristics, under different combinations, the working performance, load transfer, and failure modes of root pile groups obviously vary from other types of piles. Thus, the failure modes of root piles need to be examined further to improve the pile bearing capacity and ensure the stability of the tunnel bottom.
- (3) Under the influence of an earthquake or a mechanical vibration, root piles have to bear horizontal dynamic loading. Research on the lateral cyclic loading of root piles is currently inadequate, and the design theory remains imperfect. Therefore, China (an earthquake-prone country) should fully evaluate root piles working mechanisms under dynamic loading.

COMPETING INTERESTS

The authors declare that there is no conflict of interests regarding the publication of this paper.

ACKNOWLEDGEMENTS

This work is financially supported by the Special Fund for Basic Scientific Research of Central Colleges of Chang'an University (Grant no. 310821172004, no. 310821153312, no. 31082116011), the Key Industrial Research Project of Shaanxi Provincial Science and Technology Department (Grant no. 2016SF-412), and the Western Traffic Science and Technology Project (Grant No. 2014 318 J27 210).

REFERENCES

- [1] J. X. Lai, K. Y. Wang, J. L. Qiu et al., "Vibration response characteristics of the cross tunnel structure," *Shock & Vibration*, vol. 2016, Article ID 9524206, 2016. doi: 10.1155/2016/9524206.
- [2] M.N. Vu, W. Broere, and J. Bosch, "The impact of shallow cover on stability when tunnelling in soft soils," *Tunnelling & Underground Space Technology*, vol.50, pp. 507-515,2015
- [3] H. Xing, F. Xiong, and J. Wu, "Effects of Pit Excavation on an Existing Subway Station and Preventive Measures," *Journal of Performance of Constructed Facilities*, vol. 30, no.6, pp. 2016 ;
- [4] A. Chepurnova, "Assessing the influence of jet-grouting underpinning on the nearby buildings," *Journal of Rock Mechanics and Geotechnical Engineering*, vol.6, no.2, pp.105-112,2014
- [5] M. Cardu, and J. Seccatore, "Quantifying the difficulty of tunnelling by drilling and blasting," *Tunnelling & Underground Space Technology*, vol.60, pp.178-182,2016
- [6] D. Wang, and W. Sui, "Grout diffusion characteristics during chemical grouting in a deep water-bearing sand layer," *International Journal of Mining Science and Technology*, vol.22, no.4, pp.573-577, 2012
- [7] G. Meschke, J. Ninic. J. Stascheit, and A. Alsahly, "Parallelized computational modeling of pile-soil interactions in mechanized tunneling," *Engineering Structures*, vol.47, no.1, pp.35-44,2013.
- [8] Jiang Qingwei .Research on Stability at high digging root pile slope protection[D]. Xi'an: Chang'an University, 2014.(in chinese)
- [9] S. Seki, S. Kaise, Y. Morisaki et al., "Model experiments for examining heaving phenomenon in tunnels," *Tunnelling & Underground Space Technology Incorporating Trenchless Technology Research*, vol.23, no.2, pp.128-138,2008.
- [10] C.J. Lee, B.R. Wu, H.T. Chen, and K.H. Chiang, "Tunnel stability and arching effects during tunneling in soft clayey soil," *Tunnelling & Underground Space Technology*, vol.21, no. 2, pp. 119-132,2006.
- [11] Li Zhan, Teng Yanjing Li Qingrui et al. Micro-pile techniques for improvement project of existing buildings[J]. China Civil Engineering Journal, 2015(S2):197-201.(in chinese).
- [12] WANG Hui, CHENG jianping, QUE jinsheng. Research on design and application of root piles to Strengthening foundations[J]. Rock and Soil Mechanics,2006(s2):1290-1294.(in chinese)
- [13] S.W. Sun, B.Z. Z hu, and J.C. Wang, "Design method for stabilization of earth slopes with micropiles," *Soils & Foundations*, vol.53, no.4, pp.487-497,2013.
- [14] A.E. Elsaied, "Performance of footing with single side micro-piles adjacent to slopes," *AEJ - Alexandria Engineering Journal*, vol.54, no.4, pp. 903-910,2014.
- [15] C. Zanuy, P.D.L. Luenta, and M. Pinilla, "Bending strength of threaded connections for micropiles," *Journal of Constructional Steel Research*, vol.78, pp.68-78,2012.
- [16] R. Vlentino, E. Romeo, and A. Misra, "Mechanical Aspects of Micropiles Made of Reinforced Polyurethane Resins." *Geotechnical and Geological Engineering*, vol.31, no.2, pp.463-478,2013.
- [17] B. Nikbakhtan, and M.Osanloo, "Effect of grout pressure and grout flow on soil physical and mechanical properties in jet grouting operations." *International Journal of Rock Mechanics & Mining Sciences*, vol.46, no.3, pp.498-505, 2009.
- [18] V. Fattahpour, W.C. Sze, and B.A. Baudet, "Laboratory investigation of shaft grouting." *Geotechnical Engineering*, vol.168, no. 1, pp. 65-74,2015.
- [19] K. Zyka, and A. Mohajerani, "Composite piles: A review." *Construction & Building Materials*, vol.107, pp.394-410,2016.
- [20] J.H. Deng, J.Q. Wu, W.B. Li, and D.H. Jiang, "Application of Composite Foundation in Reinforcement Treatment for a Highway Existing Culvert." *Geotechnical Investigation & Surveying*, vol.250-253, no. 3, pp.1686-1690,2008.
- [21] J. Veludo, D. Dias-Da-Costa, E.N.B.S. Julio, and P.L. Pinto, "Bond strength of textured micropiles grouted to concrete footings." *Engineering Structures*, vol.35, no.1, pp.288-295,2012.

- [22] D.A. Bruce, A.F. Dimillio, and I. Juran, "Introduction to Micropiles: An International Perspective." *Foundation Upgrading and Repair for Infrastructure Improvement* ASCE, vol.33, pp.2081-2088,2014.
- [23] S. Thiyyakkandi, M. Mcvay, and P. Lai, "Experimental Group Behavior of Grouted Deep Foundations." *Geotechnical Testing Journal*, vol.37, no. 3, 2014.
- [24] J.M. Ortega, A. Albaladejo, J.L. Pastor, I. Sanchez, and M.A. Climent, "Influence of using slag cement on the microstructure and durability related properties of cement grouts for micropiles." *Construction & Building Materials*, vol. 38, no. 1, pp. 84-93,2013.
- [25] Q.Q. Zhang, Z.M. Zhang, and S.C. Li. "Investigation into Skin Friction of Bored Pile Including Influence of Soil Strength at Pile Base." *Marine Georesources & Geotechnology*, vol.31, no. 1, pp.1-16,2013.
- [26] B. Nikbakhtan, K. Ahangari, and N.Rahmani, "Estimation of jet grouting parameters in Shahriar dam,Iran." *International Journal of Mining Science and Technology*, vol. 20, no. 3, pp. 472-477,2010.
- [27] U.S. Okyay, and D.Dias, "Use of lime and cement treated soils as pile supported load transfer platform." *Engineering Geology*, vol. 114, no. 1, pp.34-44,2010.
- [28] H. Xing, X. Yang, C. Xu, and G. Ye, "Strength characteristics and mechanisms of salt-rich soil-cement." *Engineering Geology*, vol. 103, no.1-2, pp. 33-38,2009.
- [29] A.V.D. Fonseca, "Voids/Cement ratio controlling tensile strength of cement treated soils." *Journal of Geotechnical & Geoenvironmental Engineering*, vol.137, no. 11, pp. 1126-1131,2011.
- [30] Pang liexin. Field test study about bearing capacity of single root pile in Loess Bedding[D].Southwest Jiaotong University, 2006(in chinese)
- [31] P.M. Gallagher, S. Spatari, and J. Cucura. "Hybrid life cycle assessment comparison of colloidal silica and cement grouted soil barrier remediation technologies." *Journal of Hazardous Materials*, vol.250-251, pp.421-430,2013.
- [32] J.L. Pastor, J.M. Ortega, M. Flor et al, "Microstructure and durability of fly ash cement grouts for micropiles." *Construction & Building*, vol. 117, pp. 47-57,2016.
- [33] Z. Zhang, and G. Xin,. "The Application Effect Analysis of Post grouting Under Bored Piles with Different Bearing Strata." *Journal of Building Structures*, vol.23, no. 6, pp. 85-89,2002.
- [34] M. Ashour, and H. Ardalan, "Analysis of pile stabilized slopes based on soil-pile interaction." *Computers & Geotechnics* , vol.39, no. 1,pp.85-97,2012.
- [35] Dou Shikang. Study on the Construction Technique of Luotuochang Tunnel in Aeolian Sand Formation[D]. Xi'an: Chang'an University, 2012.(in chinese)
- [36] T. Kasper, and G. Meschke, "On the influence of face pressure, grouting pressure and TBM design in soft ground tunnelling." *Tunnelling & Underground Space Technology*, vol.21, no. 2, pp.160-171,2006.
- [37] M.A. Soomro, Y. Hong, C.W.W.W Ng, H. Lu, S. Peng, "Load transfer mechanism in pile group due to single tunnel advancement in stiff clay." *Tunnelling & Underground Space Technology*, vol. 45, pp. 63-72,2015.
- [38] SUN Shao-rui, WU Ji-min, WEI Ji-hong et al. Stability analysis and evaluation of slope reinforced with root piles[J]. *Rock and Soil Mechanics*,2003,24(5):776-780.(in chinese)
- [39] ZHU Zheng-guo, ZHU Yong-quan, WU Guang-ming et al. Strengthening method and stability analysis for tunnel base in debris flow accumulation body[J]. *Chinese Journal of Geotechnical Engineering*, 2013(s2):617-621.(in chinese)
- [40] J.X. Lai, Z.H. Feng, J.L. Qiu et al, "In-situ test of grouting reinforcement for water-enriched sandy gravel ground in river floodplain", *Advances in Materials Science and Engineering*, vol. 2016, Article ID 2129659, 2016. doi: 10.1155/2016/2129659.
- [41] C. Liang, and M. Fall, "Mechanical and thermal properties of cemented tailings materials at early ages: Influence of initial temperature, curing stress and drainage conditions." *Construction & Building Materials*, vol.125, pp. 553-563,2016.
- [42] F.S. Tehrani, P. Nguyen, R.B.J. Brinkgreve, and A.F.V. Tol, "Comparison of Press-Replace Method and Material Point Method for analysis of jacked piles." *Computers & Geotechnics*, vol. 78, pp.38-53,2016.
- [43] K. Chatterjee, D. Choudhury, and H.G. Poulos, "Seismic analysis of laterally loaded pile under influence of vertical loading using finite element method." *Computers & Geotechnics*, vol. 67, pp. 172-186,2015.
- [44] F. Liang, Z. Song, W.D. Guo, "Group interaction on vertically loaded piles in saturated poroelastic soil." *Computers & Geotechnics*, vol. 56, no.1, pp. 1-10, 2014.
- [45] P.C. Jiang, L.H. Zou, and X. Wang, "Application of Root Pile to Reinforce High Embankment." *Applied Mechanics & Materials*, vol. 226-228,pp. 1269-1274, 2012.
- [46] O.L. Ghazzaly, S.T. Hwong, and M.W. O'Neil, "Approximate analysis of a pile under dynamic, lateral

- loading." *Computers & Structures*, vol. 6, no. 4-5, pp. 363-368,1976.
- [47] SUN Shu-wei, CHEN Chong DING Hui et al. Stability analysis of earth slopes reinforced with micropiles[J]. *Chinese Journal of Geotechnical Engineering*, 2014(12):2306-2314.(in chinese)
- [48] H. Lahuta, J. Aldorf, E. Hrubesova, H. Rubisarova, and A. Janicek, "Influence of Buckling at the Rod Micropiles." *Procedia Engineering*, vol. 142, pp. 327-332.,2016.
- [49] SU Yuan-yuan, ZHANG Zhan-min, LIU Xiao-li. Computation methods of anti-sliding micropiles: an overview[J]. *Chinese Journal of Geotechnical Engineering*, 2010(s1):223-228.(in chinese)
- [50] Zhou D, Wang H L, Sun H W. Micro-pile composite structure and its design theory[J]. *Yanshilixue Yu Gongcheng Xuebao/chinese Journal of Rock Mechanics & Engineering*, 2009, 28(7):1353-1362. (in chinese)
- [51] H.L. Kou, W. Guo, M.Y. Zhang, and Y.Q. Xu, "Axial resistance of long rock-socketed bored piles in stratified soils." *Ocean Engineering*, vol. 114, pp. 58-65,2016.
- [52] HE Jie-bing, HONG Bao-ning, QIU Guo-feng. Research on cushion action mechanism of CFG pile composite foundation for expressway[J]. *Rock and Soil Mechanics*, 2004, 25(10):1663-1666.(in chinese)
- [53] J.X. Lai, H.Q. Liu, J.L. Qiu et al, "Settlement Analysis of Saturated Tailings Dam Treated by CFG Pile Composite Foundation." *Advances in Materials Science & Engineering*, vol. 2016, no. 6, pp. 1-10,2016.
- [54] J. Ching, and H.D. Lin, "Calibrating Resistance Factors of Single Bored Piles Based on Incomplete Load Test Results." *Geofluida*, vol. 137, pp. 2013-2112,2010.
- [55] Y. Zhang, K.H. Andersen, and G. Tedesco, "Ultimate bearing capacity of laterally loaded piles in clay – Some practical considerations." *Marine Structures*, vol. 50, pp.260-275, 2016.
- [56] K. Paik, J. Lee, and D. Kim, "Calculation of the axial bearing capacity of tapered bored piles." *Geotechnical Engineering*, vol. 166, no. 5, pp. 502-514,2013.
- [57] CHEN Zheng, MEI Ling, MEI Guo-xiong, Numerical simulation of lateral bearing capacity of flexible micropile [J]. *Rock and Soil Mechanics*, 2011,32(7):2219-2224. (in chinese)
- [58] DU Yanqing, BAI Mingzhou, QIU Shumao, et al. Experimental study on lateral bearing capacity of concentrated micropiles [J]. *Chinese Journal of Rock Mechanics and Engineering*, 2015, 34(4):821-830.(in chinese)
- [59] H. Shi, M. Bai, C. Li, Y. Zhang, and G. Tian, "Correspondence Analysis of Soil around Micropile Composite Structures under Horizontal Load." *Mathematical Problems in Engineering*, vol. 2015, no. 8, pp.1-12,2015.
- [60] Gong Jian, Chen Renpeng, Chen Yunmin et al. PROTOTYPE TESTING STUDY ON MICROPILES UNDER LATERAL LOADING [J]. *Chinese Journal of Rock Mechanics and Engineering*,2004, 23(20):3541-3546. .(in chinese)
- [61] R.J. Gorasia, and A. Mcnamara, "High-capacity ribbed pile foundations.", *Proceedings of the Institution of Civil Engineers - Geotechnical Engineering*, vol. 169, no. 3, pp. 264-275, 2016.
- [62] J.X. Lai, S. M, J.L. Qiu et al, "Investigation progresses and applications of fractional derivative model in geotechnical engineering", *Mathematical Problems in Engineering*, vol. 2016, Article ID 9183296, 15 pages, 2016. doi: 10.1155/2016/9183296
- [63] Dou shikang, Zhao qiuling, Huang shuangling. Brief introduction of root pile technology and its application in aeolian sand tunnel[J]. *Railway Standard Design*, 2007(s1):177-179. .(in chinese)
- [64] Peng fuqiang, Yuan hang, Yi jinhua. The application of root pile in the reinforcement of tunnel entrance loose accumulation body[J]. *Journal of China & Foreign Highway*, ,2012,32(3):35-37.(in chinese)
- [65] Yin chengfei, Ma weibin, Sun hongfang. Shuohuang Railway disease basement structure of Changliangshan tunnel remediation measures[J]. *Chinese Railway*, 2012(11):66-69.(in chinese)
- [66] Ge peng, Xu lian, Sun chunbin. Application of root pile supporting system in Nanjing area[J]. *Journal of Geology*, ,2008,32(1):46-49. (in chinese)
- [67] Liu haihong, Treatment of permanent Liuhe highway jiaoxiling No. 3 tunnel exit No. 6 Myungdong[J]. *Hunan Communication Science and Technology*, 2003,29(2):82-83. (in chinese)
- [68] Y.H. Zhang, L.J. Tang, and N. Wang, "Bridge Bored Pile Construction Management and Accident Treatment." *Applied Mechanics & Materials*, vol. 360, no. 3/4, pp. 1535-1538, 2013.
- [69] K. Ng, and S. Sritharan, "Integration of construction control and pile setup into load and resistance factor design of piles." *Soils and Foundations*, vol. 54, no. 2, pp. 197-208, 2014.
- [70] A. Yaoa, and D. Lei, "Numerical Analysis of the Influence of Isolation Piles in Metro Tunnel Construction of Adjacent Buildings." *Procedia Earth & Planetary Science*, vol. 5, no. 1-2, pp. 150-154, 2012.
- [71] R. Nazir, H. Moayed, M. Mosallanezhad, and A. Tourtiz, "Appraisal of reliable skin friction variation in a bored pile." *Proceedings of the Institution of Civil Engineers - Geotechnical Engineering* vol. 168, no. 1,



pp.75-86,2015

- [72] S.L. Shen, Z.F. Wang, W.J. Sun, L.B. Wang, and S. Horpibulsuk, "A field trial of horizontal jet grouting using the composite-pipe method in the soft deposits of Shanghai." *Tunnelling & Underground Space Technology*, vol.35,no. 4, pp. 142-151,2013.
- [73] S.J. Zhang, "The Introduction of Micro-Pile in Building Heightening and Transformation." *Advanced Materials Research*, vol. 941-944, pp. 743-746, 2014.
- [74] O. Makovetskiy, and S. Zuew, "Practice Device Artificial Improvement Basis of Soil Technologies Jet Grouting." *Procedia Engineering*, vol. 165, pp. 504-509,2016.

STRENGTHENING OF A REINFORCED CONCRETE BRIDGE WITH PRESTRESSED STEEL WIRE ROPES

Kexin Zhang, Quansheng Sun

Department of Civil Engineering, Northeast Forestry University, Harbin, 150040, China; zkx0204@yahoo.com, hrbsqs@126.com

ABSTRACT

This paper describes prestressed steel wire ropes as a way to strengthen a 20-year-old RC T-beam bridge. High strength, low relaxation steel wire ropes with minor radius, high tensile strain and good corrosion resistance were used in this reinforcement. The construction process for strengthening with prestressed steel wire ropes—including wire rope measuring, extruding anchor heads making, anchorage installing, tensioning steel wire ropes and pouring mortar was described. Ultimate bearing capacity of the bridge after strengthening was discussed based on the concrete structure theory. The flexural strength of RC T-beam bridges strengthened with prestressed steel wire ropes was governed by the failure of concrete crushing. To investigate effectiveness of the strengthening method, fielding-load tests were carried out before and after strengthening. The results of concrete strain and deflection show that the flexural strength and stiffness of the strengthened beam are improved. The crack width measurement also indicates that this technique could increase the durability of the bridge. Thus, this strengthened way with prestressed steel wire rope is feasible and effective.

KEYWORDS

Steel Wire Ropes, Prestressed, Strengthening, RC Bridges, Field Application, Load Test

INTRODUCTION

Transportation agencies are faced with a continuous challenge to keep bridges in a good operating condition. Bridge structures are deteriorating at a fast rate, and costs for maintenance and rehabilitation are continuously rising. It is both economically and environmentally satisfactory to upgrade bridge structures rather than rebuild them if simple, effective, and rapid method can be used.

To improve the working ability of concrete bridges, many techniques have been used in strengthening. The most common methods for strengthening beams are external bonding steel plate, external bounding carbon fibre reinforced polymer (CFRP), and external posttensioning tensions. Despite the capacities, stiffness and cracking performance of the steel plate strengthening beams are improved. Bonding steel plates also show some disadvantages, such as weakened bonding caused by steel corrosion, increased dead load weight and difficulties in adapting to the concrete surface profile [1-3]. CFRP materials have good structural performance, high strength and light weight. CFRP can be easily installed, as they can be attached to a curved profile [4-6]. However, when CFRP are used as externally bonded reinforcement, the flexural stiffness has very little improvement peeling failure is often occurred without warning than un-strengthened flexural members. And that the cost of CFRP is high. Adding prestressing by external tendons can significantly increase the yield load and the ultimate resistance of the beams, the deflection at the serviceability state is also reduced, the behaviour of composite beams prestressed with external tensions was investigated [7-8]. However, a large jack must be provided

for drawing of the pre-stressing tendons and need a big drawing space during construction.

Recently, a new strengthening technique with distributed prestressed high strength steel wire rope was proposed. Unreinforced masonry walls were strengthened with prestressed wire ropes in the laboratory [9]. The proposed strengthening procedure was highly effective in enhancing the in-plane shear strength and ductility of the unreinforced masonry walls. Then the prestressed steel wire mesh strengthened shear walls was studied, the cracking load, yield load, ultimate load of shear wall specimens were increased [10]. Guo [11, 12] investigated the mechanical properties of RC columns strengthened with prestressed steel wire ropes. The stiffness was increased and the stiffness degradation mitigated. The seismic strengthening effect of the reinforced columns with steel wire spacing of 30 mm did not change significantly with increasing of prestressing force level.

In order to study the effect of strengthening concrete beams. Seven RC beams were strengthened with prestressed steel wire ropes by Gang [13, 14]. The effective utilization rate of prestressed steel wire rope strengthening was higher than that of the pasting steel plate and CFRP strengthening. Zhang [15] took the stress loss and the number of steel wire ropes into consideration, and the failure mode as well as improvements of cracking resistance, bending bearing capacity and stiffness were investigated. This strengthening technique for RC beams, which was proposed to overcome the shortcomings of existing strengthening methods, utilises the advantages of traditional materials and achieves an active strengthening of RC beams with less influence on the original structure and better comprehensive performance [13-15]. The advantages of this technique also include minimum site disruption, minimal increase in the size of the repaired member, minimum scaffolding, superiority for fire and corrosion resistance, and low cost.

Nevertheless, these research projects were carried out with laboratory-scale tests and corresponding analyses. Applying and obtaining the application results in engineering are essential. This study describes a novel strengthening method using prestressed steel wire ropes to strengthen a 20-year-old reinforced concrete T-beam bridge in service, including design, field application, field test and analysis.

BACKGROUND

The bridge discussed in this paper carries Jianbian Farm in Heilongjiang Province, China. This simple span, reinforced concrete, T-beam structure was built in 1995. The bridge is 16.0-m long and about 8.5-m wide, and is supported by a total of 5 beams spaced at 1.6-m centre to centre. A lateral view and a cross-section of the bridge are shown in Figure 1 and Figure 2, respectively. The bridge has been opened to traffic without weight-limit restrictions and carries an average daily traffic of 1200 vehicles. It has two lanes and carries one lane of traffic in each direction.

The bridge has different degrees of damage caused by aging, overload, surging traffic and environment. During routine inspection, salt infiltration and excessive moisture were observed in the bridge superstructure. Many beams had been covered largely with efflorescent concrete. Serious cracks occurred in the edge-beam, as water from the pavement cracks affected the durability of the girder. The diseases of the bridge were seen in Figure 3. Heilongjiang Province Department of Transportation elected to rehabilitate the structure as opposed to replacement or load posting. A prestressed steel wire ropes strengthening method was selected based on its application being the minimum site disruption and the most practice. Strengthening work, including wire rope measuring, extruding anchor heads making, anchorage installing, tensioning and installing steel wire ropes and polymer mortar pouring was completed during July – September of 2015.



Fig. 1 - Lateral view of the bridge

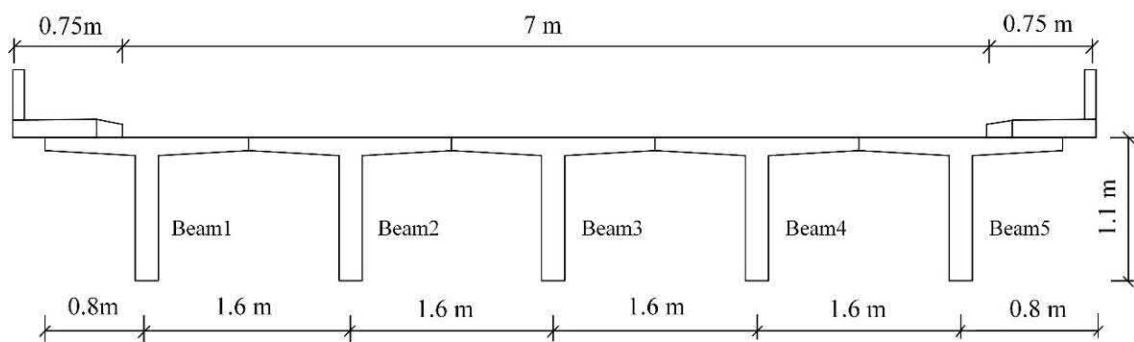


Fig. 2 - Cross-section of the bridge

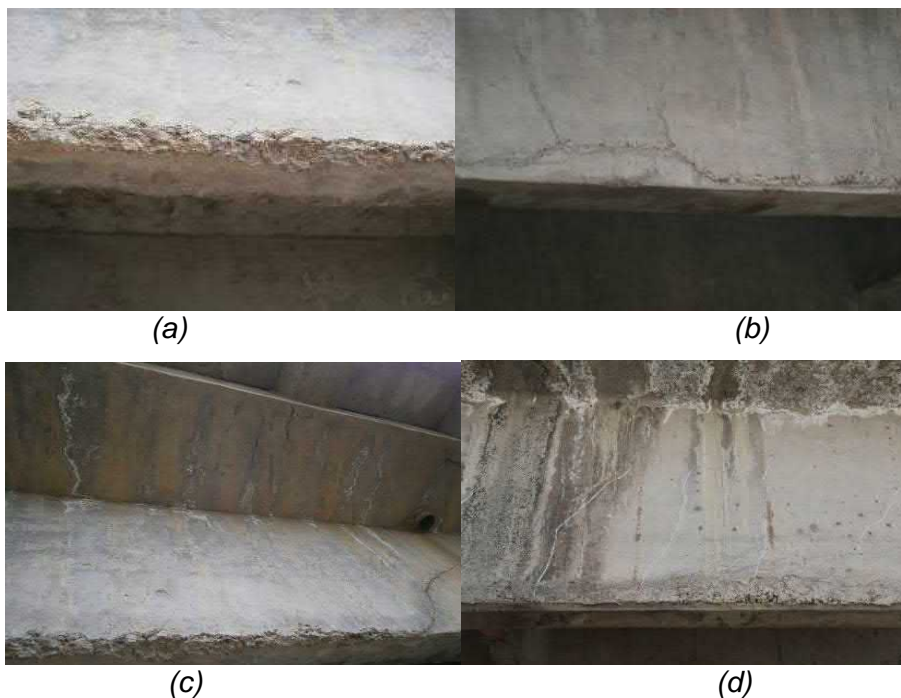


Fig. 3 - Diseases of the bridge; a) efflorescent concrete, b) cracks and efflorescent concrete, c) leakage and efflorescent concrete, d) cracks and leakage

PRESTRESSED STEEL WIRE ROPES DESIGN AND INSTALLATION

Bridge material properties such as the concrete compression strength and steel yield strength were assumed because the owner of the bridge did not allow coring to obtain the on-site strengths of the materials from the bridge girder. These basic properties f_c f_s were assumed as described by JTJ023-85 [16] for bridges of that age because no sample could be obtained onsite. Concrete compression strength, concrete elastic modulus, yield strength of steel rebar and elastic modulus of steel rebar are listed in Table 1.

High strength, low relaxation steel wire ropes with minor radius, high tensile strain and good corrosion resistance were used in this reinforcement. High strength steel wire ropes with a normal diameter of 4 mm and normal section of 10.55 mm² were chosen. A test was applied to determinate the mechanical properties of the steel wire ropes with lengths of 50 mm as shown in Figure 4. Stress-strain curve is shown in Figure 5. Before the proportional limit point, the curves indicate a fine linear relationship between stress and strain and there is no obvious yield point at the non-linear stage. The ultimate tensile strength was 1250 Mpa and elastic modulus was 130 Mpa. The stress when residual strain was 0.2% is defined to be the normal yield stress, which is about 85% of its ultimate tensile strength. The properties of wire ropes were shown in Table 1.

Tab. 1 - Material properties

Material	Property	Value
Steel wire rope	f_{ps} (MPa)	1250
	E_{ps} (GPa)	130
Concrete	f_c (MPa)	30
	E_c (GPa)	30
Steel	f_s (MPa)	335
	E_s (GPa)	200

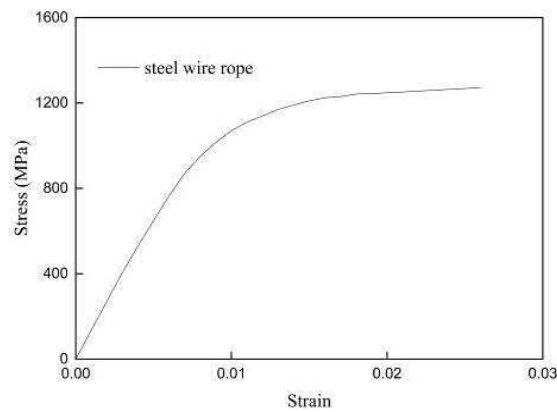


Fig. 4 - Tension test of wire ropes Fig. 5 - Stress-strain curve of steel wire ropes

Strengthening analysis

The flexural capacity is established based on force equilibrium, strain compatibility and constitutive laws of materials up to failure. Whitney's rectangular stress block was used to simulate the behaviour of the compressed concrete. Figure 6 shows the strain and stress relationship of beams at the ultimate stage. The bearing strength of the beam equals to 1622.7 kN.m. T-beams strengthened with prestressed wire ropes were the beam flexural failure because of the excellent anchorage performance. The flexural capacity of the reinforced member depended on the concrete

crushing or the steel wire rope rupture. According to strain compatibility, the strain of steel bar ϵ_s can be expressed as follows:

$$\epsilon_s = \frac{d_s - x}{d_{ps} - x} \epsilon_{ps} \tag{1}$$

Where d_s represents the depth from the centroid of steel bars to the top of the T-cross section, d_{ps} represents the depth from the centroid of the steel wire ropes section to the top of the T-cross section, x represents the depth of the neutral axis and ϵ_{ps} represents the strain of the centroid of the steel wire ropes section.

When steel wire rope failure happens, ϵ_s goes beyond the allowance strain of steel rebars, which is 0.01 according to Design Code of Concrete Structures [17]. Therefore, beam failure is not controlled by steel yield.

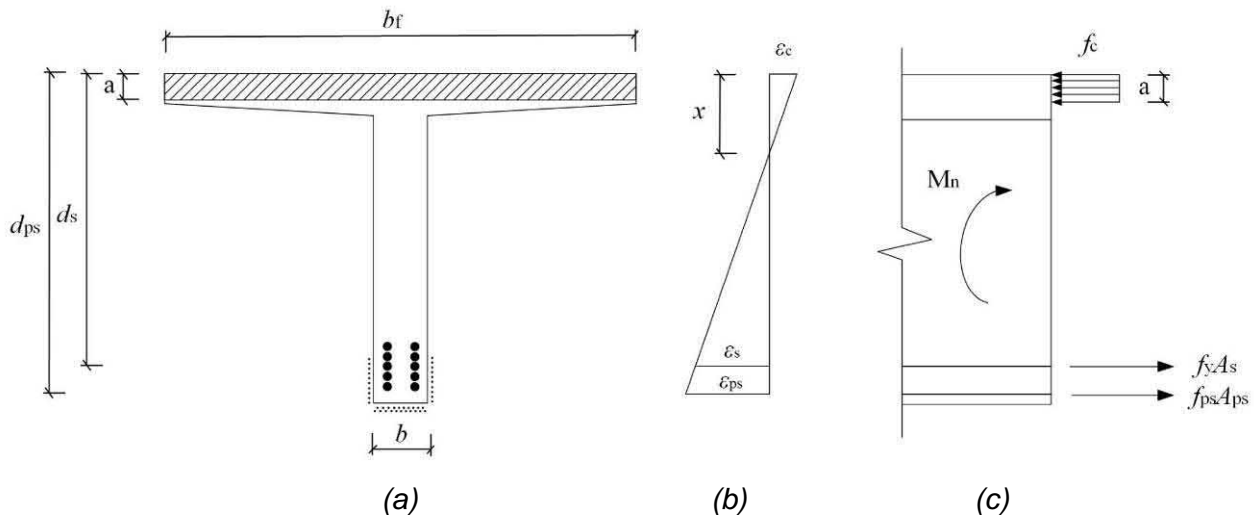


Fig. 6 - Internal strain and stress distribution for a T-shape section ; a) Reinforced concrete section, b) Strain distribution, c) Stress distribution

When concrete crushing failure happens, the ultimate compressive strain for the concrete is taken as 0.003. ϵ_s is larger than the yield strain of steel rebar and smaller than 0.01 from the relationship of strains between concrete and steel rebar. According to strain compatibility, the strain of the centroid of the steel wire ropes section ϵ_{ps} can be expressed as follows.

$$\epsilon_{ps} = \frac{d_{ps} - x}{x} \epsilon_{cu} \tag{2}$$

Due to the steel wire rope is a nearly elastic material, the stress σ_{ps} of the steel wire rope material can be calculated by the following:

$$\sigma_{ps} = E_{ps} \epsilon_{ps} + \sigma_{pe} \tag{3}$$

Where σ_{pe} is the prestress in steel wire ropes, stress relationship of beams at the ultimate stage is seen as Figure 6. From the equilibrium condition:

$$\alpha_1 f_c b_f a = f_y A_s + f_{ps} A_{ps} \tag{4}$$

$$M_u = f_{ps} A_{ps} \left(d_{ps} - \frac{x}{2} \right) + f_y A_s \left(d_s - \frac{x}{2} \right) \tag{5}$$

Where M_u is the flexural strength of the T-beam strengthened with prestressed steel wire ropes, $\alpha_1=1$, a is the depth of the equivalent rectangular concrete stress block; $a=0.8x$, b_f is the width of the flange, A_s represents the area of the steel bars and f_y represents the yield stress of the steel bars.

The flexural strength of the beams after strengthening can be calculated through a combination of Equation. (1) - Equation (5).

The above mentioned analysis shows that the bearing capacity of the strengthened beam is controlled by the failure of concrete crushing. The section of the T-beam strengthened by prestressed steel wire ropes is shown in Figure 7. All the steel wire ropes were anchored at one place near the supports. For the double-deck arrangement of wire ropes at the bottom of the beam, the two anchors were arranged separately. The designed tension stress for steel wire ropes is 650MPa. Flexural strength increased to 1075.2 kN.m through prestressed steel wire ropes.

The verification of serviceability limit state was carried out according to Design Code of Concrete Structures [17]. The deflection calculation was as follows:

$$f = \frac{5}{48} \cdot \frac{M_s l^2}{B} \quad (6)$$

Where M_s is the calculated bending moment for a combination of short-term effects of load; $l=15.7\text{m}$, B is the flexural rigidity of the equivalent section of the cracking member. The calculated deflection at serviceability limit state after being strengthened with prestressed steel wire ropes was 6.9mm. The value of 6.9mm was less than the value of $l/600$, which met the requirement.

The crack width calculation was as follows:

$$w_{\max} = \alpha_{cr} \psi \frac{\sigma_s}{E_s} l_{cr} \quad (7)$$

Where M_{cr} is the calculated maximum crack width for a standard combination of load effects (considering the long-term effects); $\alpha_{cr}=1.5$; $\psi=1$; σ_s is the equivalent stress of longitudinal tensile reinforcement; E_s is the elastic modulus of reinforcement, $l_{cr}=0.2$ m. The calculated crack at serviceability limit state after being strengthened with prestressed steel wire ropes was 0.09 mm. The value of 0.09 mm was less than the value of 0.2 mm, which met the requirement.

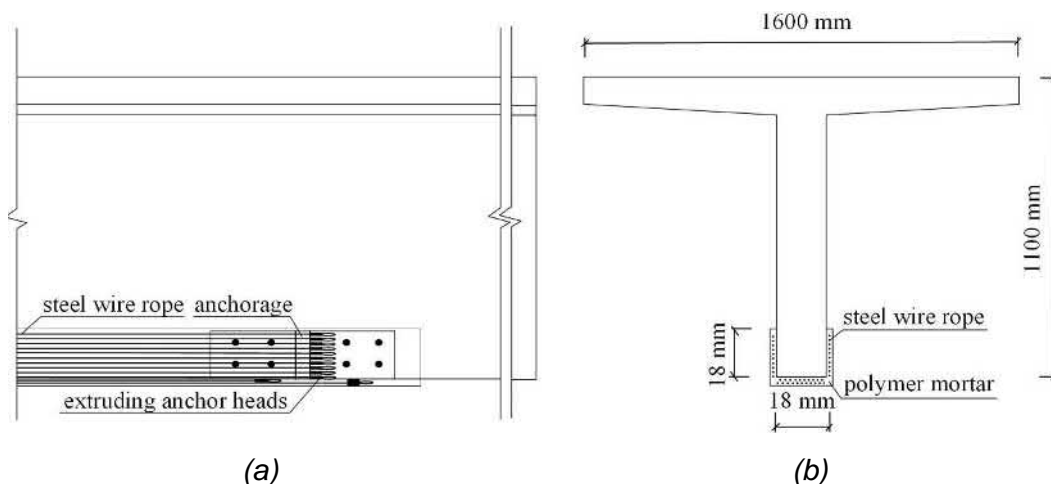


Fig. 7 - Diagram for the T-shape beam strengthened with steel wire ropes ;
a) Lateral schematic diagram, b) Cross-section

Strengthening process

Prestress steel wire ropes strengthening is similar to add prestressing by external tendons [18, 19], but the drawing space and dosage of scaffolding during construction for prestressed steel wire ropes is significantly less than adding prestressing by external tendons.

(a) Wire rope measuring (Figure 8(a)). Steel wire ropes were measured and cut into the same length according to the design.

(b) Extruding anchor heads making (Figure 8(b)). For the extruding anchor head, one end of a steel wire rope was folded into two, put through an aluminium alloy sleeve, and extruded to become an extruding anchor head through a squeezer, which could anchor a steel wire rope effectively. The applied anchorage was similar to a button-head anchorage – the length of the steel wire ropes was based on the designed tensile stress.

(c) Anchorage installing (Figure 8(d)). The U-shape steel plate was fixed on the beam end through high strength bolts and steel sticking glue. Weld anchorage was carried out on the steel plate. In order to ensure welding quality, the welding parts of steel plate were polished. Fig.8(d) shows the anchorage used in this bridge

(d) Tensioning and installing steel wire ropes (Figure 8(c) and Figure 8(d)). One end of a steel wire rope was put through an anchorage and the other was tensioned through a small tensioner. Tensioning is convenient in construction site owing to the flexibility of steel wire ropes. The steel wire rope was stretched and anchored when the extruding anchor head surpassed the anchorage. The value of tensioning force could be controlled by pre-design elongation value of the steel wire rope. A tension sensor was used to check the tensioning force in the construction site.

(e) Pouring mortar (Figure 8(e)). A U-shape wooden template was installed on the bottom of the T-beam. Polymer mortar was mixed through a blender and pressed into the template by grouting machine. To cope with the environment to which the steel wire ropes may be exposed, the polymer mortar could be used isolate steel wire ropes from natural conditions. Polymer mortar had satisfactory crack resistance and adhesion, relative to the ordinary mortar. The good liquidity and adhesion of polymer mortar could effectively wrap steel wire ropes. Thus, a relatively thin layer of polymer mortar increased the durability of the steel wire ropes.



(a) (b)

Fig. 8 - Main steps for strengthening; a) steel wire ropes tension, b) steel wire ropes installing

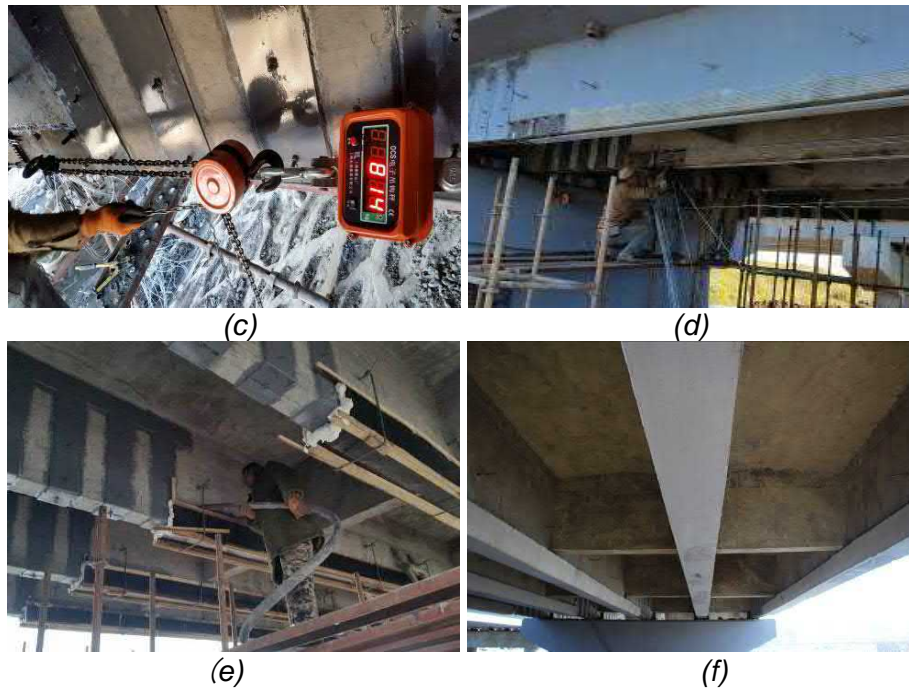


Fig. 8 - Main steps for strengthening; a) steel wire ropes tension, b) steel wire ropes installing, c) mortar pouring, d) steel wire ropes installing, e) mortar pouring, f) demolition of the template

LOAD TEST

Before strengthening and two months after strengthening, load tests were performed to obtain the service ability of the bridge. These tests are repeated once a year and they will continue over a period of three years. Four three-axle trucks were used to apply simulated traffic loading to the structure. The gross rail loads of the test trucks before and after strengthening are listed in Table 2. The sequencing, in which the four trucks were designated A through D (Figure 9), consisted of Truck A, Trucks A+B, Trucks A+B+C, Trucks A+B+C+D, Trucks B+C+D, Trucks C+D, Trucks D. Due to the actual strength of the structure was not known, three truck positions were marked to gradually increase applied moment on the bridge. Truck locations in Figure 10 during the tests were determined to result in safe stress-levels.

Table 2. Gross axle load of trucks before and after strengthening

Load-test trucks		Force axle t_1 (kN)	Back axle t_2 (kN)	Back axle t_2 (kN)
Before	(A)	58.1	135.1	135.1
	(B)	58.0	134.2	134.2
	(C)	58.3	134.4	134.4
	(D)	59.4	136.9	136.9
After	(A)	59.0	135.2	135.2
	(B)	58.6	135.0	135.0
	(C)	59.1	136.4	136.4
	(D)	58.6	134.4	134.4

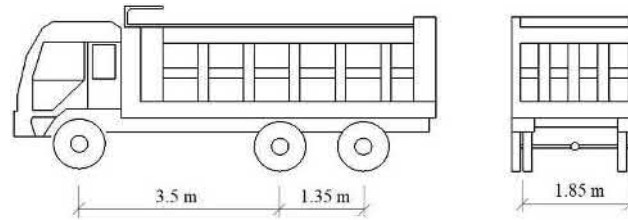


Fig. 9 - Load-test truck configuration

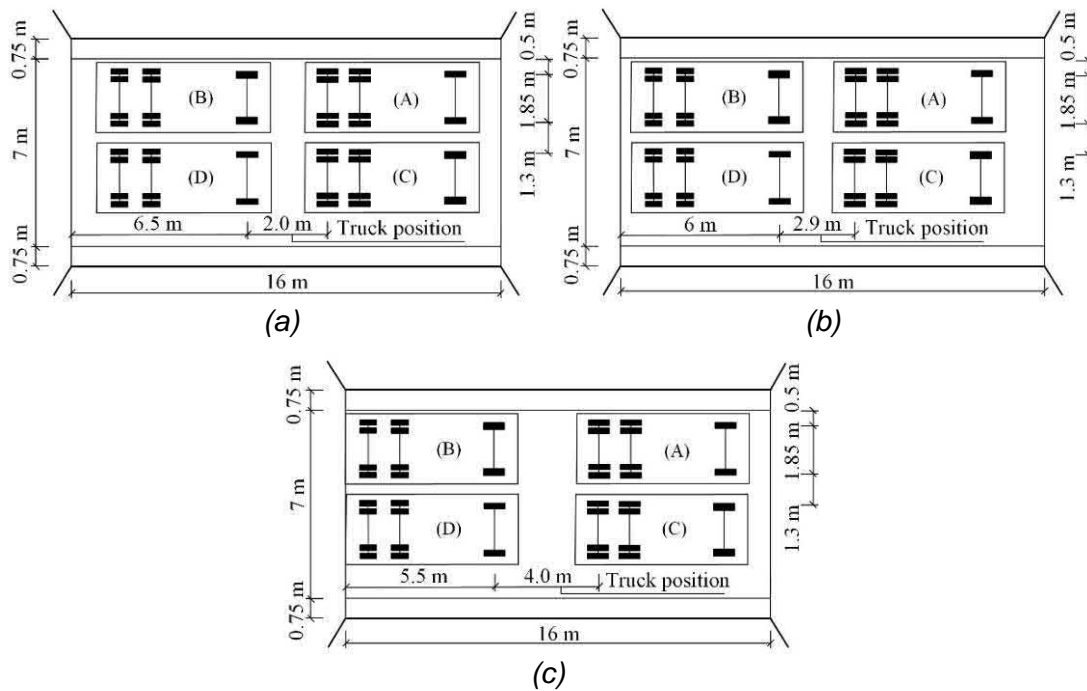


Fig. 10 - Distribution of load-test trucks on the bridge deck at different truck position; a) Truck position: 2.0 m, b) Truck position: 2.9 m, c) Truck position: 4.0 m

STRAIN MEASUREMENT

All the recorded strain gauges were arranged at the midspan. The strain gauge arrangement of each beam was the same. In the “before” strengthening test, four strain gauges were installed on the concrete surface of each beam. In the “after” strengthening test, four gauges were placed on the concrete surface of each beam, which were the same as the “before” strengthening test. In addition, two gauges were placed on the surface of the steel wire ropes.

All the strain values were recorded at different loading stages, including no live load, Truck A, Trucks A+B, Trucks A+B+C, Trucks A+B+C+D, Trucks B+C+D, Trucks C+D, Trucks D and no live load, respectively.

The strain gauges were placed on the concrete surface at the mid-span in the “before” strengthening test and the “after” strengthening test, with the detailed locations shown in Figure 11(a). The letter *n* represents the beam number, and the letter C represents the concrete strain gauges. Resistance strain gauges (Cn1) were installed on the bottom of the beam before strengthening, as the bottom of the beams was covered with polymer mortar after strengthening. The strain gauges of the steel wire ropes are shown in Figure 11(b). The letter S represents the steel wire rope strain gauges. The gauge Sn1 was installed on the steel wire rope surface at the bottom of the beam.

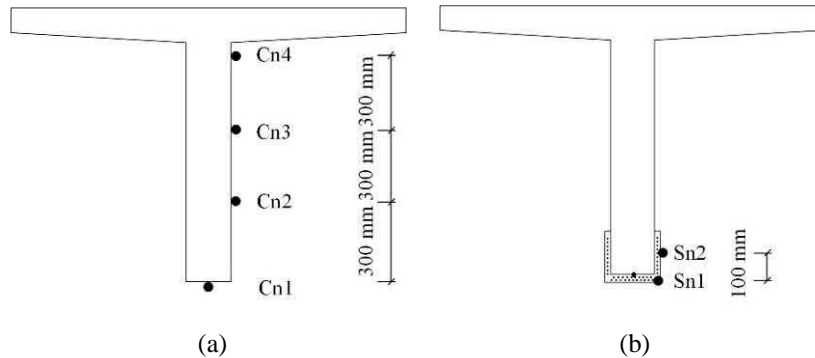


Fig. 11 - Locations of strain gauges mounted on the beams (*n* is the beam number); a) Strain gauges mounted on concrete; b) Strain gauges mounted on steel wire ropes

“Before” and “after” strengthening stains on concrete surface at midspans of beam 1-5, for the various truck combination at 4.0, 2.9 and 2.0-m positions on the bridge are shown in Figure 12. Comparing the “before” and “after” readings for gauges, it can be concluded that strengthening of the steel wire ropes obviously reduced concrete stress. The strain value was the largest when the sequencing was Trucks A+B+C+D. The maximum “before” strengthening strain of beam 1 was 225 microstrains for the case of all four trucks parked at 4.0-m position on the bridge because of the damage and the weak interaction between the beams. While, the maximum “after” strengthening strain of beam 1 was 200 microstrains. The strain was reduced to about 25 microstrains. The maximum “before” strengthening strain of beam 1 was 247 microstrains for the case of all four trucks parked at 2.9-m position. While, the maximum “after” strengthening strain of beam 1 was 219 microstrains. The strain was reduced to about 28 microstrains. The maximum “before” and “after” strengthening strains of beam 1 were 264 microstrains and 235 microstrains, respectively, for the case of all four trucks parked at 2.0-m position. Therefore, the concrete strain could be reduced after the prestressed steel wire ropes were used.

The recorded strain values of gauges Cn1, Sn1 and Sn2 of the five beams for the cases of all four trucks parked at different position are shown in Figure 13. In comparing the recorded concrete strains (gauge Cn1) and steel wire rope strains (gauge Sn1), the concrete strain values were approximately equal to the steel wire rope strain values on the same horizontal height, indicated that steel wire ropes were well anchored to the girders by anchorage and mortar and were acting as an effective part of the cross-section. Therefore, steel wire rope strain compatibility was well at the live load.

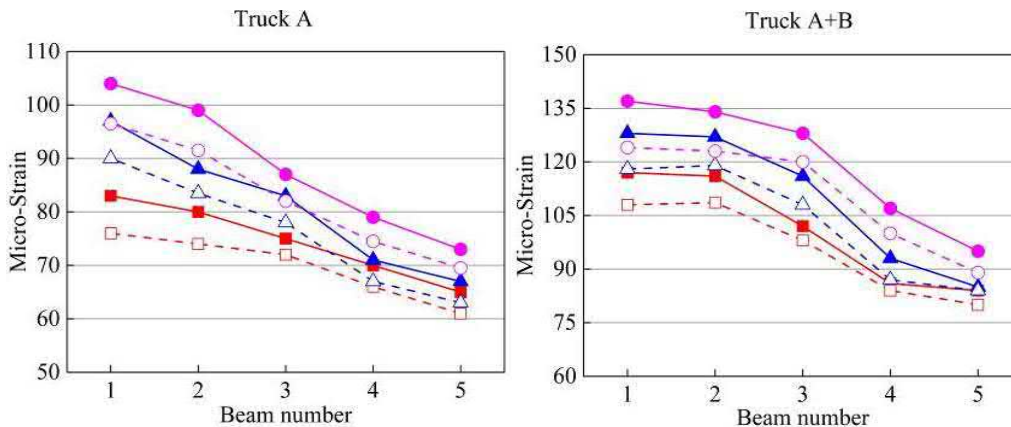


Fig. 12 - Maximum recorded strain (C_{n1}) on concrete surface in the “before” and “after” strengthening

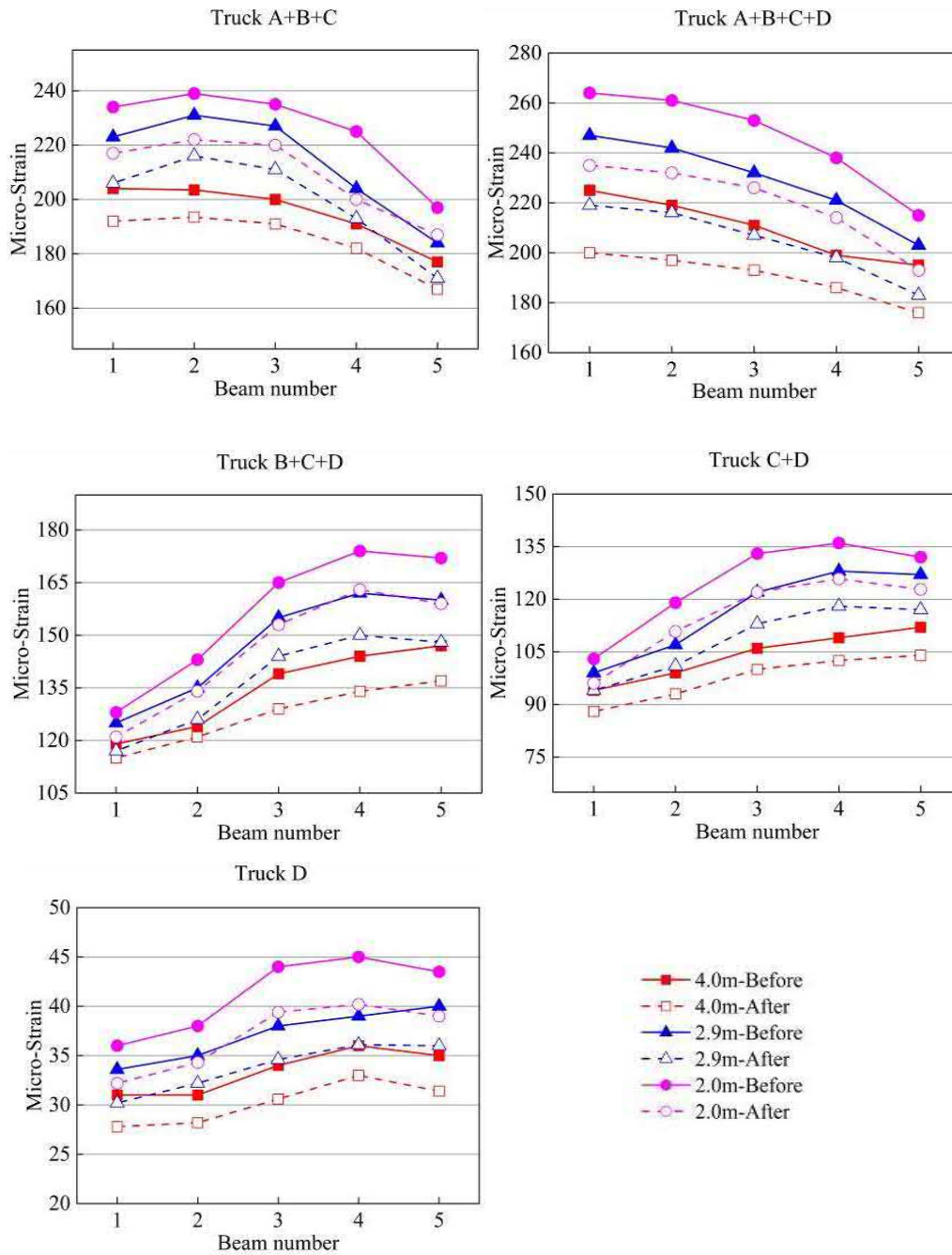
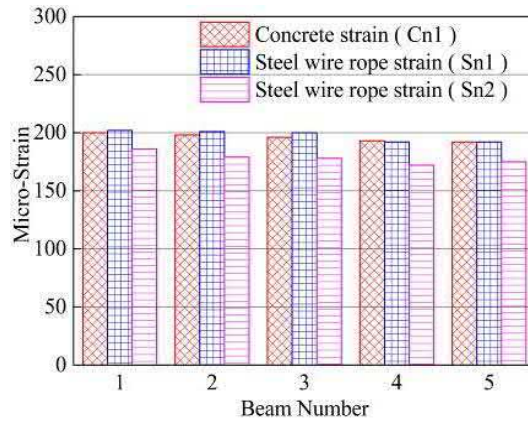
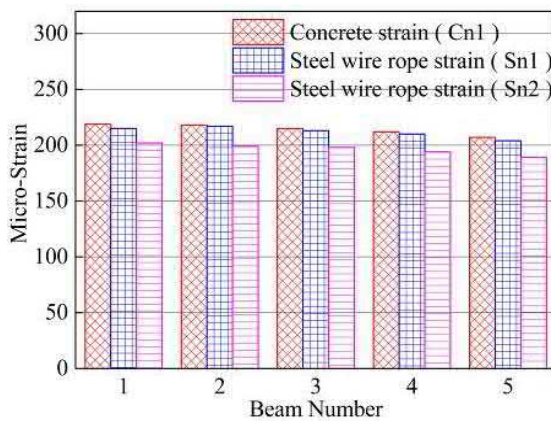


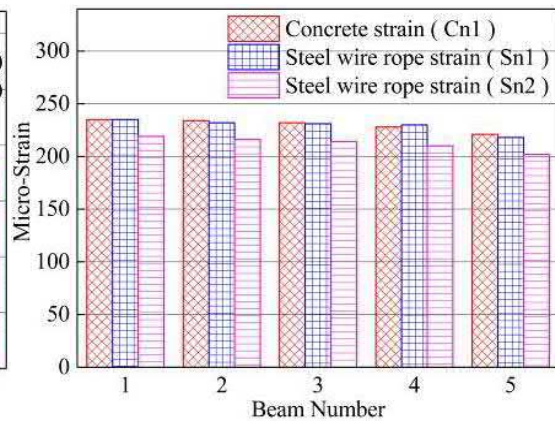
Fig. 12 - Maximum recorded strain (C_{n1}) on concrete surface in the “before” and “after” strengthening



(a)



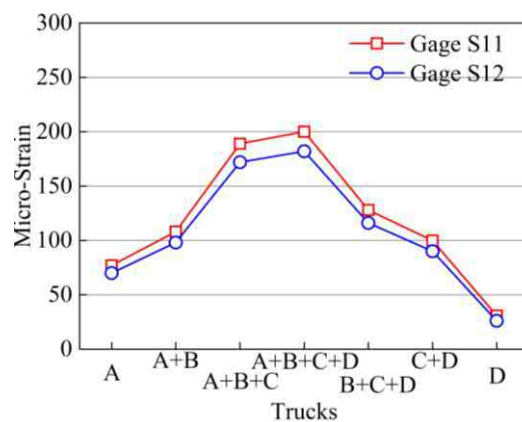
(b)



(c)

Fig. 13 - Concrete strains and steel wire rope strains for the case of all four trucks parked at different positions; a) 4.0-m position, b) 2.9-m position, c) 2.0-m position

Comparing the steel wire rope strains of gauge Sn2 with those recorded on gauge Sn1, the Sn2 strains were lower than the Sn1 strains. Strain compatibility led to the lower Sn2 strain than the Sn1 strain because steel wire rope at the bottom was physically located below steel wire rope at the side in the beam section.



(a)

Fig. 14 - Recorded strains for gauges mounted on steel wire ropes for cases of trucks parked at different positions

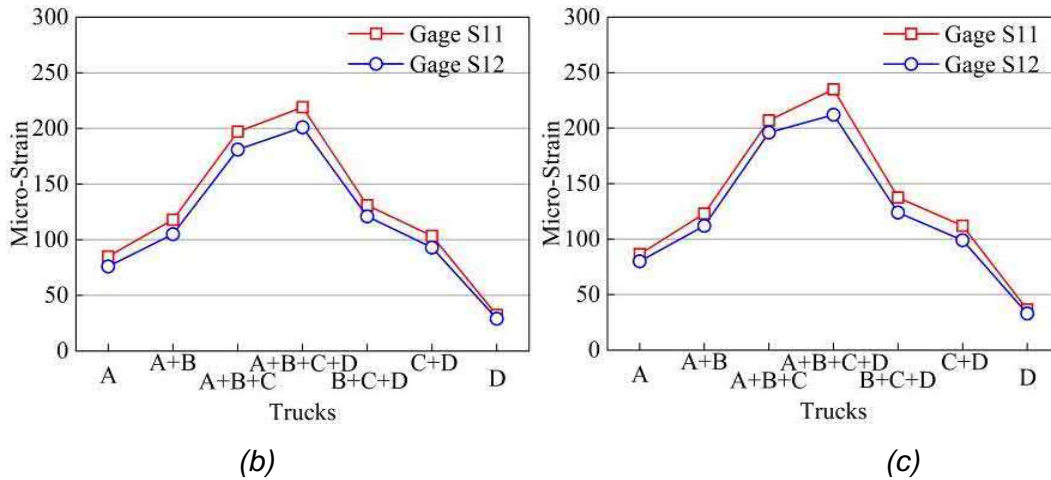


Fig. 14 - Recorded strains for gauges mounted on steel wire ropes for cases of trucks parked at different positions; a) 4.0-m position, b) 2.9-m position, c) 2.0-m position

Measured steel wire rope strains for the cases of trucks parked at different conditions and the various truck positions further confirmed consistency of the data and the effectiveness of the strengthening method in carrying load, as shown in Figure 14. From this figure, for the given truck position, reading from gauges S11 and S12 of beam 1 in 4.0-m, 2.9-m and 2.0-m position clearly showed that strains were proportional to applied bending.

The recorded strain values of beam 1 and beam 3 below the deck slab are listed in Table 3. The cases of four trucks parked at different conditions on the bridge. From this table, comparing the “before” and “after” strengthening strains for the given gauges, the compressive strains in the concrete were higher after the prestressed steel wire ropes were installed. In investigating this matter further, the neutral axes were determined as shown in Table 4. Four trucks (Trucks A+B+C+D) were parked on the bridge in 4.0-m condition. From this table, as expected, the neutral axis of beam 1 migrated downwards by about 20mm, after the steel wire ropes were installed in 4.0-m position. Meanwhile, the neutral axis of beam 1 migrated downwards by about 22mm and 24mm, when the cases of four trucks parked on the bridge in 2.9-m position and 2.0-m position, respectively.

Table 3 - Measured compressive strain on beam 1 and beam 3

Truck position (m)	Gauge C14 strain ($\mu\epsilon$)		Gauge C34 strain ($\mu\epsilon$)	
	Before	After	Before	After
4.0-m position	-7	-8	-6	-5
2.9-m position	-9	-11	-7	-6
2.0-m position	-10	-12	-9	-7

Table 4 - Neutral axis investigation

Truck position (m)	Before strengthening ($\mu\epsilon$)			After strengthening ($\mu\epsilon$)		
	Gauge C11 strain ($\mu\epsilon$)	Gauge C14 strain ($\mu\epsilon$)	Neutral axis location (mm)	Gauge C11 Strain ($\mu\epsilon$)	Gauge C14 strain ($\mu\epsilon$)	Neutral axis location (mm)
4.0-m position	225	-7	227	200	-11	247
2.9-m position	247	-9	232	219	-14	254
2.0-m position	264	-10	233	235	-16	257

DEFLECTION MEASUREMENT

The recorded deflection gauges were arranged at the midspan and at the end of the beam, respectively. The deflection gauge arrangement of each beam was the same. In the “before” strengthening test, one deflection gauge was installed at the midspan, and two deflection gauges were installed at the end of each beam. In the “after” strengthening test, the deflection gauge arrangement was as the same as the “before” strengthening test.

All the deflection values were recorded at different loading stages, including no live load, Truck A, Trucks A+B, Trucks A+B+C, Trucks A+B+C+D, Trucks B+C+D, Trucks C+D, Trucks D and no live load, respectively.

“Before” and “after” strengthening deflection at midspans of beam 1-5, for the various truck combination at 4.0, 2.9 and 2.0-m positions on the bridge are shown in Figure 15. The maximum “before” strengthening deflection of beam 1 was 7.94mm for the case of all four trucks (Trucks A+B+C+D) parked at 4.0-m position on the bridge. While the maximum “after” strengthening deflection was 7.15mm when the prestressed steel wire ropes were installed. This showed a decrease of 9.9%, compared with “before” strengthening deflection. The “after” deflection of beam1 was 7.85mm, a 11.3% decrease over “before” strengthening deflection for all four trucks (Trucks A+B+C+D) parked at 4.0-m position. The maximum “before” deflections of beam 1 was 9.43mm. After strengthening, the “after” strengthening deflection was 8.55mm for four trucks (Trucks A+B+C+D) parked at 2.0-m position. This showed a decrease of 9.3%, compared with “before” strengthening deflection. As expected, a certain decrease in deflection after the application of prestressed steel wire rope reinforcement could be observed at different positions. These findings represent an initially good performance, although the long-term performance will be monitored throughout the next year.

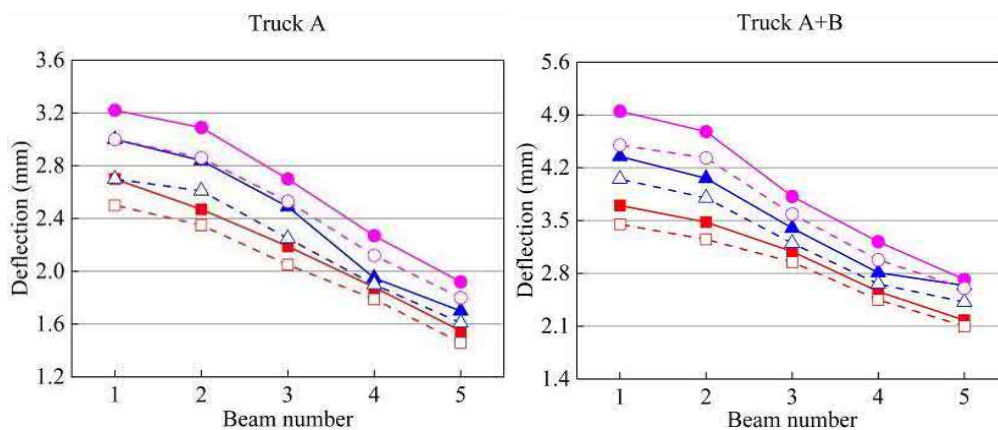


Fig. 15 - Maximum recorded deflection in the “before” and “after” strengthening

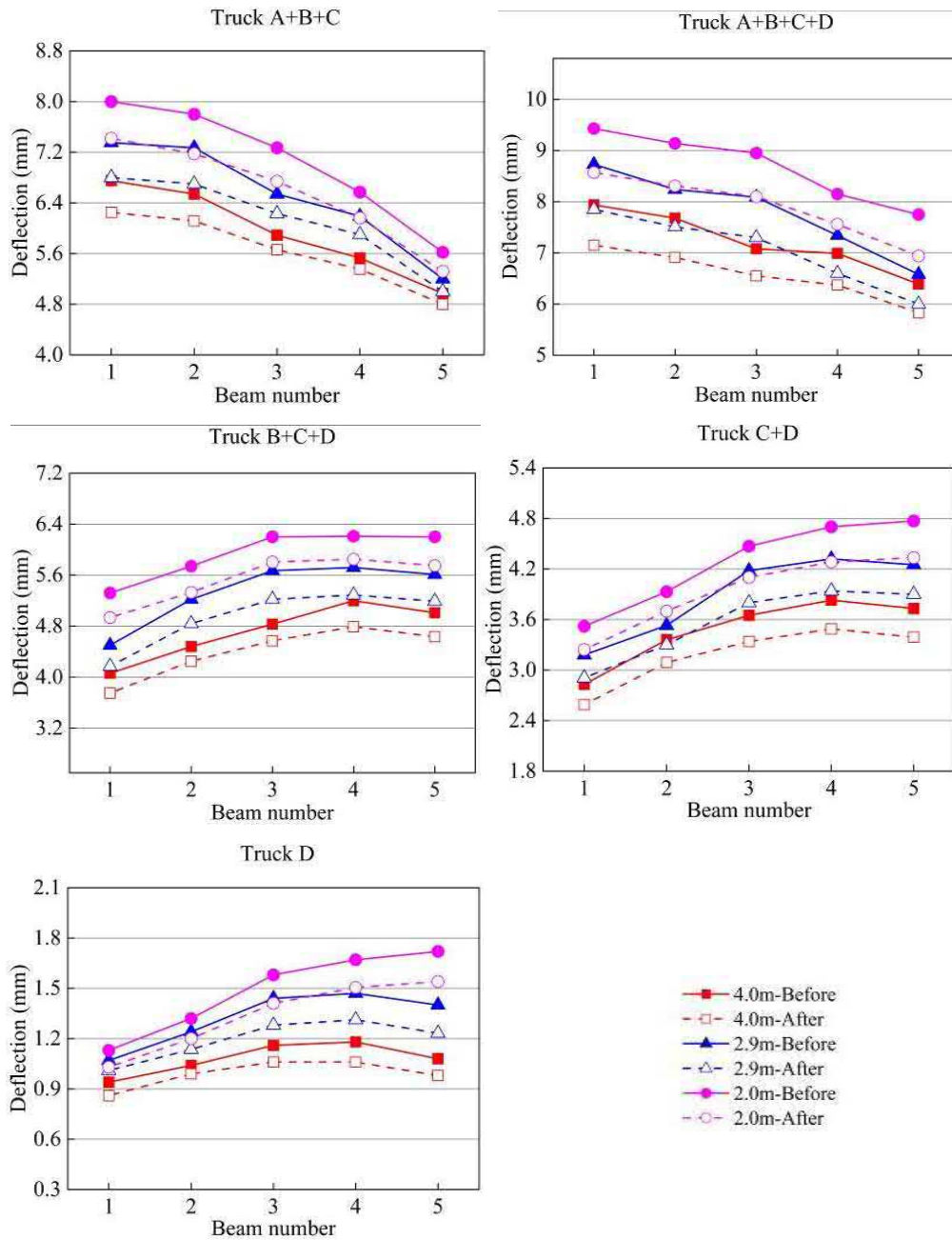


Fig. 15 - Maximum recorded deflection in the “before” and “after” strengthening

CRACKS

The monitoring location of the crack in the “before” and “after” strengthening is shown in Figure 16. The width of the cracks increased with the test load increasing, but no new cracks appeared. These cracks had affected the durability of the bridge and would have further reduced the performance of the bridge if no actions were taken. In order to monitor the development of the cracks after strengthening, a repaired crack in the midspan of beam 1 was selected to be the monitoring crack of the load test. The crack width in the “before” and “after” strengthening is shown in Figure 17. The width of the crack on the soffit of the beam is 0.25mm for the case of all four

trucks (Trucks A+B+C+D) parked at 2.0-m position on the bridge before strengthening. The monitoring location of the crack is beyond the soffit of the beam, because concrete surface for the soffit of beams was covered with polymer mortar after strengthening. The depth from the monitoring location to the soffit of the beam was 20cm. The width of the crack at the monitoring location is 0.15mm before strengthening. Its width was unchanged for two trucks (Truck A+B), 0.03mm for three trucks (Trucks A+B+C), 0.05mm for four trucks (Trucks A+B+C+D) and closed when the trucks were moved from the deck. Furthermore, periodical inspections were carried out to observe the development of surface cracks on the side of the beams. The crack was found to be stable.

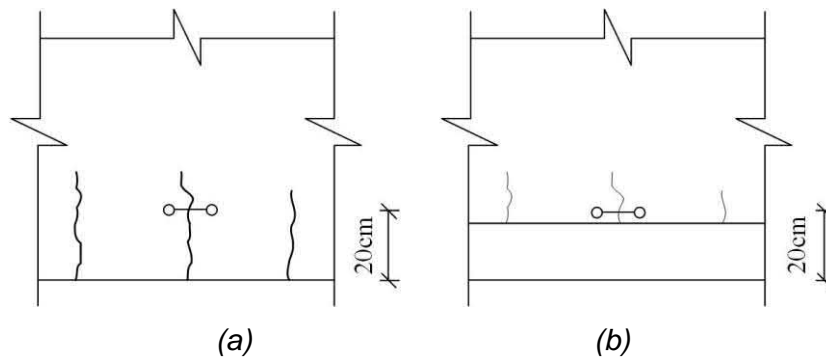


Fig. 16 - The monitoring location of the crack in the “before” and “after” strengthening;

a) “before” strengthening, b) “after” strengthening

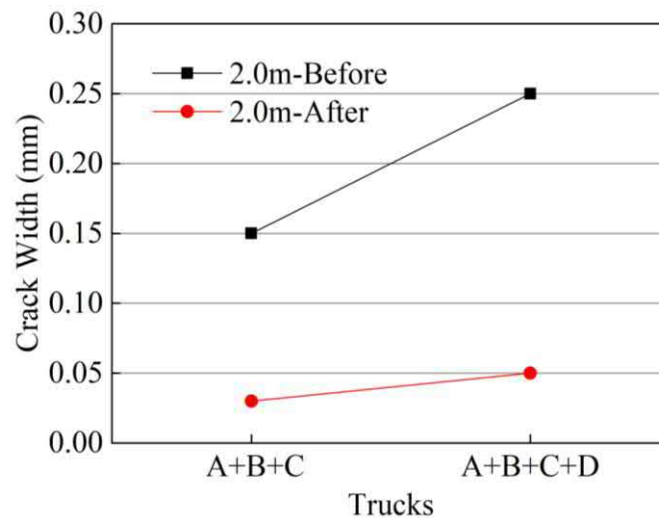


Fig. 17 - The crack width in the “before” and “after” strengthening

LIVE-LOAD DISTRIBUTION FACTORS

The live load distribution factors (DFs) is by definition the fraction of the total load that anyone of the T-beam receives. The information on live-load DFs for a given bridge type and geometry can be obtained through field tests [20-22]. By measuring the deflection of every beam in the bridge under static loading, the DFs can be determined. As the geometric size of all the T-beams is almost the same, the stiffness of every beam can be considered as having an equal value. The DF_s can be determined from field measurements using the following.

$$DF_n = f_n / \sum f_n \tag{8}$$

Where f_n is the maximum static deflection in the nth girder, and $n=1\sim5$.

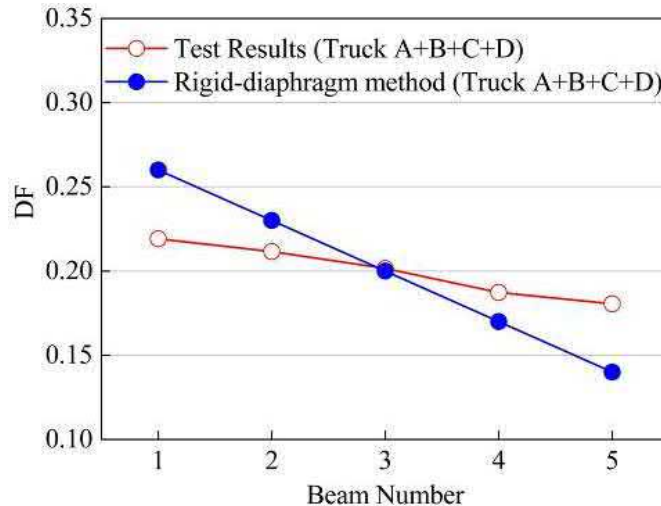


Fig. 18 - Live -load DFs calculated from test results and Rigid-diaphragm method for the case of all four trucks (Trucks A+B+C+D) parked at 2.0-m position

The deflection measurements shown in Figure 15 for the case of all four trucks (Trucks A+B+C+D) parked at 2.0-m position were used to determine the live-load DFs according to Equation. (8). From the rigid-diaphragm method [23], live-load DFs that can be compared with the measured DFs were provided as shown in Figure 18. The 1th girder (beam 1) deflected by 8.6mm for four trucks (Trucks A+B+C+D) parked at 2.0-m position. The total deflection of all the girders was 39.4mm for a live-load DF of about 8.6/39.4 or 0.22. The live-load DF is 0.26 using the rigid-diaphragm method. The live-load DFs depend on girder spacing, span, girder bending stiffness and girder torsional stiffness. The 2th girder (beam 2) deflected by 8.3mm for the four trucks (Truck A+B+C+D) parked at 2.0-m position. The total deflection of all the girders was 39.4mm for a live-load DF of about 8.3/39.4 or 0.21. The live-load DF is 0.23 using the rigid-diaphragm method. Thus, the rigid-diaphragm method is valid to evaluate the DFs of the T-shaped beam bridge after strengthening.

CONCLUSION

An innovative strengthening technique was discussed to improve the flexural strength of a 20-year-old RC T-beam bridge with prestressed steel wire ropes in this paper. The detailed construction process was described. Load tests were conducted before and after installing the prestressed steel wire ropes to evaluate the effectiveness of the strengthening method. Based on the details presented in this paper and the results of the field-loading test, the following conclusions can be drawn:

The flexural strength of the RC T-beam bridge strengthened with steel wire ropes can be determined based on strain compatibility, force equilibrium, and the controlling modes of failure. The T-beam bridge strengthened with steel wire ropes is governed by the failure of concrete crushing.

The steel wire ropes strengthening increased the flexural capacity of the superstructure, and the deflection and crack width for girders were decreased in different degrees. Static load test

showed an initial good performance of the steel wire ropes strengthened spans. The long-term performance will be monitored throughout three years with annual load tests.

The steel wire rope strain deformation complies with strain coordination under the static load. Location of the neutral axis was observed to have migrated down after the steel wire ropes were installed.

The transverse connection between beams was proven by the diaphragm and the bridge deck. The live-load DFs of the strengthened bridge calculated by experimental results were in good agreement with the rigid-diaphragm method.

REFERENCES

- [1] Jones R., Swamy R. N., Charif A., 1988. Plate separation and anchorage of reinforced concrete beams strengthened by epoxy-bonded steel plate. *Structrue Engineer*, vol. 66, no. 5: 85-94
- [2] Sabahattin A., Ilker K., Bengi A., Sinan K., 2013. Strengthening and repair of reinforced concrete beams using external steel plates. *Journal of Structural Engineering*, vol. 139, no. 6: 929-939
- [3] Dae G. P., Byung H. O., Jae Y. C., 2003. Static and fatigue behavior of reinforced concrete beams strengthened with steel plates for flexure. *Journal of Structural Engineering*, vol. 129, no. 4: 527-535
- [4] Nabil F. G., Sayed G. A., Soliman A. K., Saleh K. R., 1999. Strengthening Reinforced Concrete Beams Using Fiber Reinforced Polymer (FRP) Laminates. *Aci Structural Journal*, vol. 188, no. 8: 865-875
- [5] Bakis C., 2002. Fiber Reinforced Polymer Composites for Construction—State-of-the-Art Review." *Journal of Composites for Construction*, vol.6, no. 2: 73-87
- [6] Mohammed A. S., Tarek M. K., Walid N.M., 2016. Analysis of RC Continuous Beams Strengthened with FRP Plates: A Finite Element Model. *Civil Engineering Journal*, vol. 2, no. 11: 576-589
- [7] Wojciech L., Ernest K., 2006. Behavior of composite beams prestressed with external tendons: Experimental study. *Journal of Constructional Steel Research*, vol. 62, no. 12: 1353-1366
- [8] Kiang H. T., Farooq M. A. A., Chee K. N., 2001. Behavior of simple-span reinforced concrete beams locally strengthened with external tendons. *Aci Structural Journal*, vol. 98, no. 2: 174-183
- [9] Keun-Hyeok Y., Dae-Bong J., Jae-Il S., Jae-Hoon K., 2012. In-plane seismic performance of unreinforced masonry walls strengthened with unbonded prestressed wire rope units. *Engineering Structures*, vol. 45: 449–459
- [10] Liao Z., Zhang C., Jia T., Wang H., 2017. Experimental investigation on seismic behavior of shear wall retrofitted with pre-stressed steel wire mesh and polymer mortar. *Journal of Building Structures*, vol. 38, no. 6: 70-77
- [11] Guo J., Deng Z., Lin J., Lu H., 2014. Experimental study on seismic behaviour of RC columns strengthened with prestressed high strength steel wire mesh. *Journal of Building Structures*, vol. 35, no. 2: 128-136.
- [12] Guo J., Deng Z., Lin J., Lu H., 2014. Experimental study on seismic behaviour of RC columns strengthened with prestressed high strength steel wire mesh. *Journal of Jilin University*, vol. 44, no. 4
- [13] Gang W., Zhishen W., Yang W., Jianbiao J., and Yi C., 2012. Flexural strengthening of RC beams using distributed prestressed high strength steel wire rope: theoretical analysis. *Structural and. Infrastructure Engineering*, vol. 10, no. 2: 160-171
- [14] Gang W., Jianbiao J., Wu Z. S., Zhang M., 2010. Experimental study of RC beams strengthened with distributed prestressed high-strength steel wire rope. *Magazine of concrete research*, vol. 62, no. 4: 253-265
- [15] Zhang Y., Xu S., Yao X., 2010. Theoretical Analysis and Experiment on Flexural Strengthening Behaviors of Prestressed High-strength Steel Wire ropes and Polymer Mortar. *China Journal of Highway and Transport*, vol. 30, no. 6: 239-248
- [16] Ministry of Communications of China, 1985. Design Code of Highway Reinforced Concrete and Prestressed Concrete Bridge (JTJ023-85). China Communication Press: Beijing.

- [17] Ministry of Communications of China, 2010. Design Code of Concrete Structures (GB50010). China Building Industry Press: Beijing.
- [18] Yail J. K., Mark G., Garth J. F., 2008. Repair of Bridge Girder Damaged by Impact Loads with Prestressed CFRP Sheets. Journal of Bridge Engineering, vol. 13, no. 1: 15-23
- [19] Hamdy M. E. A., Ahmed M. A., Salah E. F. T., 2012. Behavior of Strengthened Composite Castellated Beams Pre-stressed with External Bars: Experimental Study. Arabian Journal for Science and Engineering, vol. 37, no. 6 : 1521-1534
- [20] Junsik E., Andrzej S. N., 2001. Live Load Distribution for Steel Girder Bridges. Journal of bridge Engineering, vol. 6, no. 6: 489-497
- [21] Janusz, Holowaty, 2013. Assessment of Numerical Models for Live Load Distribution in a Road Slab Bridge. Computer Technology and Application, vol. 4, : 591-598
- [22] Michael S., Jeffrey A. L., 2001. Response of Prestressed Concrete I-Girder Bridges to Live Load. Journal of bridge engineering, vol. 6, no.1: 1-8
- [23] Ministry of Communications of China, 2015. General Specification for Highway Bridge and Culvert Design (JTG D60). China Communication Press: Beijing.

APPLICATION OF DEPTH-FIRST SEARCH METHOD IN FINDING RECIRCULATION IN MINE VENTILATION SYSTEM

Huaming An¹, Jianjun Shi^{1,2}, Xuguang Wang³ and Lixing Lyu⁴*

1. *School of Civil & Resource Engineering, University of Science & Technology Beijing, China.*
2. *Key Laboratory of High-efficient Mining and safety of Metal Mines (Ministry of Education of China), University of Science and Technology Beijing, Beijing 100083, China; beikeda@hotmail.com*
3. *Beijing General Research Institute of Mining & Metallurgy, China.*
4. *School of Civil & resource Engineering, Kunming University of Science and Technology, Kunming, China*

ABSTRACT

Recirculation of airflows in a mine ventilation system can cause concentration of contaminated air which results in an unsafe working environment for people working in an underground mine. Due to the difficulty in finding the recirculation of airflows in complicated mine ventilation system, depth-first search method is proposed to find the recirculation of airflows in complicated mine ventilation systems. The searching procedure of a simply depth-first search method is introduced briefly. Then the depth-first search method is modified for searching recirculation of airflows in complicated mine ventilation systems. The proposed method is implemented through MATLAB in the form of storing ventilation information in a matrix. A few recirculation of airflows are found and are confirmed by the mine ventilation simulation result. It is concluded that the proposed method is a valuable tool in finding recirculation of airflows in a complicated mine ventilation system.

KEYWORDS

Mine ventilation, Recirculation, Booster fan, Depth-first search method

INTRODUCTION

Nowadays, booster fans are widely employed in an underground mine, which help to balance the air pressure and quantity distribution to provide a suitable working environment for human being [1, 2]. However, booster fans installed underground can cause recirculation of airflow in the mine ventilation system. Recirculation in a mine ventilation system makes it possible to induce concentration of contaminated air, including dust and gas, which make the people who work underground taking a risk. Therefore, it is imperative to find the recirculation of airflows in a mine ventilation system and to control them. Figure 1 shows an example of recirculation of airflow in an underground mine. All the roads of the mine are depicted in the figure 1 and the red arrows represent the directions of the airflows. A fan is installed underground as indicated by the green arrow. As can be seen, there is a recirculation of airflow as indicated in the white box. The air in the white area is circulating in a few connected roads instead of all the air flowing to the return roads, which significantly reduces the volumetric efficiency. It is easy to find the recirculation of airflows in a simple ventilation system as shown in figure 1 while it is difficult to find the

recirculation in a complicated ventilation system which has dozens of booster fans installed underground and hundreds or thousands of roads.

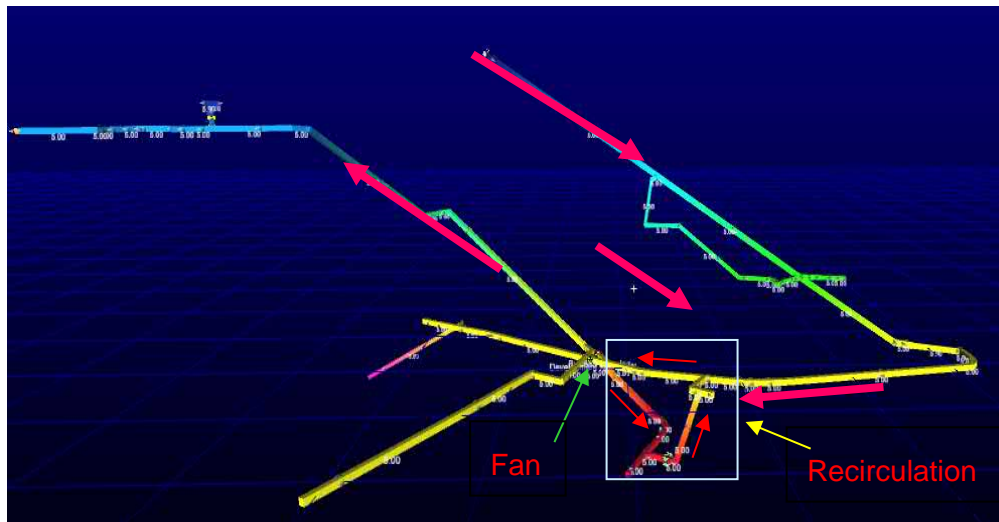


Fig. 1 - An example of recirculation airflow in an underground mine

In terms of mine ventilation, many numerical or experimental researches have been done [3-7]. However, as for the recirculation of airflows, rare study has been focused on it. With the fast development of the computer technology, researchers have begun to study the recirculation of airflows on basis of computer technology [8]. Since it is of great importance to eliminate the recirculation of airflows and it is difficult to find the recirculation of airflows in a complicated ventilation systems, this paper provides a mathematical method, i.e. depth-first search method, for finding the recirculation in a complicated mine ventilation system and applies the method in a copper mine to search the recirculation of airflows.

DEPTH-FIRST SEARCH METHOD

In this section, the simple depth-first search method is introduced first. Then the simple depth-first search method is modified for suitable finding the recirculation of airflows in a complicated mine ventilation system.

Simple Depth-First Search Method

Depth-first method has been applied in many fields [9-14]. Since the simple depth-first method had been introduced in detail by Rao and Kumar (1987) [11], the method herein is introduced briefly and the modified depth-first search method for finding the recirculation of airflows in a complicated mine ventilation system is introduced in detail.

Depth-first search method is used to find a path in a directed graph from an initial node to a goal node [11]. The search begins by expanding the initial node, i.e. by generating its successors, and ends when a goal node is found [11]. Consequently, the solution path is constructed by following the path from the initial node to the goal node. Figure 2 illustrates a step-tree generated according to the depth-first method. In figure 2, the numbers in the boxes indicate the order of the boxes generated while the expanding order of the boxes follow the alphabet order as shown in the boxes. As can be seen in figure 2, the first box, i.e. A1, on the top is the initial node which generated three nodes, i.e. 2B, 3I and 4L. Then 2B expands and generates two boxes, 5C and 6D.

After that, the tree generates and expands following the previous rules. More details can be found in the reference [15].

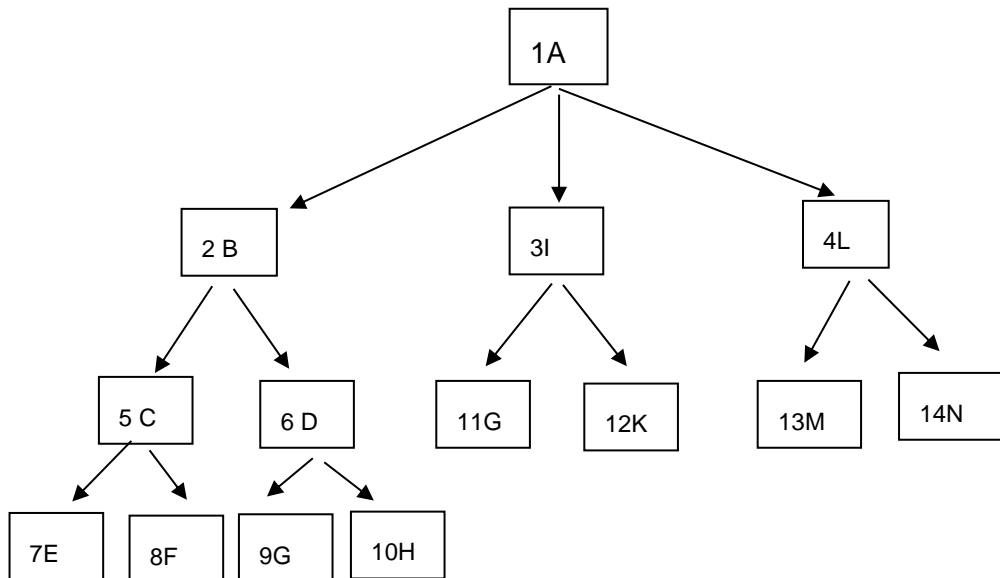


Fig. 2 - Example of Depth-first search method producer. Each number in the box represents the order of generation while the order of expansion follows the alphabet order in the box. After Rao and Kumar (1987)

Modified Depth-First Search Method for finding Recirculation in Mine Ventilation System

The simple depth-first search method mentioned above is modified for searching recirculation of airflows in complicated mine ventilation system. The basis searching rules follow simple depth-first search method while a few new rules are added for searching.

The procedure for the modified depth-first method is as follows.

- 1) The initial node is put in a stack first.
- 2) The search begins by searching adjacent nodes of the initial node along the arrow directions.
- 3) The search will visit the searched adjacent node with smaller number if there are more than one adjacent nodes and put the visited number in the stack.
- 4) The search repeats the rule 2 and 3 until the initial node is visited again. Then the visited path represents one recirculation.
- 5) The search will pop backwards to find a visited node which has unvisited adjacent node.
- 6) The search will repeat step 2 to 5 until all the recirculation paths beginning from the initial node are found.

Figure 3 shows the initial state of a network. The search will start from node 1. Figure 3 represents part of ventilation network in which all the roads are connected. It should be noted that,

in Figure 3, the node 1 and node 1` represent the same node. We put the initial node in two circles for conveniently drawing and explaining the searching procedure in the network.

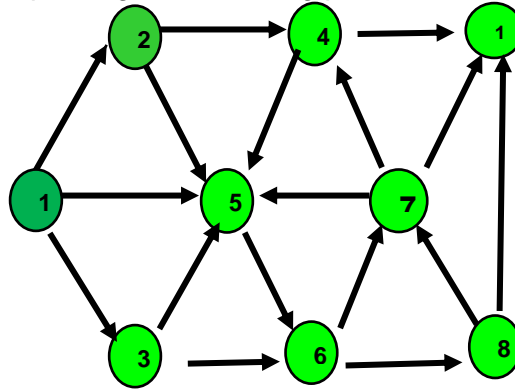
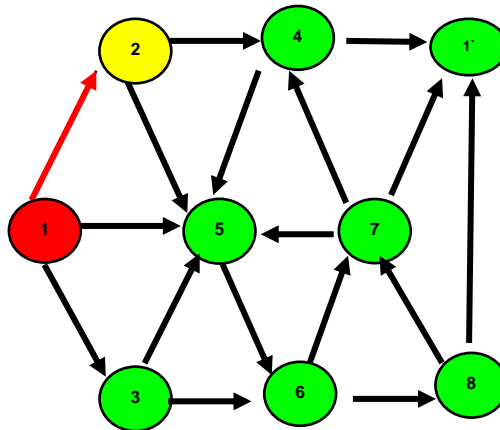
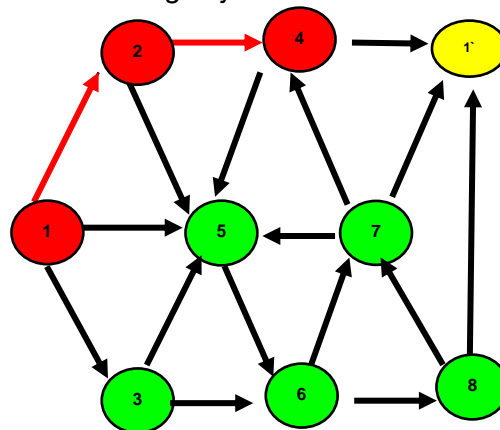


Fig. 3 - Initial state of a network



Stack	1	2							
-------	---	---	--	--	--	--	--	--	--

Fig. 4 - Searching adjacent nodes of the initial node



Stack	1	2	4	1`					
-------	---	---	---	----	--	--	--	--	--

Fig 5 - First recirculation in the network

As illustrated in Figure 4, the initial node, i.e. node 1, is put into the stack first according to rule 1. Then, the depth-first search method begins to search the adjacent nodes of node 1 along the arrow direction, i.e. the direction of airflow in a ventilation system, according to rule 2. Two nodes are found, i.e. node 1 and node 3.

The node 2 is visited and put the number into the stack according to rule 3, i.e. visiting the smaller node with smaller number. After that the node 1 and node 2 are marked using red color and yellow color, respectively. In this paper, the red color represents initial node or visited nodes while the yellow color represents the current visiting nodes. Additionally, the green color indicates unvisited nodes.

Figure 5 shows the first recirculation found in the network. After node 2 is visited, the search then continues to find the adjacent nodes of node 2, i.e. node 4 and node 5. Since the search will choose the node with smaller number to visit first, the node 4 is visited put into the stack. The rule 2 and rule 3 are repeated until the node 1` is visited. In the next step, the node 1`, i.e. node 1. Thus a recirculation of airflow is found and the numbers are put into the stack.

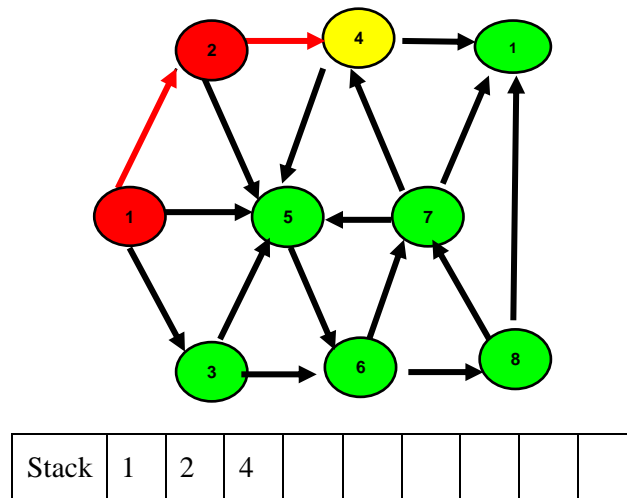


Fig. 6 - Popping back to node 4

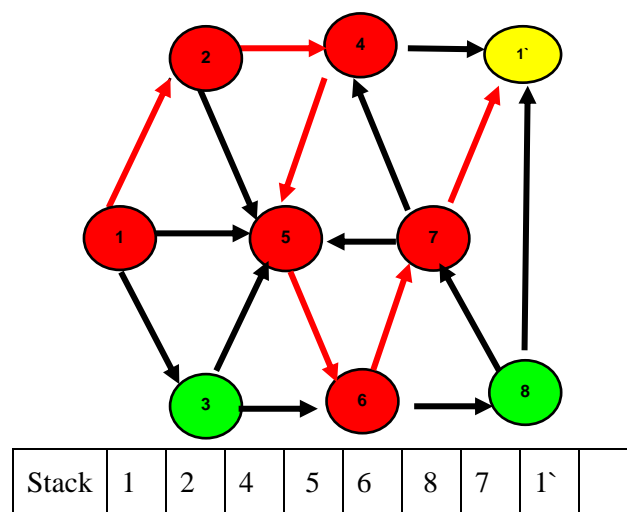


Fig. 7 - Second recirculation in the network

Since the recirculation of air flow is found, the search will pop backwards to find a visited node that has unvisited adjacent nodes. As shown in Figure 6, the search pop back to node 4 and finds that there are two adjacent nodes, i.e. node 5 and node 7, which are not visited yet.

Then the search continues to travel from node 4 as shown in Figure 7. The search follows rule 2, 3 and 4. Finally, the second recirculation of airflow is found and the nodes of the recirculation are put into the stack.

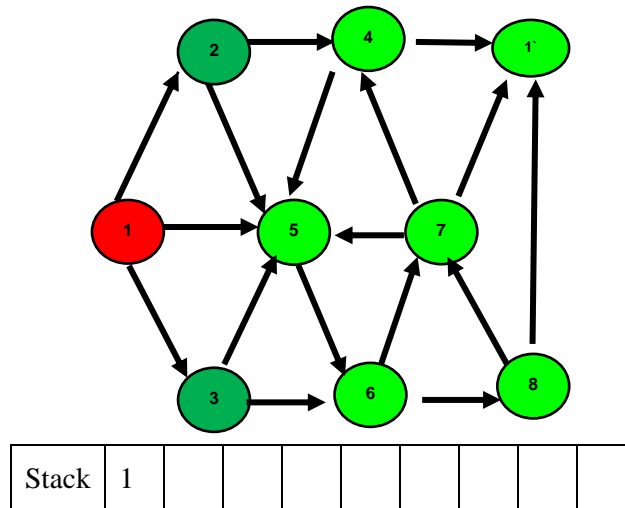


Fig. 8 - Popping back to the initial node

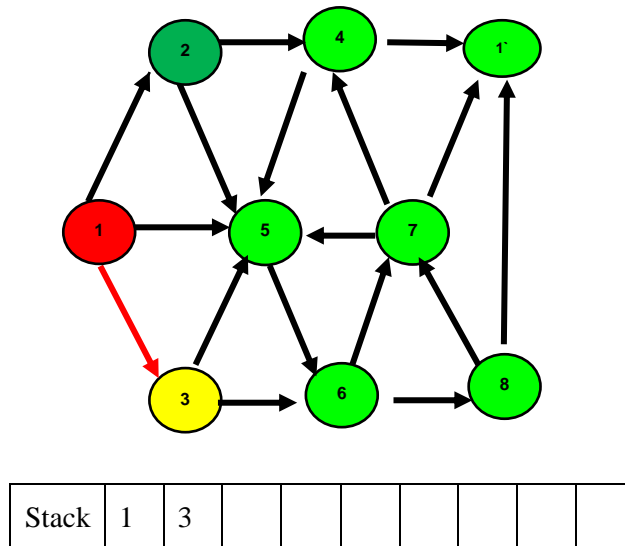


Fig. 9 - Search from the initial node again

According to rule 5, the search will pop backwards and find that only the initial node has unvisited node. Therefore, the search continues to go from node 1 (Figure 8). The node 3 is visited. Since there are not unvisited adjacent nodes for node 3, the search will pop back again. The search pops back to node 1 and the node 1 does not have any unvisited nodes (Figure 9). Therefore, the search has finished and two recirculation of airflows are found.

APPLICATION OF THE MODIFIED METHOD IN FINDING THE RECIRCULATION IN VENTILATION SYSTEM

In this section, the proposed modified depth-first search method is applied in a complicated copper mine ventilation system for finding recirculation of airflows near at the booster fan areas.

All the rules mentioned in Section 2 are made for suitable finding recirculation in ventilation system. The initial node in ventilation system represents the place where the booster fan is. Since the recirculation of airflows is mainly caused by the booster fans installed in underground mine, we mainly focus on finding recirculation of airflows around those areas where booster fans are installed. In section 2, the node with smaller number has the priority to be visited. This is because in our ventilation system the air flow from the ends with smaller number to the ends with bigger number. In another word, the search will follow the directions of airflow. In Section 2, when the initial node is visited again, a recirculation of airflow is found. This means the air flow from the intake air road and return to the intake road again instead of passing the return road to the outside. Then, it represents a recirculation of airflow.

According to rules of the depth-first method, application of the method needs to know the airflows of the ventilation system, the position of booster fans and number of the two ends of roads. With the development of the computer technology, a lot of of mine ventilation software are available at this moment. In our research, WENTSIM [16] is adopted for simulating the ventilation system and adding numbers to the two ends of each road.

The implementation of the depth-first method is then use the MATLAB [17] software, which is good at storing matrixes. All the roads will be shown in figure induced by the MATLAB software. The recirculation of airflows in the ventilation system will be marked as red color.

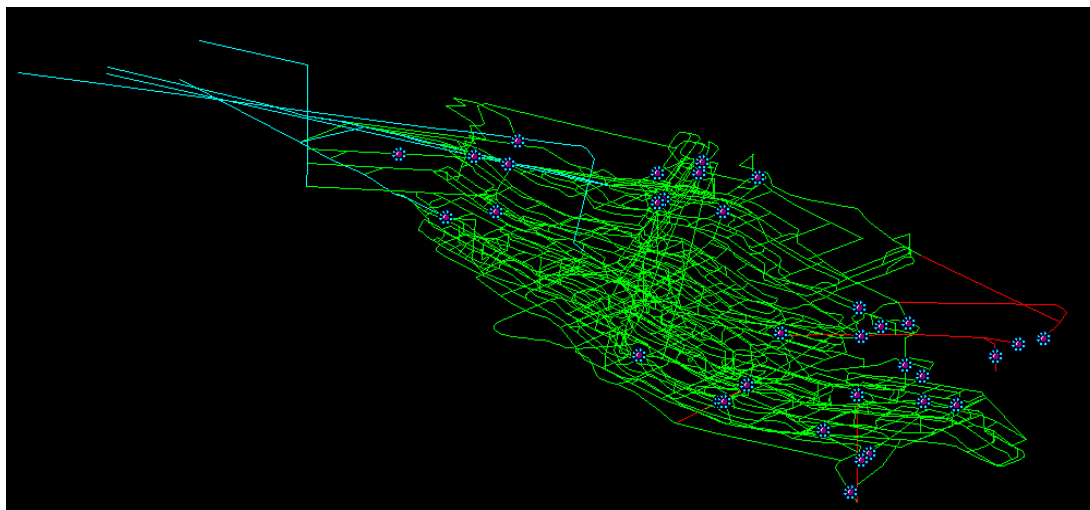


Fig. 10 - Mine ventilation system of a copper mine

Figure 10 shows a copper mine ventilation system. The blue lines represent the intake air roads while the red lines indicate the return road for the contaminated air. The fan is denoted by the fan symbols. The copper mine currently has thousands of roads and 38 fans installed underground.

The simulated results of mine ventilation system, i.e. the airflow directions and the denoted numbers on two ends of each roads are stored in the MATLAB in the form of matrix. Then the depth-first search begin to search from the initial nodes, i.e. the position of a booster fan, and follows the directions of airflows, i.e. from smaller number to big number. All the nodes which

indicate the booster fan positions are used as the initial nodes for searching the recirculation of airflows at the fan areas.

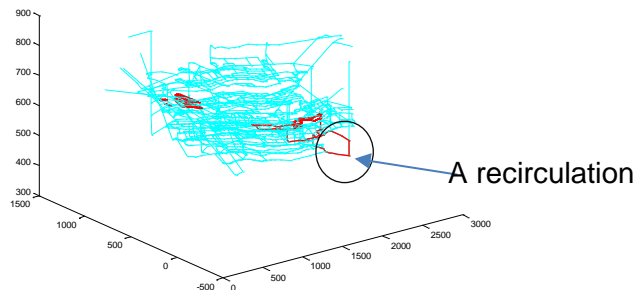


Fig. 11 - Recirculations marked in red colour in a ventilations systém

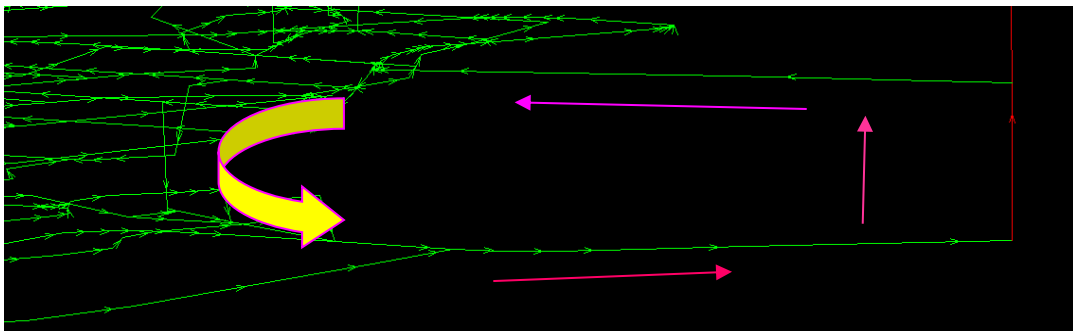


Figure 12. Corresponding recirculation circled in Figure 11

Figure 11 illustrates the searched results in which the recirculation airflows are denoted using red color. It can be seen that a few recirculation of air flow are found. The recirculation of airflow at the circled area is compared with the ventilation simulation result in Figure 10. Figure 12 shows the corresponding recirculation circled in Figure 11. It is confirmed that the depth-first search method can find the recirculation of air flows. Other recirculation of airflows illustrated in Figure 11 is also compared with the mine simulation results and all the recirculation of airflows found by the depth-first method are correct.

DISCUSSION

The implementation of the depth-first search method for finding recirculation of airflows in mine ventilation system in this research is still a little complicated. The ventilation system should be simulated for getting all the airflows information first. The simulated airflows information is then stored in a matrix. Finally, the depth-first search method is used to search recirculation of airflows in the network stored in the matrix.

More work need to be done to simplify this process. The depth-first search method could be combined in the mine simulation software. Thus, while simulating the ventilation system, the recirculation of airflows is also denoted on the ventilation network.

Although recirculation of airflows mainly occur at the booster fan areas, there are also recirculation of airflows in other places. Therefore, it is necessary to study a method to find those recirculation of airflows.

CONCLUSION

Since the recirculation of airflow in a complicated mine ventilation system makes the contaminated air concentrated and people who work in such an environment take a risk, depth-first method is introduced to find the recirculation airflows in a complicated mine ventilation system for controlling or eliminating the recirculation of airflows. The simple depth-first method is introduced first. Then the modified depth-first method for finding recirculation of airflows is then introduced in detail. The proposed method is implemented through MATLAB by storing the ventilation simulation results in the form of matrix. After that, a copper mine ventilation system is introduced and the proposed method is applied to find recirculation of airflows in this complicated copper mine ventilation system. A few recirculation of airflows are found and compared with the simulation results. The compared results show that the searched recirculation of airflows by the depth-first search method agrees with the simulation results.

It is concluded that the depth-first search method is able to find recirculation in complicated mine ventilation system. Although depth-first search method shows its capability in finding recirculation in complicated copper mine, more work still need to done to simplify the application.

REFERENCES

- [1] Calizaya, F., M. Stephens, and S. Gillies.2010.Utilization of booster fans in underground coal mines. in: SME Annual Meeting and Exhibit.
- [2] Prosser, B., J. Stinnette, and J. Paredes.2002.Ventilation optimization at the La Camorra mine. in: Proceedings of the North American/Ninth US Mine Ventilation Symposium, Kingston.57-63.
- [3] Allwine, K.J. and C.D. Whiteman. 1994.Single-station integral measures of atmospheric stagnation, recirculation and ventilation. Atmospheric Environment,Vol.4:713-721.
- [4] Aminossadati, S.M. and K. Hooman.2008.Numerical simulation of ventilation air flow in underground mine workings. in: 12th US/North American Mine Ventilation Symposium 2008. The University of Nevada, Reno,253-259.
- [5] Su, S., H. Chen, P. Teakle, and S. Xue. 2008.Characteristics of coal mine ventilation air flows. Journal of environmental management,Vol.1:44-62.
- [6] Cheng, L., T. Ueng, and C.-W. Liu. 2001.Simulation of ventilation and fire in the underground facilities. Fire Safety Journal,Vol.6:597-619.
- [7] Gillies, A., A. Wala, and H.W. Wu.2005.Simulation of the effects of inertisation of fires on mine ventilation systems. in: Proceedings, Eighth International Mine Ventilation Congress.
- [8] Wempen, J.M., Characterization of air recirculation in multiple fan ventilation systems. 2012, The University of Utah.
- [9] Bonet, B. and H. Geffner.2006.Learning depth-first search: A unified approach to heuristic search in deterministic and non-deterministic settings, and its application to MDPs. in: ICAPS.142-151.
- [10] Korf, R.E. 1985.Depth-first iterative-deepening: An optimal admissible tree search. Artificial intelligence,Vol.1:97-109.
- [11] Rao, V.N. and V. Kumar. 1987.Parallel depth first search. Part I. implementation. International Journal of Parallel Programming,Vol.6:479-499.

- [12] Tarjan, R. 1972. Depth-first search and linear graph algorithms. SIAM journal on computing, Vol.2:146-160.
- [13] Tarjan, R.E. 1976. Edge-disjoint spanning trees and depth-first search. Acta Informatica, Vol.2:171-185.
- [14] Huaming, A. and L. Bin. 2011. Positioning Mine Ventilation Recirculation Winds Based on the Depth-First Search Method. Procedia Engineering, Vol.400-403.
- [15] Heuristics, J.P., Intelligent Search Strategies for Computer Problem Solving Addison. 1984, Wesley Publishing Company.
- [16] LUO, Z.-j. and C.-I. YANG. 2009. The Application of Ventsim Software in Mine Ventilation [J]. Nonferrous Metals Engineering & Research, Vol.3:7-9.
- [17] Redfern, D. and C. Campbell. 2012. The MATLAB® 5 Handbook, Springer Science & Business Media.

COMPARISON OF SELECTED PHYSICAL PROPERTIES OF TESTED NANOSUSPENSIONS – THE RESULTS OF THE EXPERIMENTAL RESEARCH OF THE DEGREE OF SEDIMENTATION AND THE DEPTH OF PENETRATION IN REFERENCE MATERIALS IN LABORATORY CONDITIONS

Klára Kroftová¹, Markéta Šmidtová², Ivo Kuřitka³ a David Škoda³

1. CTU in Prague, Faculty of Civil Engineering, Department of Architecture, Prague, Thákurova 7, Czech Republic; klara.kroftova@seznam.cz
2. CTU in Prague, Faculty of Civil Engineering, Department of Building Structures, Prague, Thákurova 7, Czech Republic; smidtmar@fsv.cvut.cz
3. Polymer Centre Zlín, Faculty of Technology, Zlín, třída Tomáše Bati 5678, Czech Republic; kuritka@utb.cz, diskoda@utb.cz

ABSTRACT

Between used and already verified technologies for the reinforcement of plasters mainly include nanosuspension containing nanoparticles of calcium hydroxide and nanomaterials based on magnesium hydroxide and barium carbonate [1]. Individual lime nanosuspension, which consists of nanoparticles of calcium hydroxide, are dispersed in an alcoholic environment and they differ from each concentration and type of alcohol. When the material is cured, carbonatation occurs, as well as in the case of fresh plaster, where the calcium hydroxide reacts with atmospheric carbon dioxide to produce calcium carbonate. Due to the deposition of calcium carbonate in the damaged material, occurs re-strengthened ties and its hardening. The undoubted advantage of the consolidation of plaster using nanolime is the low number of impregnation cycles, where after a few applications nanosuspension occurs to the reinforcement of degraded material.

KEYWORDS

Nanolime, nanosuspension, plaster, consolidation, sedimentation, depth of penetration

INTRODUCTION

The success of the consolidation process using the "nanolime" is influenced by the mineralogical and chemical composition of the treated material, characteristics of the porous system, the structure of the surface, degree of reinforcement before treatment, the properties of the active substance of the strengthening agent (the size of the ions and particles, chemical composition, concentration, rate of drying and hardening, etc.) and last but not least, also the temperature-humidity conditions during application. At sufficiently low surface tension of the lime nanosuspension is to ensure optimum wetting, which is responsible for the depth of penetration of the dispersions in the porous structure of the plaster [2].

Until the recent past, it was possible nanoparticles of calcium hydroxide obtained either by the hydrolysis of calcium hydride (CaH_2) under specific experimental conditions or by reactions of the calcium oxide CaO , or of calcium hydride CaH_2 , with water in an organic environment, in the presence of surfactants [3]. A newer option, how to synthesize crystalline nanoparticles of calcium hydroxide, is the reaction of sodium hydroxide NaOH and calcium chloride CaCl_2 . Calcium chloride CaCl_2 is dropwise added to an aqueous solution at a temperature of 90 °C and the reaction creates

calcium hydroxide $\text{Ca}(\text{OH})_2$ and sodium chloride NaCl , which is from the suspension subsequently removed. In the last stage of production are particles of lime broken in the ball mill to a particle size of several μm to nm and the resulting clusters of particles are scattered using the ultrasound [4]. Another known manufacturing process involves the reaction of the metal calcium with water in an alcoholic medium [5].

The stability of the produced nanosuspension is directly proportional to the particle size – the smaller the particles, the lower stability and vice versa. Kinetically stable dispersions can be obtained with aliphatic alcohols with short chain. The advantage of these alcohols is that it quickly evaporates (the possibility of rapid repeat cycles) and in comparison with other solvents have low toxicity.

The size of the nanoparticles is in the lime nanosuspension usually varies in the range of 150 – 300 nm, which creates restrictions in relation to the size of the pores of the treated material. In the suspension there are also larger particles, which most often arise from accidental cluster of primary particles during the manufacture or subsequent storage. The viscosity and color of the suspension varies according to the concentration – the more concentrated the mixture is more viscous and usually whiter (or may have a pale ochre or grey, depending on the source material and method of production).

TESTED NANOSUSPENSIONS

In the framework of the research project NAKI nanosuspensions of $\text{Ca}(\text{OH})_2$ were produced from different precursors, which were subsequently modified and enriched by other components that were expected to have a positive potential for use in conservation. Production of nanosuspensions took place in close cooperation with the Center of Polymer System UTB in Zlín.

For the purposes of experimental tests were made 4 lime nanosuspensions [6]. Three samples were prepared by NaOH precipitation method (mark. CA3, CA5 and CA-Mg) and one sample (mark. CA4) by alkoxide hydrolysis, where

- a sample of CA3 was made from a portion of the CaCl_2 solution (the value of content of dry solid is 1,66 g),
- a sample of CA4 was made from a portion of the methoxide calcium $\text{Ca}(\text{OCH}_3)_2$ (the value of content of dry solid is 1,39 g),
- a sample CA5 was made from a portion of the acetate phosphate $\text{Ca}(\text{OCOCH}_3)_2 \cdot \text{H}_2\text{O}$ (the value of content of dry solid is 1,52 g),
- a sample of the CA-Mg was made from a portion of the acetate phosphate $\text{Ca}(\text{OCOCH}_3)_2 \cdot \text{H}_2\text{O}$ and acetate magnesium oxide, $\text{Mg}(\text{OCOCH}_3)_2 \cdot 4\text{H}_2\text{O}$ (the value of content of dry solid is 1,46 g).

Individual nanolime suspensions were prepared by dispersing 0.75 g of the products (CA3, CA4, CA5 and Ca-Mg) in 250 ml of isopropyl alcohol. To increase the homogeneity of the resulting dispersion was each suspension placed for 1 hour in an ultrasonic bath.

In order to compare the individual results of the tests and the effectiveness of the newly prepared nanosuspension was also prepared whitewash (mark. CA, the value of content of dry solid is 1,68 g) and used CaLoSiL®E5 (the value of content of dry solid is 0,814 g).

RATE OF SEDIMENTATION

The rate of sedimentation of dispersed particles is among the important criteria in the evaluation of the functionality nanosuspension. If the suspension is functional, “it must be able to suspend the dispersion phase after the period of the existence of the product and/or easily dispersed, if there was a sedimentation. To the stability of the dispersed phase contributes to a number of factors and these can be thermodynamic or kinetic in origin” [7].

Sedimentation means the movement of dispersed particles of the dispersion system, which in this case is induced by the action of gravitational forces. The gravitational force acts perpendicular to the surface of the earth and leads to the deposition of the particles on the bottom of the container. The rate and character of sedimentation are mainly affected by the size and shape of the particles, the viscosity of the dispersion environment, the ratio of the densities of the particles and the dispersion environment and the other. "Sedimentation occurs to the uneven distribution of concentration, which has resulted in the diffusion of dispersion of the particles. Diffusion the dispersion of particles will seek compensation concentration, will therefore work in the opposite direction than the sedimentation rate, i.e. the direction from the earth's surface. Diffusion and sedimentation operate in the opposite direction and leads to the creation of sedimentation equilibrium, when at any point of the system is the sedimentation rate equal to the rate of diffusion" [8].

For all the above-mentioned funds (nanosuspension CA3, CA4, CA5, CA-Mg, whitewash CA and CaLoSiL®E5) was monitored the rate and speed of settling of the solid ingredients in the mixture in order to determine and compare the degree of stability of the lime mixture.

In the laboratories of the FCE CTU in Prague were prepared lime nanosuspension, whitewash (mark. CA) and CaLoSiL®E5 (mark. CaL) cast into test tubes of a volume of 20 ml. Samples were left in a laboratory environment at a temperature of 24 °C. The sedimentation process was continuously monitored and after a period of 60 days recorded and photographically documented (Figure 1). Sedimentation rate is zdobrazena in a bar and a comparative chart (Chart 1, 2).

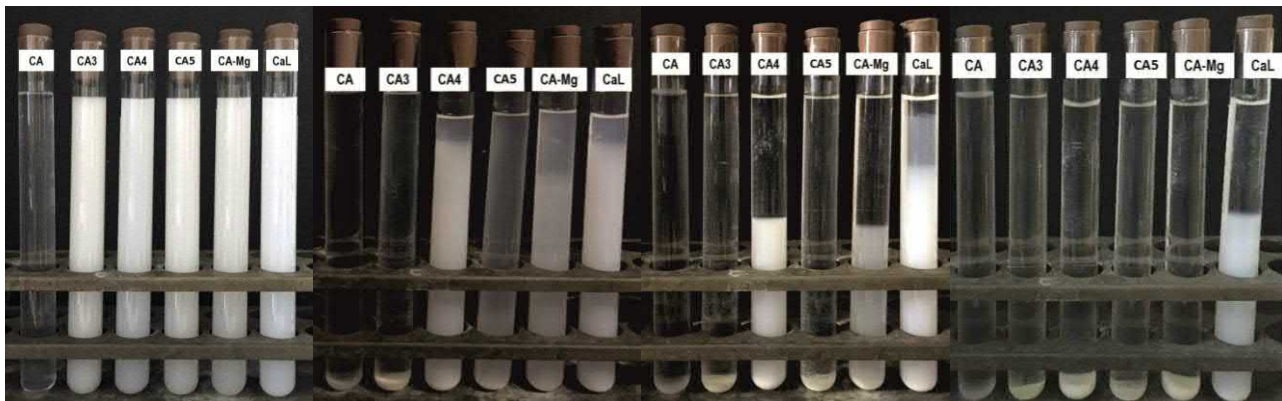


Fig. 1 - Photographic documentation of sedimentation nanosuspensions: the tube containing the studied lime nanosuspension. The documentation captures the sedimentation status: from the left after 24 hours, after 14 days, after 28 days and after 60 days. (Legend: CA = $\text{Ca}(\text{OH})_2$, CA3 = CaCl_2 , CA4 = $\text{Ca}(\text{OCH}_3)_2$, CA5 = $\text{Ca}(\text{OCOCH}_3)_2 \cdot \text{H}_2\text{O}$, CA-Mg = $\text{Ca}(\text{OCOCH}_3)_2 \cdot \text{H}_2\text{O}$ a $\text{Mg}(\text{OCOCH}_3)_2 \cdot 4\text{H}_2\text{O}$ a CaLoSiL®E5)

RESULTS OF LABORATORY RESEARCH OF THE RATE OF SEDIMENTATION

In the case of samples CA, CA3, CA5 and CA-Mg was possible to observe sedimentation of the particles almost immediately after their casting into tubes. In the case of samples CA4 and CaLoSiL®E5 occurred to the initiation of the deposition of the particles after 5 days of monitoring.

The fastest sedimentation took place in the case of the sample of whitewash, when its termination occurred already after 12 hours. Column of the settled particles reached a height of 5 mm.

The second fastest sedimentation was recorded for a sample of lime nanosuspension CA3, when the column of the settled particles reached after 3 days the height of 4 mm.

With a long interval of time – i.e. for 17 days, was terminated sedimentation of nanosuspension CA5, when the sedimentation column reached a height of 4 mm.

A sample of the CA-Mg ended the sedimentation after 38 days, the height of the sedimentation column reached a height of 5 mm.

The slowest sedimentation rate between the tested nanosuspensions, i.e. 43 days, was recorded for a sample of CA4. In terms of the amount of settled particles the results were the worst, the height of the sedimentation column was 8 mm.

Commercially available nanosuspension CaLoSiL®E5 did not shut the sedimentation even after 60 days, the height of the sedimentation column to 60th day was 4 mm. This positive result is probably influenced both by stabilizers, which suspension contains, and, secondly, the shape of the nanoparticles lime (hexagonal, very thin particles).

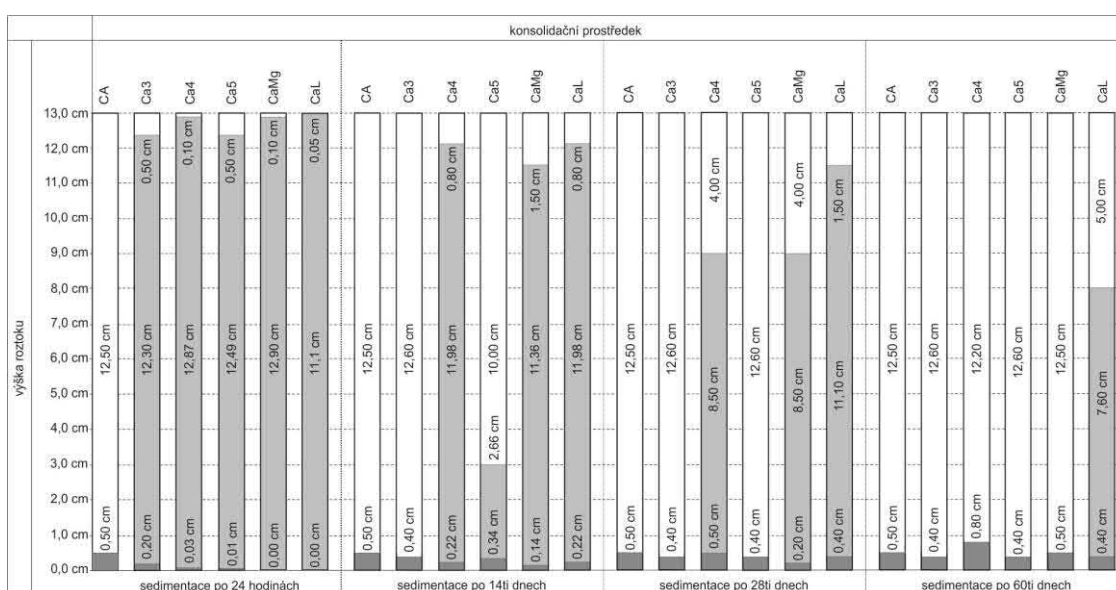


Chart 1 - The course of sedimentation of the samples CA, CA3, CA4, CA-Mg and CaL. The chart shows the progress of sedimentation from the left: after 24 hours after 14 days after 28 days and after 60 days (Legenda: CA = $\text{Ca}(\text{OH})_2$, CA3 = CaCl_2 , CA4 = $\text{Ca}(\text{OCH}_3)_2$, CA5 = $\text{Ca}(\text{OCOCH}_3)_2 \cdot \text{H}_2\text{O}$, CA-Mg = $\text{Ca}(\text{OCOCH}_3)_2 \cdot \text{H}_2\text{O}$ a $\text{Mg}(\text{OCOCH}_3)_2 \cdot 4\text{H}_2\text{O}$ a CaLoSiL®E5)

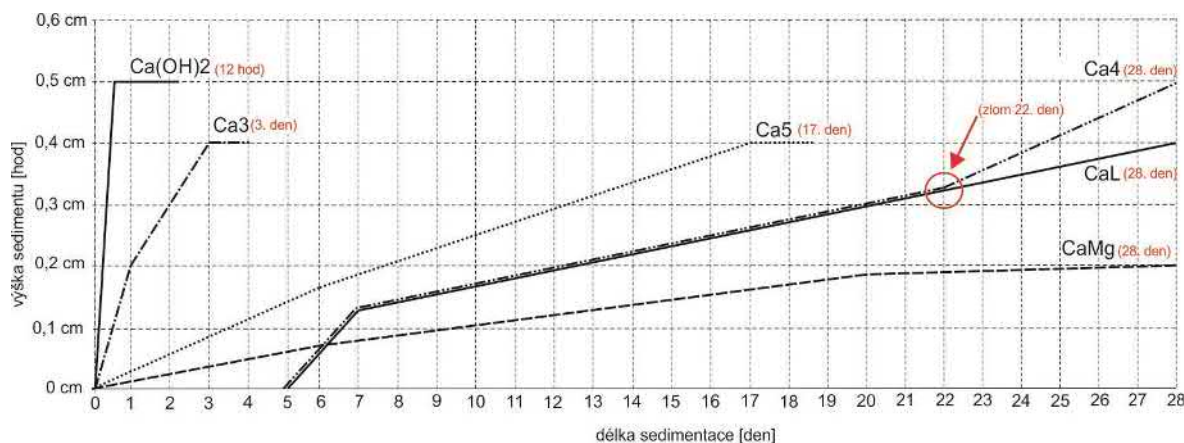


Chart 2 - Comparison of the sedimentation curves of the samples CA, CA3, CA4, CA-Mg and CaL. (Legend: CA = $\text{Ca}(\text{OH})_2$, CA3 = CaCl_2 , CA4 = $\text{Ca}(\text{OCH}_3)_2$, CA5 = $\text{Ca}(\text{OCOCH}_3)_2 \cdot \text{H}_2\text{O}$, CA-Mg = $\text{Ca}(\text{OCOCH}_3)_2 \cdot \text{H}_2\text{O}$ a $\text{Mg}(\text{OCOCH}_3)_2 \cdot 4\text{H}_2\text{O}$ a CaLoSiL®E5)

In the case of nanosuspension CA4 it is necessary to consider the positive postponement of the beginning of sedimentation for 5 days and the same course of sedimentation with commercial nanosuspension CaLoSiL®E5 (up to 22. day), which confirms approximately the same distribution of the particles in the range of 50 – 250 nm.

The best results in terms of the speed of sedimentation of solid particles of nanosuspension was achieved in the case of nanosuspension CA-Mg (38 days) and CA4 (43 days) and in terms of the height of the sedimentation column showed the best result, i.e. 4 mm, nanosuspension CA3 and CA5.

DEPTH OF PENETRATION OF NANOSUSPENSIONS

The ability of the plaster to absorb the consolidation substance, and the associated depth of its penetration, are among the basic evaluation parameters when assessing the assumption of the consolidation. Average values of penetration of the consolidants range from a few millimeters to several centimeters depending on the size and nature of the porous system and the size of the particles of the reinforcing substance [8].

For the experimental tests of verification of the depth of penetration of the tested device were used test prisms about the size of a 4 x 4 x 9 cm. The test samples were made in the laboratories of the FCE CTU in Prague. The composition of the mortar mixture was determined on the basis of the original recipe, which was detected by analysis of the removed plaster of historic building in-situ: 5 kg of dry hydrated lime, 12.5 kg of river sand (fraction 0 – 2 mm) and 3.5 l of water. Application of consolidation bars was held on the 24-month-old test samples.

The samples were put into Petri's dishes on filter paper and then was on the test samples applied consolidation substance (volume of 20 ml) using a dropper. Application of consolidants was carried out continuously only to the center of the top surface of the sample, when every other application has been made after absorbing the previous, and only to such extent, in order to avoid sagging of the solutions on the walls of the samples. The fastest absorption consolidants was recorded in the application of whitewash (mark. CA), and then the consolidation of suspensions in order CA5, CA3, CA-Mg, CA4 and CaLoSiL®E5 (mark. CAL).

After the application of consolidants were samples along their height resolved and the phenolphthalein indicator (1 % solution in ethanol) was applied on the entire surface of the cut by brush. To determine the depth of penetration was subsequently followed by a section of the sample by the change of the color caused by the phenolphthalein indicator (Figure 2) when the intense red - purple detected the non-carbonated calcium hydroxide, thus the depth of penetration of the consolidation agent.

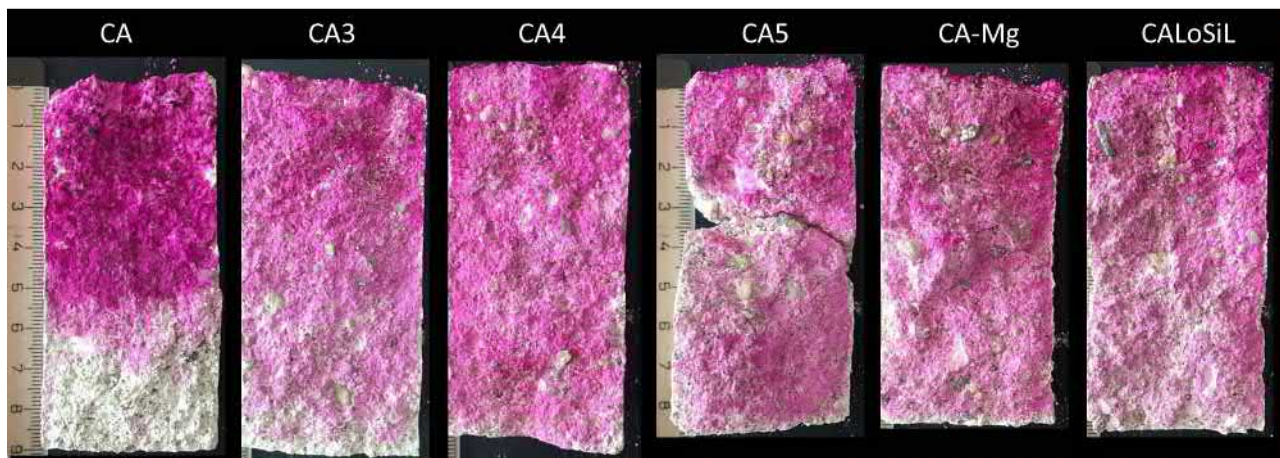


Fig. 2 - Samples of plasters treated with 20 ml of the consolidation agent: the depth of penetration of the consolidation agent was highlighted by phenolphthalein indicator in the section of the sample (Legend: CA = $\text{Ca}(\text{OH})_2$, CA3 = CaCl_2 , CA4 = $\text{Ca}(\text{OCH}_3)_2$, CA5 = $\text{Ca}(\text{OCOCH}_3)_2 \cdot \text{H}_2\text{O}$, CA-Mg = $\text{Ca}(\text{OCOCH}_3)_2 \cdot \text{H}_2\text{O}$ a $\text{Mg}(\text{OCOCH}_3)_2 \cdot 4\text{H}_2\text{O}$ a $\text{CaLoSiL}@\text{E5}$)

RESULTS OF LABORATORY RESEARCH OF THE DEPTH OF PENETRATION

The smallest achieved depth of penetration was measured in the case of whitewash (mark. CA), which was 52 mm. Stained by the phenolphthalein indicator (1 % solution in ethanol) shows a uniform saturation throughout the penetrated area, the boundary between penetrated and non-penetrated material is narrow (width 10 mm) and clearly defines the depth of penetration of the consolidation agent.

The phenolphthalein indicator applied to the sample with nanosuspension CA3 stained the cut to a depth of 75 mm, and the intensity of staining decreases after crossing the border 35 mm. This phenomenon of reducing the intensity of the discoloration in the cut below the boundary of 35 mm can be observed even in the application of nanosuspension CA5, Ca-Mg and CaLoSiL@E5. Below the threshold of 35 mm is noticeable a slight brighten of the indicator, which indicates penetration of a smaller amount of lime nanoparticles in greater depth.

The most intense discoloration of the sample in the entire area of the incision after application of the indicator was observed in the case of nanosuspension CA4. Visual evaluation of coloration of the upper surface of the test samples after the application of nanosuspensions indicates the deposition of lime and the unwanted emergence of whitish discoloration of the plaster. The possibility of removing white staining by application of H_2O was not part of the carried out laboratory tests of reason, to avoid affecting the penetration depth of nanosuspensions.

From the above results of the measurement of the depth of penetration is evident in the high rate of penetration of nanosuspensions into the plaster, where the best results were achieved by applying nanosuspension CA4.

CONCLUSION

The CA4 ($\text{Ca}(\text{OCH}_3)_2$), CA-Mg ($\text{Ca}(\text{OCOCH}_3)_2$, H_2O and $\text{Mg}(\text{OCOCH}_3)_2$, $4\text{H}_2\text{O}$) nanosuspension tests have comparable laboratory results in both sedimentation and penetration depths. In this work, different product properties were observed depending on the calcium precursor used.

The sedimentation results of tested CA4 and CA-Mg nanosuspensions demonstrate good stability and therefore long-term functionality. For these devices, laboratory tests have also proved good penetration of the suspension into sufficient depth of material to be treated.

Compared to a traditional lime-consolidating agent, CA4 and CA-Mg have a longer service life and greater penetration depth, indicating the suitability of these materials for use in reinforcing of historical plaster coats.

ACKNOWLEDGEMENTS

The results of the research carried out under this contribution have been achieved with the financial support of the NAKI II project DG16P02M005 "*Development and research of materials, processes and technologies for the restoration, preservation and consolidation of historical brick structures and surfaces and systems for the preventive protection of historical and listed buildings endangered by anthropogenic and natural hazards* (2016 - 2011, MK0 / DG) ".

REFERENCES

- [1] Chelazzi D., et al., 2012. Hydroxide nanoparticles for cultural heritage: Consolidation and protection of wall paintings and carbonate materials. *Journal of Colloid Interface Science*, vol. 392: 42-49
- [2] Machačko L., et al., 2012. Konsolidace historických omítkových vrstev v druhém NP ambitu bývalého kláštera Rosa Coeli v Dolních Kounicích pomocí vápenné nanosuspenze CaLoSiL. *Zprávy památkové péče*, roč. 72, č. 2: 122-128
- [3] Kociánová I., 2013. Restaurování centrálního výjevu na klenbě kaple sv. Isidora v Křenově, Litomyšl, Disertační práce, Univerzita Pardubice, Fakulta restaurování, Obor Restaurování a konzervace děl nástěnné malby, sochařských děl a povrchů architektury, Vedoucí práce Vojtěchovský J.,
- [4] Dei L., et al., 2001. Colloidal Particles of Ca(OH)₂: Properties and Applications to restoration of frescoes, Department of Chemistry and CSGI, University of Florence, Via Gino Capponi 9, 50121 Florence, Italy
- [5] Dunajská J., 2012. Test on sustainability of consolidation treatments with CaLoSiL® nanosuspensions on plaster reference samples, Diplomová práce, Univerzita Pardubice, Litomyšl, Fakulta restaurování, Litomyšl, Vedoucí práce Tišlová, R.
- [6] Kroftová K., et al. 2017. Synthesis nanolime suspensions and their potential use in cultural heritage preservation, konference EASEC-15, October 11-13, Xi'an, China
- [7] Bartovská L., Šišková M. 2005. Co je co v povrchové koloidní chemii, elektronická publikace. Dostupné online http://147.33.74.135/knihy/uid_es-001/ebook.copyright.htm
- [8] Drdácký M., Slížková Z., Valach J. 2015. Příspěvek technických věd k záchraně a restaurování památek, ÚTAM AV ČR, Praha, ISBN 978-80-86246-49-9

CALIBRATION OF VISSIM MODEL FOR MULTILANE HIGHWAYS USING SPEED FLOW CURVES

Seelam Srikanth, Arpan Mehar and Asish Parihar

Department of Civil engineering, National Institute of Technology, Warangal, India; e-mail: ssseelamsrikanth@gmail.com, arpanmehr400@gmail.com, civilaparihar@gmail.com

ABSTRACT

Traffic flow is a complex phenomenon that needs better understanding of basic concepts and methods for its analysis. As a solution to practical problems, computer simulation has been proved to be a powerful tool in replicating complex traffic systems which allows experimentation to the basic traffic flow system. Various methods are available in literature, some of the methods use statistical tools to verify the difference between simulated and actual outputs and some are based on optimization which tries to minimize the error. For the present work, suitable methodology is adopted for the calibration process. Field data is collected, statistical tests are performed. For the simulation, VISSIM microscopic simulation tool is used and data analysis is performed by considering individual parameters and performance measures like speed, volume and random seed number. Statistical tests have been performed to check the sensitivity of the different simulation parameters. Calibration is done using trial and error method and optimization is performed using solver function. The maximum simulated flow rate was found with default values as 4599 veh/hr, and with calibrated values is 5147 veh/hr which is close to the target capacity 4958 veh/hr as obtained using field composition. Calibrated values of CC0 and CC1 and CC2 parameters were found as most optimized values to achieve target capacity. Finally, validation of calibrated parameter was performed by using different section of a multilane highway.

KEYWORDS

Driver-behavior model, Speed-flow calibration, Capacity, VISSIM.

INTRODUCTION

In India, multilane highways are categorized as National highways or State highways, both have equal importance based on their purpose. Due to rapid increase in industrialization the importance of roads become most favourable topic for discussion as now it is contributing to economy of the country. India is a country with total of 2,56,749 km of highways including 92,851 of national highways and 1,63,898 of state highways as per 2011 census which is second highest in the world. With this much of network problems of traffic are increasing day by day, measures have been taken to control up maximum utilization of resources but still we are lacking as our traffic conditions are not same as in other countries. In India traffic is a mixed traffic as well as no particular lane behavior for highways, drivers want to get maximum speed so overtaking is main issue in moving traffic. The collection of traffic data is also difficult because of these mix traffic conditions and unpredictable traffic movement. So forth in India, the analysis is being done using HCM methodology, which is based on US traffic conditions but Indian traffic conditions are much different than the US traffic conditions. In simulation of traffic the models are of two types which are known as macroscopic and microscopic models, the macroscopic one is used when the traffic

process with aggregate quantities is need to be discussed and the microscopic one is used to describe the behaviour of individual driver/vehicle and their interaction with respect to roadway geometry.

India is a country with mixed traffic flow conditions and abrupt lane change behaviour. The main problem has been seen on highways as the heavy vehicles are moving in inner lanes with slower speed due to their slower speed other categories of vehicles like cars and two wheelers have to reduce their speeds and they try to overtake from the opposite direction which is not good as per the guidelines, as there is no space available in the right direction to overtake. Therefore, it is very difficult to apply any available conventional methods for analysis of traffic flow. Therefore, calibration of traffic flow models is required to set the parameters values which can replicate the real world scenario.

In the field of calibration of parameters to get the most effective parameters only few works have been done in India. It is necessarily required to set criteria for better analysis, and practice under Indian traffic conditions where no lane behaviour exists and, drivers accelerate vehicles and move in any lane based on the available effective sight distance to overtake leading vehicle. While overtaking, vehicles move close to each other for a while and then when they find a gap they are used to overtake. When vehicles are overtaking then some kind of parameters like headway, following distance, follow-up time etc. need to be taken under consideration but they are not easily available so we need to have video graphical survey to get data but that data is not that much accurate as it is difficult to predict the field conditions. Calibration of such kind of parameters will help to get our data up to maximum satisfaction level of actual field data. The calibrated result is now comparable with actual field conditions; there are so many methods available to compare field data with calibrated data.

LITERATURE REVIEW

Fellendorf et al. [1] validated microscopic traffic flow model VISSIM in different real-world situations. They suggested that the VISSIM after its calibration shows most realistic driving behaviour. Dey et al.[2] developed a computer simulation program for two lane highway in Indian traffic conditions. The program can handle all types of vehicles as well as mixed traffic condition Found estimated capacity is lower when compared to US condition because of slower operating speed of vehicles, it was also reported that drivers in India are more aggressive than their counter parts in Germany or US. Velmurugan et al. [3] have developed speed – flow equations based on of different vehicle types for eight lane divided urban expressways using micro-simulation model VISSIM. Authors found the roadway capacity of eight lane divided highway is about 11435 PCU/hr/direction and main percentage error in speed is ranging between 2 to 15%. Praveena et al. [4] tried to find the applicability of various performance measures under mixed traffic condition only for two lane highways. Authors proposed threshold values for different LOS based on suggested parameter for mixed traffic conditions. Chandra [5] discussed the highway capacities values including single lane, multilane highways, expressways and freeways calculated by researchers in past few decades. Author revealed that capacity values in Indian road condition is varying by considering different parameters for different conditions, also Indian driver behaviour is different and can be classified state-wise. Park et al. [6] developed a procedure for calibration of simulation models. Authors used Genetic algorithm (GA) as a base tool for calibration of simulation model VISSIM. The results clearly indicated that the calibrated parameters replicating the field conditions while defaults parameters showing significant discrepancies between simulated and field data. Hofmann [7] discussed very interesting facts on complexity of parameter calibration for simulation models. Author has introduced formal approach for the model calibration and made argument that on increasing the model size (number of parameters) calibration becomes computationally challenging even if excellent field data is available. Models are based on abstractions, idealization

and many disputable assumptions so the model calibration is a necessary step to be taken. Lownes et al. [8] did calibration of parameters and the measure of effectiveness was taken as capacity value. Author measured the variation in capacity for each driver behaviour parameter including look back distance. Method of simulation was applied using evolutionary algorithm to get most favourable results found close to default values. This methodology was also compared with traditional method of calibration and shown that this method performance is better. Mehar et al. [9] performed calibration of simulation model and developed speed flow curves for 4-lane divided highway. The speed flow curves from both field data and simulated data were compared. For the simulation only two driver behaviour parameters were taken into consideration i.e. CC0 (standstill distance) and CC1 (Time Headway in seconds) as these two parameters are the most effective parameters for calibration, the values suggested by Shukla and Chandra. Jingtao et al. [10] studied calibration of micro simulation with heuristic optimization methods and proposed a new heuristic calibration algorithm which is based on simultaneous perturbation stochastic approximation (SPSA) scheme. The results obtained using this technique have the same level of accuracy with considerably less iteration and less time as compared to other heuristic algorithms like Genetic algorithm (GA) and the trial and error iterative adjustment (IA) algorithm.

FIELD INVESTIGATION AND DATA COLLECTION

Field data was collected at different mid-block sections of multilane divided intercity highways. Five different sections of divided highway were identified and a field investigation was carried out. Section I is located at NH 58 which is a four lane divided intercity highway having unpaved shoulders. Section II, Section III and Section V are located on NH 163 and sections are four lane divided intercity highway having 1.5 m shoulder in both direction of travel. Section IV is located at NH 332. Video graphic method was used for collecting speed and volume data. A trap length of 50 metres was marked on highway sections to estimate the speed of vehicles by noting down the travel time. Traffic flow data was collected about 3 hours from 04:00 PM to 7:00 PM on Section I, four hours from 09:00 AM to 01:00 PM on Section II, 07:00 AM to 11:00 PM on section III, 09:00 AM to 11:00 AM on section IV and 03:00 PM to 06:00 PM on Section V. Vehicle type survey was also carried out to obtain the clear dimensions of different vehicle types and is given in Table 1. Traffic volume and speed data was extracted manually from the video recording played on big screen monitor in traffic engineering laboratory.

Tab. 1 - Dimension of vehicles.

Types of Vehicles	Length of Vehicles (m)	Width of Vehicles (m)
Standard Cars (CS)	4.11	1.50
Big Cars (CB)	5.00	1.70
Buses (Bus)	11.54	2.50
Autos (3W)	2.36	1.40
Two-Wheelers (TW)	2.0	0.60
Heavy Vehicles (HV)	10.21	2.40

DATA ANALYSIS

Data collected from the field is analysed using statistical techniques and Mathematical distributions are used to understand behaviour of the traffic flow. Vehicle composition data for different sections of highways are collected and are given in Table 2. Statistical tests are applied on speed and vehicle arrival rate and found that the speed of all vehicle types follows normal distribution and vehicle arrival rate follows poisson distribution. Field capacity is difficult to achieve on highways, because congestion condition is rarely occurring. To calculate field capacity value, literature based method is used which is given by Chandra et al. [11] based on the composition of the vehicles.

$$C_{mix} = 4950 - 24.1 \times P_{CB} - 65.7 \times P_{HV} - 20.6 \times P_{3W} + 34.8 \times P_{2W} \quad (1)$$

Where, C_{mix} is the capacity of the mixed traffic and P is the proportion of the respective vehicle type. Mathematical signs represent effect of vehicle type, either increasing capacity or decreasing. Capacity is calculated for all highway sections and results are given in Table 3. It was found that when percentage of heavy vehicle is more, capacity is less and vice versa. Chandra et al. [11] found that the capacity of the four-lane divided highway is 4950 vph and it is close to Section I. For the purpose of calibration of capacity, Section-I is taken into consideration for further analysis.

Tab. 2 - Vehicular Composition on different Sections of Multilane Highways.

Traffic Composition (%)					
	Section I	Section II	Section III	Section IV	Section V
	NH58	NH163	NH163	NH45 A	NH163
CS	41	31	11	27	20
CB	8	7	3	13	6
3W	3	5	22	9	12
LCV	3	3	5	8	7
HV	14	8	16	20	17
TW	34	46	43	23	45

Tab. 3 - Capacity for different Highway Sections

NH No.	Constant	Percentage Share				Capacity (vph)
		CB	HV	3W	2W	
NH58	4950	8	14	3	34	4958
NH45 A		13	20	9	23	3937
NH163		3	16	22	43	4869
NH163		6	17	12	45	5007
NH163		7	8	5	46	5753

CALIBRATION METHODOLOGY

Microscopic traffic simulation software VISSIM was used for the simulation work. Figure 1 shows calibration methodology for calibration as well as for validation of the model parameters. To develop microscopic simulation model initial steps were taken for input data which was extracted from the field studies. The input data included Speed distribution of each vehicle type, observed volume, number of lanes and lane width, vehicular composition, dimension of each type of vehicles. The driver behaviour such as car-following, lane-change and overtaking were also considered during calibration process. The calibration was done on the basis of field data and analysis to replicate the mixed traffic condition.

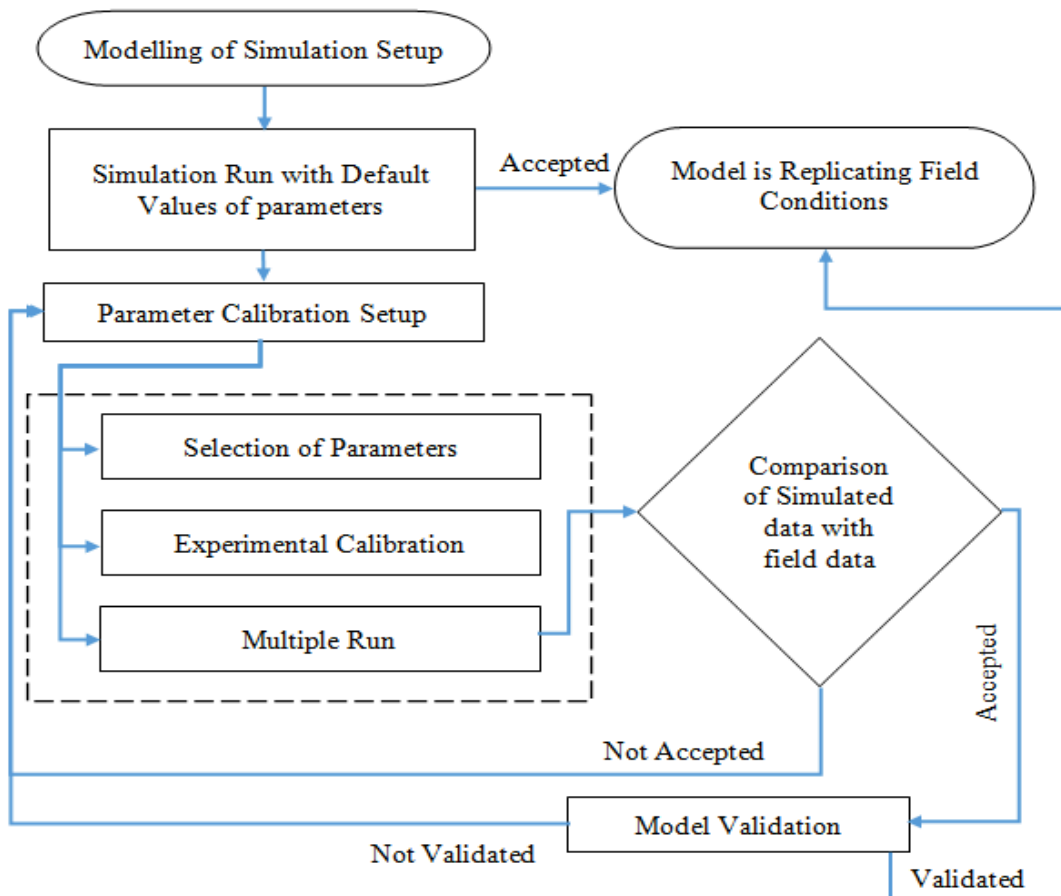


Fig. 1 - Calibration Methodology

DEVELOPMENT OF SIMULATION MODEL

The field data collected from the highway section NH 58 was used as input to the VISSIM and base link network was created.

Preparation of Base link network

A straight link of more than 1000 meters was created in VISSIM and inputs were assigned as per field data. A travel time section of 50 m was assigned at the 600 m away from the point of vehicle input that allowed vehicles to get warm up before reaching the travel time section. Vehicle type data such as length and width was assigned as per field data. Speed is given in terms of percentile speed, 15th, 50th and 85th percentile speed obtained from the field is given as an input in the desired speed distribution. Speed distribution for each vehicle type is given individually. The new traffic composition was created in VISSIM by assigning proportional share and desired speed profile of each vehicle type. Simulation runs were performed based on the default values of parameters. The speed flow relationship is drawn for simulated data and is overlapped with the field speed flow curves, significant difference has been noticed. Traffic volume data and Speed data are matching with the simulated data but when compared together, showing variations is shown in Figure 2 and hence calibration is required to match speed flow curve of field and simulated data. Mehar et al. [9] suggested that the effect of CC0 and CC1 is more on capacity and is used to calculate safety distance. So, Wiedemann 99 parameters are taken into consideration for the calibration purpose. For this work one more parameter i.e. CC2 following variation is considered.

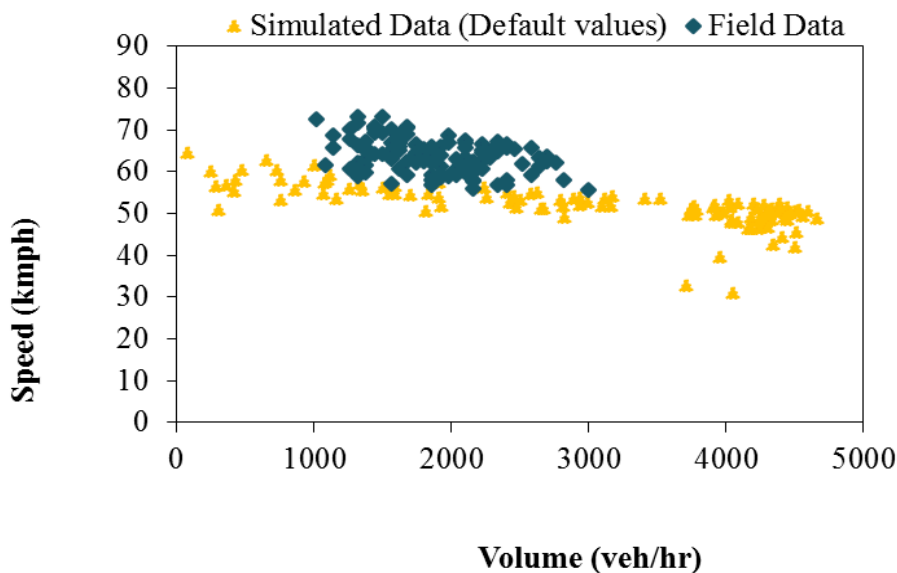


Fig. 2 - Comparison of Speed-flow Curves on four Lane Divided Highway

SENSITIVITY ANALYSIS

To calibrate the model, analysis was performed to check the sensitivity of the parameters which was done by making groups of parameters. In first trial, group of CC0 and CC1 was made and the parameter values were changed and effect of variation of parameter value was observed in flow values. In another set the group of CC1 and CC2 was made. Sensitivity analysis was performed for all the parameters and found that the sensitivity of CC1 was more.

To check the variation of CC1 on flow values, CC1 values changed from 0.5 seconds to 1.5 seconds and simulation has been run for 3 hours to get more accuracy. From the Figure 3, the effect on flow value on changing CC0 shows almost flat lines, which indicates that the effect of CC0 parameter is very less. On increasing standstill distance between vehicles, the capacity values decrease but with a small amount.

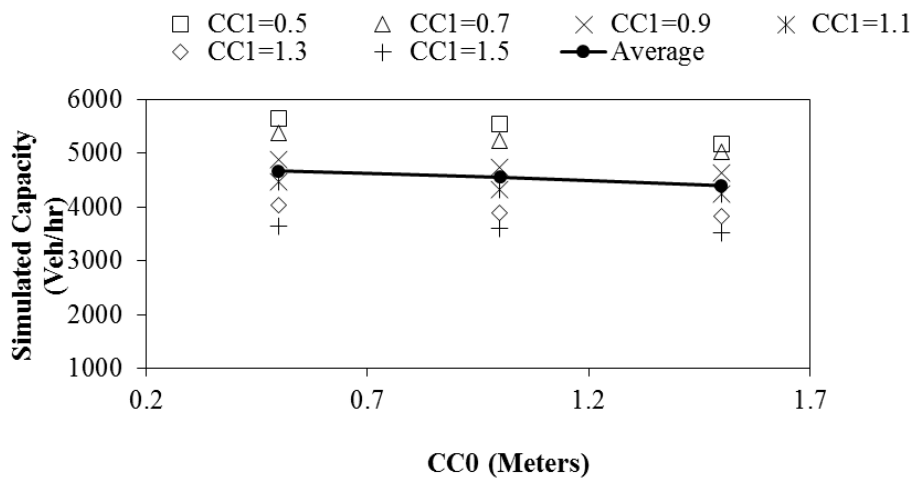


Fig. 3 - Variation in traffic flow values (CC0, m)

From the Figure 4, the effect on flow value on changing CC1 shows decreasing trend, which indicates that, the effect of CC1 parameter is more. On increasing the CC1 value the flow value decreases linearly. Practically, on increasing spacing between vehicles capacity of roadway section will decrease which is proved with the following curve.

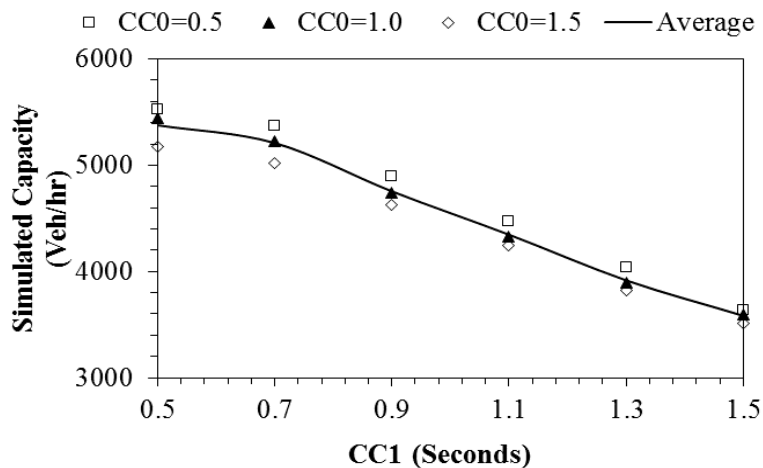


Fig. 4 - Variation in capacity due to CC1 (sec.) on different CC0 values

On increasing the parameter value (CC2), flow values decreases linearly and the desired field capacity exists in between these parameter values. Trend in Figure 5 also shows significance difference. On increasing both the parameters i.e. CC1 (Headway) and CC2 (following variation) the capacity value of the road section will decrease. Although, parameter CC2 does not show significance difference compared to CC1 parameter.

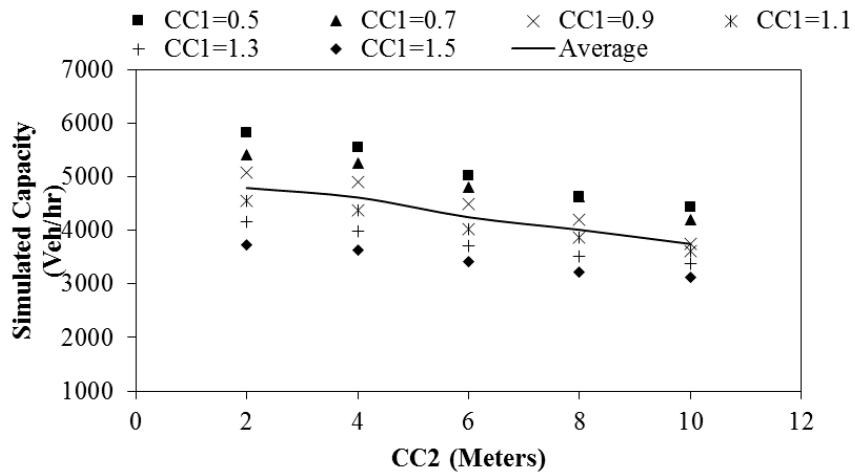


Fig. 5 - Variation in capacity due to CC2 (sec.) on different CC1 values

Figure 6 shows a drop in capacity value due to change in CC1 values for different CC2 combinations and found significant, groups have been made between parameters, calibration of all parameters is not possible at the same time, so sensitivity is discussed individually and found that each parameter affects flow value effectively. Some parameters affect more and some affect less. To understand the combined effect of parameters several statistics methods can be used.

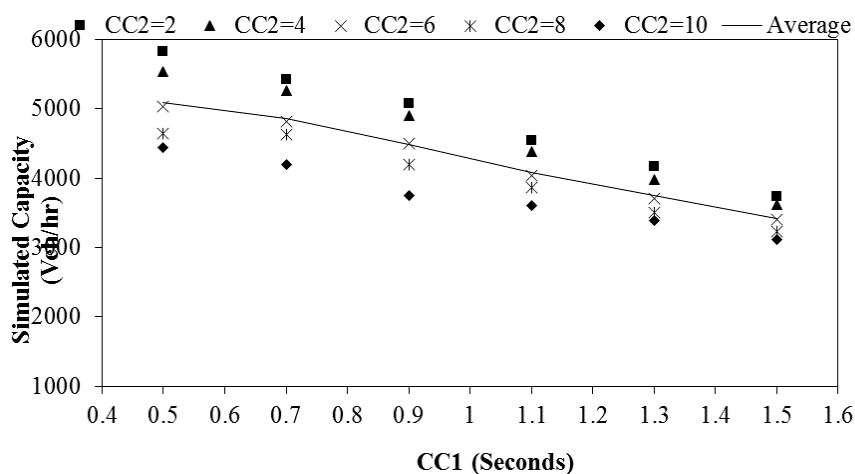


Fig. 6 - Variation in capacity due to CC1 (sec.) on different CC2 values

DEVELOPMENT OF OBJECTIVE FUNCTION

It has been noticed that parameters (CC0, CC1 and CC2) affect each other, to get the effect of three parameters at the same time regression analysis was done.

Tab. 4 - Range and Interval of driver behaviour parameters

Parameters	Range	Interval
CC0 (m)	0.5-1.5	0.5
CC1 (Sec.)	0.5-1.5	0.2
CC2 (m)	2-10	2

Table 4 shows the variation of the parameters, based on the variation simulated capacity was measured using speed-flow curves obtained from the simulated data. Equation 2 was prepared in which capacity is dependant variable and parameters are independent variables.

$$\text{Capacity} = 7034.2 - 183.6 \times \text{CC0} - 1801.4 \times \text{CC1} - 130.4 \times \text{CC2} \quad \dots\dots\dots (2)$$

Equation 2 can be used as an objective function for the purpose of the optimization as left side variable i.e. capacity is a measure of effectiveness. To get the optimum value of the parameters, optimization technique was used and constraints equations have been formed using the simulated data and ranges for the decision variables have been fixed for the case. The following constrained equations have been formed

$$6326.23 - 183.67 \times \text{CC0} - 1801.49 \times \text{CC1} \leq 5333 \dots\dots\dots (3)$$

$$6850.51 - 1801.49 \times \text{CC1} - 130.41 \times \text{CC2} \leq 5689 \dots\dots\dots (4)$$

$$5232.69 - 183.67 \times \text{CC0} - 130.41 \times \text{CC2} \leq 4788 \dots\dots\dots (5)$$

To solve the optimization problem, solver function was used in MS excel and template was prepared to solve optimization function for different values of decision variables and is shown in Figure 7.

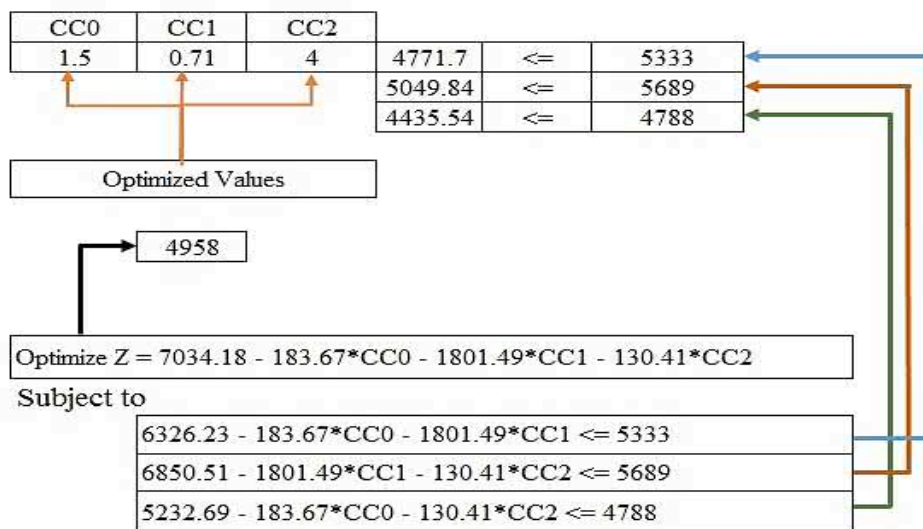


Fig. 7: Template to solve optimization problem using solver function in MS Excel

Two optimal points (i.e. 1.8, 0.53, 6 and 1.2, 0.74, 4) have been found and simulation was run for these parameter values. Speed flow curves obtained for the optimal points is shown in Figure 8 and found that the speed flow curves are replicating field condition.

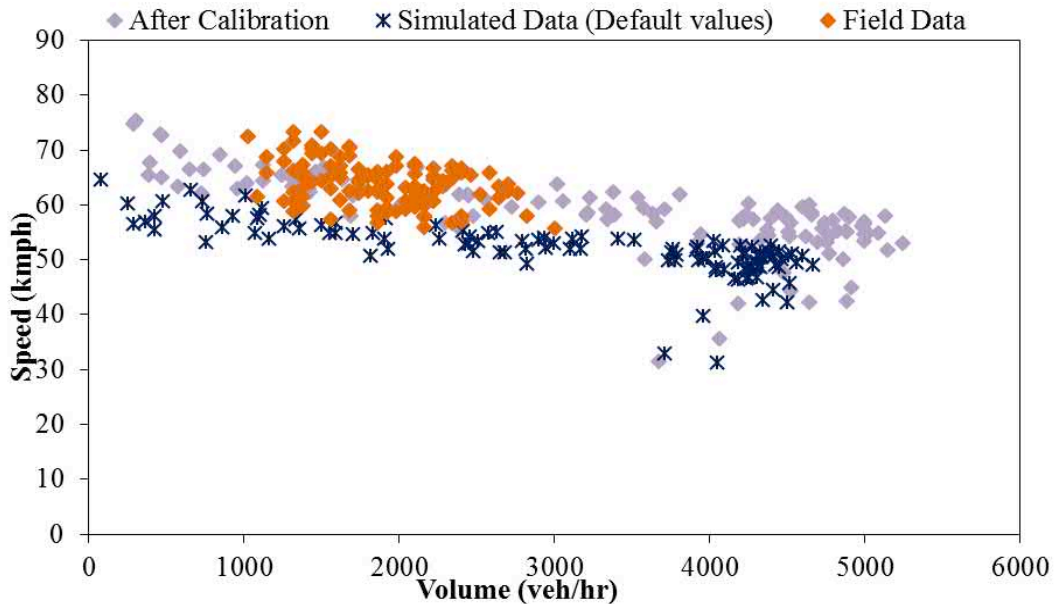


Fig. 8 - Speed flow comparison before and after calibration

VALIDATION OF CALIBRATED PARAMETERS

For the purpose of the validation, data set from NH-16, a 6-lane highway having 1.8 m paved shoulder was used. Six-lane highway section was selected in such a way that the composition of vehicle types should be closed to the composition of the data used for the purpose of the calibration. Six-lane highway used for validation was to make sure that calibrated values of CC0, CC1 and CC2 for four-lane highway were also used for to estimate the capacity of six-lane highway. Field data were analysed and descriptive statistic is given in Table 5.

Tab. 5: Descriptive statistics for field data

	CS	CB	LCV	Auto	TW	HV
Mean (km/h)	84.04	81.61	58.99	48.93	56.20	56.27
Std Dev (km/h)	13.32	18.63	13.34	5.82	11.87	11.37
Total Number	571	252	92	38	1191	311
Composition (%)	23.3	10.3	3.7	1.5	48.5	12.7
Minimum (km/h)	40.01	33.18	34.79	35.58	12.92	21.90
Maximum (km/h)	129.50	143.88	91.09	64.47	112.22	91.93
15th Percentile (km/h)	70.41	62.74	42.82	43.13	44.68	45.41
50th Percentile (km/h)	84.03	81.89	59.41	47.87	55.37	56.64
85th Percentile (km/h)	96.96	100.88	72.68	54.78	67.99	67.62

Calibrated values were used for the simulation of the data and it was found that the calibrated parameters of four-lane highway are able to reflect field traffic condition on 6 lane highway as well. Speed flow curves obtained after calibration are shown in Figure 9. Simulation was run using default parameters values and it was found that maximum flow value to 4925 veh/hr after using calibrated parameters the capacity value is coming to 6142 veh/hr.

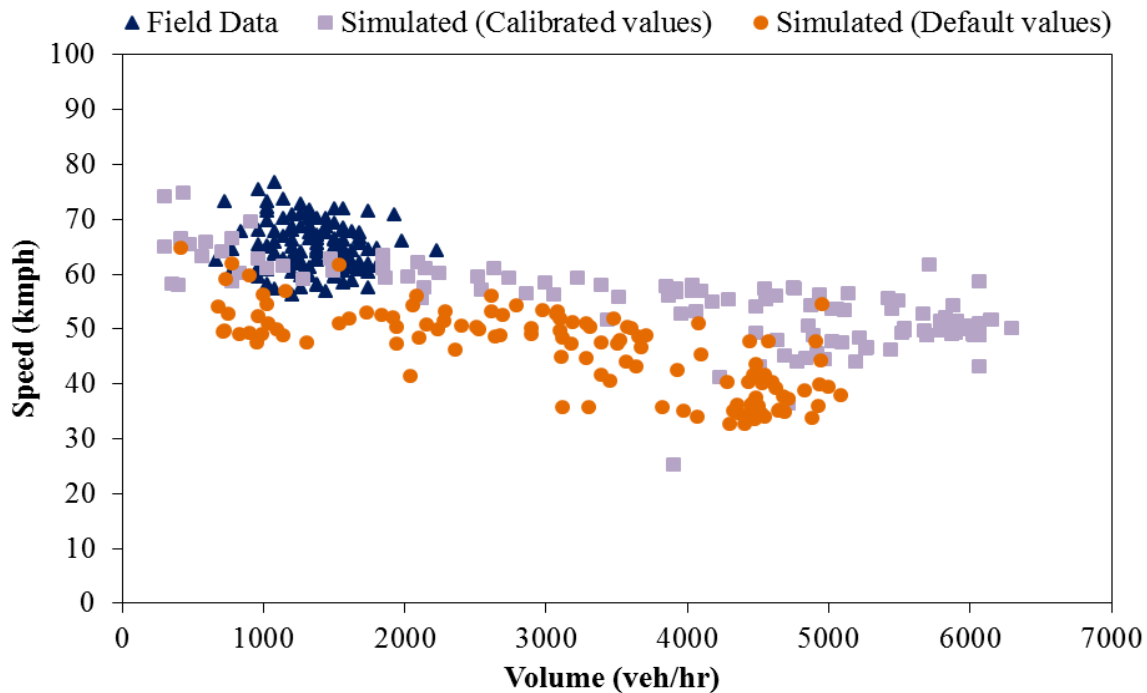


Fig. 9 - Speed flow comparison before and after calibration of parameters

CONCLUSION

- Speed data analysed on different sections of four lane divided highways were analysed to fit to mathematical probabilistic distributions. As a result, normal distribution was failed to fit the field speed data but Poisson distribution was found best fit for mixed traffic condition.
- Among the available popular microscopic simulation tools, model VISSIM 5.4:32 was found more flexible and user friendly for mixed traffic conditions.
- Random seed numbers (RSN) variation was found insignificant with volume output at 5% level of significance. Hence, any value of random seed can be taken for simulating mixed traffic flow. However, the change in RSN values changes the volume outputs inconsistently. RMSE estimated to compare field and simulated speed data were found less than 5% at different RSN.
- Sensitivity analysis performed on simulated capacity with the different combinations of model parameters (CC0, CC1 and CC2) were found significant at 5% level. However, CC0 and CC2 were found significant when tested at 1% significance level.
- Sensitivity analysis was performed for all the parameters and found that the sensitivity of CC1 is more. Slightly increase in CC1 parameter reduces the capacity consistently.
- Optimal values for CC0, CC1 and CC2 are 1.8, 0.53, 6 and 1.2, 0.74, 4 to obtained accurate capacity of multilane highways under mixed traffic conditions.

REFERENCES

- [1] Fellendorf M, Vortisch P., 2001. Validation of the microscopic traffic flow model VISSIM in different real-world situations. Transportation Research Board 80th Annual Meeting.
- [2] Dey PP, Chandra S, Gangopadhyay S., 2008. Simulation of mixed traffic flow on two-lane roads. *Journal of Transportation Engineering*, 134(9): 361-369.
- [3] Velmurugan S, Errampalli M, Ravinder K, Sitaramanjaneyulu K, Gangopadhyay S., 2010. Critical evaluation of roadway capacity of multi-lane high speed corridors under heterogeneous traffic conditions through traditional and microscopic simulation models. In *Journal of Indian Roads Congress*, 71(3): 235-264.
- [4] Penmetsa P, Ghosh I, Chandra S., 2015. Evaluation of Performance Measures for Two-Lane Intercity Highways under Mixed Traffic Conditions. *Journal of Transportation Engineering*, 141(10).
- [5] Chandra S., 2015. Highway Capacity Research on Inter-urban Highways in India. *Transportation in Developing Economies*, 1(1): 20-24.
- [6] Park B, Qi H., 2005. Development and Evaluation of a Procedure for the Calibration of Simulation Models. *Transportation Research Record: Journal of the Transportation Research Board*, 1934: 208-217.
- [7] Hofmann M., 2005. On the complexity of parameter calibration in simulation models. *The Journal of Defence Modelling and Simulation: Applications, Methodology, Technology*, 2(4): 217-226.
- [8] Lownes N, Machemehl R., 2006. Sensitivity of simulated capacity to modification of VISSIM driver behaviour parameters. *Transportation Research Record: Journal of the Transportation Research Board*, 1988: 102-110.
- [9] Mehar A, Chandra S, Velmurugan S., 2014. Highway capacity through VISSIM calibrated for mixed traffic conditions. *KSCE journal of Civil Engineering*, 18(2): 639-645.
- [10] Ma J, Dong H, Zhang H., 2007. Calibration of microsimulation with heuristic optimization methods. *Transportation Research Record: Journal of the Transportation Research Board*.
- [11] Chandra S, Mehar A, Velmurugan S., 2016. Effect of traffic composition on capacity of multilane highways. *KSCE journal of Civil Engineering*, 20(5): 2033-2040.

APPLICATION OF AEM IN PROGRESSIVE COLLAPSE DYNAMICS ANALYSIS OF R.C. STRUCTURES

Osama El-Mahdy¹, El-Sayed El-Kasaby², Hala Abusafa², Amr El-Gamal²

1. *Department of Civil Engineering, Faculty of Engineering at Shoubra, Benha University, Shoubra, Cairo, Egypt*
2. *Department of Civil Engineering, Benha Faculty of Engineering, Benha University, Benha, Egypt; email: amr.ali@bhit.bu.edu.eg, engamrramadan@yahoo.com*

ABSTRACT

The Finite Element Method (FEM) and the other numerical strategies are viably actualized in linear and non-linear analysis of structures. Recently, a new displacement based on Applied Element Method (AEM) has been developed. It is applicable for static and dynamic for both linear and non-linear analysis of framed and continuum structures. In AEM, the structural member is partitioned into virtual elements connected through normal and shear springs representing stresses and strains of certain portion of structure. FEM assumes the material as continuous and can indicate highly stressed region of structure, however it is difficult to model separation of element unless crack location is known. The main advantage of AEM is that it can track the structural collapse behavior going through all phases of the application of loads.

In the current research, the application of AEM is illustrated through a non-linear dynamic analysis. Progressive collapse simulation is conducted using Extreme Loading for Structures software (ELS), which follows the AEM. The experimental and analytical works carried by Park et al. [17 and 28] for 1/5 scaled 3 and 5 stories reinforced concrete structures are used for verification. Good matching between the experimental and numerical results has been obtained using ELS. Therefore, it can be confirmed that ELS is capable in simulating the structures' behavior up to collapse.

Furthermore, a study has been made to investigate the effect of considering the floor slabs on progressive collapse. The results show that considering slab in progressive collapse analysis of multistory buildings is important as neglecting the slabs' contribution leads to incorrect simulation and uneconomic design.

KEYWORDS

Applied element method, Progressive collapse analysis, Extreme loading for structures, Reinforced concrete structures, Dynamic analysis, Slab contribution.

1. INTRODUCTION

Progressive collapse became a hot point for research because of the several collapses that have occurred since the beginning of the twentieth century. For example, progressive collapse that happened in Ronan Point apartments tower - London in 1968, 2000 Commonwealth Avenue building – Boston in 1971, Murrah Federal Office building – Oklahoma in 1995 and World Trade Center – New York in 2001.

Therefore, many international structural codes and standards started to consider the progressive collapse resistance, such as the General Services Administration (GSA) [1] published in 2003, and the Unified Facilities Criteria (UFC) [2] by Department of Defense (DoD), USA published in 2005 and 2009. Precautions can be taken in the new design of structures to limit the effect of the local failure and resist progressive collapse. According to DoD guidelines, two general approaches are used for reducing the possibility of progressive collapse; Direct and Indirect Design. For the Indirect Design approach, the structure resistance to progressive collapse is considered implicitly through the provision of minimum levels of strength, continuity and ductility. Direct Design incorporates explicit consideration of resistance progressive collapse through two methods. One is the Alternate Path Method, which requires that the structure be capable of bridging over a missing structural element, with the resulting extent of damage being localized. The other method is the Specific Local Resistance Method, which seeks to provide sufficient strength to resist a specific threat.

Simulation of progressive collapse behaviour is not an easy job using available numerical techniques. Therefore, the use of highly efficient numerical modelling procedures for progressive collapse of reinforced concrete (R.C.) structures is needed. The available numerical methods for structural analysis can be classified into two categories. In the first category, model is based on continuum material equations. The Finite Element Method (FEM) is typical example of this category. The mathematical model of the structure is modified to account for reduced resistance of yielding components. However, to perform collapse far exceeding their elastic limit is a difficult task to many numerical methods. There are several limitations in adopting FEM in high non-linear case where crack has initiated and element is not detached from the structure, smeared crack approach is followed. However, smeared crack approach cannot be adopted in zones where separation occurs between adjacent structural elements. Therefore, FEM assumes the material as continuous and is able to indicate highly stressed region of structure but it is difficult to model separation of element unless crack location is known. While, Discrete Crack Methods assume that the location and direction of crack propagation are predefined before the analysis. With this group of the methods, analysis of concrete structures can be performed at most before collapse. The second category of methods uses the discrete element techniques, like the Rigid Body and Spring Model, RBSM [3] and Extended Distinct Element Method, EDEM [4]. The main advantage of these methods is that they can simulate the cracking process with relatively simple technique compared to the FEM. On the other hand, the main disadvantage is that crack propagation depends mainly on the element shape, size and arrangement. Analysis using the RBSM could not be performed up to complete collapse of the structure. Whereas, the EDEM can follow the structural behaviour from zero loading and up to complete collapse of the structure.

The Applied Element Method (AEM) is simple in modelling and programming and has high accuracy of the results with relatively short CPU time. Also, the response of the structure can be followed all the way to collapse involving the elastic stage, crack initiation and propagation, reinforcement yielding, large deformations, element failure and separation, rigid body motion of falling elements, collision between elements, and impact forces resulting from falling debris. This method can be easily applied to a wide range of applications; both for small and large deformation ranges under static or dynamic loading conditions, and for linear or non-linear materials. In this paper, AEM is used to perform the analysis.

There are many available researches that used AEM. Helmy et al. [5], used Extreme Loading for Structures (ELS) software which is based on AEM and following GSA and UFC guidelines to study the progressive collapse resistance of 10-storey reinforced concrete building. Helmy et al., [6] used ELS to investigate the effect of slab modelling considering slab reinforcement and slab thickness on progressive collapse. Lupoae and Bucur [7 and 8], presented a controlled implosion for structure collapse behaviour using ELS. Lupoae et al. [9], discussed the effect of infill walls provided on periphery of frame with and without openings on progressive collapse using ELS. Salem et al. [10], used AEM to propose an optimum and economic way of design to prevent progressive collapse of multi-storey reinforced concrete structure due to column removal. Khalil [11], studied a progressive collapse potential of 4-storey moment resisting steel building using AEM by following alternate load path method specified in UFC guidelines and made a comparison between results obtained by AEM and FEM. Dessousky [12], discussed a special algorithm to model the interface between the blocks and added to an Applied Element-Based solver. These algorithms predicted the strength and stiffness at interfaces when cracks opened and closed. Tagel-Din and Meguro [13], gave a simulation of collapse processes of scaled reinforced concrete structure by using AEM and compared with results obtained by shake table experiments. Raparla et al. [14], considered four bare frames designed as per Indian Standards for studying performance of building up to collapse using AEM. All bare frames were subjected to Northridge earthquake ground motion (freq. 1-4 Hz). Vikas et al. [15], performed linear static analysis of portal 2-D frame subjected to lateral loading to study the effect of mesh size and spring numbers and compared the results with FEM. Ismail, [16] studied the effect of the element size, spring distribution and shear stiffness of the spring on the accuracy of the AEM in obtaining the buckling load of a simply supported rectangular plate and compared the results with the theoretical solution.

2. OBJECTIVE

The objective of this paper is to verify the capability of AEM in simulating the non-linear dynamic analysis for progressive collapse of the experimental work conducted by Park et al., [17]. The 1/5 scaled 3 and 5 stories reinforced concrete structures are modelled using ELS software that follows the AEM and compares the numerical results with the experimental ones. Moreover, a study has been made to investigate the effect of contribution of the R.C. slab on the overall collapse mechanism.

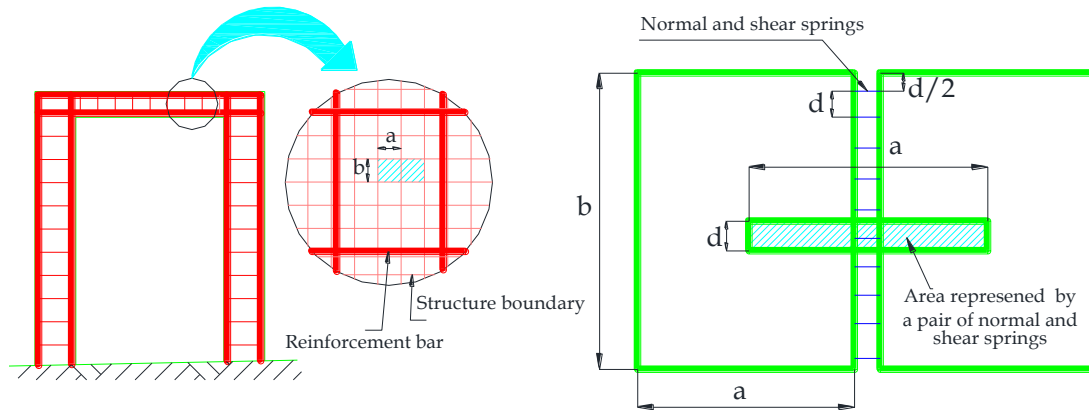
3. APPLIED ELEMENT METHOD OVERVIEW

The Applied Element Method (AEM), was developed by Tagel-Din and Meguro [13]. This method combines the advantages of Finite Element Method (FEM) and the Discrete Element Method (DEM). AEM discretizes the domain into a grid of rigid finite elements with six degrees of freedom, three translations and three rotations that represent the rigid body motion of the element located in the geometric centre of the element as shown in Figure 1. The connection of the elements is established through a mesh of springs on the contact faces of the elements, Meguro and Tagel-Din [18]. Two elements shown in Figure 1-b are assumed to be connected by one normal and two shear springs located at contact points, which are distributed around the elements edges. Each group of springs completely represents stresses and deformations of a certain representative volume of the element as illustrated in Figure 1-b. The spring stiffness is determined as shown in Equations 1 and 2.

$$K_n = \left(\frac{E \times d \times t}{a} \right) \quad (1)$$

$$K_s = \left(\frac{G \times d \times t}{a} \right) \quad (2)$$

Where, K_n is the stiffness of normal spring; K_s is the stiffness of the shear spring; d is the distance between the springs; t is the element thickness; a is the length of the representative area; and E and G are the Young's modulus and shear modulus of the material, respectively.



(a) Element generation for AEM (b) Spring distribution and area of influence of each pair of springs

Fig. 1 - Modelling in AEM [18]

To consider the effects of collision, it is necessary to check the collision between elements during analysis. To simplify the problem, element shape is assumed as circle during collision. This assumption is acceptable if the element size is relatively small. Even in case of relatively large elements used, it may be reasonable because in the deformation range of collision, the sharp corners of elements are broken due to the stress concentration and the edge of the elements becomes rounded shape. Based on these assumptions, only distance between the centres of the elements is calculated to check collision, Tagel-Din [19]. Contact and collision forces are considered in the analysis through collision springs, which are added at the locations where collision occurs. These effects can be considered easily with high accuracy and without large increase of the CPU time.

Figure 2 shows the constitutive models adopted in AEM. For modelling of concrete under compression, Maekawa [20] and Okamura and Maekawa [21], model is adopted. In this model, the initial Young's modulus, the fracture parameter and the compressive plastic strain are introduced to define the envelope for compressive stresses and strains. Therefore, unloading and reloading can be conveniently described. The tangent modulus is calculated according to the strain at the spring location. After peak stresses, spring stiffness is assumed as a minimum value (1% of initial value) to avoid negative stiffness. This results in difference between calculated stress and stress corresponds to the spring strain. These residual stresses are redistributed by applying the redistributed force values in the reverse direction in the next loading step.

For concrete springs subjected to tension, spring stiffness is assumed as the initial stiffness until reaching the cracking point. After cracking, stiffness of springs subjected to tension is set to be zero. The residual stresses are then redistributed in the next loading step by applying the redistributed force values in the reverse direction. For concrete springs, the relationship between shear stress and shear strain is assumed to remain linear till cracking of concrete. Then, the shear stresses drop down as shown in Figure 2-b. The level of drop of shear stresses depends on the aggregate interlock and friction at the crack surface.

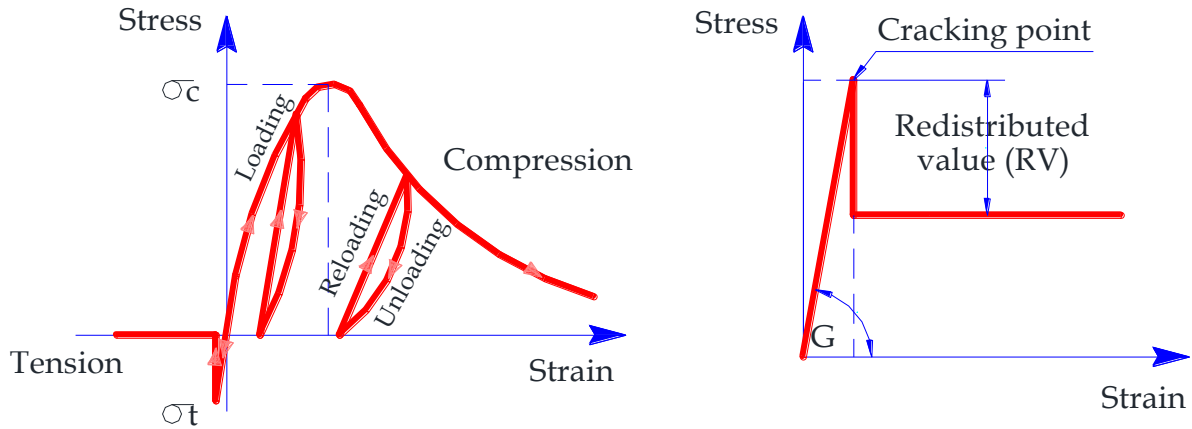


Fig. 2 - Tension, compression and shear models for concrete [20 & 21]

For reinforcement springs, the model presented by Ristic et al. [22], is used as shown in Figure 3. The tangent stiffness of reinforcement is calculated based on the strain from the reinforcement spring, loading status (either loading or unloading) and the previous history of steel spring which controls the Bauschinger's effect. The main advantage of this model is that it can consider easily the effects of partial unloading and Bauschinger's effect without any additional complications to the analysis. After reaching 10% tensile strain, it is assumed that the reinforcement bar is cut. The force carried by the reinforcement bar is redistributed, when it reaches the failure criterion, Tagel-Din and Meguro [23], by applying the redistributed force to the corresponding elements in the reverse direction.

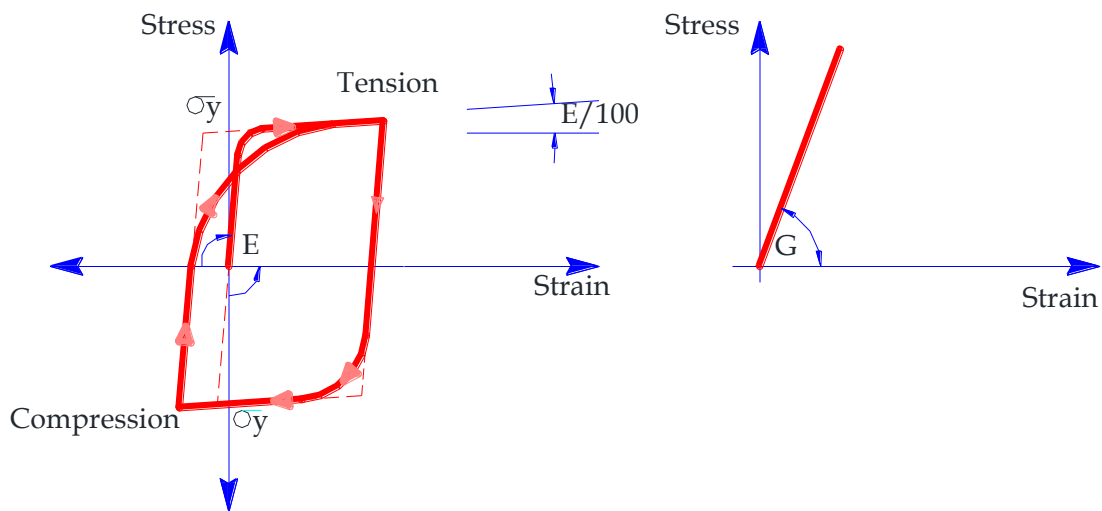


Fig. 3 - Reinforcement under axial stresses and shear stresses [22]

3.1. Dynamic Equation Formulation in of Large Displacement

In the AEM, the equation of motion under any dynamic loading is described in Equation 3, [13 & 24]:

$$[M]\Delta\ddot{u} + [C]\Delta\dot{u} + [K]\Delta u = \Delta f(t) + R_M + R_G \quad (3)$$

Where, $[M]$ is the mass matrix, $[C]$ is the damping matrix, and $[K]$ is the matrix of global nonlinear stiffness, $\Delta\ddot{u}$, $\Delta\dot{u}$ and Δu are the incremental acceleration, velocity, and displacement vectors, respectively, $\Delta f(t)$ is the incremental applied load vector, R_G is the residual load vector due to geometric changes and, R_M is the residual load vector due to cracking or incompatibility between spring stress and the corresponding strain. The effects of material nonlinearity are considered in R_M and $[K]$, [24].

After applying a small load increment, the structure geometry is modified and hence, incompatibility between external loads and other forces occurs. The main difference between the AEM and the conventional methods is that the geometrical stiffness matrix is omitted and its effects were replaced by adding the geometrical changes effects as an additional load vector R_G as shown in Equation 4.

$$R_G = f(t) - [M]\ddot{u} + [C]\dot{u} - F_m \quad (4)$$

It should be emphasized that this technique can be applied in both static and dynamic loading conditions. In case of static loading condition, the mass and damping matrices are set equal to zero. The main limitation in static analysis is that separation of elements is prohibited during analysis as it makes the stiffness matrix singular. On the other hand, analysing structures subjected to dynamic loading condition enables us to follow both geometrical changes of the structure and the rigid body motion during failure. As the deformations are assumed to be small in each load increment, small time increment should be used. In the following subsections, the matrices in Equation 3 are presented.

3.1.1. Formulation of stiffness matrix

The stiffness matrix components corresponding to each degree of freedom are determined by assuming a unit displacement in the studied direction and by determining forces at the centroid of each element. The element stiffness matrix size is (6x6). The matrix in Equation 5 shows the components of the upper left quarter of the stiffness matrix [24]. All used notations in this matrix are shown in Figure 4. It is clear that the stiffness matrix depends on the contact spring stiffness and the spring location.

$$\begin{bmatrix} \sin^2(\theta + \alpha)K_n & -K_n \sin(\theta + \alpha) \cos(\theta + \alpha) & \cos(\theta + \alpha)K_s L \sin(\alpha) \\ +\cos^2(\theta + \alpha)K_s & +K_s \sin(\theta + \alpha) \cos(\theta + \alpha) & -\sin(\theta + \alpha)K_n L \cos(\alpha) \\ -K_n \sin(\theta + \alpha) \cos(\theta + \alpha) & \sin^2(\theta + \alpha)K_s & \cos(\theta + \alpha)K_n L \cos(\alpha) \\ +K_s \sin(\theta + \alpha) \cos(\theta + \alpha) & +\cos^2(\theta + \alpha)K_n & +\sin(\theta + \alpha)K_s L \sin(\alpha) \\ \cos(\theta + \alpha)K_s L \sin(\alpha) & \cos(\theta + \alpha)K_n L \cos(\alpha) & L^2 \cos^2(\alpha)K_n \\ -\sin(\theta + \alpha)K_n L \cos(\alpha) & +\sin(\theta + \alpha)K_s L \sin(\alpha) & +L^2 \sin^2(\alpha)K_s \end{bmatrix} \quad (5)$$

The stiffness matrix in Equation 5 is for only one pair of contact springs. However, the global stiffness matrix is determined by summing up the stiffness matrices of individual pair of springs around each element. Consequently, the developed stiffness matrix is an average stiffness matrix for the element according to the stress situation around the element. This technique can be used in load and displacement control cases.

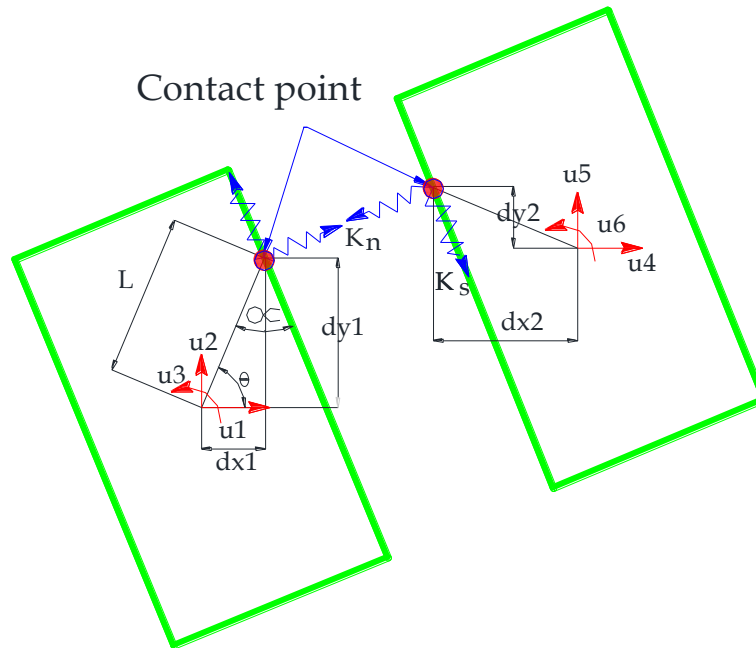


Fig. 4 - Element shape, contact point and degree of freedom [24]

3.1.2. Formulation of mass matrix

The mass of the rigid element is lumped at the element centre. As the size of the AEM element is relatively small, the effect of the lumped mass is similar to that of a distributed mass. The mass matrix of a square element of thickness t is determined in Equation (6) [24]:

$$\begin{bmatrix} M_1 \\ M_2 \\ M_3 \end{bmatrix} = \begin{bmatrix} D^2 \times t \times \rho \\ D^2 \times t \times \rho \\ D^4 \times t \times \rho / 6 \end{bmatrix} \quad (6)$$

Where, D is the element size, ρ is the material density, M_1 and M_2 are the element mass in X and Y directions, and M_3 is the element mass relative to the moment of inertia about the axis which passes through the element centre. The mass matrix is diagonal positive definite, so the diagonal elements of the mass matrix should be also positive. The addition of the mass matrix to the stiffness matrix in dynamic analysis prevents the occurrence of a singular stiffness matrix, especially where element separation occurs. Element separation is prohibited in static analysis, due to the absence of the mass matrix.

3.1.3. Formulation of damping matrix

In the non-linear response stage of R.C. structures, internal damping can arise due to the following [24]:

1. Concrete cracking.
2. Energy dissipation due to the loading and unloading of compression springs.
3. Unloading of reinforcement after yielding.
4. Energy dissipation due to crack opening and closure.
5. Friction between elements during contact.
6. Unloading factors during contact.

The sources of internal damping forces mentioned above, are automatically considered in the non-linear response of structures using the AEM. In the elastic range, these effects from internal damping forces are neglected. Thus, an external damping matrix, $[C]$, is required at this stage to account for internal damping [25]. The damping matrix is mass proportional and depends on the first mode of vibration, as in Equation 7.

$$[C] = 2\zeta\omega_1[M] \quad (7)$$

Where, ζ is the damping ratio, and ω_1 is the first natural frequency.

3.2. Solving the Nonlinear Dynamic Equation

The non-linear Equation 3 is implicitly solved utilizing a step-by step integration Newmark-Beta approach [26 and 27]. The equilibrium equations represent a linear system of equations for each step. The solution of the equilibrium equations is commonly solved using Cholesky upper-lower decomposition. Once elements are separated, the stiffness matrix becomes singular. However, the stability of the overall system of equilibrium equations is kept because of the existence of the mass matrix. Separated elements may collide with other elements. In that case, new springs are generated at the contact points of the collided elements.

4. VALIDATION OF AEM USING ELS

In this paper, Extreme Loading for Structure software (ELS) which is based on the AEM is used [25]. In order to validate the AEM models, the analytical results are compared with existing experimental data obtained from previously performed tests. The details of the comparisons for each case are described in this section. The effects of failure criteria on the collapse process are investigated, since these are anticipated to be one of the key parameters that can control the collapse phenomenon. Experimental test conducted by Park et al. [17] at Chonbuk National University is modelled using ELS (V. 2.3) to validate the AEM.

4.1. Experiment description

This experimental test studied the collapse of designed and fabricated 1/5 scaled 3 and 5 stories R.C. reinforced concrete frames. To consider the collapse possibility of upper dead load, fabricated R.C. frames were demolished by means of felling method. To observe the collapse behaviour of the R.C. structures during felling, displacements of horizontal and vertical directions were analysed

The R.C. structures for 3-story and 5-story models are illustrated in Figure 5. The reinforcement details of the structural components and the measured material properties are presented in Tables 1 and 2.

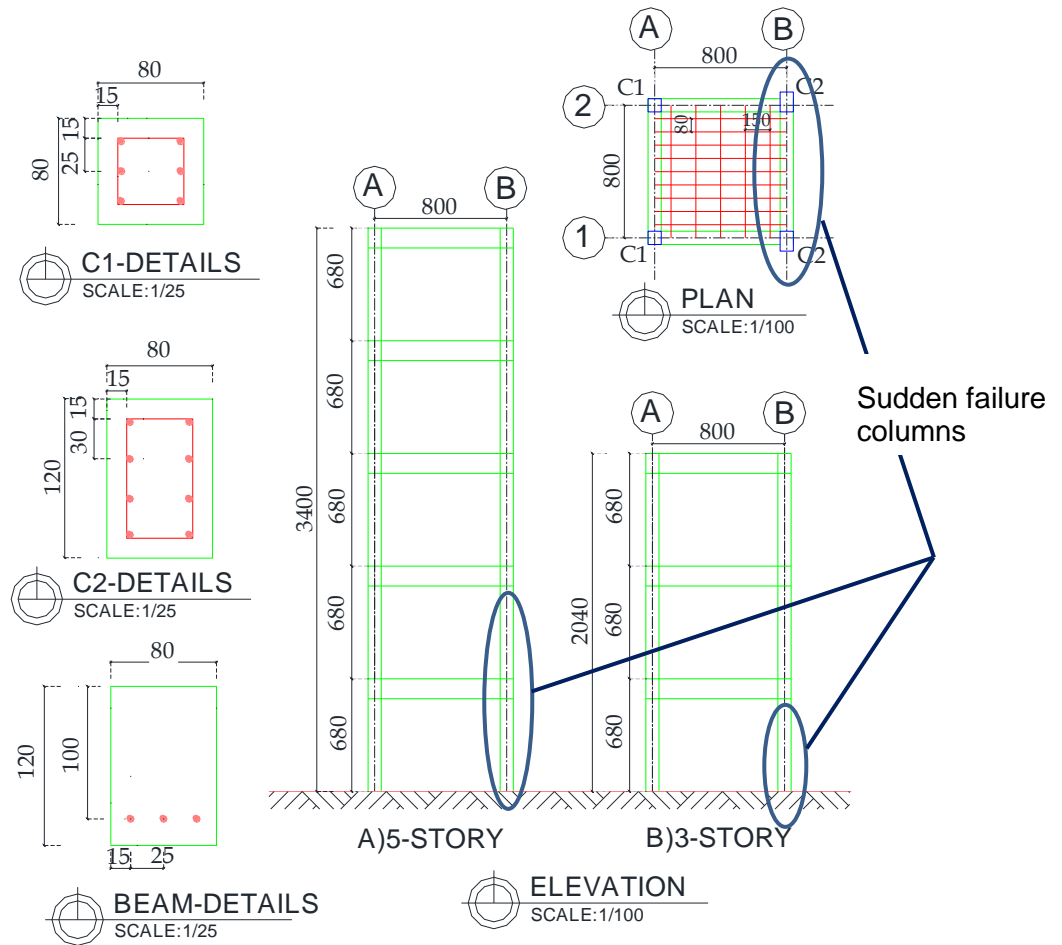


Fig.5 - Model dimension, cross section of members, and arrangements of steel reinforcement (mm) [17]

Tab. 1 - The steel reinforcement details [17]

Type	Scaled model reinforcement (Refer to KS D3552 low carbon steel wires)	
	Designation	Diameter (mm)
Main reinforcement	SWM-A, 4.00	3.81
Tie and distributing reinforcement	SWM-A, 3.20	3.18

Tab. 2 - Material mechanical properties [28]

Property	Young's modulus (MPa)	Shear Modulus (MPa)	Tensile yield stress (MPa)	Compressive yield stress (MPa)	Specific Weight (Kg/m ³)
Concrete	2.610E4	1.0210E4	3.1	31.7	2500
RFT	2.010E5	8.010E4	3.1310E2	3.1310E2	7840

4.2. Modelling and Simulating

As in the experiment, the numerical simulation of a sudden failure of the three floors structure, the two main columns labelled C2 at first-storey are performed in a dynamic after the self-weight of the structural components was completely loaded. Also, for the five floors structure, the numerical simulation of a sudden failure of the two main columns labelled C2 at first-storey and second-storey are performed in a dynamic after the self-weight of the structural components was completely loaded (refer to the marked columns in Figure 5). However, the sensitivity analysis for mesh, springs, time steps and calibration of the constitutive models should be firstly done.

4.2.1. Sensitivity analysis

A mesh sensitivity analysis is performed for the experimental works to study the effect of the element size and the number of connecting springs between elements. The experiments are analysed using three increasingly smaller-sized elements (approximately cubic shapes with edges of 100, 50 and 25 mm). For each different element size, two models are considered using 5 and 10 connecting springs for each pair of adjacent element faces. The convergence is considered to be achieved when the changes in the load-displacement result from one analysis to the next are too small to be visually noticeable. For all experiments, the estimates for load- displacement achieved for a mesh with edge of 50 mm and 5 connecting springs between element faces and therefore, this combination is considered an appropriate mesh and used for all tests reported in this paper.

A similar analysis is performed to calibrate the time step on model. Time effects are continuous from start till end of analysis. As the nonlinear dynamic phenomenon is very complicated to be solved using exact solutions, approximate numerical solution for the dynamic equation is adopted. The numerical solution is based on assumption of a small-time step that can follow the structural behaviour. The selection of the time step is very important. Having too short time step will result in very long analysis time. Whereas, using a large time step will result a short analysis time as well as a less accurate analysis. The numerical solution may fail to converge if the selected time step is large. Time - displacement curves are obtained using 0.10, 0.05, 0.01, 0.005, 0.001, 0.0005, and 0.0001 seconds loading steps and no noticeable differences were obtained between the resulting capacity curves. So, a time step of 0.001 second is used.

4.2.2. Calibration of the constitutive models

Due to the lack of information for steel stress-strain curves used in the experiments, the material characterization under tensile tests were simulated numerically and used to calibrate the parameters defining the Ristic constitutive model of steel [22]. The mechanical properties presented in experimental were used, considering a Young's modulus, a shear modulus presented in each experimental and a post yield stiffness factor of 0.01.

All concrete material characterization is used to calibrate parameters defining Maekawa [20], constitutive model for concrete, especially normal and shear contact stiffness ratio and also loading ratio. Many groups are examined and it is found that, the best group giving good simulation with experiment is [0.0001,0.000001,10]. Also, damping will be calibrated as 0%, 1%, 2%, 4%, and 5% damping ratios are examined. It is found that the best ratio which gives good simulation with experiment is 0%. Another important parameter is the separation strain. This parameter defines the strain value in the springs located between two neighbouring elements where the elements are considered to be physically separated. According to the ELS modelling manual [25], for reinforced concrete elements, the separation strain should be higher than the ultimate tensile strain of the rebar. Mesh division and reinforcement details similar to experimental works are shown in Figure 6.

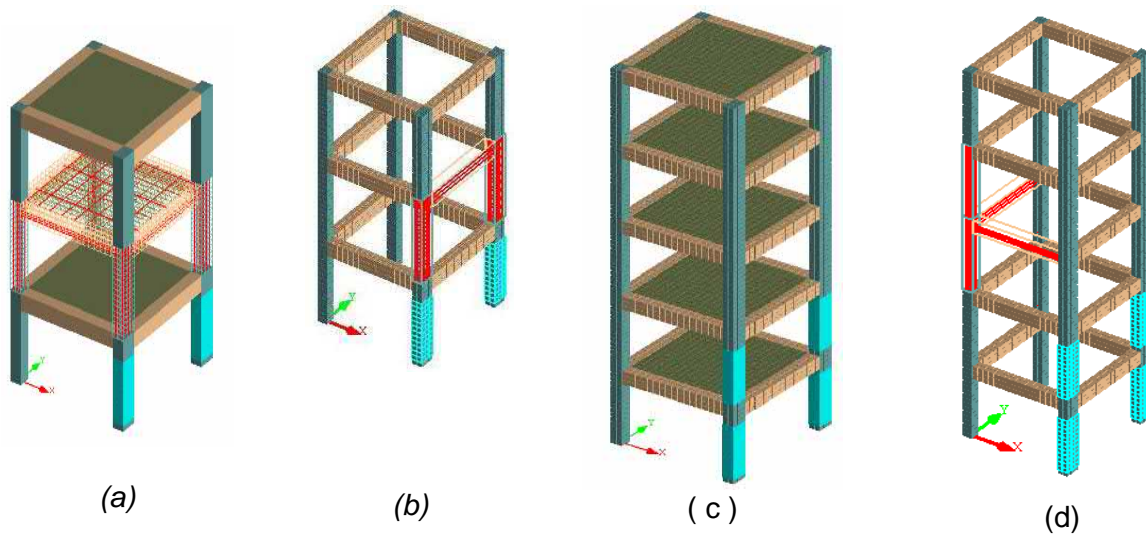


Fig. 6 - ELS Models for a) three-story with slab model, b) three-story without slab model, c) five-story with slab model, and d) five-story without slab model

5. RESULTS AND DISCUSSION

Figures 7a and 7b show the collapse shapes for the three-story structure at every 200 ms obtained from experiment and ELS model performed by Park et al. [28] and the author. From these figures, it can be observed that the collision with the ground occurs from time 800 ms to 1200 ms. Also, no plastic hinges were formulated until the building completely falls on the land at 1200 ms. The first cut off steel between column of second floor and first floor beam occurred at 1400 ms. The comparison shows that the results obtained from present model are similar to those obtained either experiment or analytically by Park et al. [28].

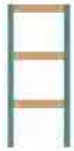
Three stories [28]		AEM Model (This work)	
Experimental	Analytical	with Slab	without Slab
			
			
			
			
			
			
			

Fig. 7a - Experimental and analytical collapse shapes for 3-storey building

Three stories [28]		AEM Model (This work)	
Experimental	Analytical	with Slab	without Slab
			
			
			
			
			

Fig. 7b - Experimental and analytical collapse shapes for 3-storey building

Similarly, Figures 8a and 8b show the collapse shapes for the five-story structure at every 200 ms obtained from experiment and ELS model performed by Park et al. [28] and the author. It can be observed that, the collision with the ground occurs from time 1000 ms to 1600 ms. Also, no plastic hinges formulated until the building completely falls on the land at 1000 ms and the first cut off steel between column of second floor and first floor beam occurred at 1400 ms. Again, the comparison shows that the results obtained from present model are similar to those obtained either experimentally or analytically by Park et al. [28].

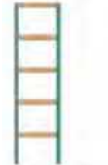
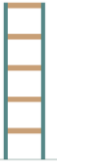
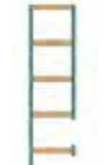
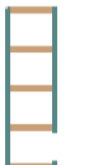
Five stories [28]		AEM Model (This work)	
Experimental	Analytical	with Slab	without Slab
			
			
			
			
			
			
			

Fig. 8a - Experimental and analytical collapse shapes for 5-storey building

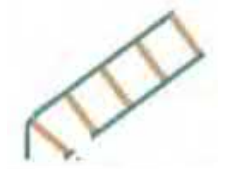
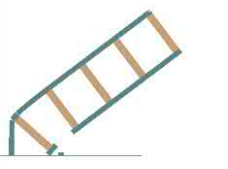
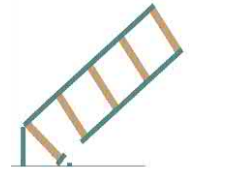
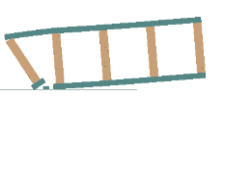
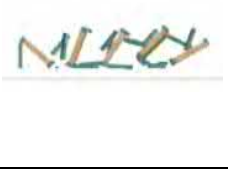
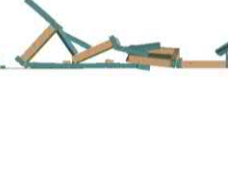
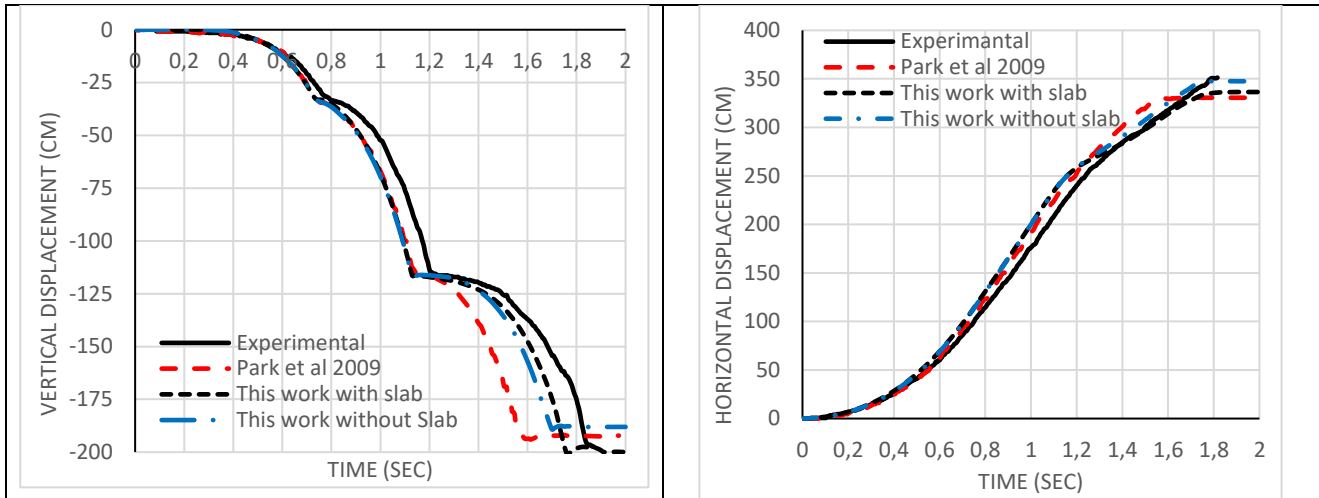
Five stories [28]		AEM Model (This work)	
Experimental	Analytical	with Slab	without Slab
			
			
			
			
			

Fig. 8b - Experimental and analytical collapse shapes for 5-storey building

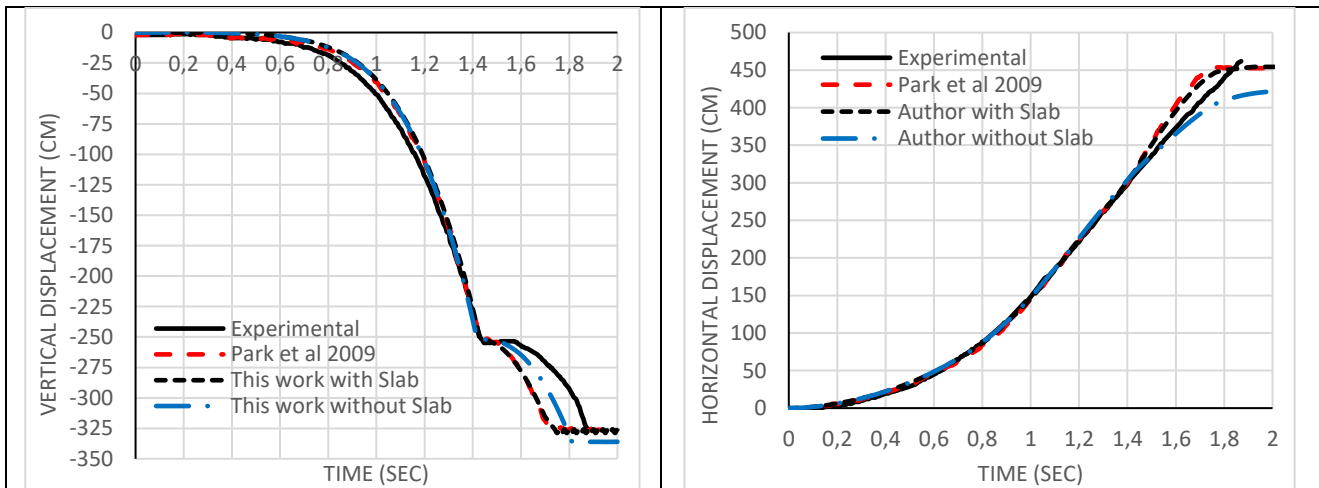
Figures 9 and 10 show the vertical and horizontal displacements time history of top point for three and five story buildings, respectively. It can be noticed that, the numerical results obtained using ELS are in good agreement with those obtained from experimental and analytical results performed by Park et al. [28]. Moreover, the present modelling gives better results than the analytical results by Park et al. [28].



a) Vertical displacement

b) Horizontal displacement

Fig. 9 - Displacement-Time history of top point for 3-Story building



a) Vertical displacement

b) Horizontal displacement

Fig. 10 - Displacement-Time history of top point for 5-Story building

6. EVALUATION OF CONTRIBUTION OF FLOOR SLABS

Numerical models are investigated where slabs do not exist for both three and five-story buildings, as depicted in Figures 7 to 10. In these models the beam weights are increased to account for slab dead loads. Hence, the density of the concrete beams is taken as 40 kN/m³ instead of 25 kN/m³.

From Figures 7 to 10, it can be noticed that the numerical ELS results with and without considering concrete slabs are matching the experimental results until the structure completely collision with the ground. After that, the collapse of the model without considering slab is different from both the experiment and the model considering slab because of the plastic hinge formulation in different places. The floor slab connects all beams and acts as a rigid diaphragm. On the other hand, every beam in the floor behaves like an individual element when slabs do not exist. Also, the contribution of slabs decreases the beams deflection and straining actions. Therefore, it is

confirmed that considering of slabs in progressive collapse analysis of multi-storey buildings is important as neglecting the slabs' contribution leads to incorrect simulation and uneconomic design.

7. CONCLUSION

In this study, a numerical investigation is conducted using Extreme Loading for Structures (ELS) software which is based on the Applied Element Method (AEM) and the results are compared to the experimental and analytical data performed by Park et al. [17 and 28]. The main findings in this study can be summarized as follows:

1. The applied element method is a trust tool for progressive collapse analysis of reinforced concrete structures.
2. Normal, shear contact stiffness ratio and loading and unloading stiffness ratio are very important factors in simulating progressive collapse.
3. Good matching between the experimental and numerical results has been obtained using ELS. Therefore, it is confirmed that progressive collapse behaviour of R.C. structures obtained using AEM is reliable and accurate.
4. It is confirmed that the importance of considering the floor slabs in progressive collapse analysis of multi-storey buildings as neglecting the slabs' contribution leads to incorrect simulation and uneconomic design.
5. ELS software can be recommended in further progressive collapse analyses of R.C structures.

ACKNOWLEDGEMENTS

The authors acknowledge *Benha University* for its effort to provide us with all scientific papers and references needed to complete this research. Also, the authors would like to thank Eng. *Mahmoud Abbas* for support in modelling by ELS.

REFERENCES

- [1] General Service Administration, GSA, "Progressive Collapse Analysis and Design Guidelines for New Federal Office Buildings and Major Modernization Projects"; Washington DC, 2003.
- [2] Department of Defense, DoD, "Design of Buildings to Resist Progressive Collapse", Unified Facilities Criteria (UFC, 4-023-03). USA; 2005 & 2009.
- [3] Kawai T, "Developments of The Rigid Body and Spring Model (RBSM) in Structural Analysis", Seiken Seminar Text Book, Institute of Industrial Science, The University of Tokyo, pp. 226-237, 1986.
- [4] Meguro K. and Hakuno M., "Fracture Analyses of Structures by the Modified Distinct Element Method", Structural Eng./Earthquake Eng., Vol. 6. No. 2, 283s-294s., Japan Society of Civil Engineers, 1989.
- [5] Helmy H., Hamed S. and Sherif M., "Computer Aided Assessment of Progressive Collapse of Reinforced Concrete Structures According to GSA Code", Journal of Performance of Constructed Facilitie, 2012.
- [6] Helmy H., Hamed S and Sherif M., "Progressive Collapse Assessment of Framed Reinforced Concrete Structures According to UFC Guidelines for Alternative Path Method", Engineering Structures, 42, pp. 127-141, 2012.
- [7] Lupoae M. and Bucur C., "Building Demolition – Positive Aspect of Progressive Collapse", MTA Review, XIX (4), pp. 399-408, 2009.
- [8] Lupoae M. and Bucur C., "Use of Applied Element Method to Stimulate the Collapse of a Building", Proceedings of SISOM and Session of the Commission of Acoustics, Bucharest, May 28-29, 2009.
- [9] Lupoae M., Baciuc C., Constantin D. and Pascau H., "Aspects of Concerning Progressive Collapse of a Reinforced Concrete Frame Structure with Infill Walls", Proceedings of World Congress on Engineering (WCE), London, UK, July 6-8, 2011.

- [10] Salem H. M., El-Fouly A. K. and Tagel-Din H. S., "Toward an Economic Design of Reinforced Concrete Structures Against Progressive Collapse", *Engineering Structures*, 33, pp. 3341-3350, 2011.
- [11] Khalil A., "Enhanced Modeling of Steel Structures for Progressive Collapse Analysis using Applied Element Method", *Journal of Performance of Constructed Facilities*, 2011.
- [12] Dessousky A. S., "Collapse Analysis of Stone-Blocks Structures under Seismic Excitation using Applied Element Method", *Twelfth International Colloquium on Structural and Geotechnical Engineering*, 10-12 December 2007.
- [13] Tagel-Din H and Meguro K., "Analysis of a Small-Scale RC Building Subjected to Shaking Table Tests using Applied Element Method", *Technical University of Tokyo, Institute of Industrial Science*, 1999.
- [14] Raparla H. B., Bodige N., Pradeep Kumar R., "2D Numerical Modeling of Progressive Collapse during Earthquakes: A Case Study on RC Bare Frame", *Proceedings of International Conference on Advances in Civil Engineering*, pp. 1-25, Department of Civil Engineering, K L University, Guntur Dist., A.P., India, 2011.
- [15] Vikas, G. , Paresh, V. and Digesh, J., "Analysis of Frame using Applied Element Method (AEM)", *Procedia Engineering* 51, pp. 176 – 183, 2013.
- [16] Ismail, M., "Sensitivity Analysis of the Applied Element Method for the Buckling of Uni-Axially Compressed Plates", *MSC, Applied Mathematics, North Carolina State University*, 2013.
- [17] Park, H., Suk, C., Lee, H., Yoo, J., Song, j. and Kim, S., "Collapse Behavior of Small-Scaled RC Structures Using Felling Method", *Journal of Korean Society for Rock Mechanics, Tunnel & Underground Space*, 17 (5), 381-388, 2007.
- [18] Meguro, K. and Tagel-Din, H., "Applied Element Simulation of RC Structures Under Cyclic Loading", *Journal of Structural Engineering*, 127(11):1295–1305, 2001.
- [19] Tagel-Din, H., "Collision of Structures during Earthquakes", *Proceedings of the 12th European Conference on Earthquake Engineering*, London, UK, 9-13 September, 2002.
- [20] Maekawa, K., "Nonlinear Analysis and Constitutive Models of Reinforced Concrete", *Tokyo, Gihodo Co. Ltd*, 1991.
- [21] Okamura, H. and Maekawa, k., "Nonlinear Analysis and Constitutive Models of Reinforced Concrete", *Gihodo Co. Ltd., Tokyo*, 1991.
- [22] Ristic, D., Yamada, Y. and Lemura, H, "Stress-Strain Based Modeling of Hysteretic Structures Under Earthquake Induced Bending and Varying Axial Loads", *Research Report No. 86-ST-01. Kyoto (Japan): School of Civil Engineering. Kyoto University*, 1986.
- [23] Tagel-Din, H. and Meguro, K., "Applied Element Method for Simulation of Nonlinear Materials: Theory and Application for RC Structures", *Structural Eng./Earthquake Eng., International Journal of the Japan Society of Civil Engineers (JSCE) Vol. 17, No. 2, 137s-148s, July 2000*.
- [24] Meguro K. and Tagel-Din, H. S., "Applied Element Method Used for Large Displacement Structural Analysis", *Journal of Natural Disaster Science*, 24 (1), pp. 25-34, 2002.
- [25] Applied Science International (LLC), 2010 www.appliedscienceint.com.
- [26] Bathe, K., "Solution of Equilibrium Equations in Dynamic Analysis", *Prentice Hall, Englewoods Cliffs, N.J.*, 1995
- [27] Chopra, A., "Dynamics of Structures: Theory and Applications to Earthquake Engineering", *Prentice Hall, Englewoods Cliffs, N.J.*, 1995.
- [28] Park H, Suk C, Kim S., "Collapse Modeling of RC Structures using the Applied Element Method", *Journal of Korean Society for Rock Mechanics, Tunnel & Underground Space*, 19 (1), 43-51, 2009.
- [29] Tagel-Din, H., "High Fidelity Modeling of Building Collapse with Realistic Visualization of Resulting Damage and Debris Using the Applied Element Method", *Report HDTRA1-09-P-0006*, 2009.

RESEARCH ON RISK CLASSIFICATION METHOD OF ASSEMBLY OCCUPANCIES

Hao Yu

School of Emergency Management, Henan Polytechnic University, Jiaozuo, Henan, China

ABSTRACT

Due to the densely population and mobility characteristics of the crowd, generally accidents happened in assembly occupancies will trigger a chain reaction, and then bring heavy casualties and property loss, and result disastrous consequences. In the context of safety regulation resources limited, building risk classification system of assembly occupancies is important for "scientific predicting, and hierarchical controlling". In this paper, a software with a graphical user interface is designed using MATLAB GUI to analyze and calculate risks of stampede accident caused by gathered crowds in the video. A velocity extraction method based on cross-correlation algorithm is adopted, and the risk characteristic parameters such as velocity variance is also applied. In this way, real-time analysis and early-warning for risks of stampede accident in time and space can be achieved. Also, the algorithm is applied to the surveillance video of the stampede in Shanghai and its feasibility is proved. Empirical research shows that, the assembly occupancies risk rating model built in this paper has good effectiveness, simplicity and practicability, applies to the government safety regulation and organization safety management, and can improve the safety situation of assembly occupancies effectively.

KEYWORDS

Assembly occupancies; risk analysis; velocity variance; accident forewarning

INTRODUCTION

Since the 21st century, the modern public gathering places in the city have become common, and some undertake public functions such as religious places, sports venues, the public meeting places, etc. They are faced with potential threat in all kinds of large-scale activities, such as a large number of participants, complex risk factors, wide social impact and serious accident consequence. According to statistics, since 150 major crowded stampede, has killed 5867 people, and 12722 people were injured, Asian areas are prone to this kind of accident in this century [1]. In China, the 2004 Beijing miyun county crowded stampede accident on Rainbow Bridge, 37 people were killed and 37 injured [2]. In 2014, at Shanghai Chenyi square, the opponent of people form a hedge and caused crowded stampede, 36 people were killed and 49 injured [3]. This shows that this kind of crowded stampede happened in crowded places, large public activities have several prominent features, namely, complex causes, sudden, difficult to control, and easy to cause wounds and dies in groups [4]. It also makes study and guard against crowded stampede become extremely urgent demand in developing countries with the rapid population growth and relatively backward management.

Traditional large public activity dense crowd management mainly based on the human field monitoring and artificial video monitoring, which is very difficult to implement in the populated areas, and requires a lot of manpower and material resources. Moreover, omission, false positives, appear easily and it is difficult to ensure its accuracy and could not meet the needs of large public activity dense crowd management [5]. Therefore, to take effective intelligent video analysis technology is one of the ideal ways to solve this difficulty.

At present, the method based on intelligent video analysis is not only used in scientific research, but also in the safety management to the crowd in practice. This method has gradually become mature for dynamic scene visual surveillance technology. With strong applicability and credibility [6], it has derived a series of intelligent video surveillance system. For example, W4 system can be used to detect and track crowds in outdoor environment, and monitor their abnormal behaviour [7]; Pfinder system can make three dimensional reconstruction for indoor individual, and track individual in complex scene [8]; System developed by Carnegie Mellon university can monitor scenario group activities through networked multiple cameras and complete a long-time detection and tracking of multiple moving targets under complex scene [9]. But, basically, this kind of monitoring and control system is based on the monitoring and analysis of the individual. However, when large crowds gathered and crowded with each other, the human body movement is a kind of group behaviour, and the individual role is nearly lost [10]. So it is difficult to reflect crowd movement trend through detecting individuals, moreover, once overlap appears the detection and tracking error will increase. The most important thing is that the original system did not involve the inner mechanism of the crowded stampede happened in large public crowds gathering activities, so it cannot give a real and precise risk early warning information.

To make a real-time risk analysis for possible stampede of crowds that gathered in the large public activities, and to serve safety management of large public activity, this paper has designed a software algorithm which can be used to analyze the risk of crowded stampede, and has adopted image processing techniques based on cross-correlation theory to extract the crowd movement velocity field [11]. Besides it also uses the risk characterization method, which put forward by the Helbing and others [12], to extract the crowd movement velocity field information in risk quantification, and through man-machine interactive graphical user interface designed by the platform of MATLAB GUI, it allows the user to make synchronous risk analysis of imported video.

ALGORITHM DESIGN

(1) MATLAB GUI platform

MATLAB GUI is a powerful extensible system development platform, it provides the GUIDE development environment, which can be easy for the design of man-machine interactive graphical user interface and the corresponding function module development. By using the development environment, this paper has designed the algorithm software with a graphical user interface, which can be used to conduct risk analysis and calculation for monitoring video.

(2) Velocity field extraction algorithm

The velocity field is a physical field of velocity vectors at each moment, at each point. The velocity field algorithm was first proposed by Helman and Hesselink [13]. The core idea of this method is that the coordinate point of velocity field can be divided into two categories: the velocity vector of non-zero often singularity point and the velocity vector 0, and the singularity of the

streamline through the singularity and to describe the shape of the velocity field, the structure and evolution process.

Based on video analysis, traditional speed extraction algorithm which adopts the individual motion detection and tracking has formed many applications algorithm in the field of crowd's analysis [14]. Also some scholars use methods based on clustering low levels of particle trajectory [15] and simplify velocity field [15] to extract the mainstream of the crowd movement information, but they are not very accurate, especially under the condition of the population increased significantly. The applicability of the methods above is facing huge challenges, and its operation efficiency also falls sharply.

Therefore, this article uses the velocity field extraction algorithm based on cross-correlation algorithm [16-17], and the process of this method is as follows:

(1) To divide every frame image into smaller diagnosis windows, and define the centre of the window as a calculation point;

(2) The fast Fourier transform can be used to convert the original image from time domain to frequency domain;

(3) In the frequency domain, the two consecutive frames in the same position of two diagnostic window cross-correlation calculations, then the above results are fast Fourier inverse transformation.

(4) The origin of the displacement peak migration is the displacement of the window in the pixel space. In order to get real physical space displacement orthogonal projection transformation is also required. The displacement value and the time interval for two consecutive frames division can get the speed of the calculation point, which is the average speed of the diagnostic window.

(3) Risk characterization methods

Many researchers have tried to study the inner mechanism of the stampede occurred through the analysis of video data from the real crowded stampede, and analysis the dynamic process of crowd movement status and movement characteristic parameters before and after the accident, in order to get measured crowded stampede risk parameters and the threshold value.

The most representative is Helbing, who has put forward the concept of "population pressure", and is used to quantify 2006 hajj stampede in the change process of the risk, which can make warning for crowded stampede in advance. Its computation formula is:

$$P(\vec{r}) = \rho(\vec{r}) \cdot \text{Var}_{\vec{r}}(\vec{V}) \quad (1)$$

The speed variance press type calculation as follows:

$$\text{Var}_{\vec{r}}(\vec{V}) = \left\{ \left[V(\vec{r}, t) - \bar{U}(\vec{r}) \right]^2 \right\}_t \quad (2)$$

In formula, $\bar{U}(\vec{r})$ is the time t in the average velocity field.

Since then, Helbing and others also organize experiments and use the simulation verify the applicability and accuracy of "population pressure" [18]. Considering the case with large population, although local density is not completely consistent, but the difference is little, so speed variance can react time and space distribution characteristics of risk to a certain extent [19].

On the one hand, algorithm designed in this paper can make use of the velocity field information of extraction to draw the real-time velocity vector diagram and flow chart, and used to observe the whole crowd motion state; At the same time, calculate the scene of average speed of graph in the crowd, which along with the change of time, so that to see whether it has appeared in speed drop; Then the average speed of over a period of time is used to calculate the real-time speed variance spatial distribution, and to characterize the time-space distribution characteristics of risk.

On the other hand, in order to reduce the random interference in real-time information, also needs to take a fixed time interval, and to take average of the velocity field. It can draw the average velocity vector diagram and vector flow chart, watching the movement of population overall in a certain time period; At the same time, drawing the histogram of speed size distribution, used to observe the velocity distribution state, judge whether the crowd movement in a laminar flow, and other special stage go stop wave; In addition, drawing the direction of speed distribution, used to observe the crowd distribution state of direction of motion, judge whether the crowd movement in the one-way flow, two-way flow or the main direction of mixed and disorderly state; Finally is drawing space distribution, the average velocity variance need to calculate the overall average velocity field over a period of time, then the type (3) is used to calculate the speed of each moment, spatial distribution of variance matrix and average velocity variance for space distribution matrix, it can be more accurate and comprehensive description population as a whole movement lead to accumulation of risk distribution within a certain time.

APPLICATION CASE

(1) Video source

Based on the stampede of surveillance video to verify this algorithm, which happened in the Shanghai "12.31" Chenyi square, and the monitoring point is in the south of Chenyi square and time is December 31, 2014, and the frame rate is 25 frames/s, 704 x 576 pixels, 23:35:32, 23:31:18 - a total of 254 seconds to capture the analysis.

It can be observed from the surveillance video, the scenario is at a viewing platform, stairs in 23:35:05, namely someone in the bottom of the stairs down at the interception of 227 seconds in the video compression, and happened crowded stampede subsequently.

(2) Parameter input

In order to take projection transformation for the scene in the monitor video, and acquire real space displacement and velocity information, the software requires the user to input scene space coordinate parameters in turn. The process of parameter input needs to guarantee the corresponding of space coordinates and the pixel coordinates points, and the software also allows the user to check by the means of images, so that more intuitive to corresponding display the actual location and pixels points, and easy to check.

(3) Risk calculation

This software can implement synchronization analysis of risk profile of the crowded stampede in the crowd gathered in the video broadcast video. First by using the parameter calculation of space projection transformation matrix, at the same time to get the velocity field of each point in the pixel field and the actual space abscissa and ordinate matrix, and the information stored in the suffix for the .mat files and added to the GUI handles variable. Intervals of 1 s, after taking two frames to calculate a real-time velocity field, the two frames for 0.2 s between before and after two consecutive images. Games to calculate the speed of information including the pixels in the x, y direction matrix, the speed of the actual space x, y direction matrix, the actual speed

scalar matrix and the space average speed of the time value, the above information will be saved to the frame number naming suffix for the .mat, which on behalf of the real-time velocity information of the moment. In addition, the real-time speed calculation of variance of process will be carried out in accordance with the method of mentioned above, the actual average velocity in the x, y direction matrix, the speed of real-time speed variance matrix, maximum variance and spatial information such as the average value of variance can also be saved to a suffix for the mat files. Finally, the software will call all .mat data in the file into various analysis results, for users to real-time observation and judgment the crowds gathered the risks and their distribution state.

(4) Results analysis

Through analysis and calculation, we can get the average velocity vector diagram as shown in Figure 1, they represent respectively the accident before 75 ~ 100 s, 25 ~ 50 ~ 75 s, 50 s and between 0~25 s the average results of velocity vector field. We can find that, the crowd movement speed itself is not big due to the extremely crowded, but the individual has lost his self-control and had to follow the whole crowd surging, so the speed and direction is mixed and disorderly, and speed appears obvious zoning phenomenon, namely the speed of populations in an area is larger, and its neighbouring areas of the crowd movement did not occur. In the process of the crowd movement, accident within 0 ~ 25 s before the crowd movement speed increases suddenly, as shown in Figure 1 (d), it is extremely dangerous cause to crowd, in which the stampede immediately after this period of time.

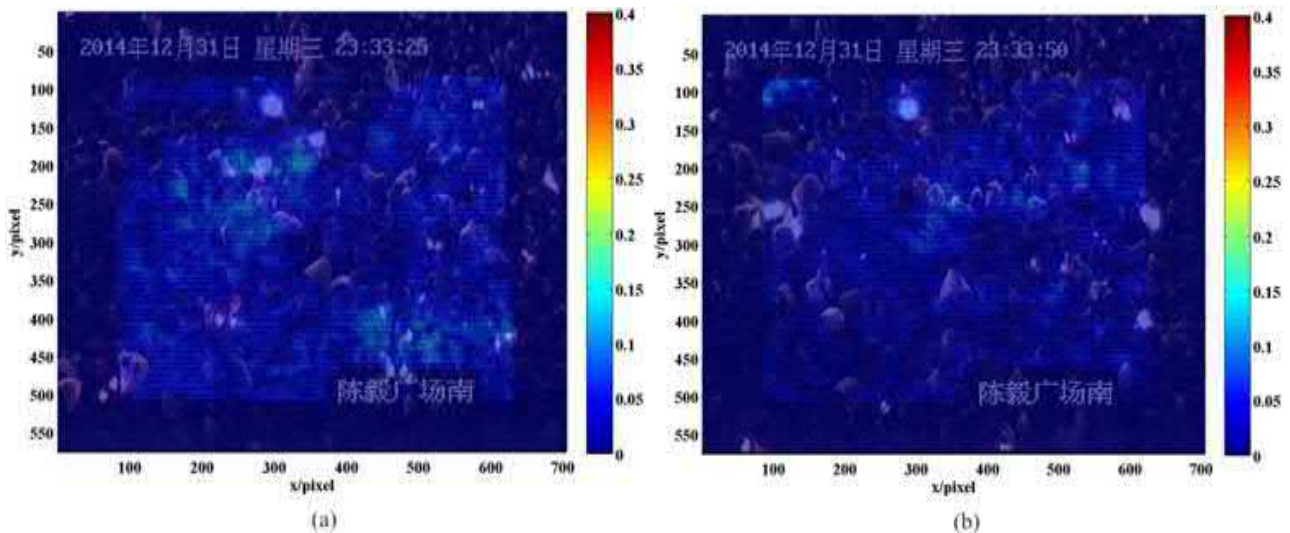


Fig. 1 - Respectively before the accident of 75 ~ 100 s, 50 ~ 75 s (a) (b)

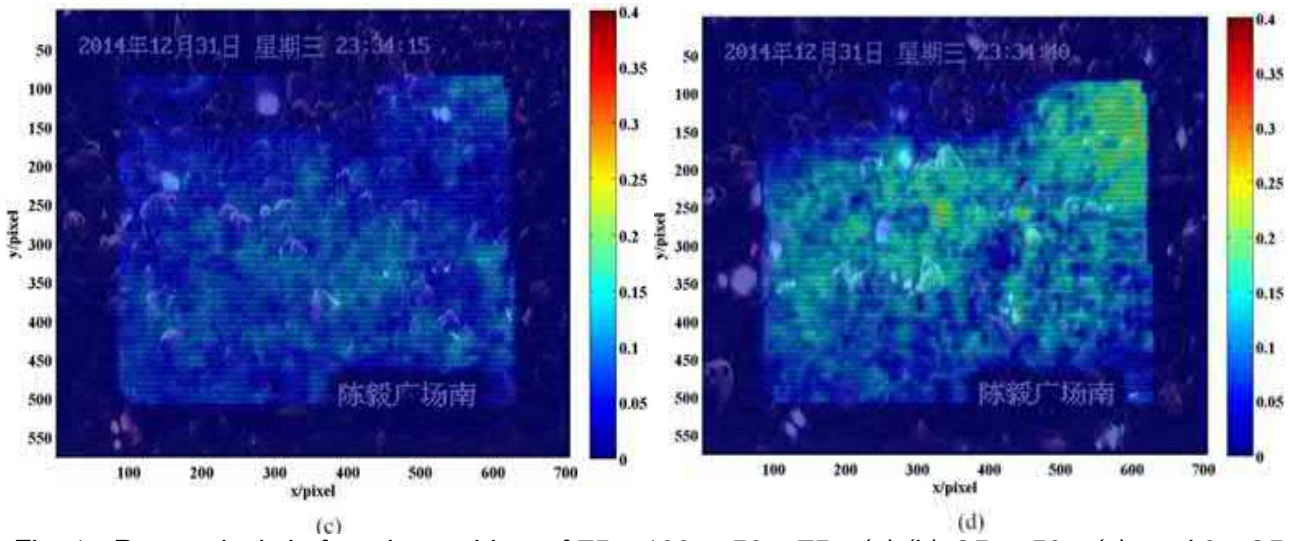


Fig. 1 - Respectively before the accident of 75 ~ 100 s, 50 ~ 75 s (a) (b), 25 to 50 s (c), and 0 ~ 25 s (d) the average velocity vector distribution.

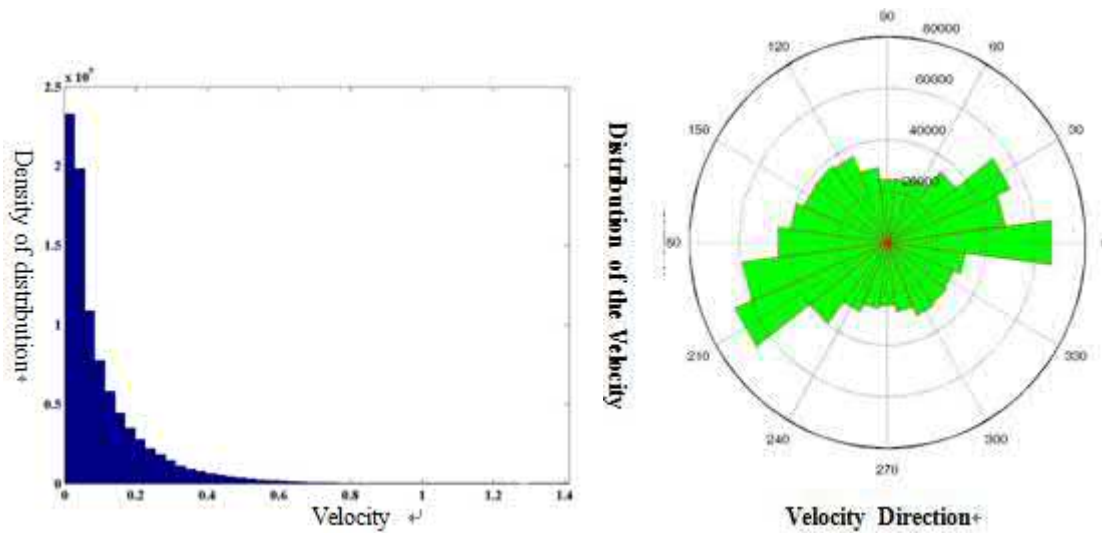


Fig. 2 - The velocity profile of the video time scale Fig. 3 - The velocity direction of the video time range

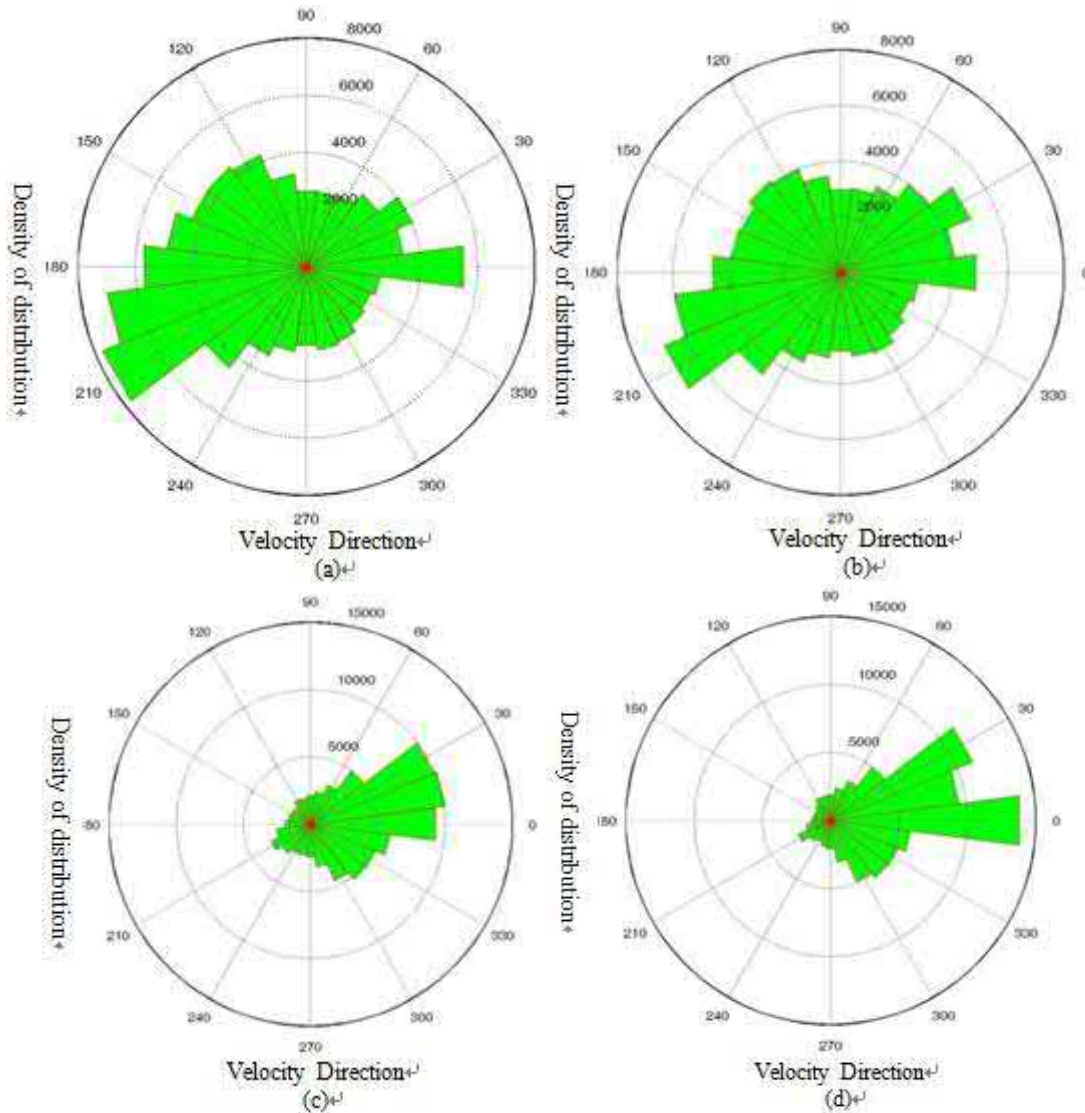


Fig. 4 - Respectively before the accident of 75 ~ 100 s, 50 ~ 75 s (a) (b), 25 to 50 s (c), and 0 ~ 25 s (d) direction of the velocity distribution

Figure 2 shows the velocity size map of the overall video time scale, and Figure 3 maps the velocity direction of the overall video time range. It can be found that the population moving speed is relatively slow from the overall, and flowing direction is random, so that every direction exists. It is difficult to ensure consistency of movement direction, and easy to make people into chaos. It can be observed viewing platform on the basic of stream of people is in a state of movement to the left, then a sudden change of direction, rapid movement to the right in the video before the accident of a period of time, which directly caused the stampede, as shown in Figure 4 (a, b, c, d).

The results of the analysis above can help managers to identify closely risk from multiple angles, but it belongs to the qualitative judgment basically, which needs to be combined with existing knowledge experience. Therefore, software also provides a more intuitive risk analysis results from the time and space.



(a)

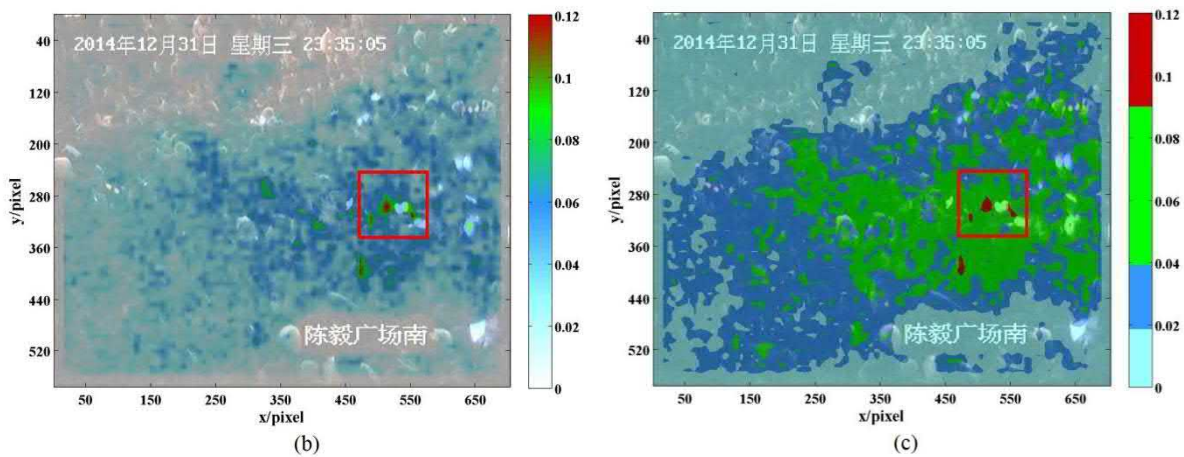


Fig. 5 - Video capture the accident moment (a), 210s~235s (accident happened in the 227s, namely 23:35:05) the average speed of spatial distribution of variance (b) And the space of the 210s ~235s risk classification figure (c)

From the point of the judgment of the time of an accident, it can be obviously found that speed in the whole period of time within the scope of the near peak appeared in the 200s and 215s, and trample accident occurs in the later 227s; Also appeared in 210s near peak velocity variance, and the difference is very apparent before and after the peak. This means that both of them above have crowded stampede's ability to provide risk early warning in advance in certain circumstances; From the angle of estimate the location of the accident, as shown in Figure 3, for the 210 s to 235 s in the video, that is a total of 25s average velocity variance of space distribution, and accident happened in the 227s. Darker area means higher risk, and it can be found in the figure that more obvious high-risk areas have basic match the actual position of stampede, and the specific area of the accidents can be roughly estimated, as shown in Figure 3 (a, b). If carried out in accordance with the spatial distribution of the average velocity variance risk classification, the crowd movement can be described as "sparse - normal - crowded - dangerous" four levels, corresponding to different velocity variance interval, as shown in Figure 3 (c). Speed variance is more conducive to take distinguish of the crowd gathered compared to make grade of crowd motion state from the angle of the speed size, and launched the emergency response plan to provide more reliable basis for emergency treatment.

DISCUSSION

- (1) In this study, we also need to realize that as a result of the crowded stampede mechanism understanding is not deep, we have some limitations in risk calculation and analysis methods, and it cannot apply to all situations.
- (2) In addition, before the accident monitoring phase, the corresponding risk characterization of threshold parameters is of great importance, both to reduce the false alarm and avoid the occurrence of omission, so that we need further research to better applied to crowd safety management of the crowd gathering filed, and provide accurate information for the accident early warning and things.

CONCLUSIONS

- (1) This research in view of the crowds gathering places may be crowded stampede, to help management to better identify and analyze the crowded stampede risks brought by the crowds gathered, has carried on the related algorithm and the software design.
- (2) Using the MATLAB GUI software development platform, design the relatively friendly graphical user interface, the velocity field extraction method based on cross-correlation algorithm, and the extraction of the velocity field and the velocity and quantitative calculation, the parameters of variance told the crowd gathered from the time and space at the same time the scene may be crowded stampede of risk analysis.
- (3) This research verifying the Shanghai "12.31" stampede video data by using the algorithm, acquire consistent results, and prove the applicability of the algorithm has certain.

ACKNOWLEDGEMENTS

This study is financially supported by the project of the humanities and social science fund project of the Ministry of Education of China (No. 16YJCZH026), by the project of philosophy and Social Sciences in Henan Province of China (No.2015CZH007), by the project of the Subject of Henan provincial government decision making of China (No.2016B290) and by the project of the Education Department of Henan Province of China (No.2017-ZZJH-188). Our gratitude is also extended to reviewers for their efforts in reviewing the manuscript and their very encouraging, insightful and constructive comments.

REFERENCES

- [1] ZHOU Jin-ke, LIU Cui-ping, JIN Feng-bin, et al. "An analysis on the casualty and causes of human stampede incidents". Chinese Journal of Disaster Medicine, 2015, 3(2): 67-71. (in Chinese)
- [2] ZHANG Qing-song, LIU Jin-lan, ZHAO Guo-min. "Discussion on cause mechanism of crowd crushing and trampling accident in large-scale public places", Journal of natural disasters, 2009, 18(6): 81-86. (in Chinese)
- [3] LU Wen-gang, CAI Yu-lan. "City Large-Scale Mass Character Activity Trample Incident Emergency Management Research: Based on the Analysis of Shanghai the Bund "12. 31" Especially Big Stampede". Urban Development Studies, 2015, 22(5): 118-124. (in Chinese)
- [4] ZHANG Hui, WU Ai-zhi, ZHANG Xin, et al. "The Response to Crowded Stampede Accident in Urban Public Places". Safety, 2015, 06: 16-18, 26. (in Chinese)
- [5] Ning Jun-li. "The Research on Crowds Gathered Risk Monitoring and Warning System in Crowded Places". Safety, 2013, 11: 59-60.

- [6] HU Wei-ming, TAN Tie-niu, WANG Liang, et al. "survey on visual surveillance of object motion and behaviors", IEEE Transactions on Systems, Man, and Cybernetics, Part C: Applications and Reviews, 2004, 34(3): 334-352.
- [7] Haritaoglu I, Harwood D, Davis L S. "W4: real-time surveillance of people and their activities", IEEE Transactions on Pattern Analysis and Machine Intelligence, 2000, 22(8): 809 – 830.
- [8] Wren C R, Azarbayejani A, Darrell T, et al. "Pfinder: real-time tracking of the human body", IEEE Transactions on Pattern Analysis and Machine Intelligence, 1997, 19(7): 780 – 785.
- [9] Lipton A J, Fujiyoshi H, Patil R S. "Moving target classification and tracking from real-time video", Fourth IEEE Workshop on Applications of Computer Vision, NJ: IEEE Press, 1998: 8 – 14.
- [10] Helbing D, Johansson A, Al-Abideen H Z. "Crowd turbulence: the physics of crowd disasters". arXiv preprint arXiv:0708.3339, 2007.
- [11] WENG Wen-guo, LIAO Guang-xuan, WANG Xi-shi. "A Diagnosing Method by DPIV Based on Cross-correlation Algorithm". Journal of experimental mechanics, 1999, 14(3): 323-329.
- [12] Helbing D, Johansson A, Al-Abideen H Z. "Dynamics of crowd disasters: An empirical study", Physical review E, 2007, 75(4): 046109.
- [13] Helman J, Hesselink L. Visualizing vector field topology in fluid flows. IEEE Computer Graphics and Applications. 1991, 11(3) : 36-46.
- [14] ZHAN Bei-bei, Monekosso D N, Remagnino P, et al. "Crowd analysis: a survey", Machine Vision and Applications, 2008, 19(5-6): 345-357.
- [15] ZHANG Dong-ping, TONG Chao, LU Ya-fei. "Dominant motions detection in dense crowds based on particle video", Computer Technology and Its Applications, 2012, 38(4): 123-125. (in Chinese)
- [16] LI Nan, Zhang Zhi-min. "Crowd behavior analysis based On velocity field simplification", Chinese High Technology Letters, 2012, 22(5): 490-496.
- [17] ZHANG Xiao-le, WENG Wen-guo, YUAN Hong-yong. "Empirical study of crowd behavior during a real mass event", Journal of Statistical Mechanics: Theory and Experiment, 2012(08): P8012.
- [18] ZHANG Xiao-le, WENG Wen-guo, YUAN Hong-yong, et al. "Empirical study on unidirectional dense crowd during a real mass event", Physica A: Statistical Mechanics and its Applications, 2013.
- [19] Moussaïd M, Helbing D, Theraulaz G. "How simple rules determine pedestrian behavior and crowd disasters", Proceedings of the National Academy of Sciences, 2011, 108(17): 6884-6888.